UNIVERSITÀ DEGLI STUDI DI TRIESTE

XXX CICLO DEL DOTTORATO DI RICERCA IN

FISICA

DETECTION AND ORBITAL ARCHITECTURE CHARACTERIZATION OF PLANETARY SYSTEMS AROUND COOL STARS

Settore scientifico-disciplinare: **FIS/05 ASTRONOMIA E ASTROFISICA**

DOTTORANDO / A
MATTEO PINAMONTI

COORDINATORE
PROF. LIVIO LANCERI
Livio Lanceri

SUPERVISORE DI TESI
DOTT. ALESSANDRO SOZZETTI
Alessandro Sozzetti

ANNO ACCADEMICO 2016/2017

Riassunto

Rivelazione e caratterizzazione dell'architettura orbitale di sistemi planetari intorno a stelle fredde

Le nane M si sono dimostrate dei target affascinanti per la ricerca di esopianeti, grazie alla crescente evidenza dalle survey di transiti (ad esempio Kepler) e di velocità radiali (ad esempio HARPS ed HARPS-N), anche se diversi ostacoli intralciano la ricerca e l'analisi di sistemi planetari intorno ad esse. Per queste ragioni, è di fondamentale importanza intensificare gli sforzi rivolti alla rivelazione e caratterizzazione di pianeti extrasolari intorno a nane M, poiché le nuove scoperte contribuiranno a portare il supporto statistico necessario allo studio di classi peculiari di pianeti, mentre la precisa caratterizzazione orbitale sia di sistemi noti che appena scoperti aiuterà a vincolare meglio i processi di formazione e migrazione planetaria. Le molte domande aperte sulle nane M ospiti e sui loro sistemi planetari, e lo sviluppi di nuove metodologie per investigarle, sono la base delle motivazioni del mio lavoro di Dottorato.

Nella mia tesi, per prima cosa presento la tematica dei sistemi esoplanetari intorno a nane M, sia dal punto di vista osservativo che statistico. Poi riporto il mio lavoro di analisi delle prestazioni di tre diverse tipi di analisi di periodogramma, il "Generalised Lomb-Scargle periodogram" (GLS), la sua versione modificata che sfrutta la statistica bayesiana (BGLS), ed il periodogramma multifrequenza chiamato FREquency DEComposer (FREDEC), motivato dall'ubiquità di sistemi multipli di pianeti di piccola massa. I risultati illustrati sostengono la necessità di rafforzare e sviluppare ulteriormente le più aggressive ed efficaci strategie per la robusta identificazione di segnali planetari di piccola ampiezza nei dati di velocità radiale. In seguito descrivo gli algoritmi ad alte prestazioni usati dal gruppo di ricerca di cui sono parte per la modellizazione di segnali Kepleriani singoli e multipli, e la loro applicazione sia su dati simulati di velocità radiale analizzati alla cieca, e contenenti rappresentazioni realistiche di segnali stellari e planetari, che su dati HARPS ad alta precisione di archivio di una stella M con un sistema multiplo di super Terre.

Riporto quindi i primi risultati che ho ottenuto nell'analisi di dati di velocità radiale raccolti come parte del progetto HADES (HArps-n red Dwarf Exoplanet), cioè la rivelazione di un pianeta di piccola massa e lungo periodo intorno alla nana M1 GJ15A, una delle stelle più vicine al Sole, che era già nota ospitare una super Terra di corto periodo. Poiché la stella ospite è parte di un sistema binario con la nana M GJ15B, ho derivato una soluzione orbitale migliorata per GJ15B e studiato un set di simulazioni numeriche dell'evoluzione a lungo termine del sistema planetario affetto da oscillazioni eccentriche di Lidov-Kozai, che provano che l'interazione dinamica può facilmente aumentare l'eccentricità del pianeta esterno, anche al di sopra dei livelli osservati. Per concludere, descrivo la strategia e i risultati preliminari dell'analisi bayesiana ancora in corso del campione HADES, che mira a calcolare la frequenza di pianeti intorno a stelle di piccola massa e la rivelabilità globale della survey.

Abstract

Detection and Orbital Architecture Characterization of Planetary Systems Around Cool Stars

M dwarfs have proven to be fascinating targets for exoplanetary search, from the growing evidence from transit (e.g., Kepler) and radial-velocity (e.g, HARPS, HARPS-N) surveys, even if several complex obstacles hamper the analysis and detection of planetary systems around them. For these reasons, it is pivotal to intensify the efforts towards the detection and characterization of extrasolar planets around M dwarfs, since new discoveries will help bring the statistical support still needed for the study of peculiar classes of planets, while the precise orbital characterization of both known and new systems will tighten the constraints on formation and migration processes. The many open issues on M dwarfs host and their planetary systems, and the development of new methodologies to investigate them, are the foundation of the motivation for my PhD work.

In my thesis I first present the topic of M dwarfs exoplanetary systems, both from the observational and statistical point of view. I then report my work on performance analysis of three periodogram tools, the Generalised Lomb-Scargle Periodogram (GLS), its modified version based on Bayesian statistics (BGLS), and the multi-frequency periodogram scheme called FREquency DEComposer (FREDEC), motivated by the ubiquitousness of multiple systems with low-mass components. The results illustrated reinforce the need for the strengthening and further developing of the most aggressive and effective ab initio strategies for the robust identification of low-amplitude planetary signals in RV data sets. I describe the high-performance algorithms for single and multiple Keplerian signals modeling used by the research group I am part of, and their applications both on blindly analyzed simulated RV measurements including realistic stellar and planetary signals, and on high- precision HARPS archive data of an M dwarf star with a multiplanet system of Super Earths.

I then report the first results I obtained from the analysis of RV data collected as part of the HADES (HArps-n red Dwarf Exoplanet Survey) project, that is the detection of a long-period low-mass planet orbiting the M1 dwarf GJ15A, one of the nearest stars to the Sun, which was already known to host a short-period Super Earth. Since the host star is part of a binary system with the M dwarf GJ15B, I derived an improved orbital solution for GJ15B and studied a suite of numerical simulations of the long-term evolution of the planetary system under eccentric Lidov-Kozai oscillations, which proved that this dynamical interaction can easily enhance the eccentricity of the outer planet, up to and even above the observed value. Finally, I describe the strategy and preliminary results of the ongoing Bayesian analysis of the full HADES sample, aiming to compute the occurrence rates of planets around small mass stars and the global detectability of the survey.

Contents

List of Figures

List of Tables

Chapter 1

Introduction

1.1 Historical and scientific context

The indirect search for extrasolar planets and the study of their structural and architectural characteristics is one of the most exciting and rapidly growing area of modern astrophysics.

When in 1995 the first extrasolar planet orbiting a main sequence solar-type star was announced by Mayor and Queloz (1995), it was already an astonishing object: 51 Pegasi b, recently renamed Dimidium, is a Jupiter mass planets with an orbital period of ~ 4 d, the very prototype of the exotic class of planets which became famous under the name of hot-Jupiters. The planet was discovered by measuring the small Doppler displacement in the absorption lines of the stellar spectra, which is now known as the Radial Velocity Method for exoplanets discovery. In the following years many more planets were discovered both from radial velocity measurements and with other techniques: the first exoplanet detected through the transit method was announced by Konacki et al. (2003), even if the transits of already known planets had been observed before (e.g. Charbonneau et al., 2000), and the first discovery through gravitational microlensing of a distant star followed just one year later (Bond et al., 2004).

Most of the first surveys hunting for exoplanets, which employed the radial velocity method, directed their efforts towards dwarf stars of spectral type G or K, usually in a range around the mass of the Sun ($\sim 0.7 - 1.5$ $M_\odot$). The large surveys were usually magnitude limited, thus preferentially selecting bright Solar-type stars. Even if some smaller mass stars were observed, the samples of targets selected were typically one order of magnitude smaller than for larger stars. This choice was spurred by many factors that helped the detection of giant planets around them, the only ones detectable with the precision of the early instruments: solar-type stars are relatively bright, thus easy to observe with high signal-to-noise ratios, have numerous absorption lines and are usually slow rotators, which facilitate the calculation of radial velocities. Examples include the OHP-ELODIE survey, which observed 324 G K dwarfs (Queloz et al., 2001), the Keck+Lick+AAT observation of 1040 F G and K stars (Valenti and Fischer, 2005) or the La Silla-CORALIE survey of 1650 stars between spectral class G and K (Tamuz et al., 2008).

The firsts extensive studies of the properties of the exoplanets discovered by these radial velocity surveys (e.g. Marcy et al., 2008; Udry and Mayor, 2008) revealed close-in giant planets ($M_p > 0.5$ $\mathrm{M_J}$, $a < 5$ AU) to be quite common, orbiting around $\sim 6-7\%$ of the observed stars, with a significant fraction ($\sim 15\%$) of hot-Jupiters ($a < 1$ AU). These planets were completely unexpected by the formation models, and this abundance of close-in orbits was even accentuated by recent transit discoveries, mostly from the Kepler satellite (Howard et al., 2012). As unexpected as the appearance of hot-Jupiters it was the high fraction of highly eccentric orbits ($e > 0.3$) which again contested the expectations from the study of our own Solar System (e.g. Lissauer, 1995). These evidences already forced to take into account new theories for formation and migration of extrasolar planets, to explain the unexpected observations (e.g. Murray et al., 1998; Ruden, 1999). One other fascinating result of the first surveys was that, even if the observational bias strongly hindered the observation of small rocky planets, their distribution appeared to rise quite consistently with decreasing mass (e.g. Udry and Mayor, 2008). As the number of observed planets grew larger and larger, the detection surveys started to focus on different type of host stars, eager to study how their characteristics influenced the orbiting planets.

Both early- and late-type main sequence stars were scarcely selected as targets by the early surveys due to different observational obstacles: high mass stars, while bright, present a small number of spectral lines as well as strong surface inhomogeneities which prevent precise radial velocity derivation (e.g. Galland et al., 2005), and M dwarfs are intrinsically faint, requiring larger telescope sizes to obtain high signal-to-noise spectra. Furthermore early studies considered M dwarfs to be unsuitable hosts for habitable exoplanets (e.g. Tarter et al., 2007, and references therein), which made them even less appealing for exoplanet searches.

Nevertheless some groups declined this course of action, and pointed directly to low mass M dwarfs, which are extremely common in the solar neighborhood, yearning for the discovery of smaller mass planets, fostered by the higher mass ratios. The early surveys ranged from the pioneering observation of 65 M dwarfs with the Mount Wilson 2.5-m telescope (Marcy et al., 1986) to the ELODIE and SOPHIE-N survey of 127 nearby stars (Delfosse et al., 1999). Finally the first exoplanetary systems around an M dwarf was detected simultaneously by Marcy et al. (1998) and Delfosse et al. (1998) around GJ876, which later was found hosting other three planets (Rivera et al., 2010, and references therein). The detection of the giant planet GJ876 b brought hope that many more similar discoveries would follow. Instead, several years passed before other M-dwarf Neptune-mass planets were detected (Butler et al., 2004; Bonfils et al., 2005). But the hunt didn't stop, aiming towards smaller and smaller masses in search for the missing planets.

In the last years most of the doubt concerning the exoplanet search around cool dwarfs were dispelled: with the arrival of high-precision spectrographs mounted on larger class telescopes, led by HARPS at La Silla (Mayor et al., 2003) and recently backed up by his younger twin HARPS-N at TNG Cosentino et al. (2012), high signal-to-noise high-precision spectra became easy to collect, and astronomers became fully able to benefit from the advantages offered exoplanet hosting M dwarfs: the smaller masses enhance the planet/star ratio,strongly increasing the amplitude of the Doppler signal in spectroscopic measurements (to the order of 5-10 m s^{-1}), due to the larger reflex motion of the star. Photometric measurements of planetary occultations are also fostered, because the higher radius ratio lead to deep transits (> 5 mmag) easily detectable even from ground modest-size telescopes (e.g. Sozzetti et al., 2013). At the same time the skepticisms about their habitability were lifted, as new studies judged it much easier than thought before, and also enhanced the likelihood of remote detection of life around them (e.g. Seager and Deming, 2010; Barnes et al., 2011b, and references therein). Due to the low luminosities of M dwarfs, the incident stellar fluxes required by planets to maintain surface temperatures compatible with the presence of liquid water are acquired at much closer orbits than in the case of the Solar System. This should produce a population of easily observable potentially habitable planets, since the detectability with most observing techniques strongly decreases with the distance from the host.

Many physical properties of low-mass stars are not yet known with enough precision to consent fine estimates of their planets characteristics, as is the case for the radius (e.g. Charbonneau et al., 2009, and references therein), the metallicity (e.g. Rojas-Ayala et al., 2010) or age (e.g. Jenkins et al., 2009). All of these uncertainties hamper the interpretation of detections and characterization of exoplanetary systems.

Nonetheless, the gathering evidence over the frequencies of different classes of planets orbiting around M dwarf and their differences with those for other types of central stars will greatly advance our knowledge of the numerous issues concerning the detailed mechanisms of stellar and planetary formations. It's becoming clear that giant gas planets are less frequent around low-mass than around Solar-type stars, as expected from theoretical studies (e.g. Laughlin et al., 2004; Mordasini et al., 2009), while small mass rocky planets are showing to be much more common than around solar-type stars (e.g. Tuomi et al., 2014, and references therein). Along with the familiar Solar System-like rocky and gas giant planets, the combined measurements of radius and mass of planets observed with both the radial velocity and transits techniques, revealed a wide range of densities. This could correspond to a myriad planetary structures and compositions, from planets like GJ1214 b, with a mean density of $\rho \simeq 1.9 \times 10^3$ Kg m^{-3} suggesting a rich water envelope comprising $\sim 50\%$ of its mass (Marcy, 2009), to extremely low-density giant planets like HATS-6 b with $\rho \sim 400$ Kg m^{-3} (Hartman et al., 2015), to high density super-Earths like LHS1140 b ($\rho \sim 12 \times 10^3$ Kg m^{-3} Dittmann et al., 2017).

However, it is just a handful of planets for which the mean density is known, and even for them there could be different structures that could match the observations: the true compositions of most planets from giant to Earth-like is unknown. And many more other open issues remains: how does the frequency of small-size planets vary with orbital architecture, planetary and stellar parameters? What is the influence of outer giant planets on the presence and properties of inner rocky planets? How many small-size planets are potentially habitable?

For these reasons, it is pivotal to intensify the efforts towards the detection and characterization of extrasolar planets around M dwarfs. New discoveries will help bring the statistical support still needed for the study of peculiar classes of planets. At the same time, the precise orbital characterization of both known and new systems will tighten the constraints on formation and migration processes.

M dwarfs have proven to be fascinating targets for exoplanetary search, even if several complex obstacles hamper the analysis and detection of planetary systems around them. Therefore, astronomers involved in the study of cool stars equipped themselves with more and more sophisticated tools in order to overtake those hurdles, in particular focusing on comprehending and treating the stellar noise strongly affecting the data. Yet there is still a long way to go. The many open issues on M dwarfs host and their planetary systems, and the development of new methodologies to investigate them, are the foundation of the motivation for my PhD work.

In conclusion it is clear how we live in the most exciting times for exoplanetary science, urged forward by the study of cool stars. The evidence is given by the extraordinary discoveries disclosed in these last few years, as the detection of a potentially habitable planet around the closest star to our Sun (Anglada-Escudé et al., 2016a) or the announcement of three rocky planets in the habitable zone of the M dwarf Trappist-1 (Gillon et al., 2017).

1.2 Chapter summaries

In Chapter 2, I present the topic of M dwarfs exoplanetary systems, both from the observational and theoretical point of view. I describe in details the Radial Velocity detection method, which is responsible for the first confirmed extrasolar planet discovery along with the confirmation and mass measurements of most of the sub-stellar mass companions detected with other techniques. It is also the method used for planetary discovery and characterization throughout the thesis. Then I describe the transit method, which, even if not used directly in my work, is crucial for the statistical knowledge of exoplanets, being the technique that discovered the most of the systems known today. An important drawback in the study of small mass stars is that the analysis of low-amplitude signals is often complicated by stellar activity, that can induce false positive signals mimicking the RV signature of a low-mass planet, and induce systematic effects comparable in magnitude to (and even exceeding) the amplitudes of the sought after Keplerian signals.

I then discuss the statistical properties known so far, mainly from the combined results of the HARPS spectrograph and of the Kepler satellite: planets in the range between Super Earths and Neptunes are not only very common, but they are often found in multiple systems, tightly packed close to the central star, and almost perfectly coplanar when seen in transit. I also briefly discuss the topic of circumstellar habitability in the case of M-dwarf host stars.

In Chapter 3, I report my work on performance analysis of periodogram tools, motivated by the ubiquitousness of multiple systems with low-mass components. I carried out a comparative analysis of the performances of three algorithms widely used to identify significant periodicities in radial-velocity (RV) datasets: the Generalised Lomb-Scargle Periodogram (GLS), its modified version based on Bayesian statistics (BGLS), and the multi-frequency periodogram scheme called FREquency DECComposer (FREDEC). These algorithms are applied to a suite of numerical simulations of (single and multiple) low-amplitude Keplerian RV signals induced by low-mass companions around M-dwarf primaries. I describe the results, which prove that the three period search approaches have quite similar performances in the limit of an idealized, best-case scenario, but start to differ when it comes identify more complex signals (including correlated noise of stellar origin, eccentric orbits, multiple planets). The largest discrepancy is recorded in the number of false detections: the standard approach of residual analyses adopted for GLS and BGLS translates in large fractions of false alarms ($\sim$30 per cent) in the case of multiple systems, as opposed to $\sim$10 per cent for the FREDEC approach of simultaneous multifrequency search.

The results illustrated reinforce the need for the strengthening and further development of the most aggressive and effective ab initio strategies for the robust identification of low-amplitude planetary signals in RV data sets. This is particularly important now that RV surveys are beginning to achieve sensitivity to potentially detect habitable Earth-mass planets around late-type stars.

This work has been published on MNRAS, with myself as the first author (Pinamonti et al., 2017).

In Chapter 4, I describe the high-performance algorithms for Keplerian signals modelling used by my research group, and their applications. The first is on blindly analyzed simulated RV measurements including realistic stellar and planetary signals, with the results compared with those of other groups techniques. This analysis was part of the Radial Velocity Fitting Challenge, in which our methods proved to be strongly efficient, ranking among the best techniques which took part in the challenge. We then applied our method on high-precision HARPS archive data of GJ273, an M dwarf star with a multiplanet system of Super Earths, in which we found a very-low amplitude (~ 0.44 m s^{-1}, $M_{\rm P} \sin i = 0.62$ M$_{\oplus}$) signal candidate. Due to the uncertain nature of such a small signal, I performed a series of numerical simulations, in which I studied different possible configurations of the GJ273 planetary systems, analysing the respective RV time series with the three algorithms studied in the previous chapter, to assess the reliability of the signal candidate. I present the preliminary results of this still ongoing analysis.

The results of the Radial Velocity Fitting Challenge have been published on A&A(Dumusque et al., 2017).

In Chapter 5, I outline the structure and purpose of the GAPS long-term program, which was aimed at the comprehensive characterization of the architectural properties of planetary systems as a function of the hosts' characteristics, and it has now concluded its last observations with the HARPS-N@TNG spectrograph. I report in details the characteristics of the instrument. I then describe the HADES (HArps-n red Dwarf Exoplanet Survey) project, a collaboration between the M-dwarfs GAPS research group and the Institut de Ciències de l'Espai de Catalunya (ICE), and the Instituto de Astrofísica de Canarias (IAC).

In Chapter 6, I report the first result I obtained from the HADES data, that is the detection of a long-period low-mass planet orbiting the M1 dwarf GJ15A, one of the nearest stars to the Sun, which was already known to host a short-period Super Earth. These detection was made combining 5 years of intensive RV monitoring with the HARPS-N spectrograph with 15 years of archival RV data from the LCES HIRES/Keck Precision Radial Velocity survey. The analysis is carried out with the techniques reported in the previous chapters, and confirms the presence and refines the orbital solution for the known 11.44 d period Super Earth, significantly reducing its mass to $M_{\rm b} \sin i_{\rm b} \simeq 3$ M$_\oplus$, and successfully models a long-term term trend in the combined dataset in term of a Keplerian orbit with period around $\sim$ 8400 days and an amplitude of 2.88 m s^{-1} ($M_{\rm P} \sin i \simeq 44$ M$_\oplus$), with low eccentricity ($e \simeq 0.21$). Since the host star is part of a binary system with the M dwarf GJ15B, I derived an improved orbital solution for GJ15B, combining HARPS-N RV measurements of the two stars with astrometric data from the WDS catalog. This allowed to perform a suite of numerical simulations performed to study the long-term evolution of the planetary system under eccentric Lidov-Kozai oscillations, which proved that this dynamical interaction can easily enhance the eccentricity of the outer planet, up to and even above the observed value.

In Chapter 7, I describe the ongoing Bayesian analysis of the HADES survey, aiming to compute the occurrence rates of planets around small mass stars and the global detectability of the survey. This is a collective effort of the GAPS M dwarfs group, which requires several steps to be completed over the next few months, like the homogeneous analysis of the full sample and the identification of activity signals in the ancillary photometric data from the APACHE and EXORAP programs. I illustrate the methods and initial results of this work, as well as report the results of similar analysis performed by other groups on different samples, to explain how our results will confirm and expand our knowledge of the architecture of planetary systems around small mass stars.

In Chapter 8, I conclude by summarising the results of my PhD work, comparing them with the current scenario of M dwarf exoplanet research, and outlining the ongoing studies and future perspective of my work as part of the GAPS community.

Chapter 2

M dwarfs planetary systems: detection techniques and statistical properties

Due to the many observational advantages which facilitate the detection of rocky planets in close orbits around them, M dwarfs have become increasingly popular as target for surveys for extrasolar planet search. These advantages are however counterweighted by the difficulties both in detection and characterization of exoplanetary systems caused by the stellar activity of the host stars, which for some observational techniques produce signals comparable to those from actual planets, leading to possible misinterpretations.

In this Chapter, I describe the most important techniques of extrasolar planets detection, focusing on their application to low-mass stars. I then discuss the problematic of stellar noise and its influence on the search for exoplanets, as well as the main statistical properties derived from the observed samples of M dwarfs exoplanetary systems.

2.1 Detection techniques

With an open debate on whether or not our own Solar System contains a ninth planet (Millholland and Laughlin, 2017, and references therein) only some hundreds of AU aprt from us, it's not surprising that the detection of exoplanets orbiting around stars distant tens of light-years is a difficult task at best.

Due to their intrinsic faintness and proximity to their host stars, exoplanets' light is usually overwhelmed by the stellar luminosity, leaving the direct observation all but straightforward. Up to date, only 20 planets over more than 3500[1] have been directly imaged, and all of them in very particular orbital and evolutionary configurations.

---

[1] Defining as planets objects with $M \leq 13$ M_J; source: NASA Exoplanet Archive - 06 October 2017.

Among the indirect techniques for exoplanet detection, one of the most important and successful is the Radial Velocity (RV) method, which is responsible for the first confirmed discovery of an extrasolar planet orbiting a main-sequence star (Mayor and Queloz, 1995), along with the confirmation and mass measurements of most of the sub-stellar mass companions detected with the transit method. That is in fact the second most important technique, which enabled the Kepler satellite (Borucki et al., 2009) to discover the vast majority of the exoplanets known today.

In this section I will illustrate the radial velocity, transit, and microlensing techniques, with particular focus on the first, since it is also the method used for planetary discovery and characterization throughout this thesis. The other two are briefly presented for further information, due to their importance in the study of M dwarfs planetary systems. For a complete review of the techniques for detecting extrasolar planets see Perryman (2011) or, for a more practical guide, Bozza et al. (2016).

2.1.1 The radial velocity method

As planetary bodies orbit around a star, their gravitational pull causes it to orbit in a reflex motion around the centre of mass of the system. Due to the extreme host star - planet mass ratio, the centre of mass usually lies inside the star itself, but this motion can nevertheless be measured, as its component along the line of sight can be detected from the Doppler shift of the star's spectral lines.

Orbit derivation

The Keplerian orbit in the 3D space of a body around the centre of mass of the system is completely described by the seven parameters $a, e, P, t_P, i, \Omega, \omega$, where:

- a is the semi-major axis of the elliptical orbit;
- e is the eccentricity of the ellipse;
- P is the orbital period;
- t_P is the time of the pericentre passage;
- i is the inclination of the orbit with respect to the reference plane, which is commonly chosen to be the plane of the sky, i.e. $i = 0°$ correspond to a face-on orbit;
- Ω is the longitude of the ascending node, which is the angle on the reference plane between a reference direction and the the node where the object is moving away from the observer;
- ω is the argument of the pericentre, which is the angle on the orbital plane between the ascending node and the pericentre.

The period P and the semi-major axis a are connected by Kepler's third law, which in the case of the absolute orbit of a star around the barycentre of the system is:

$$P^2 = \frac{4\pi^2}{GM'} a^3, \tag{2.1}$$

where

$$M' = \frac{M_P^3}{(M_\star + M_P)^2}, \tag{2.2}$$

where M_P and $M_\star$ are the mass of the planet and star respectively.

I will now describe how the orbital parameters can be retrieved from the radial velocity information.

The position z of the star along the line of sight is defined as:

$$z = r(t) \sin i \sin(\omega + \nu(t)), \tag{2.3}$$

where $r(t)$ is the distance from the pericentre and $\nu(t)$ is the true anomaly, i.e. the angle on the orbital plane between the current position of the object and the the direction of the pericentre, which can be derived from the orbital elements by means of the eccentric and mean anomalies, $E(t)$ and $M(t)$:

$$\tan \frac{\nu(t)}{2} = \left(\frac{1+e}{1-e} \right)^{1/2} \tan \frac{E(t)}{2}, \tag{2.4}$$

$$M(t) = E(t) - e \sin E(t), \tag{2.5}$$

$$M(t) = \frac{2\pi}{P}(t - t_P), \tag{2.6}$$

where Eq. 2.5 is Kepler's Equation.

From Eq. 2.3, deriving with respect of time and performing some algebraic substitutions, the equation for the radial velocity v_r can be derived as:

$$v_r(t) = K[\cos(\omega + \nu(t)) + e \cos \omega], \tag{2.7}$$

where K is the radial velocity semi-amplitude, which can be derived from the orbital elements as:

$$K = \left(\frac{2\pi G}{P} \right)^{1/3} \frac{M_P \sin i}{M_\star^{2/3}} \frac{1}{(1 - e^2)^{1/2}}, \tag{2.8}$$

where the assumption of $M_P << M_\star$ is taken into account.

From just radial velocity measurements it is impossible to determine the longitude of the ascending node Ω, because different values of Ω represent the same orbit rotated around the line-of-sight axis, which are of course indistinguishable from pure radial information. The other important limitation of the RV method is that neither the real mass of the body orbiting the star nor the inclination of the orbit can be determined, but only their combination $M_P \sin i$, the minimum mass.

The seven orbital parameters that define the orbit are thus reduced to three observables, P, e, t_P, along with $K = f(e, P, M_P \sin i)$. In addition to them, two other quantities are usually considered to define the full radial velocity curve of the star with respect of the observer: the systemic velocity γ, which defines the barycentre motion of the system with respect to the observer, and a linear trend parameter d, which can be used to take into account long term accelerations, due to instrumental drift or unidentified long-period companions. Eq. 2.7 then becomes:

$$v_r(t) = K[\cos(\omega + \nu(t)) + e\cos\omega] + \gamma + d(t - t_0). \tag{2.9}$$

It's worth mentioning that this derivation is for the radial velocity of the star: if we were to measure the radial velocity of the planet itself, e.g. in the case of high resolution spectroscopy of atmospheric features (e.g. Brogi et al., 2014), the semi-amplitude would be larger by a factor given by the mass ratio $K_P = M_\star/M_P * K_\star$, while the other parameters would be unchanged, a part from ω which would differ by π.

In the case of a multiplanet system, the total radial velocity of the star can be approximated as the sum of the radial velocities due to the pulls of the single planets, plus the two common terms γ and $d(t - t_0)$ which are due to systemic and instrumental effects. The resulting total radial velocity for a system with n_P planets is then:

$$v_{r,\mathrm{tot}}(t) = \sum_{k=1}^{n_P} v_{r,k}(t) + \gamma + d(t - t_0), \tag{2.10}$$

where $v_{r,k}(t) = K_k[\cos(\omega_k + \nu_k(t)) + e_k\cos\omega_k]$ is the stellar RV due to the kth planet.

To detect the periodic signals embedded in the radial velocity curve of a star, a variety of different techniques are used. We will discuss in details some of the most common in Chapter 3.

Radial velocity measurements

The radial velocity of the star with respect to the observer can be measured from the displacement in the star's spectral lines, due to the relativistic Doppler effect:

$$\Delta\lambda = \lambda_{\mathrm{obs}} - \lambda_{\mathrm{em}}. \tag{2.11}$$

For a source emitting at a wavelength λ_{em} and moving with velocity v at an angle θ with respect to the line of sight, the observed wavelength, λ_{obs}, is given by (e.g. Lang, 1980):

$$\lambda_{\mathrm{obs}} = \lambda_{\mathrm{em}}\frac{(1 + \beta\cos\theta)}{(1 - \beta)^{1/2}}, \tag{2.12}$$

where $\beta = v/c$.

In the non-relativistic case, as it is the stellar reflex motion, and considering the radial velocity, i.e. $\theta = \pi/2$, we get:

$$v_r = \left(\frac{\Delta\lambda}{\lambda_{\mathrm{em}}}\right)c. \tag{2.13}$$

The radial velocity curves due to the presence of extrasolar planets have usually very small amplitudes, $K \sim 1 - 10$ m s^{-1}, and thus require a very high wavelength resolution to detect the lines displacement. If a spectrograph can resolve two monochromatic beams with spectral separation $\delta\lambda$, then

$$R = \frac{\lambda}{\delta\lambda} \tag{2.14}$$

is its resolving power, which is a dimensionless quantity that is larger for higher resolution. The resolving power R is often improperly called "spectral resolution", which is in fact the quantity $\delta\lambda$. Typical spectrographs used for RV exoplanet detections have resolving powers $R \sim 50,000 - 100,000$.

From Eq. 2.13 and 2.14 it is possible to derive the velocity resolution of the spectrograph, i.e. the error with which the spectrograph can measure velocity shifts of a spectral line. The total error on the radial velocity, $\sigma_{\rm rv}$, is further reduced by a factor $\propto 1/\sqrt{N_{\rm lines}}$ by taking into account $N_{\rm lines}$ different spectral lines for the Doppler measurements. It also depends on the signal-to-noise ratio S/N as $\sigma_{\rm rv} \propto (S/N)^{-1}$.

Two other main problems for precise RV measurements are stability and wavelength calibration. High stability is achieved by controlling vibration, temperature and pressure of the instrument with cryostats and vacuum chambers. The precision in wavelength needed for planet detection is obtained by simultaneous calibration, because the standard use of a calibration lamp observed right after or before the target observation is limited by the change in optical path and time difference. The main calibration techniques are:

- **The Telluric Method:** it simply consists in using the Earth's atmosphere's telluric absorption features as a reference spectrum (Griffin and Griffin, 1973). Despite it being straightforward to implement and inexpensive, it suffers from the limited wavelength range covered by strong enough telluric lines and from the intrinsic variability of the atmosphere, which limit the accuracy to ~ 20 m s^{-1} (Gray and Brown, 2006).

- **The Gas Cell Method:** the direct improvement of the telluric method is to use a controlled gas instead of Earth's atmosphere, placing it in an absorption cell in the optical path of the telescope. This cell can be temperature and pressure stabilized to avoid variation in the absorption features. Early instruments used Hydrogen-Fluoride (HF) gas (Campbell and Walker, 1979), but several difficulties arose because it had still a small wavelength coverage, and also for safety reasons being the HF highly corrosive. A much safer alternative is to use molecular iodine (I_2), first applied to radial velocities by Marcy and Butler (1992), which solved many of the problems of HF, and allowed to reach accuracies up to ~ 3 m s^{-1}.

- **Simultaneous Th-Ar** With the advent of optical fibres, it became possible to observe both the calibration lamp and the target, recording the adjacently on the CCD detector at the same time. The precision this technique allow to achieve is exemplified by the HARPS and HARPS-N spectrographs (Pepe et al., 2000; Cosentino et al., 2012) which employ a thorium-argon emission lamp. The main advantages of the simultaneous Th-Ar calibration are that without any absorbing elements there is no photon loss, and that a very broad spectral range is covered, ~ 2000 Å. There are nonetheless some critical points to this technique too, like the fact that the lamp ages, and when replaced will introduce an offset with respect to the previous data collected. Moreover strong emission lines can spill into adjacent orders, contaminating the stellar spectrum. The latter problem is particularly serious when these spilling are in correspondence to spectral lines crucial for the data analysis, as it happens for the case of the Ca II H & K activity index, as I will discuss in Sec. 6.2.

Other contributions to Doppler shifts

The displacement of the spectral lines, given by Eq. 2.11, is not in the real case only given by the line-of-sight velocity of the target, but includes also other effects, both regarding the source star and the observer. The magnitude of these effects variates, and in some cases they may be less critical or even safely ignored when deriving the relative radial velocity, which is the key to detect extrasolar planets orbital signals. Instead they of course must all be taken into account to determine the absolute line-of-sight motion of an object.

Some of these effects are:

- **Earth motion:** our spectrograph itself is not a non-moving reference frame, because it is (hopefully) fastened to Earth's surface, and so bound to move with it during its rotational and orbital motions. So, it is best practice to correct the radial velocity measured to refer them to the solar system barycentre which, if not non-moving, is at least in constant rectilinear motion in space. If unaccounted for, Earth rotation and orbital motion cause perturbation up to ~ 0.5 and ~ 30 km s^{-1} respectively;
- **Stellar space motion:** the secular evolution of the host star parallax and of its proper motion cause a change in the systemic radial velocity γ. Also known as perspective acceleration this can be calculated as (Dravins et al., 1999):

  $$v_r = -A \frac{\dot{\mu}}{2\pi\mu}, \tag{2.15}$$

  where A is the astronomical unit, μ is the proper motion and π is the parallax of the star.

  This effect is particularly significant for long term monitoring of interesting targets, because the modulation in the systemic velocity can be mistaken for a long period planetary signal. In example, in the case of the GJ15A system, treated in Chap. 6, the perspective acceleration is $dv_r/dt \simeq 0.69$ m s^{-1} yr^{-1}.
- **Line shifts:** various physical effects change the position and shapes of the stellar spectral lines, such as the gravitational redshift, which can be calculated as (Lang, 1980):

  $$v_r \simeq \frac{GM_\star}{R_\star c}. \tag{2.16}$$

  This effect is of the order of ~ 500 km s^{-1} for M dwarfs, but usually constitutes only a constant effect and can be ignored for relative RV derivation. Other more pressing effect for RV planet detection the line shifts and distortions due to convective motions and surface features due to stellar activity, but, due to their central importance in the study of M dwarfs we will discuss them thoroughly in Section 2.2.

Most of these effects are usually taken into account into the pipelines for RV derivation themselves, since they can be easily derived from the information about the target, like its parallax and proper motion. The Earth motion is also taken into account, even considering the perturbations due to other solar system planets, and very precise data are provided by institutions like JPL (e.g. Konopliv et al., 2006) or IMCCE (e.g. Fienga et al., 2009).

2.1.2 The transit method

The transit method consists in detecting the drops in the luminosity of the host star due to the periodic eclipses caused by the planets crossing in front of it, also called transits. From the depth and shape of these transits many key system parameters can be derived. The idea of detecting extrasolar planets from the drops in stellar luminosity predates the first exoplanet by more than 40 years, being first proposed by Struve (1952), who also estimated the likelihood of transits occurrence. This probability can be approximated as a function of the stellar radius, $R_\star$, and semi-major axis of the planet's orbit:

$$Pr_{\mathrm{transit}} \simeq 0.0046 \left(\frac{R_\star}{R_\odot}\right)\left(\frac{1\mathrm{AU}}{a}\right). \tag{2.17}$$

From Eq. 2.17 is evident how the detection of hot planets in close orbits is strongly favoured. As an example, the probability of observing the Earth at its 1 AU orbit is only 0.46%. This is why transit surveys like Kepler, which aimed to discover Earth-like planets in an Earth-like orbits, have to monitor more than an hundred thousands objects to detect just a handful of such exoplanets (e.g. Jenkins et al., 2015).

The relative flux deficit in the mid of the transit can also be easily calculated, and it roughly depends only on the planet-star radius ratio (Seager and Mallén-Ornelas, 2003):

$$\frac{\Delta f}{f} \simeq \left(\frac{R_p}{R_\star}\right)^2, \tag{2.18}$$

where f is the star flux and Δf is the difference between the flux in and out of transit. This is of course just a first approximation, because for a more precise measurement of transit depth additional effects, as limb darkening, should be taken into account. The clear outcome of Eq. 2.18 is nonetheless that the transit technique allow to measure the planetary radius, from the planet-star radius ratio, given that stellar radii are known from stellar physics with uncertainties of roughly $\simeq 10\%$ (e.g. Ribas, 2006).

The transit duration, t_T, can also be easily derived from the planet's and star's radii and orbital parameters, and in the case of a circular orbit, and $\cos i \ll 1$ is given by:

$$t_T = \frac{PR_\star}{\pi a}\sqrt{\left(1+\frac{R_p}{R_\star}\right)^2 - \left(\frac{a}{R_\star}\right)^2}, \tag{2.19}$$

which gives another measurement of the radius ratio $R_p/R_\star$. Other planetary and stellar quantities can be derived model-independently from the transit characteristics, such as the stellar bulk density ($\rho_\star$, Sozzetti et al., 2007), and the planetary surface gravity (g_p, Southworth et al., 2007).

Since to observe a transit the planets impact parameter with respect to the line of sight, b, has to be smaller than the stellar radius, $b = a \cos i \lesssim R_\star$, the orbital inclination has to be $\simeq 90°$. For this reason, when the transit information is combined with radial-velocity observations, from both the planetary radius (from Eq. 2.18) and mass (from Eq. 2.8, derived with the assumption of $i = 90°$) the planetary density can be derived, and this gives basic knowledge of the internal physical structure.

2.1.3 The gravitational microlensing method

The deflection of light rays from background objects due to the presence of a massive object along the line of sight, also called gravitational lensing, was the first observational confirmation of Einstein's General Relativity (Dyson et al., 1920). Several decades later, the regime of microlensing, in which the deflected images are unresolved (Paczynski, 1986), was studied in its applications on stellar mass scales and therefore exoplanetary systems.

Gravitational microlensing occurs when a star (i.e. the lens) passes in front of another more distant star (i.e. the source), and its gravitational field acts like a lens, magnifying the light of the background star. If the lens star host a planetary systems, and one of the planets passes in a favourable position, the gravitational field of the planet itself can contribute to the lensing effect, producing a distinct feature in the magnification curve.

The gravitational lensing effect depends on the disposition of the lens and source objects in space, as well as on the mass of the lens. Due to the relative motion of involved objects with respect to each other, lensing events are transients, lasting for weeks or days, and require the random alignment which have very small probabilities to occur: there is roughly a 10^{-7} probability of detecting the microlensing signal of any given planet.

For this reason, very dense star field have to be monitored in order to maximize the number of potential sources. This is done usually by observing the Galactic bulge. The lensing is most effective when the lens is roughly at half distance with respect to the source, which means distances of ~ 4 kpc, in the case of a bulge star source. In these conditions the lens star is usually invisible.

In these requirements lie both the main strength and weakness of the gravitational microlensing method: the advantage is that it allows to detect exoplanets that lies at great distances, which are mostly unreachable for other techniques of detections, while the detriment is that the observations can not be repeated, because a favourable lensing alignment for the same planetary system is almost impossible to occur ever again. Also the great distance, and the fact that the host star is usually undetected make any follow-up observation with other methods impossible.

Nevertheless the gravitational microlensing technique has contributed to the current knowledge of exoplanetary systems, due to its ability of detecting planets mainly at distances of $1 - 10$ AU, a region of the parameter not well sampled by the other techniques. This method is also significant for M dwarf planetary systems studies, because a lower planet-to-star mass ratio increases the microlensing effect due to the planet. Also the abundance of M dwarfs with respect to other main sequence stars produce a much higher probability of random alignment than for other type of systems.

2.2 M dwarfs stellar noise

I already discussed in Sec. 2.1.1 some source of errors for RV planet detection, such as an imperfect wavelength calibration or the Earth motion. These and similar effects are usually referred to as "human" errors because, even if they are not directly caused by the observers, they can be treated to minimize their effect and produce better RV data.

The other and more wicked category of errors is that of the "stellar" errors, which are in fact Doppler shifts caused by physical phenomena taking place on the target star. To call those "errors" is somewhat a stretch, because these deviation from the pure Keplerian RV signal are in fact measurements of different phenomena, but if undetected they can mimic or twist planetary signals beyond recognition. Furthermore, contrary to "human" errors, there is nothing we can do to minimize them (a part from selecting particularly well behaving targets, of course). The only thing we can do is to model this physical phenomena and subtract them from our RV data. And this is the tricky part.

2.2.1 Identifying stellar signals

With the improvement of spectrographs down to meter-per-second precision, the stellar noise problem surfaced in all its magnitude: to monitor a potential host star with such exquisite precision lead to detect several stellar phenomena which produce shifts in the RV. The main effects are:

- Stellar oscillations: cause small shifts in the measured RV of ~ 0.5 m s^{-1} in dwarf star (while are much more significant in giants and subgiants). The period and amplitude of the oscillations increase with increasing mass for main sequence stars (Christensen-Dalsgaard, 2004) and they act on short time scales, $\sim 5 - 15$ min, and thus can be easily averaged out by taking longer exposures (Udry and Mayor, 2008);

- Stellar granulation and supergranulation: caused by the convective outer layers of dwarf stars, have however a small effect on the stellar spectra since their effect largely compensate between granules and intergranular lanes, which have opposed velocities (Dumusque et al., 2011b);

- Changes in the convection pattern: associated with the stellar magnetic cycle, cause shifts of the order of ~ 1 m s^{-1} that follow their long time scales (e.g. 11 yr for the solar cycle), and so cause problems only in the search for long period planets, whose periods can be similar to those of activity cycles;

- Short-term stellar activity: in the form of spots, faculae, and plages, causes the most disturbance to RV planet detections: all of these phenomena contribute in generating RV signals of the order of several meter-per-seconds, which shows distinct periodicities corresponding to the stellar rotation periods (i.e. some tens of days for a typical dwarf star). The amplitude of the RV signal due to stellar spots can be estimated, as a function of the spot filling factor, f, and the projected rotational velocity of the star, $v \sin i$, as (Hatzes, 2002):

$$A_{\mathrm{RV}}[\mathrm{m\ s^{-1}}] \simeq (8.6 v \sin i - 1.6) f^{0.9}. \tag{2.20}$$

> For spots and plages with lives longer than the rotation period, $\Delta T > P_{\rm rot}$, the signal due to stellar activity would appear periodic. However, due to the erratic nature of stellar spots, which change in shape and migrate on the stellar surface, combined with the stellar differential rotation, many stars will present multiple complex signals at different periods, which could strongly conceal the presence of planetary signals, or on the other hand be mistaken for planets themselves (as we will discuss in Sec. 2.2.3).

Activity indicators

Of course the stellar activity is not known a priori, and so different diagnostics should be used in order to infer the presence of the stellar RV signals. I will briefly discuss some of the most common.

The surface magnetic activity of the star, which creates the spots and plages, can be traced from the emission feature in the core of the Ca II H & K lines. This emission is concentrated in the active regions, and thus may show a modulation corresponding to the rotational period. One common way to measure it is through the $S_{\rm HK}$ index (e.g. Baliunas et al., 1985, and references therein):

$$S_{\rm HK} = \frac{H+K}{C_{3900}+C_{4000}}, \tag{2.21}$$

where H and K are the fluxes in the cores of the Ca II H and K lines, while C_{3900} and C_{4000} are the fluxes of the continuum around 3900 Åand 4000 Å. Another common way to measure the calcium emission is through the activity indicator $\log(R'_{\rm HK})$, which includes a correction for the stellar energy distribution, allowing a more straightforward comparison between different spectral types (Noyes et al., 1984):

$$\log(R'_{\rm HK}) = \log\left[1.34\times10^{-4} C_{\rm cf} S_{\rm HK}\right], \tag{2.22}$$

$$C_{\rm cf} = 1.13(B-V)^3 - 3.91(B-V)^2 + 2.84(B-V) - 0.47. \tag{2.23}$$

Another characteristics of the active regions is the spectral line distortion caused by stellar spots. This is due to the temperature difference between spots and the surrounding photosphere, which correspond to a colour and luminosity difference, causing line asymmetry. This asymmetry is usually quantified by means the line bisector span (BIS SPAN), since Voigt (1956) showed its application to measure the convection in the Sun: it is the locus of median points of the spectral line, and its distortion can be calculated in different ways, e.g. the the difference in slope between the upper and lower half of the bisector. Instead of studying the bisector of single spectral line, a common way to operate is to derive it from the cross-correlation function (CCF) of the whole spectra (even if some studies call for caution, e.g. Dall et al., 2006). Another indicator to quantify the line distortion is the full width at half maximum (FWHM) of the CCF.

The Balmer Hα is another common indicator of stellar chromospheric activity: the Hα photon emission of magnetically active regions alters the depth of the Hα absorption line, in an activity-dependent way correlated with the rotational period. Some studies also suggest this to be a more suitable activity indicator for M dwarfs than the $S_{\rm HK}$ index, due to their lack of flux around the

Calcium lines (Robertson et al., 2013).

The RV signal due to active regions depends mainly from the luminosity contrast between cool spots and the surrounding hot photosphere. This contrast ratio is colour dependent and can be easily calculated from the black body law, as:

$$\frac{F_{\mathrm{p}}}{F_{\mathrm{s}}} = \frac{e^{hc/k\lambda T_{\mathrm{s}}} - 1}{e^{hc/k\lambda T_{\mathrm{p}}} - 1}, \tag{2.24}$$

where F_{p} and T_{p} are the flux density and temperature of the photosphere, while F_{s} and T_{s} are those of the spot. This of course implies that the RV signal caused by active regions would be wavelength dependent, while a real planetary signal should instead be constant in amplitude for every wavelength. Thus one method to distinguish between planetary signals and activity-induced RV shifts is to monitor the host star in different wavelength (usually optical and infrared) and check for the correspondence of the signal's amplitude: if at longer wavelengths the signal (if any) has a smaller amplitude, than rest assured that it's not a planet.

All of these diagnostics are not in anyway 100% accurate: even if there is no apparent modulation in the line bisector corresponding to the candidate planet's period does not mean that the planet is real, as well as even if a planetary signal correspond to the stellar rotational period it does not mean that the planet does not exist. Indeed nothing forbids planets to orbit in synchrony with the stellar rotation (but in this case amazing care should be taken before claiming the discovery).

2.2.2 Correcting stellar signals

Once the presence of stellar activity RV signals has been identified, there can be different way to deal with it and subtract it from the RV time series, in order to recover the potential underlying planetary signals.

If the rotational period has been identified, from the activity indicators or from photometric monitoring of the star, one of the simplest way to account for stellar activity is to fit a sine wave with period corresponding to the rotational period, and study the RV residuals as it would be done for multiplanet systems (see Eq. 2.10). The main drawback of this technique is that, even if related to the stellar rotation, the activity RV variation is not always strictly periodic, and can produce additional signal at many other periodicities. A way to deal with this is to discard any periodicity which is present both in the RV and in any activity indicator.

Another simple method is to look for correlation between the RV and any activity indicator: if a significant correlation is found, the RV could be "corrected" for the presence of the activity signal by fit the linear trend found between the RV and the indicator and subtracting it from the data. This is also a relative inexpensive technique, but due to the complex nature of chromospheric activity stellar induced RV do not always correlate with the activity indicators.

There are many more sophisticated techniques to deal with stellar activity, some of which I will discuss in detail in Chapters 4 and 6. To show a more wide view of the problem in the next section I will describe some cases of exoplanets discoveries questioned or disproved by stellar activity studies.

2.2.3 Examples of systems affected by stellar activity

GJ674

GJ674 is a nearby M2.5 dwarf star, at a distance of only 4.5 pc. It was observed as part of the HARPS hunt for exoplanet in the southern hemisphere. Bonfils et al. (2007) identified in the RV time series two periodic signals, at $P_b = 4.69$ d and $P_c = 35$ d, with amplitudes corresponding both to a minimum mass of $\simeq 11$ $\mathrm{M}_\oplus$.

Yet, in the very same work, Bonfils et al. (2007) demonstrated the longer period signal to be caused by photospheric activity of the star. They found a clear 35 d periodicity both in the differential photometry of the star and in the time series of the CaII H & K activity index, concluding it to correspond to the rotation period of GJ674. They also discussed that a single spot is consistent with both the photometric and spectroscopic activity signals, and it can also produce the observed 35-d RV signal. The other shorter period signal, instead, was confirmed to be of Keplerian nature.

But the identification of RV signals caused by stellar activity is not always this straightforward.

GJ581

GJ581 is a M3 dwarf star, at a distance of 6.25 pc from the Sun, which was thought to harbour four planets, with periods $P_b = 5.36$ d, $P_c = 12.91$ d, $P_d = 66$ d and $P_e = 3.15$ (Mayor et al., 2009, and references therein). Other two planets ($P_f = 433$ d and $P_g = 36.5$ d) were successively claimed (Vogt et al., 2010), but planet g was quickly contradicted (e.g. Gregory, 2011; Hatzes, 2013), while planet f remained trusted. The attention towards the system remained great, since GJ581 d laid inside the habitable zone (see Sec. 2.3.2), which would have made it among the first potentially habitable exoplanets discovered.

However, Baluev (2013a) casted doubt over the actual Keplerian nature of the 66 d periodic signal. Baluev showed that the significance of the signal drops when a red noise model is taken into account. One year later, Robertson et al. (2014) investigated in details the effects of stellar activity on the RV time series of GJ581. They analysed the correlation between the RV and the Hα activity index, $I_{\mathrm{H}\alpha}$. They initially found no significant correlation between the two completes datasets, but identified the stellar rotation period of 125 d. At further analyses, they found that the $I_{\mathrm{H}\alpha}$ showed different behaviours in three chunks of the 6-years long observations, with stronger signals in the first and last chunk, and almost two times smaller in the middle one. They deduced that the star probably passed from an active to a quiescent phase and back. In the active epochs the RV$-I_{\mathrm{H}\alpha}$ correlation was much higher than on the whole datasets, and, once individually corrected the RV by subtracting the best fit RV$-I_{\mathrm{H}\alpha}$ relation, they re-analysed the datasets to look for the fate of the planets: b, c, and e were almost unaffected, maintaining their known periodicities and amplitudes, but the power of the signal of planet d dropped as a result. They also observed that the significance of the 66 d signal decreases during the "quiescent" epoch, contrary to what expected by a real planetary signal which should always increase in power by adding more observations. Thus they concluded the assumed planet d to be "an artifact induced by the stellar rotation rather than an exoplanet".[2]

This story comes with a moral: you should never blindly trust any activity indicator, but always perform multiple checks. Planet *d* signal was considered to be truthful because the star showed very low photometric variability, and thus the possible presence of active regions was discarded. But activity is not always associated to photometric variability, and in some cases Hα emissions can be produced even in absence of high contrast spots (Kürster et al., 2003).

Kapteyn's star

Another M dwarf which raised a fierce debate over the presence of potential habitable planets and the correct way to deal with the influence of stellar activity on RV signals is Kapteyn's star, a high-proper motion halo star, which at 3.9 pc is the nearest halo star to the Sun. Anglada-Escudé et al. (2014) detected two planetary signals in the combined HARPS, HIRES and PFS RV time series, with periods of $P_b = 48.6$ d and $P_c = 121.5$ d. The orbital period of planet *b* put it inside the circumstellar Habitable Zone, with the additional appeal due to the extreme age of the halo star ($\sim$ 11 Gyr, Kotoneva et al., 2005).

Once again Robertson et al. (2015b) questioned the presence of the habitable planet, denying the activity analysis performed by Anglada-Escudé et al. based on the S_{HK} index and on the photometric monitoring of the star, and again used the $H\alpha$ index to re-examine the influence of the chromospheric activity on the planetary system. They also found the stellar rotational period to be 143 d $\sim$ 3 times the orbital period of planet *b*. Their conclusions were similar to those on the GJ581 system, that is that the HZ planet was just an artifact due to stellar activity. Anglada-Escudé et al. (2016b) firmly rejected this conclusion, and performed a new analysis of the $I_{\mathrm{H}\alpha}$ using the same data as Robertson et al. (2015b) but a more statistically sound techniques: using both a frequentist and a Bayesian analysis, they claimed there to be no evidence of the 143 d rotational period, and the correlation between the RV and the $I_{\mathrm{H}\alpha}$ was far less strong than suggested by Robertson et al., thus concluding that the presence of the planet explained the data more easily than the activity correlation.

The Kapteyn's star's case well exemplifies how different analysis techniques can produce opposite results, and how easily a different way of treating the stellar activity can mean the disappearance or survival of an exoplanet. M dwarfs have proven to be arduous to study, because the exact nature of their magnetic activity is far from understood, but they are not the only ones for which exoplanets have been questioned or disproved (e.g. the "ghost" planet Alpha Cen Bb, Rajpaul et al., 2016, and references therein).

2.2.4 Activity relationships

For solar-type stars there are well known relationships between the activity indicators, the rotational velocity, and the stellar parameters, due to the fact that most of them are linked by the stellar dynamo which governs the star magnetic fields. It is also known how the stellar rotation slows and the activity dwindles as the star grows old. To study the activity behaviour a common

---

[2] It's worth noticing that this was not the end of the debate on this controversial system: Anglada-Escudé and Tuomi (2015) questioned the statistical validity of the analysis of Robertson et al., and were in turn opposed by Robertson et al. (2015a).

approach is to consider the relationship between pairs of fluxes of the lines of different activity indicators, like the CaII H & K pair I discussed above, or other like the Na D_1, D_2 doublet or Mg I b triplet.

Even if low-mass stars are now insistently monitored in search for planets, their atmospheres and magnetic activity is poorly understood, mainly due to the intrinsic faintness of the optical spectra of these stars. Nonetheless some studies were performed on the connection between rotation, activity, and age in early-M dwarfs, although with different results (e.g. West et al., 2015; Messina et al., 2014).

Recently, Maldonado et al. (2017) and Scandariato et al. (2017) studied the activity indicators behaviour in the M dwarf sample monitored by the HADES programme (see Section 5.3 for a description of the HADES programme). The analysed sample could have some biases, being selected for RV studies, but they anyway found some interesting results, i.e. that most of the relations known to hold for F-G-K stars hold also for early M dwarfs: Maldonado et al. (2017). found that there seems to be a positive correlation between activity and rotation velocity, that the chromospheric emissions is roughly constant throughout the spectral range studied and that the cooler stars of the sample (M3 type) show lower rotation levels than the earlier types (M0); Scandariato et al. (2017) assert that, while the Ca II K & K emission is linearly correlated with activity, the Hα could not be a good indicator at very low activity levels, when the absorption by filaments dominate the line profile.

2.3 Properties of M-dwarf planetary systems

As shown by Equations 2.8 and 2.18 both radial velocity and transit signals are larger for cooler dwarf stars, which have smaller masses and radii.

In spite of this advantage, of the 3500 extrasolar planets known to date, only 287 orbit around an M-dwarf star, with 54, 174 and 37 planets discovered with the radial velocity, transit and gravitational microlensing methods respectively[3]. Even if M dwarfs themselves have a very high frequency in the Solar neighbourhood (e.g. Winters et al., 2015), planets discovered around M dwarfs constitutes a small fraction of the total exoplanetary population. One of the reasons of this bias is the intrinsic faintness of cool dwarf stars in the V band, which limited the possibility to get the high signal-to-noise ratios required for high-resolution spectroscopic observations, and also excluded them from magnitude limited photometric catalogues like the Kepler survey: of the 200 000 monitored by the Kepler spacecraft, only $\sim 2\%$ have M spectral type (Gaidos et al., 2016).

The period distribution of planets discovered with both the radial velocity and transit techniques is shown in Figure 2.1[4]: we can see how both the distributions peak around ~ 2 d. Of course the raw distribution of the observed exoplanetary properties cannot be taken as equivalent to the intrinsic statistics, because observational biases indeed play a major part in sculpting the observed characteristics. Thus specific precautions must be taken into account to infer it (as discussed in Chapter 7).

---

[3] NASA Exoplanet Archive, Confirmed Planets - 09/10/2017

[4] Figures 2.1, 2.2 and 2.3 in this Section have been produced with the Exoplanet Orbit Database website (Han et al., 2014).

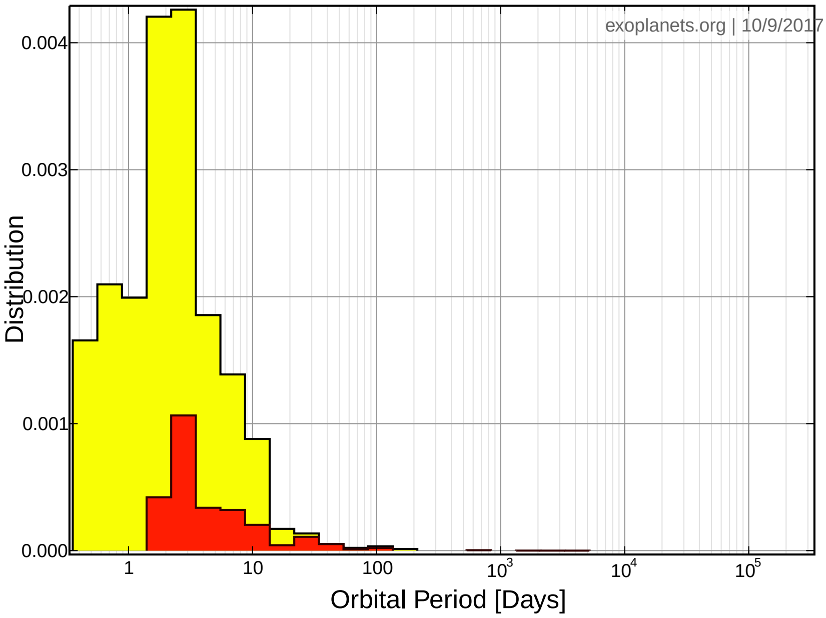

Figure 2.1: The period distribution of exoplanets orbiting M dwarfs: in yellow are shown those from transit observations and in orange those from radial velocity.

In the next Sections I will discuss the general properties of the observed populations of extrasolar planets around M-dwarf hosts, as well as briefly introduce the topic of planetary habitability and its implications for planetary systems around cool stars.

2.3.1 Population analysis

Bonfils et al. (2013a) analysed the M dwarf sample observed as part of the radial velocity search for southern extrasolar planets with the ESO/HARPS spectrograph (Mayor et al., 2003). The sample was composed of 102 M dwarfs closer than 11 pc, with small projected rotational velocity to avoid fast rotating stars, observed over the course of 6 years, from 2003 to 2009.

From the statistical analysis of this survey they derived the occurrence of M-dwarf planets, with different behaviours for different regions of the $m \sin i$-P parameter space. Their study, even if based on a limited sample with only 14 planets detected, points towards a much higher abundance of super-Earths with respect to giant planets, with an occurrence rate $f \simeq 0.37$ for $m \sin i \in [1, 10]$ $\mathrm{M}_\oplus$ and $f \simeq 0.01$ for $m \sin i \in [100, 1000]$ $\mathrm{M}_\oplus$, despite the fact that their sample indeed contained GJ 876, a star already known to harbour two giant planets (Marcy et al., 2001).

This behaviour can be seen also in the distribution of observed minimum masses of RV exoplanets, depicted in Figure 2.2, and was already suspected from previous studies (e.g. Endl et al., 2006).

Bonfils et al. (2013a) also found that small mass planets are more abundant toward longer periods, even if the detectability decreases with increasing periods,

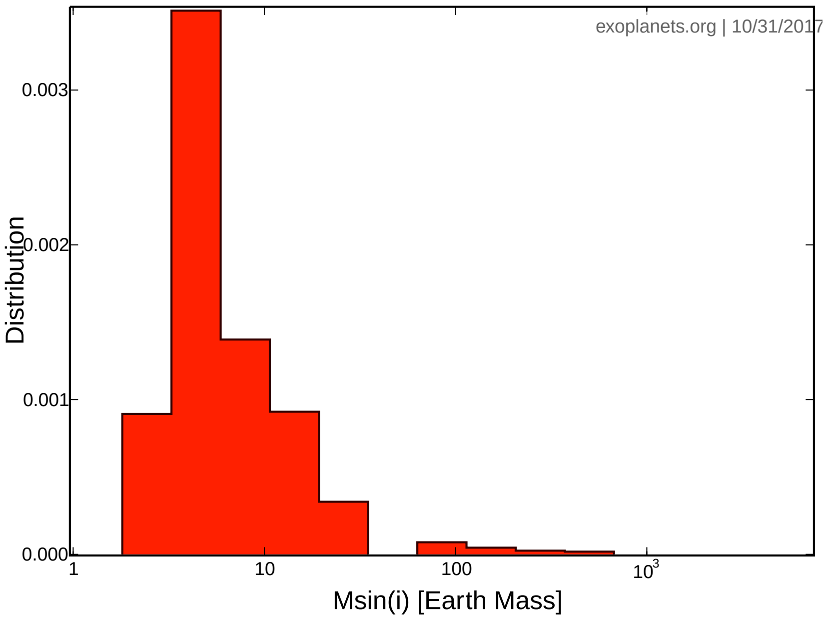

Figure 2.2: The $m \sin i$ distribution of RV exoplanets orbiting M dwarfs.

both for the smaller semi-amplitude for equal masses (Eq. 2.8) and for the difficulty to adequately sample longer time spans.

Tuomi et al. (2014) studied a similar, if smaller, sample of M dwarfs observed with both the HARPS and UVES spectrographs (Dekker et al., 2000). They nonetheless detected more planets than Bonfils et al. (2013a) did in a larger sample, and thus obtained a somewhat larger estimates for the planetary occurrence rates for masses $m \sin i \in [3, 10]$ $\mathrm{M}_{\oplus}$, $f = 1.08^{+2.83}_{-0.72}$. All the other trends were confirmed: the lack of short period giant planets, and the possibility of an abundance of low-mass long-period planets (even if this was not conclusive due to the lack of such planets in their sample).

The exoplanets statistical properties in the Kepler M dwarfs sample were analysed by Gaidos et al. (2016). One of the main obstacles in such a statistical analysis of selected stellar samples from the Kepler survey, is that most of faint stars observed by Kepler lacked of precise spectral and distance information to have well constrained spectral classes. (Gaidos et al., 2016) had thus to perform a statistical classification to avoid contamination of the sample due to giant or different mass stars. Their final sample was composed of 4216 stars with colour index $r - J > 2.2$, in which they identified 106 planets candidates. From this they derived a very high occurrence fraction for small planets, $f = 2.2 \pm 0.3$ for $R_p \in [1, 4]$ $\mathrm{R}_{\oplus}$, consistent with the results of similar analysis of transiting planets. This is much higher than the number found for solar-type stars (Howard et al., 2012). This trend seems to be corresponding to an opposite trend in the occurrence of large planet (Gaidos and Mann, 2014).

They also studied the intrinsic planet radius distribution in their sample. For comparison in Figure 2.3 the general observed radius distribution for transiting exoplanets is shown. Gaidos et al. (2016) found the distribution to peak at $\simeq 1.2$ $\mathrm{R}_{\oplus}$, reaching zero around 4 $\mathrm{R}_{\oplus}$. They tested the hypothesis that longer

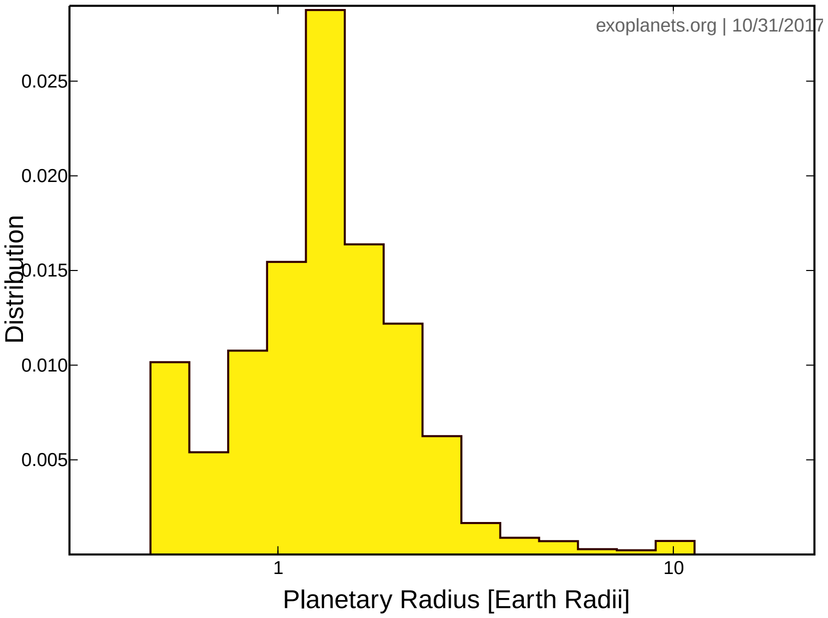

Figure 2.3: The R_p distribution of transit exoplanets orbiting M dwarfs.

period planets should have larger radii, expected from formation models (e.g. Luger et al., 2015), but found no evidence for distinct radius distributions for long and short period planets.

The period distribution is essentially flat in logarithmic scale, as derived from previous analysis for both small-mass and solar-type stars (e.g. Howard et al., 2012).

A visual representation of the inferred period and radius distribution of Kepler planets is shown in Figure 2.4, from the study of Dressing and Charbonneau (2015), which performed a similar analysis to Gaidos et al. (2016).

Another characteristics of exoplanet hosts, is the dependence of giant planet occurrence on stellar metallicity, where the former is known to increase for increasing metallicity, both for solar-type and M-dwarf stars (e.g. Santos et al., 2005; Gaidos and Mann, 2014). For small planets the relation is much more uncertain: Gaidos et al. (2016) found no evidence for a difference in metallicity between planet hosting M dwarfs and lone stars, although the analysis was limited by the large uncertainties correlated with photometric based metallicities. This is in agreement with other studies both on RV and Kepler planets (e.g. Sousa et al., 2008; Mann et al., 2013), even if other authors disagree (e.g. Buchhave et al., 2014; Wang and Fischer, 2015).

The analysis of the Kepler M-dwarf systems also highlighted how small mass planets usually reside in high-multiplicity systems, with mutual inclination close to zero. This results in a high fraction of multiplanet system, with however a lower probability of intersecting the line of sight producing the transit, due to the lower range of inclinations covered by the planets in each system.

Several studies analysed the occurrence rate of exoplanets that can be inferred from the current microlensing detections: Gould et al. (2010) found a high occurrence rate for giant planets in a selection of unbiased high-magnification

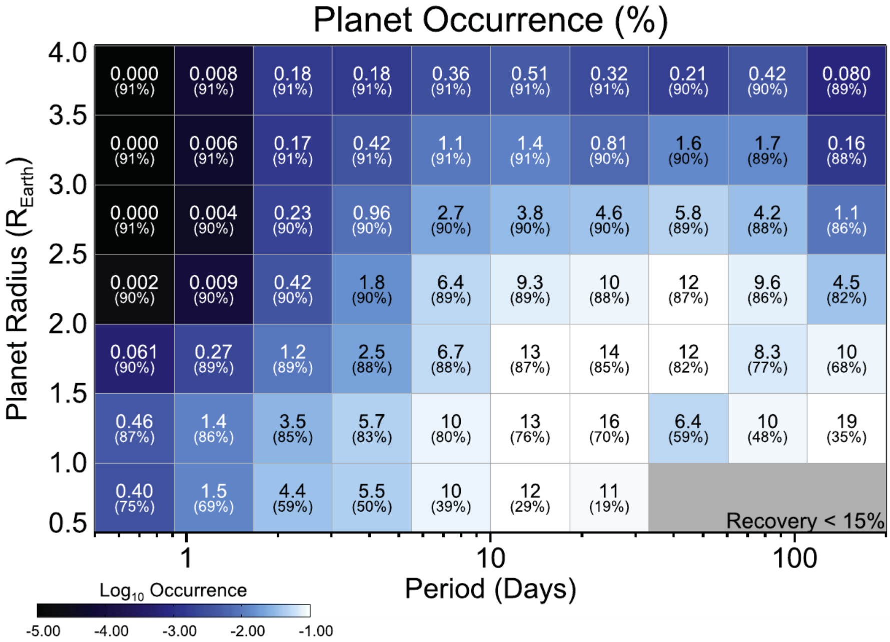

0.000 (91%)	0.008 (91%)	0.18 (91%)	0.18 (91%)	0.36 (91%)	0.51 (91%)	0.32 (91%)	0.21 (90%)	0.42 (90%)	0.080 (89%)
0.000 (91%)	0.006 (91%)	0.17 (91%)	0.42 (91%)	1.1 (91%)	1.4 (91%)	0.81 (90%)	1.6 (90%)	1.7 (89%)	0.16 (88%)
0.000 (91%)	0.004 (90%)	0.23 (90%)	0.96 (90%)	2.7 (90%)	3.8 (90%)	4.6 (90%)	5.8 (89%)	4.2 (88%)	1.1 (86%)
0.002 (90%)	0.009 (90%)	0.42 (90%)	1.8 (90%)	6.4 (89%)	9.3 (89%)	10 (88%)	12 (87%)	9.6 (86%)	4.5 (82%)
0.061 (90%)	0.27 (89%)	1.2 (89%)	2.5 (88%)	6.7 (88%)	13 (87%)	14 (85%)	12 (82%)	8.3 (77%)	10 (68%)
0.46 (87%)	1.4 (86%)	3.5 (85%)	5.7 (83%)	10 (80%)	13 (76%)	16 (70%)	6.4 (59%)	10 (48%)	19 (35%)
0.40 (75%)	1.5 (69%)	4.4 (59%)	5.5 (50%)	10 (39%)	12 (29%)	11 (19%)	Recovery < 15%		

Figure 2.4: Planetary occurrence rate in the period-radius parameter space. The upper number in each cell indicates the occurrence rate, while the lower number indicates the Kepler pipeline sensitivity. (Dressing and Charbonneau, 2015).

microlensing events, while Sumi et al. (2010) found a distribution function of the planet-to-star mass ratio consistent with the one found found for solar-type stars from RV surveys (Cumming et al., 2008). Even if these results seem to clash with the the results from the other methods I presented, which implied a much smaller frequency of giant planets around M dwarfs, Clanton and Gaudi (2014) determined that the measured distributions are in fact consistent, corresponding to a frequency of $f_J = 0.029^{+0.013}_{-0.015}$, for planets with $1 \leq m \sin i/\mathrm{M_{Jup}} \leq 13$ and $1 \leq P/\mathrm{days} \leq 10^4$. Moreover Clanton and Gaudi (2016) demonstrated that the observed distribution of giant exoplanets from various methods, including RV and microlensing, can be explained by a simple joint power-law distribution, which also predicts the observed abundance of low mass planets orbiting M dwarfs.

One of the main common results of the analysis of the observed populations from different techniques is the lower occurrence of giant planets around small-mass stars than around solar-type stars. This feature was in fact predicted by theoretical studies of planetary formation via core-accretion: Laughlin et al. (2004) determined that several effects contribute to hinder the formation of giant planets in M dwarfs protoplanetary disks, like the shorter life-time and lower surface density of the disk itself, which impede the accretion of a gaseous envelope.

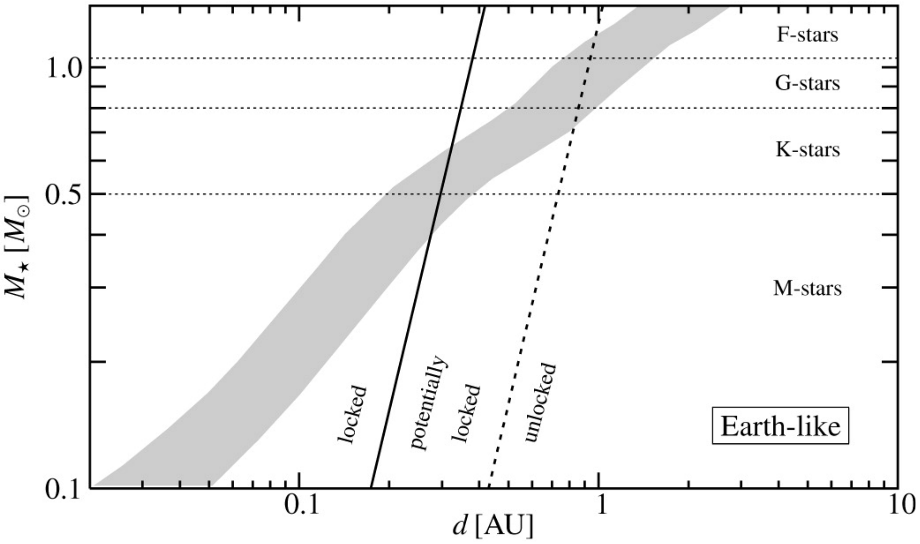

Figure 2.5: Circustellar habitable zone as function of stellar mass for zero-age main sequence stars, with the assumption of Earth-like planet and atmosphere. The solid and dashed line indicate the transition region between freely-rotating (on the right) and tidally-locked (on the left) planets. (Grießmeier et al., 2009).

2.3.2 M dwarfs habitability

Concluding this overview of the main characteristics of planetary systems hosted by M dwarfs, I will spend a few words on the topic of habitability and habitable zone.

The Circumstellar Habitable Zone (CHZ, or simply HZ) was defined even before the discovery of the first exoplanet, by Kasting et al. (1993) using one-dimensional climate models to assess the region in semi-major axis space in which the surface temperature of a rocky planet is compatible with the presence of liquid water, i.e. $T_{\mathrm{surface}} \in [T_{\mathrm{f}}, T_{\mathrm{b}}]$ where T_{f} and T_{b} are the freezing and boiling temperatures of water, respectively. This depends on the specific assumptions on the planetary atmosphere composition and pressure, as well as on the stellar luminosity and spectra. The circumstellar habitable zone, as calculated from the definition of Kasting et al. (1993), is shown in Figure 2.5 from Grießmeier et al. (2009).

Being M dwarfs much fainter than solar-type stars, their HZ is much closer to the central star. This means that potentially habitable planets are much easier to detect around M dwarfs than around solar-type stars. This is of course one of the main reason of the increasing interest in M dwarfs planetary systems discovery and characterization.

The exact boundaries of the HZ are somewhat difficult to define, since different climatic and geologic mechanisms could be invoked to shift the inner or outer limit in one direction or the other. Kopparapu et al. (2013a) updated the HZ limits derived by Kasting et al. (1993), using again a one-dimensional radiative–convective, cloud-free climate model, even if some more complex surface climate models have been proposed (e.g. Vladilo et al., 2015).

An interesting value for habitability studies is $\eta_\oplus$, the frequency of habitable planets which can be calculated for different types of host stars. Using the model by Selsis et al. (2007), Bonfils et al. (2013a) estimated the frequency of habitable planets around M dwarfs to be $\eta_\oplus = 0.41^{+0.54}_{-0.13}$, for planetary masses $m \sin i \in [1, 10]$ $\mathrm{M}_\oplus$. Instead Tuomi et al. (2014), using the updated definition by Kopparapu et al. (2013b), calculated an occurrence rate of habitable planets of $\eta_\oplus = 0.21^{+0.03}_{-0.05}$, for planetary masses $m \sin i \in [3, 10]$ $\mathrm{M}_\oplus$, consistent with the findings of Dressing and Charbonneau (2015), who found $\eta_\oplus = 0.24^{+0.18}_{-0.08}$ and $\eta_\oplus = 0.21^{+0.11}_{-0.06}$ for Earth-size planets and super-Earths, respectively, on the same sample as for Gaidos et al. (2016) if with somewhat different assumptions on stellar parameters and detection efficiency.

However, the topic of cool stars habitability should be addressed with some caution, because there could be drawbacks due to the proximity of the habitable zone to the host star. Some useful examples can be taken in the vast literature on M dwarfs habitability triggered by the discovery of the seven super-Earth system around Trappist-1 (Gillon et al., 2017):

- the closer orbit of the potentially habitable planets to the host stars will make them subject to a much higher UV flux than today's Earth, and this could be a serious hazard for the development of surface life, even causing atmospheric losses in the case of strong stellar chromospheric activity (O'Malley-James and Kaltenegger, 2017, and references therein);
- in the case of ultra-cool dwarfs, the high pre-main sequence luminosity may cause the planet to experience a phase of runaway greenhouse prior to its entrance in the HZ, causing the loss of large quantities of surface water (Bolmont et al., 2017, and references therein);
- rocky planets at close distance from the host stars, are effected by strong tidal forces, which would potentially lock their rotation in a few million years. This can be seen in Fig. 2.5, where the habitable zone for M-stars lies on the left of the tidal locking limit (solid line). Tidal locking would remarkably change the surface climate, and thus mostly invalidating the typical habitable zone models, which assume an Earth-like planetary rotation (Kopparapu et al., 2017, and references therein).

Another thing to take into account is the relation between the position of the habitable zone as a function of the stellar mass and the rotation period of the star. We have seen in Sec. 2.2 how the chromospheric activity can conceal or mimic planetary signals with orbits corresponding to the stellar rotation period (or its harmonics). This is particularly problematic when one of these periodicities lies inside the circumstellar habitable zone, calling into question the existence of potential habitable planets, as in the case of GJ581 d (see Sec. 2.2.3). For this reason Newton et al. (2016) collected a wide sample of rotation periods of field stars as well as of Kepler targets, and compared them with the limits of the habitable zone calculated as from the prescriptions of Kopparapu et al. (2013a): the result can be seen in Figure 2.6, where the Kepler sample is treated like an ensemble distribution instead of individual objects, due to the high uncertainties of stellar parameters for Kepler targets, as discussed in the previous Section. Considering also the harmonics signals from stellar activity, we can see how M dwarfs with masses in the range $0.25\ \mathrm{M}_\odot < M_\star < 0.5\ \mathrm{M}_\odot$ will have strong contamination in the radial velocity signals for periods corresponding to the CHZ, virtually hindering the presence of habitable planets.

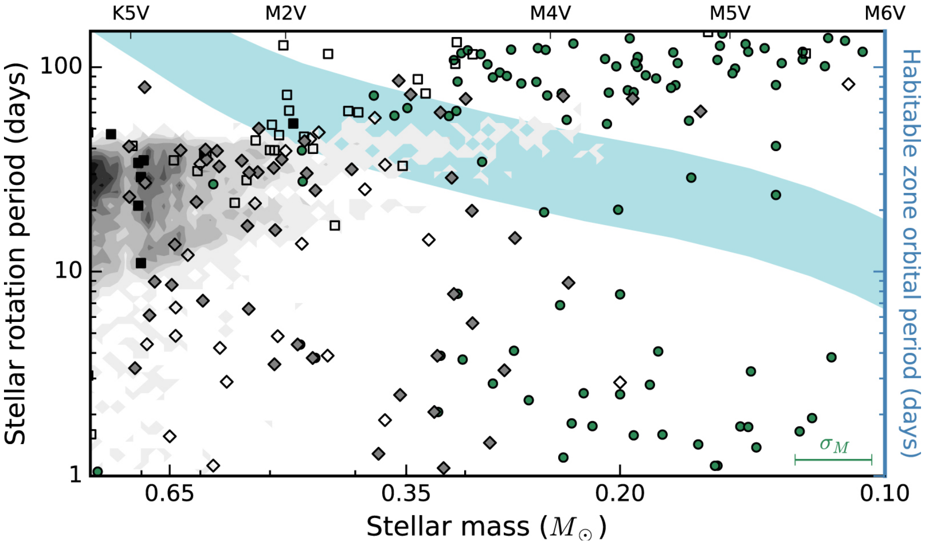

Figure 2.6: Comparison between the stellar rotation period and the circumstellar habitable zone, as a function of the stellar mass or spectral type. The gray shaded area represents the distribution of rotation period of Kepler targets, while the different symbols indicate data from different surveys (see Newton et al., 2016, for complete references).

Nonetheless none of this issues should be taken at face value, as most of the studies agree that there could be several mitigating circumstances, and life could still emerge in such conditions. But again, caution should not be forgotten.

Chapter 3

Searching for planetary signals in Doppler time series: a performance evaluation of tools for periodograms analysis

In Chapter 2 I outlined the complexity of the topic of exoplanet search around M-dwarf hosts. The presence of overlapping signals from multi-planet systems, mixed with quasi-periodic perturbations of stellar origins pose a formidable challenge in the analysis of radial velocity time series for the detection of low-amplitude Keplerian signals. Even if complex high-level analysis techniques have been developed to overcome or at least to confront with this problematic, most of the studies still rely on simple methods for the identification of periodic signals in the data, first of all periodogram analysis techniques.

In this Chapter, I report my simulation and analysis study of the performances of the most common tools used for periodogram analysis of RV data sets. This work has been published on MNRAS as Pinamonti et al. (2017).

3.1 Introduction

The growing evidence from transit (e.g., Kepler) and radial-velocity (e.g, HARPS, HARPS-N) surveys points towards a high occurrence rate of low-mass ($\leq$ 30 $M_{\oplus}$), small-size ($\leq$ 3 $R_{\oplus}$) planets (e.g., Mayor et al., 2011; Howard, 2013), with a large fraction of late-type M dwarfs hosting habitable-zone terrestrial-type companions (see, e.g., Winn and Fabrycky 2015, and references therein). The combined statistical inferences from HARPS and Kepler indicate that planets in the range between Super Earths and Neptunes are not only very common, but they are often found in multiple systems, tightly packed close to the central star, and almost perfectly coplanar when seen in transit (e.g., Batalha et al., 2013; Rowe et al., 2014; Fabrycky et al., 2014). The observational evidence is posing a formidable challenge for planet formation and evolution models, but it is also inducing a fundamental change of perspective in radial velocity (RV) observing strategy. The ubiquitousness of multiple systems with low-mass components requires a very significant investment of observing time for a proper modelling of the complex signals. Usually, multi-year campaigns with hundreds of RVs are presented in discovery announcements of Super Earths and Neptune-like planets (e.g., Bonfils et al., 2013b; Astudillo-Defru et al., 2015). In addition, the analysis of low-amplitude signals is often complicated by stellar activity, that can induce false positive signals mimicking the RV signature of a low-mass planet, and induce systematic effects comparable in magnitude to (and even exceeding) the amplitudes of the sought after Keplerian signals (e.g., Pepe et al., 2013).

In the search for low-mass planets with spectroscopic surveys, the first step in the investigation of unevenly spaced RV time series relies on the identification of statistically significant periodic signals via a variety of implementations of a periodogram analysis. The Lomb-Scargle periodogram (LS, Lomb, 1976; Scargle, 1982), which performs a full sine-wave fit over a large grid of trial frequencies, has historically been the first tool adopted for the task. More recently some authors have extended the LS formalism to include weights for the measurement errors and constant offsets for the data in the Generalized Lomb-Scargle (GLS) periodogram (Zechmeister and Kürster, 2009), and generalizations based on Bayesian probability theory in the Bayesian Lomb-Scargle and Bayesian Generalized Lomb-Scargle periodograms (BLS, BGLS) (Bretthorst, 2001; Mortier et al., 2015). Due to the high fraction of low-mass multiple-planet systems, and also to the presence of activity related signals in the data, the correct identification of multiple, low-amplitude signals is of course a central issue in RV time series analysis as applied to exoplanet science. However, all the above algorithms fit only a single sine-wave, or Keplerian signal, and multiple signals must be detected via subsequent fits and residual analysis. To overcome some of the shortcomings of standard periodograms when dealing with data containing two or more periodicities Baluev (2013b) has developed the multi-frequency periodogram FREquency DEComposer (FREDEC).

In this work we expand on the study by Mortier et al. (2015) and carry out a set of detailed numerical experiments aimed at 1) gauging the relative effectiveness of the GLS, BGLS, and FREDEC algorithms, including completeness and false positives, and 2) understand their biases and limitations when applied to the systematic search of single and multiple low-amplitude periodic signals produced by low-mass companions, using M dwarfs as choice of reference for the central star. The performance evaluation in the presence of representative complex signals element constitutes a novel analysis that has not been undertaken before, to our knowledge. This comparative study should not be interpreted as a way of ranking the intrinsic effectiveness of a periodogram analysis method against another. Rather, it has to be seen as one of the steps that will help towards the definition and implementation of the most aggressive and effective strategies (e.g., Dumusque et al. 2017; Hara et al. 2017, and references therein) for a robust identification of terrestrial planetary systems with state-of-the-art instrumentation (e.g. HARPS, HARPS-N) that guarantees meter-per-second accuracy, as well as next-generation facilities for extreme precision RV measurements, such as ESPRESSO. In section 3.2 we describe the numerical setup adopted in our study, while the main results of our suite of simulations are presented in Section 3.3. We provide a summary and discussion of our findings in

Section 3.4.

3.2 Simulation setup

3.2.1 Assumptions and Caveats

The suite of simulated catalogs of RV observations described below and utilized in the analysis has been produced using a set of working assumptions and simplifications. In particular:

- The comparative performance evaluation of GLS, BGLS, and FREDEC is expressed in terms of the dependence of the efficiency of signal recovery (parametrized through the theoretical false alarm probability FAP) on the main orbital elements it is expected to depend upon, i.e. orbital period P, eccentricity e, RV semi-amplitude K, and the 'signal-to-noise' ratio K/σ, where σ is the single-measurement RV error. The adoption of the theoretical FAP rather than its calculation via bootstrap methods was dictated by the need to keep processing time within reasonable boundaries given the computational resources at our disposal;
- RV measurements are affected by a random (Gaussian) noise component. In one experiment, a simple synthetic stellar activity signal was added to the RV data. This was done as a metric of comparison with recent literature works, while a full-scale study of the effect of correlated stellar noise is left for future developments. We also did not consider the presence of outer companions, stellar or planetary, that would introduce long-term RV drifts;
- Up to two low-mass planets where simulated. The growing evidence for the existence of compact multiple systems with a number of planets significantly exceeding 2 naturally calls for relaxation of this assumption. Our aim is to identify proxies for interpreting in a simple manner any differences in behaviour of the three algorithms that might arise in the case of two-planet systems that might be used in a future work for easing the understanding of the efficiency of periodogram analyses carried out with a variety of methods in cases of even more complex RV signals.
- In the simulations we included the elements of the window function appropriate for reproducing the gaps in the data due to the seasonality of the observations as well as the alternation between day and night. The number of RV measurements per season (a few tens) was that typical of current RV surveys, rather than that used in very intensive observational campaigns (with hundreds of datapoints) focused on few targets. No prescriptions were made for either the generation of gaps in the data due to long stretches of bad weather, or the generation of RVs with large uncertainties as if obtained under not optimal weather conditions.

3.2.2 Synthetic catalogs

We created several catalogs of synthetic RV time series. Each time series consists of N radial velocity measurements y_i distributed over a number N_s of observing seasons, their respective times t_i, and the associated errors σ_i ($i = 1, \ldots, N$). The Keplerian RV signal induced by the j^{th} planetary companion is evaluated from Eq. 2.9, as discussed in Sec. 2.1.1.

From the orbital parameters the planets' minimum mass $M_{p,j} \sin i_j$ can be recovered inverting Eq. 2.8:

$$M_{p,j} \sin i_j \propto K_j P_j^{1/3} M_\star^{-2/3} (1 - e_j^2)^{1/2}, \tag{3.1}$$

where $M_\star$ is the mass of the primary. The value of $M_\star$ and γ were kept constant to $M_\star = 0.5 M_\odot$ and $\gamma = 0.0$ m s^{-1}, respectively, throughout our study.

The instrumental noise was modelled as purely white, with the single-measurement error σ_i drawn from a Gaussian distribution with standard deviation of 1.5 m s^{-1}, which is representative of typical values of internal errors in Doppler time-series of relatively bright M dwarfs. The generation of the synthetic systems and relative RV signals was carried out with a set of prescriptions detailed below.

Single-planet circular orbits catalog

The first catalog consists of 10 000 synthetic systems composed of a single companion on a circular orbit ($e = 0.0$). The orbital parameters and RV amplitudes where drawn from the following distributions:

P: log-uniformly distributed over the interval $[10.0, 365.25]$ d;

K: uniformly distributed over $[1.5, 5.0]$ m s^{-1};

T_0: uniformly distributed over the range: $[0, P]$;

Given the range of K and the adopted value of $M_\star$, the corresponding interval of minimum planetary masses is between $\sim 3\ M_\oplus$ and $30\ M_\oplus$. All 10 000 RV time series were generated with $N = 60$ observations uniformly distributed over $N_s = 3$. The season duration was set close to 6 months, with a daily observing window of approximately 12 hr.

Single-planet eccentric orbits catalog

The second catalog is composed of 10 000 synthetic eccentric systems and their relative time series. The probability distribution function adopted for e was the Beta distribution, following the recipe of Kipping (2013):

$$\mathcal{P}_\beta(e; a, b) = \frac{1}{B(a,b)} e^{a-1} (1 - e)^{b-1}, \tag{3.2}$$

with $a = 0.867$ and $b = 3.03$. The remainder of the simulation setup was identical to that described in §3.2.2.

Multi-planet circular orbits catalog

The third catalog is composed of 10 000 synthetic two-planet systems on circular orbits, and their relative time series. To generate each pair of companions, we first use the same P distribution as in the first two catalogs, and then assign the orbital period P' of the second planet following the distribution of period ratios observed for Kepler candidates by Steffen and Hwang (2015):

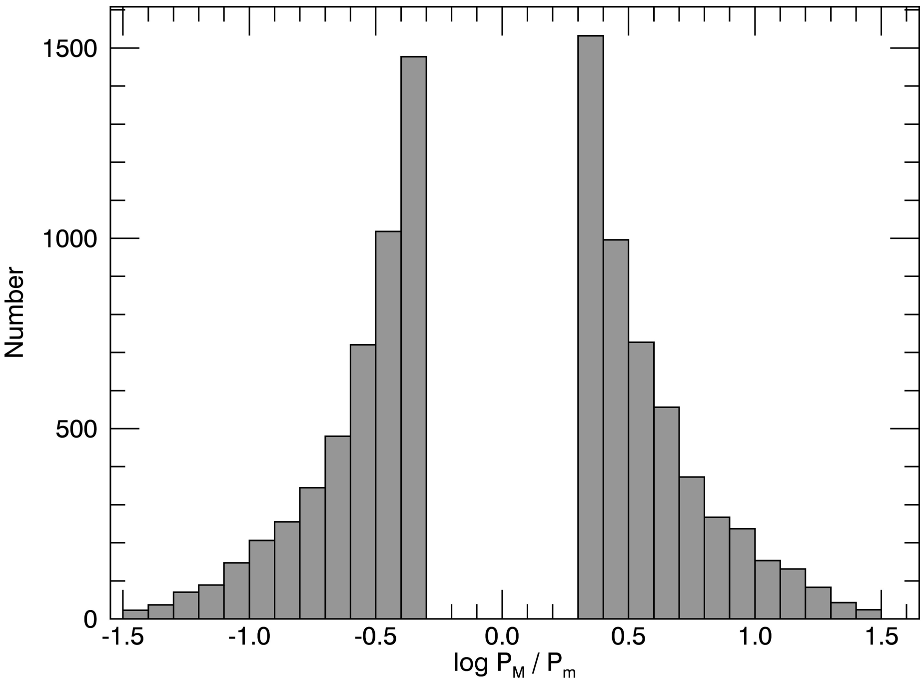

Figure 3.1: Period ratio distribution function, with P_M and P_m the period of the planet with the larger and smaller amplitude, respectively.

$$\mathcal{P}(\mathcal{R}) \propto \mathcal{R}^{-1.26}, \tag{3.3}$$

where $\mathcal{R} = P_\mathrm{o}/P_\mathrm{i}$, P_i and P_o being the periods of the inner and outer planet, respectively. The relation is valid for $\mathcal{R} \gtrsim 2$. We do not require $P = P_\mathrm{i}$, so the probability density function for P' is:

$$\mathcal{P}(P'; P) = \begin{cases} \left(\frac{P}{P'}\right)^{-1.26}, & \text{if } P' < P/2, \\ \left(\frac{P'}{P}\right)^{-1.26}, & \text{if } P' > P/2. \end{cases} \tag{3.4}$$

P' was also required to be in the interval $[10.0, 365.25]$ d. All other parameters in the simulated catalog were generated following the same prescriptions as in §3.2.2. The resulting period ratio distribution is shown in Fig. 3.1.

We denote the largest and smallest amplitude K_M and K_m respectively, and the corresponding periods P_M and P_m. The distribution function of amplitude ratios is shown in Fig. 3.2.

Multi-planet eccentric orbits catalog

The last catalog generated encompassed a set of 10 000 eccentric two-planet systems, and their corresponding RV time series. As done in §3.2.2, the e values for both orbits were drawn from the Beta distribution (Kipping, 2013). In order to avoid unrealistic configurations corresponding to clearly dynamically

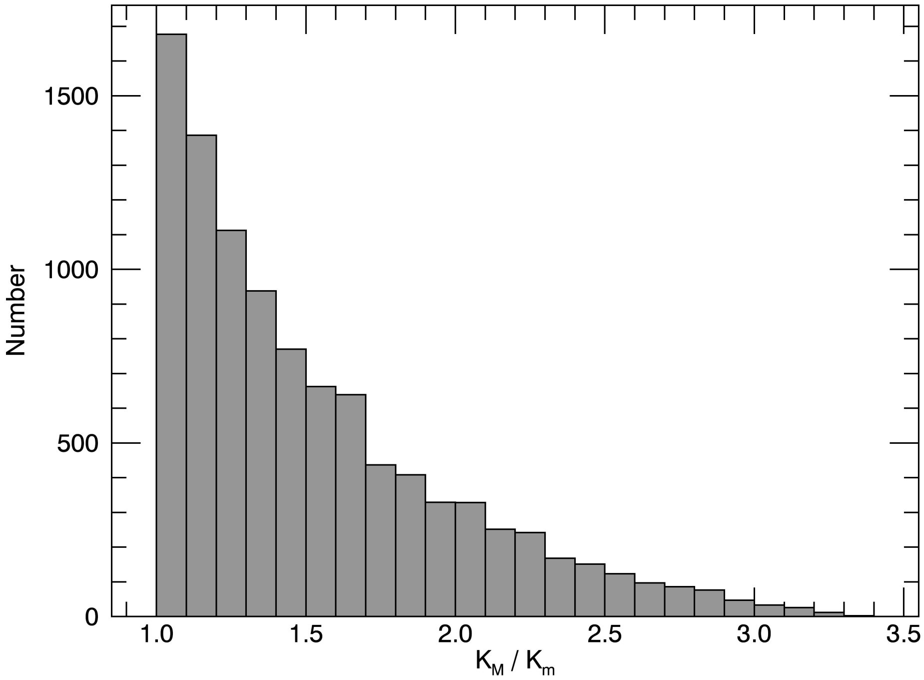

Figure 3.2: Amplitude ratio distribution function, with K_{M} and K_{m} the larger and smaller amplitude, respectively.

unstable orbits, the masses, orbital separations, and eccentricities of a pair of synthetic planets were generated in order to fulfil the analytic Hill-stability criterion (Giuppone et al., 2013, and references therein):

$$\left(\mu_1 + \mu_2 \frac{a_1}{a_2}\right) \left(\mu_1 \gamma_1 + \mu_2 \gamma_2 \sqrt{\frac{a_2}{a_1}}\right)^2 > \alpha^3 + 3^{4/3} \mu_1 \mu_2 \alpha^{5/3}, \tag{3.5}$$

with $\mu_i = m_i/m_\star$, $\alpha = \mu_1 + \mu_2$, a_i the semi-major axis of planet i and $\gamma_i = \sqrt{1 - e_i^2}$. Systems violating this criterion were discarded.

Since the stability criterion penalizes highly eccentric orbits, in order to avoid a statistically insignificant sample of highly eccentric wide systems, we cut the eccentricities distribution at the $e = 0.5$ level, which includes roughly 90% of the systems.

In order to study the sensitivity to the $P/2$ harmonics of eccentric orbits, we raised the period ratio lower limit in Equation 3.4 to $\mathcal{R} = 2.5$, to avoid overlapping with signals from planets in 2:1 resonance.

3.3 Results

The comparative study of the efficiency of the three period search algorithms presented here is carried out applying sequentially GLS, BGLS, and FREDEC to each of the four simulated datasets described in §3.2.2. Indeed, other studies in the past (e.g. Walker et al., 1995; Nelson and Angel, 1998; Cumming et al., 1999; Eisner and Kulkarni, 2001; Endl et al., 2002; Cumming, 2004; Narayan et al., 2005; Endl et al., 2006; Cumming et al., 2008; Bonfils et al., 2013a; Faria et al., 2016) have focused on gauging the sensitivity of RV planet searches to single-planet architectures utilizing periodogram analysis tools applied to synthetic as well as actual datasets in a variety of situations (large/small number of observations, periods shorter/longer than the duration of the observations, small and large companion masses). The systematic performance evaluation of GLS, BGLS, and FREDEC in the single planet case is useful in this context as it provides the opportunity to define and train on grounds that are better understood the comparison metrics to be used later for the comparative analysis of multiple circular and Keplerian signals, which has not been investigated in the past.

For the purpose of maximizing the homogeneity of the analysis, we have set the maximum value of FAP considered for evaluation of a signal at 10%, driven by the in-built FAP < 0.1 limit in FREDEC (see Baluev, 2013b, section 4.2). For GLS, the FAP has been calculated following Eq. 24 and 25 in Zechmeister and Kürster (2009). For BGLS, we followed Mortier et al. (2015) and adopted as FAP value the relative probability between the two highest peaks. In practice, statistically significant detections are considered only those with FAP below the threshold $\mathrm{FAP}_{\mathrm{thr}} = 1 \times 10^{-3}$.

To further quantify the quality of the results of the different algorithms we also calculated for each time series the true fractional error between the best output period P_{out} and the true simulated one P_{in}:

$$\Delta P = \frac{P_{\mathrm{in}} - P_{\mathrm{out}}}{P_{\mathrm{in}}}, \tag{3.6}$$

and considered a correct identification of a given period when $\Delta P < 0.1$. For FREDEC we considered a planetary system as correctly identified if all the input periods were recovered in the output set with a fractional error lower than 10%, even in the presence of additional output periodicities, as well as we considered as wrong solutions that did not contain the input periods, even if they contained some of their harmonics.

To compare the algorithms we describe their performances by means of two global performance metrics: the completeness $C = N_{\mathrm{corr}}/N_{\mathrm{cat}}$ identifies the fraction of correctly identified planets signals N_{corr} with respect to the total simulated planets in the catalog N_{cat}; the reliability $R = N_{\mathrm{corr}}/(N_{\mathrm{corr}} + N_{\mathrm{FP}})$ is the ratio of correct detections to the total of correct plus false alarms N_{FP}. Finally, we quantify dependencies of the performance on the relevant parameters by using simple scaling relations expressing, for example, the detection efficiency as a function of the ratio K/σ between planetary signal amplitude and single-measurement uncertainty. All the analysis is carried out using FAP $<$ $\mathrm{FAP}_{\mathrm{thr}}$.

3.3.1 Sanity check on white noise

The standard experiment to gauge the false alarm rate in the presence of pure white noise due to the statistical FAP threshold adopted for each algorithm should give expected results (e.g. 1% of false positives for a FAP of 1%). We have generated 10 000 time series with pure white noise, $N = 60$, and $N_s = 3$, and run the three algorithms sequentially. We show in Figure 3.3 the fraction

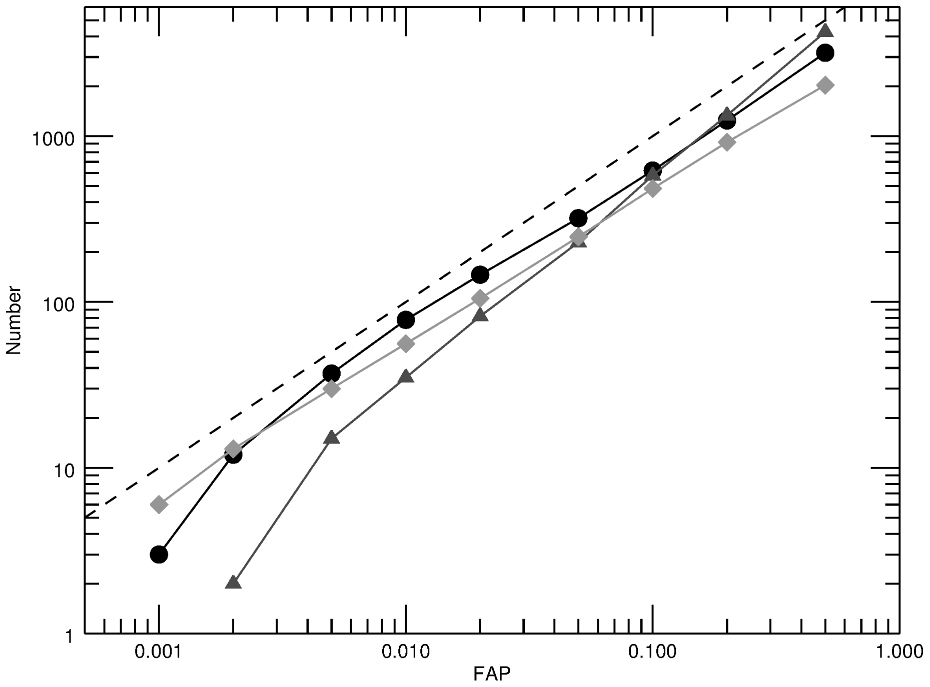

Figure 3.3: Number of false positives found in 10 000 white noise realizations as a function of the FAP threshold: black circles for the GLS, dark grey triangles for BGLS, and light grey squares for FREDEC. The dashed line is the theoretical expectation.

Table 3.1: Circular orbits catalog results

	C	FP fraction	R
GLS	94.0%	0.3%	99.6%
BGLS	87.9%	0.0%	100.0%
FREDEC	87.8%	0.4%	99.6%

of false alarms as function of FAP threshold.

We can see that all three curves are systematically lower than the dashed line, corresponding to the ideal relation between FAP and number of false positives. All three algorithms appear robust against false positives, within the limits of the FAP definition for each method.

3.3.2 Single-planet circular orbits catalog

We applied GLS, BGLS, and FREDEC on the circular orbits catalog computing the periodograms at 10^3 logarithmically spaced periods over the interval $[1, 10^3]$ d.

In Table 3.1 are shown the overall C and R values for the three algorithms, along with the fraction of false positive signals found in the catalog. All methods show very high C values, GLS performing slightly better ($\sim$ 6%) than BGLS and FREDEC. Reliability levels are virtually at 100% for all methods, given the extremely low fraction of false positive signals. There is however a significant discrepancy in the level of concordance between the three methods, that is the fraction of detected systems that is common: only 80% of all detected signals is in common between GLS, BGLS, and FREDEC. These effects are best understood by looking at the structure of the dependence of the FAP on K/σ in the three cases.

As shown in Fig. 3.4 (upper two panels and bottom left panel), the FAP decreases approximately log-linearly with increasing K/σ, as expected, BGLS highlighting a steeper dependence, and much larger spread in (statistically significant) FAP values in any given bin in K/σ. Furthermore, we notice that for BGLS very high FAP values are obtained even for $K/\sigma \gtrsim 3$, which is not the case for GLS. FREDEC also highlights a systematically different behaviour with respect to GLS, stemming from its simultaneous multi-frequency identification approach. In this case, the small fraction of high-FAP systems that is recorded, independently of K/σ, corresponds to systems in which more than 1 signal is identified by FREDEC. No such cases are seen below the $\mathrm{FAP_{thr}}$ level.

The bottom right panel of Fig. 3.4 quantifies the dependence of detection efficiency on K/σ. For GLS, $K/\sigma \simeq 1.5$ is enough for correct recovery of the signals with $> 95\%$ efficiency, while this result is achieved by BGLS at $K/\sigma \simeq 2.0$. Unlike the other two methods, FREDEC never reaches close to the 100% efficiency level, due to the systematic effect described above, that identifies $\approx 5\%$ of low-FAP systems, independently of K/σ. Overall, GLS appears $\sim$ 10% more efficient than the other two algorithms, even in the limit of $K/\sigma \approx 1$. The results obtained here are in agreement with the findings of Cumming (2004), but highlight slight differences between the three algorithms.

We show in Fig. 3.5 the behaviour of FAP with P for GLS, BGLS, and

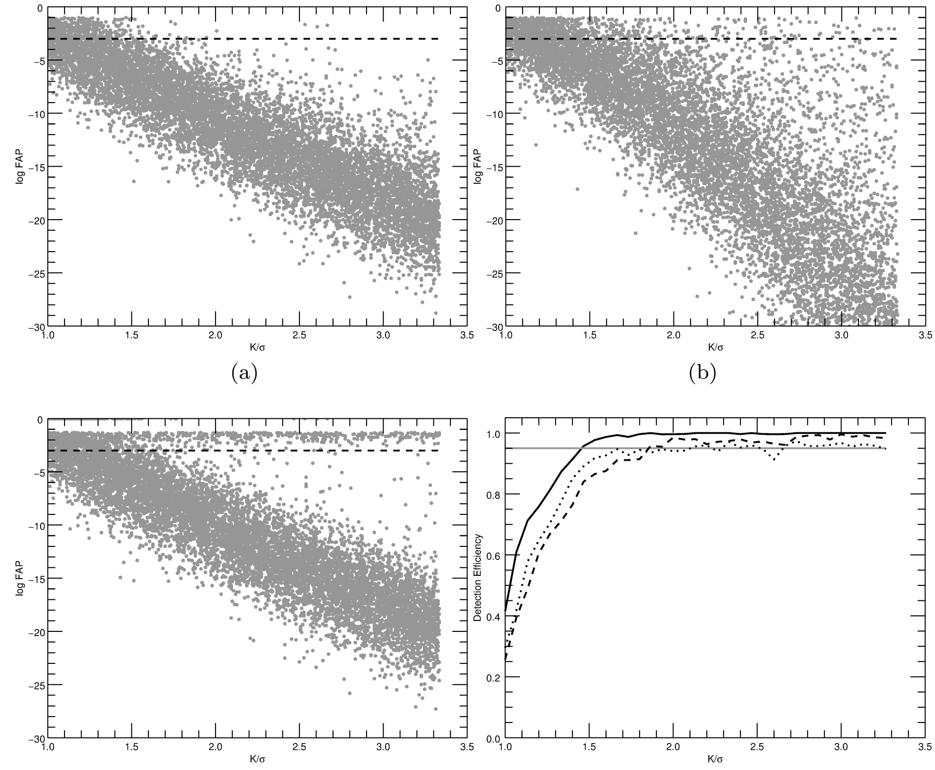

(a) (b)

(c) (d)

Figure 3.4: Dependence of the FAP on the K/σ, for top left) GLS, top right) BGLS and bottom left) FREDEC applied to the circular orbits catalog. The black dashed line represents the 10^{-3} FAP level. bottom right) Detection efficiency as a function of K/σ, for the circular orbits catalog. The solid back line is for GLS, the dashed black line for BGLS, and the dotted black line for FREDEC. The grey solid line indicates the 95% level of detections with FAP $<$ $\mathrm{FAP}_{\mathrm{thr}}$.

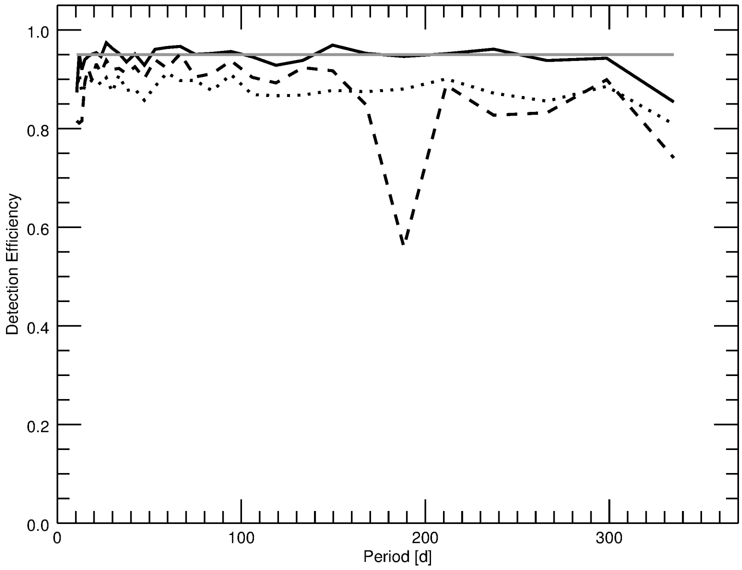

Figure 3.5: Dependence of the FAP on the orbital period for the three algorithms applied to the circular orbits catalog. Line coding as in Fig. 3.4

FREDEC. No clear dependence of the FAP on the period of the detected signals is derived. This confirms the behaviour found by Cumming (2004) using the LS periodogram coupled to a Keplerian fit, i.e. that the detection threshold is independent of P, for P shorter than the time span of the observations. However, a clear loss in sensitivity for BGLS is seen for periods around 180 d. This effect is related to the simulated length of the observing seasons, and is neither observed in GLS nor in FREDEC. The feature in correspondence of $\sim$ 180 d disappears from the BGLS analysis in the limit of higher sampling and unequal duration of each observing season (results not shown).

3.3.3 Single-planet eccentric orbits catalog

All of the three algorithms fit pure sine waves[1]. We applied them (with the same boundaries in trial period as before) to a catalog of eccentric signals, to gauge their different biases and limitations (such as spurious detections of harmonics produced by eccentric signals) in the correct identification of P and K as a function of the eccentricity. In the analysis we distinguished between high and low eccentricity signals, the threshold being set to $e = 0.5$.

Also in this case, we find that GLS and BGLS are in excellent agreement on the output values of the first periodogram analysis when both their signals are significant. Table 3.2 shows again C, R and fraction of false positives of the different algorithms based on the analysis of the eccentric catalog. We can

---

[1] Zechmeister and Kürster (2009) presented also a fully Keplerian version of the GLS periodogram. The algorithm is significantly heavier computationally than its circular version, and it would have required applying Keplerian fits to the data analysed with BGLS and FREDEC as well in order to keep homogeneity, thus making this study impractical given the available computational resources.

Table 3.2: Eccentric orbits catalog results

	C	FP fraction	R
GLS	86.1%	0.9%	99.0%
BGLS	80.0%	0.2%	99.8%
FREDEC	76.0%	0.8%	98.9%

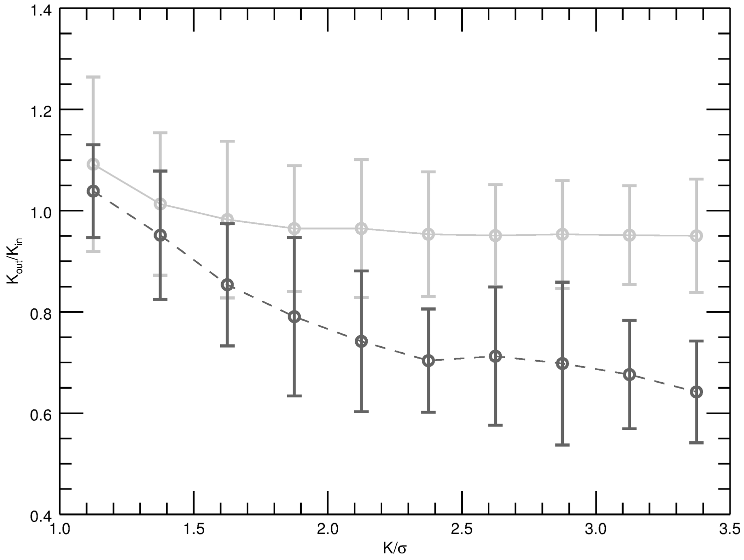

Figure 3.6: The ratio $K_{\rm out}/K{\rm in}$ as function of K/σ, for the $e < 0.5$ and $e \geq 0.5$ samples.

see that both C and R are lower than for the circular orbit catalog, while the fraction of false positives is higher. The behaviour of the individual algorithms is the same as before, with GLS being the most complete, and BGLS the most reliable. As expected, most of the incorrect identifications come from time series in which no significant period is found and/or those with particularly high eccentricity. We next take a closer look at the results of the individual algorithms.

We show in Fig. 3.6 the ratio $K_{\rm out}/K_{\rm in}$ of the fitted amplitude to the input K value expressed as a function of K/σ for two regimes of eccentricity for GLS. The derived K is systematically underestimated for the high-e subsample. It is worth noticing that the result is opposite to that observed by Shen and Turner (2008) in their analysis of eccentric RV signals. In that work, a systematic overestimate of the fitted K values is a result of force-fitting Keplerian orbits with non-zero e even in the limit of $K/\sigma \simeq 1$, for which systematically large, and statistically not significant, eccentricities are obtained. The results for BGLS (not shown) are essentially identical.

Cumming (2004) observed a quick decrease in detection efficiency for systems with $e \gtrsim 0.6$, finding that for too high eccentricities it is impossible to reconstruct the planetary signals. We derive in Fig. 3.7 (top panel) a very similar result for all signal detection algorithms. For both GLS and BGLS detection efficiency drops to 50% at $e \simeq 0.4$, and no signals are detected (even with the largest K/σ values) for $e \gtrsim 0.6$. As for FREDEC, the behaviour is also similar to that of GLS and BGLS, with its detection efficiency reaching zero for $e \approx 0.6$ (Fig. 3.7). However, an even steeper dependence of the algorithm on e is seen, with the efficiency already lower by a factor of two with respect to GLS and BGLS at $e \simeq 0.4$.

As force-fitting a full Keplerian orbit to a low-amplitude signal often results in badly constrained (and artificially high) e values, in practice signal subtraction is often carried out assuming a circular orbit. We carried out a GLS and BGLS analysis (with the same FAP thresholds as before) on the residuals to a circular-orbit fit to learn about the possible distortions in the time series induced by this approximation, particularly in the limit of high eccentricities for which residual power at first and higher order harmonics is expected.

From the results of the residual analysis we notice that the fraction of significant signals found increases with increasing e (Fig. 3.7, bottom panel), up to the eccentricity limit set by detection efficiency dropping to zero. For GLS, in 70% of these systems the significant signal in the residuals is the first harmonic ($P/2$) of the input period. For BGLS this happens in 55% of the cases. As for FREDEC, twice as many multiple significant signals are identified with respect to the circular orbit case. In this sample, the first harmonic at $P/2$ is found in 49% of the cases, with a mean eccentricity of $\langle e \rangle = 0.41$ which is significantly higher than the average on the subsample and on the whole catalog.

Finally, for all algorithms we tested whether increasing the length of the RV monitoring (up to 5 observing seasons) and/or doubling the number of observations per seasons (40 instead of 20) allowed to improve a) detection efficiency and/or b) mitigate the underestimation of the K value. No statistically significant changes in the behaviour shown in Fig. 3.6 and Fig. 3.7 were detected.

3.3.4 Additional experiment: correlated noise

As an additional experiment, we tested the performance of GLS and BGLS on a catalog with a more realistic stellar noise model. We added a simple correlated stellar activity signal, modelled with the analytical recipe by Aigrain et al. (2012). Our model considered 200 stellar spots, a realistic value for an M dwarf (Barnes et al., 2011a), and a rotation period of 30 d; no differential rotation was included. We generated different spot distributions and sizes, in order to produce stellar activity signals with amplitudes $K_\star$ ranging between 1.5 m s^{-1} and 5 m s^{-1}. The planetary parameters were generated as in the circular orbits catalog of Sec. 3.2.2.

We compared the results with an analogous catalog with the same planetary signals but no stellar activity, in order to quantify the decrease in detection efficiency of the planetary signals present in each time series. For both algorithms we used the same measure of relative detection efficiency utilized by Vanderburg et al. (2016) ($R_{\mathrm{S/N}}$, see their Eq. (1)). For GLS this is the square root of the ratio between the periodogram power measured with and without the stellar signal included, while for BGLS the quantity is the ratio between two Bayesian probabilities. An analogous experiment was not carried out using FREDEC, as no direct output in terms of periodogram power can be obtained from the software in its release.

Vanderburg et al. (2016) found that the presence of correlated stellar noise

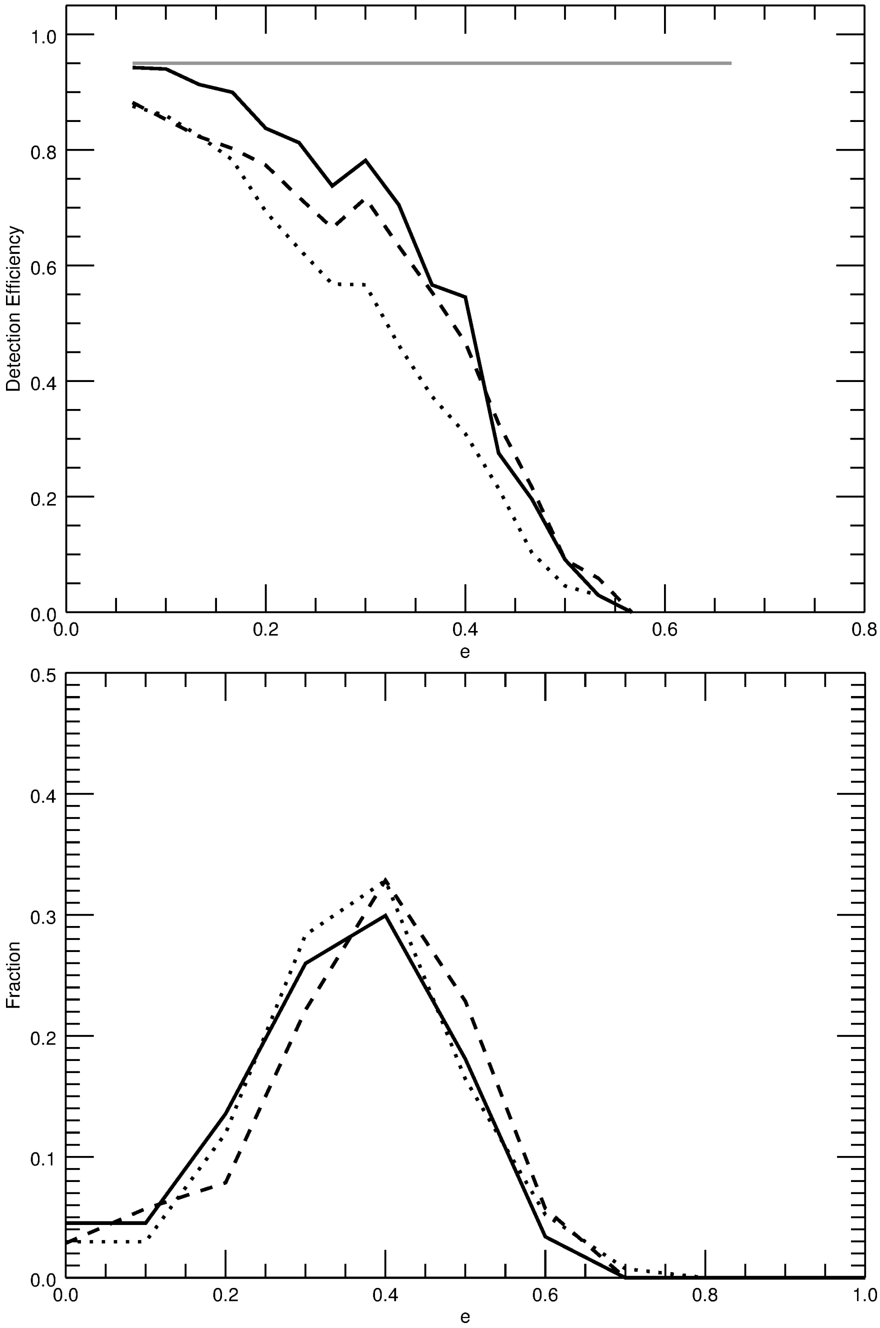

Figure 3.7: Top: Detection efficiency above the 10^{-3} FAP threshold as function of eccentricity. The solid back line is for GLS, the dashed black line for BGLS, and the dotted black line for FREDEC. The grey solid line indicates the 95% level. Bottom: histogram of the fraction of significant periods identified in the residuals as function of eccentricity. Line coding is the same as in the upper panel.

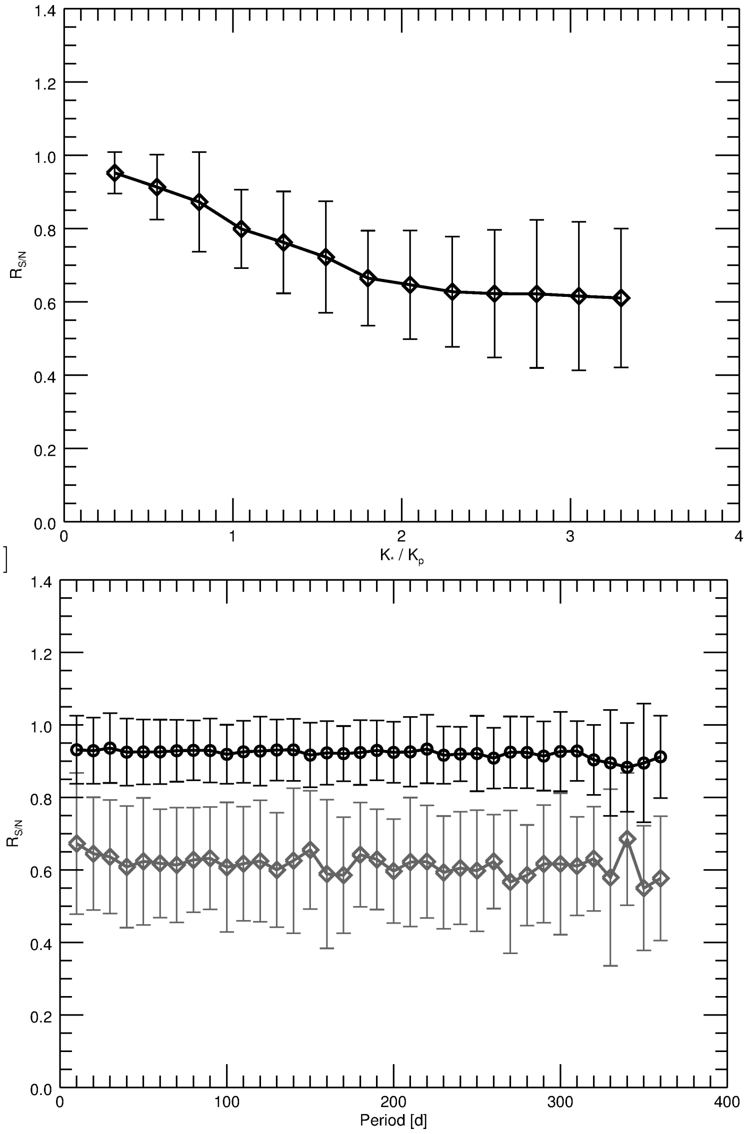

]

Figure 3.8: Top: Relative detection efficiency as function of the amplitude ratio $K_\star/K_P$. The dots and errorbars indicate the binned means and standard deviations. Bottom: Relative detection efficiency as function of orbital period. The upper line is for the time series with $K_\star/K_P < 1$, the lower one for $K_\star/K_P > 2$.

Table 3.3: Multi-planet circular orbits catalog results

	C	FP fraction	R
GLS	73.1%	21.2%	77.5%
BGLS	61.0%	28.7%	68.0%
FREDEC	72.8%	8.5%	89.5%

produces a systematic degradation of $R_{\mathrm{S/N}}$ at all orbital periods investigated, with a stronger effect in the neighbourhood of the stellar rotation period and its first two harmonics. As we can see in the bottom panel of Fig. 3.8, our analysis using GLS confirms the systematic effect. Furthermore, the simulations allow us to quantify the dependence of the loss of detection efficiency as a function of the amplitude ratio $K_\star/K_P$ (kept constant at $K_\star/K_P = 2$ by Vanderburg et al. (2016)). The result is shown in the upper panel of Fig. 3.8, in which we plot the relative detection efficiency as function of $K_\star/K_P$. We can see that for $K_\star/K_P \simeq 2$ the detection efficiency integrated over all periods drops by about 30%.

The effect at the stellar rotation period and harmonics, discussed by Vanderburg et al. (2016), is not present in our analysis. The drop in $R_{S/N}$ observed by Vanderburg et al. (2016) was due to the subtraction of the fitted stellar activity signal from the RV dataset, translating in additional dilution of the planetary signal. Instead, we did not use any mock activity indicators to correct the RVs for the stellar signals, but simply studied the results of the periodogram analysis. It's also important to remember that the magnitude of the effect at P_{rot} and its harmonics depends on the stellar spot configuration, but investigation of these aspects is beyond the scope of this experiment.

The results with BGLS (not shown) follow similar trends, with the probability of the peak in presence of stellar activity being typically 10^2 and 10^3 times lower at $K_\star/K_P \simeq 2$ and $K_\star/K_P \simeq 3$, respectively.

3.3.5 Multi-planet circular orbits catalog

For GLS and BGLS, analysis of the multiple-planet simulations in the case of circular orbits proceeded (adopting the same periodogram setup as before) up to the period search in the RV residuals after removal of the second planetary signal. For FREDEC, up to 3 significant peaks were recorded.

We start by comparing directly the output periods of the GLS and BGLS algorithms. The first most significant period is identified by both GLS and BGLS in 100% of the cases, thus both algorithms return the same results as in the single circular orbits catalog (see Section 3.3.2). As expected, the same result is obtained in the analysis of the residuals after removal of the first and second significant periodicity, whenever the identified periods are the same for both algorithms (thus giving the same output structure of the post-fit residuals).

As we can see in Table 3.3, the levels of completeness and reliability for the correct detection of both injected planets are significantly lower than in the one planet case (see Table 3.1). Interestingly, BGLS shows the worst C value for this catalog, thus proving its difficulties in dealing with multiple signals, as stated by Mortier et al. (2015). Both GLS and BGLS are prone to a large number of false positives, thus decreasing their R value. While completeness for FREDEC is similar to that of GLS, its R is significantly higher on the face of a much smaller number of false positives. This is likely due to the simultaneous multiple period search approach intrinsic to FREDEC.

The top panel Fig. 3.9 captures, for three methods, the effect on the global efficiency of detection of both signals on the ratio of amplitudes $K_{\mathrm{M}}/K_{\mathrm{m}}$. Efficiency never rises above $\sim 80\%$ for either of the three algorithms. This value is maximum at $K_{\mathrm{M}}/K_{\mathrm{m}} \approx 1$, the loss of $\sim 20\%$ being due to the sample of systems with similar amplitudes, both close to the single-measurement precision. At $K_{\mathrm{M}}/K_{\mathrm{m}} \approx 3$, efficiency is lower by a typical factor of 2 to 3, quantifying the difficulty in identifying correctly a second planet with $K_{\mathrm{m}} \simeq \sigma$ in the presence of a larger-amplitude signal, within the simulated observational scenario. Among the three methods, BGLS appears to suffer the most, performing typically a factor 1.3 to 2 with respect to GLS and FREDEC. We next turn to discuss some detailed features of the analysis carried out with each of the algorithms.

No significant signals are detected by GLS in 5.7% of the systems. This occurs when both the input amplitudes are small, typically with $K/\sigma \lesssim 1.8$ in both cases, and with the amplitude ratio being typically close to unity. There is no clear dependence on the periods, or their ratio. For 18.6% of the systems only one significant period is identified. The input periods of this subsample are usually both long (typically $\sim$ 150 d), and the ratio between the largest and the smallest amplitude is typically ~ 2. In Fig. 3.10 we show the period distribution for the output and input for this subsample: the distribution is almost the same, except for a clear aliasing effect for a significant fraction of systems with the strongest signal at $\sim$ 1 yr, which are identified instead as being systems at 6 months of orbital period. The above results highlight some of the potential limitations for detection of these specific architectures of multiple-planet systems.

GLS finds 2 significant periodicities in 75.1% of the time series. In the overwhelming majority of cases (96%) two input signals are both identified correctly. In the remainder of the cases, incorrect identification of one or both periods is related to systems in which aliases created by the window function and its harmonics are detected. In only 0.65% of the cases a third additional significant period is found after removal of the first two. This small sample is dominated by short-period aliases.

In the BGLS analysis the fraction of 0, 1, 2, and 3 detected periods (with FAP $< 10^{-3}$) is 10.3%, 27.5%, 61.9%, and 0.3%, respectively. The global features of the sub-samples in the four cases are essentially identical to those discussed for the GLS cases. It is worth noticing the significant increase in null detections and in detections of only one period, which explains the lower C value for BGLS in this experiment.

In the FREDEC analysis the fraction of 0, 1, 2, and 3 detected periods (with FAP $< 10^{-3}$) is 18.7%, 0.0%, 80.8%, and 0.6%, respectively. The distributions of amplitudes and periods in the cases of no detections are similar to those of GLS and BGLS, although with somewhat larger average ratio of amplitudes and $K/\sigma \simeq 1.5$ for the smallest of the two amplitudes in a system. The fraction of systems with two detected period is characterized by slightly longer periods and smaller amplitudes with respect to the GLS and BGLS cases, and a slightly lower fraction (90%) of systems with both periods correctly identified is also recorded. Similarly to GLS and BGLS, incorrect identification of one or both

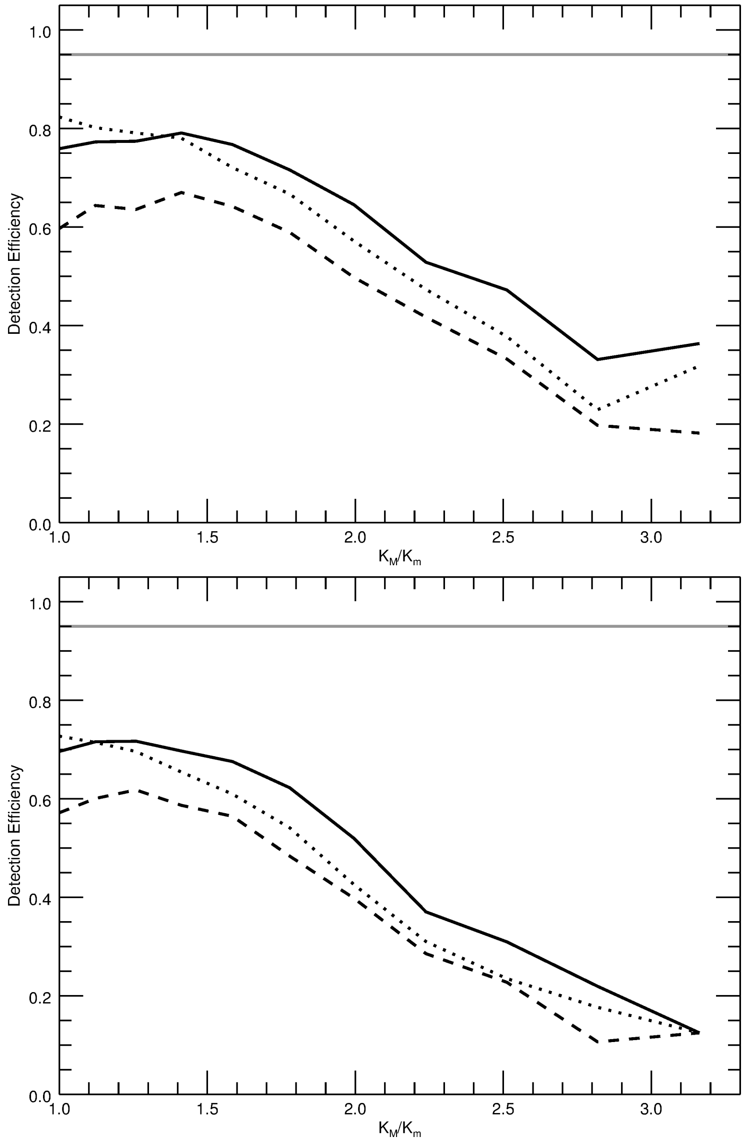

Figure 3.9: Top: Detection efficiency above the 10^{-3} FAP in the multiple-planet, circular orbits case. The solid back line is for GLS, the dashed black line for BGLS, and the dotted black line for FREDEC. The grey solid line indicates the 95% level. Bottom: The same, for the multiple Keplerian orbits case. Line coding is the same as in the upper panel.

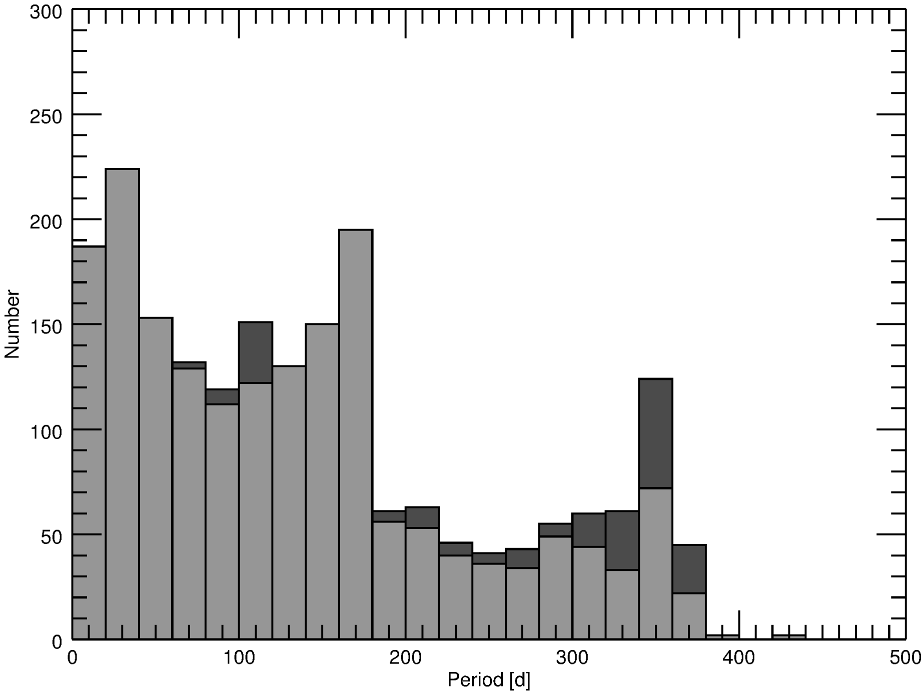

Figure 3.10: Period distribution for GLS, on the multi-planet circular orbits catalog. The light grey area shows the output and the dark grey the strongest input signal, for the subsample with only one significant period identified.

Table 3.4: Multi-planet eccentric orbits catalog results

	C	FP fraction	R
GLS	65.0%	26.3%	71.2 %
BGLS	55.2%	33.1%	62.5 %
FREDEC	62.2%	12.4%	83.4 %

periods is related to systems in which aliases are detected that are created by the window function and its harmonics. Contrary to GLS and BGLS, in the 0.6% of cases with three significant periods detected, the sample is dominated by longer-period aliases (e.g., 1 yr).

3.3.6 Multi-planet eccentric orbits catalog

The analysis of the multiple eccentric orbits catalog was performed as in the previous section. The completeness and reliability levels of the algorithms are listed in Table 3.4, and as we can see are both lower than for the previous catalog. Again BGLS shows the lowest C value, and also in this case FREDEC and GLS have comparable C values but the former has higher R, and half has many false positives. The lower completeness levels translate in larger values of null detections and detections of only one significant period.

The dependence of the number of detected systems on the main parameters (amplitude, period, eccentricity) follows generally the same behaviour observed in the previous experiments, for all methods. In particular, the mean amplitude increases with increasing number of signals found (as in Sec. 3.3.5 and the average eccentricity of both planets is lowest (~ 0.15) when all signals are correctly identified (as in Sec. 3.3.3). As in the multiple circular orbits case, the overall behaviour of detection efficiency for all three methods is mostly sensitive to the amplitude ratio, as demonstrated by the plot in the bottom panel of Fig. 3.9. The impact of eccentric orbits is quantified in an additional efficiency loss of 10%-20%, slightly increasing towards larger $K_{\mathrm{M}}/K_{\mathrm{m}}$ values.

There is however one difference: in the circular catalog the average period increased when more signals than in the input were found, while in this case it decreases. This is likely because the excess of signals recovered is due to poorly reconstructed orbits, which for the circular catalog is mainly due to not optimal sampling (and thus long periods), while for the eccentric catalog the extra signals found are also due to harmonics of the eccentric orbits, whose impact becomes more significant with better orbit sampling. As a matter of fact, the fraction of cases when in addition to both the input signals one or both the harmonics are detected is 72.2%, 77.8%, and 86.3% for the GLS, BGLS, and FREDEC respectively, thus dominating over spurious detections.

3.4 Summary and discussion

In this paper we have carried out an extensive suite of numerical experiments aimed at a direct performance evaluation of three commonly adopted algorithms (GLS, BGLS, and FREDEC) in the search of significant periodicities in radial-velocity datasets, indicative of the presence of planetary companions. Using simple scaling relations (detection efficiency) and global performance metrics (completeness, reliability, false positives fraction) we have gauged the strengths and weaknesses of the three period search algorithms when run on a variety of classes of Doppler signals (one and two planets, circular and fully Keplerian orbits) of low amplitude ($1 \lesssim K/\sigma \lesssim 3$), with representative realizations of observational strategies, different measurement noise prescriptions (simple Gaussian noise, stellar correlated noise), and adopting as reference an M dwarf primary. The main results can be summarized as follows:

- The degree of completeness and reliability are very high for GLS, BGLS, and FREDEC in the single-planet, circular orbit case, with GLS being slightly more complete than the latter two methods. As a consequence, the fraction of false positives is very low. The overall detection efficiency is close to 100% for all methods as long as $K/\sigma \gtrsim 2$, with a sharp decrease below 50% in the limit $K/\sigma \simeq 1$. Also in this case, GLS appears to be slightly ($10-15\%$) more efficient than BGLS and FREDEC in signal recovery when RV amplitudes get close to the single-measurement error;
- The effect of eccentricity on correct signal identification by all methods is significant, as expected. A typical loss of 10% in completeness is found, with GLS returning again the largest C value. Reliability of detections remains however close 100% given the mild increase in false detections. The latter are a clear function of increasing e, as long as detection efficiency

remains above $\sim 50\%$. The loss in efficiency of period recovery is a steep decreasing function of e, dropping to zero for all algorithms for $e \gtrsim 0.6$. However, FREDEC shows a higher sensitivity to this parameter, with detection efficiency reduced by up to a factor of 2 in regime of intermediate e;

- A preliminary investigation of the levels of degradation of detection efficiency in presence of stellar correlated noise indicates efficiency losses of 20% to 40% in the range $1 \lesssim K_\star/K_P \lesssim 3$ for GLS, and decrease of 2 to 3 orders of magnitude in the Bayesian probability of a detection for BGLS in the in the same $K_\star/K_P$ interval.
- The difficulty in correctly identifying multiple planets is quantified through a typically reduced completeness level between 70% (circular orbits) and 60% (for Keplerian orbits), with BGLS performing slightly worse (10%) with respect to the other two methods. Within the realm of the simulation scenario, and based on an analysis of the dependence of detection efficiency on the amplitude ratio $K_\mathrm{M}/K_\mathrm{m}$, the limitations induced by sub-optimal orbit sampling (particularly in the case of eccentric orbits) indicate as the most challenging architectures those containing signals with very similar amplitudes and $K/\sigma \lesssim 1.8$. In configurations containing two long-period companions with dissimilar amplitudes, the one with the lowest K value is not detected in a significant fraction of cases (particularly for $K_\mathrm{M}/K_\mathrm{m} \gtrsim 2$). Degradation in the degree of reliability is also clear, on the face of large fractions ($\sim 30\%$) of false detections. In this respect, FREDEC appears more reliable than GLS and BGLS, with a false positive rate $\sim 10\%$.

The results presented in this paper complement and extend the comparative analysis of period search tools for planet detection in RV datasets carried out by Mortier et al. (2015). Our study encompasses a wide range of single-planet architectures, it includes a preliminary assessment of the effects of increasing levels of stellar correlated noise, and it addresses for the first time some of the complications induced by multiple-planet architectures. The most most important lessons learned are the following: 1) even under idealized, best-case conditions (one planet, circular orbits, white noise, well-sampled orbits) different period search algorithms do not perform in an exactly identical fashion, particularly when it comes to the regime of signal amplitudes close to the single-measurement error; 2) in the presence of more complex signals, the most conspicuous element to underline is the different behaviour in the identification of false alarms: the standard approach of successive signals removal and investigation of the residuals (using GLS and BGLS) appears to be prone to as much as 3 times the amount of false positives obtained by an approach in which all statistically significant signals are searched simultaneously (using FREDEC), even in the idealized case of perfectly circular orbits.

The analysis presented here is by no means exhaustive. Within the scope of this work, our results nevertheless underscore the urgent need for strengthening and further developing sophisticated analysis techniques for the simultaneous identification of low-amplitude planetary signals in the presence of stellar activity. This is a crucial topic in the case of low-mass M-type hosts, for which stellar noise is often coupled to complex planetary RV signals induced by small-mass multiple systems, as testified by the significant literature presenting disputes on the nature, interpretation, and sometimes existence of multiple planets around some of our nearest low-mass neighbours (e.g., GJ581, Kapteyn's star. See Anglada-Escudé et al. (2016b), and references therein). This is a particularly sensitive issue as M dwarf primaries constitute the fast track to the identification of potentially habitable terrestrial-type planets, whose abundance, albeit with large uncertainties, appears to be very high (e.g. Dressing and Charbonneau, 2013; Kopparapu, 2013; Bonfils et al., 2013a,b; Tuomi et al., 2014; Anglada-Escudé et al., 2016a).

It will be certainly necessary to use the largest possible set of observational constraints, including simultaneous photometric measurements for determining rotation periods and activity signals, and spectroscopic indicators and/or RV measurements at different wavelengths for mitigating and (hopefully) removing activity signals (e.g., Vanderburg et al. (2016), and references therein). It will be equally important, however, to pursue aggressively advances in the path to the determination of the complete information content of RV datasets, via techniques that not only shy away from the standard residual analysis and implement global model fitting approaches (e.g., Hara et al. 2017; Dumusque et al. 2017), but also through the application of improved methodologies for the simultaneous, robust identification of credible signals in time series (with very small fractions of false alarms), of which algorithms such as FREDEC constitute possible seeds. This necessity is expected to become pressing very soon, with facilities for ultra-high precision RV work such as ESPRESSO, that will seek to find (multiple) planetary signals with amplitudes even orders of magnitude smaller than other sources (primarily stellar in nature) of correlated RV variations.

Chapter 4

High-performance algorithms: tests and applications

As pointed out in Chapters 2 and 3, the analysis of high-precision radial velocity data in search for Keplerian signals from small-mass exoplanets is often hampered by the presence of similar-amplitude stellar signals, also referred to as stellar jitter or stellar noise. These Doppler signals due to the stellar chromospheric and magnetic activity can conceal planetary signals, distort the measured orbital parameters or mimic altogether the Keplerian signal, leading to false detections.

As we have seen in Sec. 2.2.3, different analysis techniques can lead to opposite conclusions in the analysis of radial velocity signals, and thus cast doubts on the very existence of planetary companions. In Sec. 3.3.4 we have seen how simple periodogram analysis algorithms are strongly impaired by quasi-period stellar signals. An optimal model to deal with stellar signal does not exist to date, and various different methods have been proposed thus far.

In this Chapter, I will illustrate the technique developed by the research group I am part of for the search of planetary signals around moderately active small mass stars, as well as its application both on synthetic data sets with simulated stellar activity signals (Sec. 4.1) and on real RV data in the detection of an extremely small mass exoplanet candidate (Sec. 4.2). The techniques applied on synthetic RV data in Sec. 4.1 are the same as those used in Chapter 6 in the analysis of the GJ15A system, and thus I discuss them in details.

4.1 Radial velocity fitting challenge

I will here outline the structure and main results of the Radial Velocity Fitting Challenge, as described in Dumusque (2016) and Dumusque et al. (2017). The Challenge consisted in several teams blindly analysing a set of real and simulated RV and activity indices time series, containing both planetary and stellar activity signals. Each group used their own techniques to recover the candidate planetary signal and distinguish them from stellar signals.

The use of synthetic data is demanded by the necessity to compare the results of the different methods, as well as with the true signals present in the time series, which are of course unknown for real observations. Nonetheless, real time series from known exoplanet host stars are used as part of the challenge data sets, to check the realism of the simulated stellar activity.

The systems analysed as part of the challenge represent the typical stellar activity levels and orbital architectures for inactive G-K dwarfs, which are the main targets of high-precisions extrasolar planets searches, and have also better understood chromospheric and magnetic activity than smaller mass stars. The general results presented here can anyway be applied to M dwarfs systems analysis as well.

4.1.1 Simulated data sets

I will now briefly summarize the simulation techniques used to generate and main properties of the systems analysed as part of the challenge. A more thorough and detailed description of the data sets can be found in Dumusque (2016).

15 systems were generated, containing more than 50 planetary signals. The crux of the problem was of course the realism of the planetary and stellar signals injected in the data. For planetary signals this was easily accomplished, since the Doppler shift from the Keplerian motion of a planet is straightforward (see Sec. 2.1.1) and realistic orbital parameters can be easily derived from the observed distribution of planets. To simulate realistically the stellar signals is instead more arduous.

To achieve a realistic representation of the different kinds stellar activity, as detailed in Sec. 2.2.1, real observations of solar type stars were used. The signals induced by stellar oscillations and granulations, as well as the instrumental noise, were generated by fitting the signals recovered in the high-cadence observations of the G8 dwarf τ Ceti (Teixeira et al., 2009) using the technique from Dumusque et al. (2011b) which consists of fitting the signal in the frequency domain and then return in the time domain changing the phases to produce different time sampling than the original data. The simulated data were checked with observations of different quiet solar-type stars (G8 to K5): a good agreement was found between the rms of the observed and simulated data, showing the goodness of the adopted procedure.

The signals from active regions, i.e. stellar spots and plages, were simulated using the SOAP 2.0 code (Spot Oscillation And Planet, Dumusque et al., 2014) which estimates the photometric and RV variations, as well as the BIS SPAN and FWHM (as defined in Sec. 2.2.1), induced by a given configuration of active regions and stellar rotation. SOAP 2.0 was further modified to produce also an estimate of the calcium activity index, $\log(R'_{\rm HK})$, which is not calculated by the published version of the code. Nevertheless due to the assumptions made in this estimate, only the time variation of the calcium index is correctly reconstructed, and not the total amplitude of the oscillations, but the latter is not crucial in the analysis of the rotation period and of the activity influence on the RVs.

The observational calendar from publicly available HARPS observed stars were used for the simulated observations, and signals from detected Kepler and HARPS planetary systems were injected in the time series along with the stellar activity. Some simulated planetary signals were injected in some time series, as well as some detected planets were not included in the respective systems. Also the periastron passage time T_P was altered, to avoid the recognition of known systems by the participating teams. This procedure was used to generate 10 planetary systems, containing 45 planets.

In addition to those, 5 datasets composed of real measurements from the HARPS spectrograph were used in the challenge, which included known planetary signals[1]. Again some expedient were performed to prevent the teams from recognizing the real data, like shifting the initial date of the time series or inverting the time of the observations.

One of the systems was later discarded due to an error in the generation of the RV time series. The complete data set consisted then of 14 systems, containing 51 planets in total.

The 14 systems produced for the RV fitting challenge contained several hundreds of data points each, with planetary signals much shorter than the data time span, typically of $3-4$ years. This data sets well represent the high cadence observations of bright solar-type stars, while they are quite different from the typical survey-level observations of M dwarfs, as those simulated in Sec. 3.2 or discussed in Chap. 7.

4.1.2 Implemented analysis techniques

Here I report the analysis procedure and algorithms applied by the research group I am part of during the RV fitting challenge, as reported in Appendix B of Dumusque et al. (2017). Our group is referred during the course of the challenge as Team 1, or the Torino Team, for the affiliation of most of the members to the Osservatorio Astrofisico di Torino. The team was composed by M. Damasso, A. Sozzetti, R. D. Haywood, A. S. Bonomo, M. Pinamonti, and P. Giacobbe. I took part in the analyses of several systems, mainly assisting M. Damasso in the signals identification and model selection (Step 3 and 5, discussed below).

The following description outlines also the main features of the analysis techniques I will employ in the next Chapters of this thesis.

The step-by-step approach

1. *Pre-treatment phase: removing long-term trends of stellar origin:* when generating the data of the RV fitting challenge Dumusque (2016) considered magnetic cycles and their effect on the different observables, that is $\log(R'_{\rm HK})$, BIS SPAN and full width at half maximum (FWHM) of the CCF. In this case, strong correlation between $\log(R'_{\rm HK})$ and FWHM, and between $\log(R'_{\rm HK})$ and RV are expected (Lovis et al., 2011a; Dumusque et al., 2011a; Lindegren and Dravins, 2003). To test those correlations, the Torino team calculated Spearman's rank correlation coefficients and found, in most cases, a very strong correlation between these observables, that is $\rho > 0.9$. In the case of significant correlation, that is $\rho > 0.5$, team 1 detrended the RV and the $\log(R'_{\rm HK})$ using linear fits between $\log(R'_{\rm HK})$ and RV, and $\log(R'_{\rm HK})$ and FWHM, respectively (Meunier and Lagrange,

---

[1] One of the planets present in the real time series adopted for the challenge, α Cen B b, was later discovered to be an artifact due to the sampling and the incorrect modelization of the stellar activity (Rajpaul et al., 2016)

2013). Detrending the RV and the $\log(R'_{\mathrm{HK}})$ allows suppressing almost entirely the long-term activity effect induced by magnetic cycles, and therefore leaves only the short-term activity effect, that team 1 further modelled using GP. In the case of systems 9, 10, and 11, RV were detrended with a linear fit as a function of time, as significant long-term signal, probably due to a binary, was still visible after correcting for magnetic cycle effect.

2. *GP regression of the activity index* $\log(R'_{\mathrm{HK}})$: to model $\log(R'_{\mathrm{HK}})$ with a GP, team 1 used the combination of a *rational quadratic* (RQ) and a *quasi-periodic* (QP) covariance function (Pont et al., 2013; Rasmussen and Williams, 2006):

$$k_{\mathrm{RQ,QP}}(t,t') = A^2 \exp\left(-\frac{\sin^2[\pi(t-t')/\theta]}{2L^2}\right) \times \left(+\frac{(t-t')^2}{2\alpha l^2}\right)^{-\alpha} + \sigma_t^2 \delta_{tt'}, \quad (4.1)$$

where t and t' represent epochs of observations, θ the stellar rotation period, σ_t is the uncertainty of the measurement at time t, and $\delta_{tt'}$ is the Kronecker's delta. When there is no a suitable guess about the timescale over which the data are varying, the RQ kernel can be assumed as a reasonable choice, because it is intended to model the data by accounting for many different timescales. In fact, it is equivalent to an infinite sum of squared exponential (SE) kernels:

$$k_{\mathrm{SE}}(t,t') = h^2 \exp\left[-\frac{(t-t')^2}{2l^2}\right], \quad (4.2)$$

with different length-scales l (Rasmussen and Williams, 2006), with the inverse squared timescales l^{-2} distributed according to a Gamma distribution with parameters α and $\beta = l^{-2}$. When $\alpha \to \infty$ the RQ kernel converges to the SE kernel. The function $k_{\mathrm{RQ,QP}}(t,t')$ describes the degree of correlation between each pair of measurements at times t and t', reducing to uncorrelated noise, that is white noise, when $t = t'$. This form of covariance function is suitable for data sets spanning a few years. For example, for the long-term photometry data set of HD 189733, Pont et al. (2013) discussed the choice of a $k_{\mathrm{RQ,QP}}(t,t')$ instead of a simpler exponential decay covariance function to model observed signal due to stellar activity.

The best-fit values of the covariance function hyper-parameters were obtained using an MCMC analysis. Initial guess for hyper-parameter θ was derived by performing a periodogram analysis with the Generalized Lomb-Scargle algorithm (GLS, Zechmeister and Kürster, 2009). After a burn-in phase, typically consisting of 1500 steps per chain, team 1 maximized the following log-likelihood function:

$$\ln \mathcal{L} = -\frac{n}{2}\ln(2\pi) - \frac{1}{2}\ln(\det \mathbf{K}) - \frac{1}{2}\underline{r}^T \cdot \mathbf{K}^{-1} \cdot \underline{r}, \quad (4.3)$$

where $\mathbf{K}$ is the covariance matrix built from the covariance function in Eq. 4.1, and $\underline{r}$ is the detrended $\log(R'_{\mathrm{HK}})$. The best-fit estimates of the hyper-parameters, inferred from their posterior distribution, were used as guess values for the subsequent modelling of the RVs, as explained below. Team 1 derived stellar rotation periods from the posterior distribution of θ.

3. *First identification of significant signals; GLS analysis of the RV time series:* the Torino team applied the GLS algorithm to search for significant signal in the originals RVs. Team 1 explored the frequency space below the Nyquist frequency and estimated peak significance using p-values determined through a bootstrap with replacement analysis consisting of 10000 random shuffles of the data by keeping the time stamps fixed. Team 1 selected for further considerations only peaks with p-values $< 10^{-3}$, except for system 14 and 15, because of the lower number of data points.
   Team 1 iteratively removed sinusoidal fits from the data, with periodicity corresponding to the periodogram peaks, and obtained guess values for the orbital period of the candidate Keplerian signals. Team 1 looked at the window function to discard aliases.
   As a general rule, only significant RV signals with period shorter than the data time span were considered, except for system 7, where a signal with longer period that the data time span was modelled with a Keplerian in the global fit, despite the inability of characterizing reliably the potential orbit. Moreover, the approach followed by the team was conservative, that is aimed at avoiding as much false positives as possible, favouring the analysis of signals with the highest semi-amplitudes.

4. *RV model and MCMC analysis:* after the analysis of the GLS periodogram, and the identification of significant signals that could be due to planetary candidates, the Torino team performed a global fit of the RVs with a model consisting of Keplerian orbits and correlated noise, to account for short-term stellar activity signals. This correlated noise is modelled using the GP covariance function seen in Eq. 4.1. The training of the GP on the $\log(R'_{\mathrm{HK}})$ gives initial guess for the GP hyper-parameters used when fitting the RVs. Doing so, team 1 assumes that short-term activity signals seen in RV and $\log(R'_{\mathrm{HK}})$ have similar covariance.
   The general Keplerian model fitted to the RVs is described by:

$$\begin{aligned}\Delta\mathrm{RV}_{\mathrm{Kep}}(t_i) &= \sum_{j=1}^{n_{\mathrm{planet}}} \Delta\mathrm{RV}_{\mathrm{Kep},j}(t_i) + \gamma \\ &= \sum_{j=1}^{n_{\mathrm{planet}}} K_j \left[\cos(\nu(t_i, T_{0j,\mathrm{peri.}}, P_j) + \omega_j) + e_j \cos(\omega_j)\right] + \gamma.\end{aligned} \tag{4.4}$$

   Instead of fitting e_j and ω_j separately, team 1 introduced:

$$C_j = \sqrt{e_j} \cdot \cos(\omega_j) \qquad S_j = \sqrt{e_j} \cdot \sin(\omega_j), \tag{4.5}$$

   to uniformly sample the eccentricity parameter space (Ford, 2006). Short-term stellar activity is fitted simultaneously by the GP applied to the RV residuals obtained by subtracting the Keplerian model from the raw RV data. The best-fit is found by maximizing the log-likelihood seen in Eq.

4.3. Note however that in this case the array $\underline{r}$ represent the RV residuals. The MCMC analysis used a number of random walkers, typically in the range 50-150, and was characterized by a burn-in phase, in general consisting of 1500 steps. For each fitted parameter the team adopted non-informative, uniform priors. The hyper-parameters of the covariance function were constrained within a range with reasonable finite lower and upper limits comprising the best-fit estimates found in the analysis of $\log(R'_{\mathrm{HK}})$, except for the semi-amplitude term A of the covariance function, which for the RVs is necessarily different from that of $\log(R'_{\mathrm{HK}})$ and was only imposed to be positive. No upper limits were fixed for $T_{0j,\mathrm{peri.}}$ and semi-amplitude K, while orbital periods were constrained over ranges of reasonable semi-amplitude centred on the guessed values obtained from the GLS periodogram analysis. To test the convergence of the different chains, team 1 used the Gelman-Rubin statistics described in Ford (2006). The best estimate of each parameter is derived using the median of its posterior distribution, with their asymmetric uncertainties derived from the 16th and 84th percentile (1σ uncertainty).

5. *Model selection:* the GP analysis requires a significant computational effort. Due to the relatively short timescales of the RV fitting challenge, team 1 could only test a limited number of different models for each system. Team 1 performed a Bayesian selection based on the truncated posterior mixture (TPM) method described in Tuomi and Jones (2012). In some cases, team 1 tested models with an equal number of planets, but fixing or not the eccentricity to zero. In few other cases, when signals could be of planetary or stellar nature, team 1 compared models with different number of planets, limiting the analysis to circular orbits. Finally, when the Bayesian analysis showed to be inconclusive, team 1 selected the model with fewest parameters, following the principle of Occam's razor. Note however this was not the case for system 15, because the three candidate signals appear to be well modelled by a sinusoid, even if the true nature of one Keplerian was flagged as doubtful.

Algorithms and tools

Here is a list of the different tools that team 1 used to perform the analysis:

- Spearman's rank correlation coefficients were evaluated with the R_CORRELATE function, which is part of the IDL library.

- Linear fits ($\log(R'_{\mathrm{HK}})$ vs. FWHM and $\log(R'_{\mathrm{HK}})$ (or time) vs. RV), and estimation of the GP hyper-parameters and Keplerian parameters were performed using the publicly available EMCEE Affine Invariant MCMC Ensemble sampler, developed by Foreman-Mackey et al. (2013)[2].

- The search for sinusoidal modulations in the $\log(R'_{\mathrm{HK}})$ and RV data were performed with the generalized Lomb-Scargle (GLS) algorithm developed by Zechmeister and Kürster (2009).

---

[2] See also `http://dan.iel.fm/emcee/current/`

4.1.3 Results

In total eight teams took part to the RV fitting challenge. The approaches used can be distinguished in two main categories: fives teams, including us, used Bayesian modelling to select the best solution for each system, while the other three did not, and instead used pre-whitening or other techniques to deal with the multiple signals present in the time series.

The complete results and analysis techniques adopted are thoroughly discussed in Dumusque et al. (2017). I will briefly discuss some of the main points which are of interest as part of my PhD work.

Many of the methods applied to the challenge required as a first step the identification of the rotation period of the host star, as was the case for ourselves and other three teams. The detected rotation periods were correct most of the time. Even so, in some cases ($20 - 45\%$) an harmonic of the stellar rotation period was recovered instead of the period itself. This could cause problems since periodic signals observed at multiples of the rotation periods (e.g. $2P_{\rm rot}$, $3P_{\rm rot}$) are not expected to be due to stellar activity, and therefore are assumed to be planets. This problem could be avoided if the stellar rotation is known by other means, like from the photometric monitoring of the star, or if it can be derived from the average calcium activity levels which is known to be related with the rotation period (Mamajek and Hillenbrand, 2008). This remark the importance of knowing the exact rotation period in order to correctly treat the stellar activity signals. Unfortunately, the different teams recovered the wrong rotation periods in different systems, so no conclusive evidence is found as for the origins of such mistakes.

As a criterion of the strength of a planetary signals in its time series, Dumusque et al. (2017) defined the K/N ratio, as:

$$K/N = \frac{K_{\rm pl}}{{\rm RV}_{\rm rms}} \sqrt{N_{\rm obs}}, \tag{4.6}$$

where $K_{\rm pl}$ is the semi-amplitude of the planetary signal, $N_{\rm obs}$ is the number of observations composing the time series and ${\rm RV}_{\rm rms}$ is the rms of the RV time series corrected for the correlation with the $\log(R'_{\rm HK})$ plus a second-order polynomial which take into account the magnetic cycle and potential long-period companions.

The results of the different teams which analysed the complete data set of the challenge is shown in Fig. 4.1. The recovered signals are colour coded by comparison with the true signals present in the data. The code goes as follow:

- Dark green: a signal actually present in the data is recovered, and the team is certain enough of its presence that would have published it;
- Light green: a signal actually present in the data is recovered, but the evidence for its presence is not strong enough for a publication;
- Yellow: a signal actually present in the data is recovered, and the team is certain enough of its presence that would have published it, but the period or semi-amplitude of the signal is not correctly identified;
- Gray: a signal actually present in the data is recovered, but the evidence for its presence is not strong enough for a publication, and the period or semi-amplitude of the signal is not correctly identified;

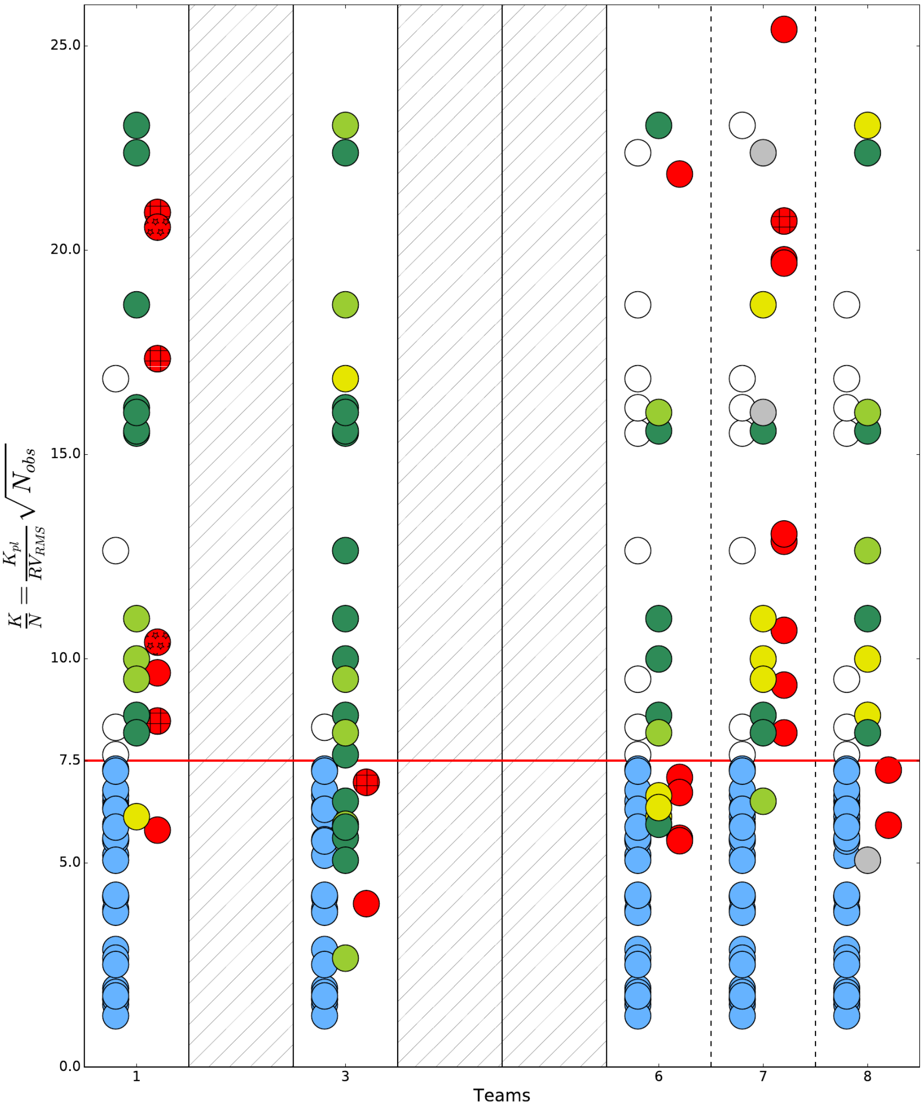

Figure 4.1: K/N ratio for all the planets present in the entire data set of the RV fitting challenge, as announced by the different teams which performed the full analysis of all the systems. See text for the complete description f the colour coding. (from Dumusque et al., 2017)

- White: a planet with $K/N > 7.5$ is not detected by the team;
- Cyan: a planet with $K/N < 7.5$ is not detected by the team;
- Orange: a signal that is not present in the data is recovered, but the evidence for its presence is not strong enough for a publication;
- Red: a signal that is not present in the data is recovered, and the team is certain enough of its presence that would have published it. The red points are further labelled in three different kinds: unexplained false positives (plain red), signals corresponding to the rotation period of the star when the period itself was correctly identified (hatched red) and signals corresponding to the rotational period when the wrong period was identified (starred red).

The second and third type of false positives (red dots), could have been avoided by exploiting the additional information usually available on the host star to better constrain the stellar rotation, or by ignoring potential signals near the rotation period itself, and thus were not considered in the general discussion of the results of the RV fitting challenge.

From Fig. 4.1 is clear how the number of detections drops below $K/N = 7.5$, which was thus concluded to be a good estimate of the lower limit for confident detections. Below this threshold the detection rate swiftly decreases, down to $\sim 20\%$, and no method was able to detect confidently signals below $K/N = 5$.

Our team announced three planets at the stellar rotation period which in fact proved to be false positives. This showed how sometimes the GP regression technique we used was not able to fully model the stellar activity, and some signal remained around the rotation period. This point out that a great care should be taken when analysing signals close to the modelled activity signal of the star, and supplementary tests (which we couldn't run for lack of additional time to invest in the challenge) should be used to verify the planetary nature of ambiguous signals.

It's worth noticing that, while teams 1 (ourselves) and 3 detected most of the signals above the $K/N = 7.5$ threshold, that was not the case for teams 6,7 and 8. The main difference between the analysis techniques adopted by these teams is that teams 1 and 3 used a Bayesian framework for model selection, while the others did not. Also teams 2, 4 and 5 used methods based on Bayesian statistics, but due to the short time scale for the challenge, were not able to analyse the full data set provided. On the systems they analysed, a similar behaviour than of teams 1 and 3 was showed, with very few false positives and most planets detected for $K/N > 7.5$. It thus seems that Bayesian techniques performs better in the recovery of planetary signals despite the presence of stellar noise.

The results of the RV fitting challenge are of course not the final word on the subject, since many factors could have altered the performances of the different methods and teams, like the short time scale for the challenge along with the individual availability of the participants, or the preliminary status of some of the adopted techniques. Also the wide range of systems characteristics and huge number of parameters involved make difficult to asses strong conclusions from the results. For these reasons, it is clear how more focused tests, like the one presented in Chap. 3, can integrate the results of extensive analyses such as the RV fitting challenge.

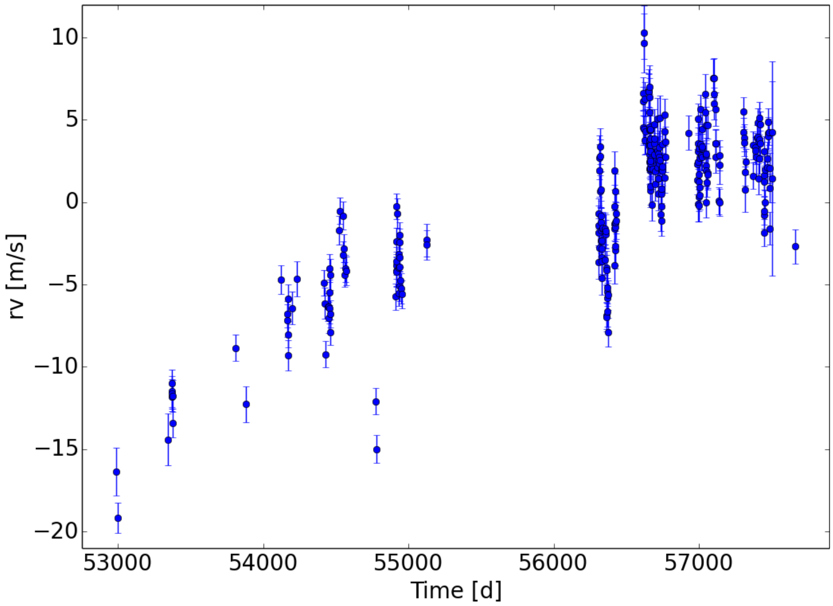

Figure 4.2: RV time series of GJ273, from Astudillo-Defru et al. (2017).

4.2 GJ 273: a very low-mass planet in a compact multiple system

In March 2017, Astudillo-Defru et al. (2017) announced the discovery of twelve planets around five M dwarfs from the HARPS M dwarf sample (Bonfils et al., 2013a). One of these systems in particular was fascinating: GJ273 was claimed to host one Earth-like planet and a super-Earth just inside the habitable zone, being one of the closest multi-planet systems to our Sun, and the second closest system hosting potentially habitable planet after Proxima Centauri (Anglada-Escudé et al., 2016a). For these reasons we decided to further investigate the public RV time series of this system, applying to them the analysis techniques described in Sec. 4.1.2.

I report here the outline of the analysis I performed alongside Mario Damasso. The details and complete results of this study will be the content of Damasso, Pinamonti et al. (in prep.).

4.2.1 The known system

Astudillo-Defru et al. (2017) studied 280 RV points of the GJ273 system, collected with the HARPS (south) spectrograph (Mayor et al., 2003) at ESO/La Silla Observatory. The dataset has a standard deviation of 2.75 m s^{-1}, which is almost 3 times greater than the average uncertainty, thus suggesting the presence of stellar or planetary signals in the data. The RV data are shown in Fig. 4.2.

The stellar parameters for the studied stars were recovered from the literature, and the fundamental are listed in Table 4.1.

A GLS periodogram analysis was performed on the data, iterating until the

Table 4.1: GJ273 main properties. (For complete references see Astudillo-Defru et al., 2017)

Parameter	GJ273
Spectral Type	M3.5
T_{eff} [K]	3382 ± 49
[Fe/H] [dex]	0.09 ± 0.17
Mass [$M_\odot$]	0.29
Radius [$R_\odot$]	0.293 ± 0.027
$L_*/L_\odot$	0.0088 ± 0.0066
P_{rot} [d]	99
α (J2000)	07^h:27^m:24.49^s
δ (J2000)	$+05°$:$13'$:$32.8''$
V [mag]	9.872
J [mag]	5.714 ± 0.032
H [mag]	5.219 ± 0.063
K [mag]	4.857 ± 0.023
π [mas]	262.98 ± 1.39
μ_α [mas yr^{-1}]	572.51 ± 1.50
μ_δ [mas yr^{-1}]	-3693.51 ± 0.96

residuals showed no significant signal under a 1% FAP level. The final Keplerian solution was corrected fitting the model with the YORBIT code (Ségransan et al., 2011). To discriminate between planetary and stellar signals, a GLS analysis was performed also on the $\log(R'_{\text{HK}})$ activity indicator, and every periodicity found in both time series was discarded as stellar-induced.

Astudillo-Defru et al. (2017) detected four periodic signals in the RV time series, at 5, 20, 420, and 700 d. The two longest periodicities were associated to the stellar magnetic cycle, since they disappeared when the RVs were corrected for the $P \sim 2000$ d signal found in the Calcium index. The other two signals did not appear in the activity index time series, and were very different from the rotation period of the star ($P_{\text{rot}} \sim 99$ d), so they appeared to be of planetary nature. A further test of their nature was to check that the two signals were coherent across the entire time series, which was done by splitting the dataset in several parts with roughly the same number of RVs and analyse them separately. A power excess was found in the periodograms of all the epochs, thus confirming the stability of the two planetary signals.

The RV data were then fitted with a YORBIT model for two planetary signals, obtaining the final solution for the orbital parameters of the two planets GJ273 b and GJ273 c as listed in Table 4.2. The phase folded RV curves over the two planets' periodicities are shown in Fig. 4.3.

As previously mentioned, planet b, with its semi-major axis $a_b = 0.09110 \pm 0.00002$ AU is well within the inner edge of the habitable zone, calculated taking into account the likely tidal locking of the planet following the recipe by Kopparapu et al. (2016). Hosting the second closest known planet in the HZ, after Proxima Centauri b, GJ273 is a fascinating star, even further considering it is a much quieter star than the flaring Proxima Centauri.

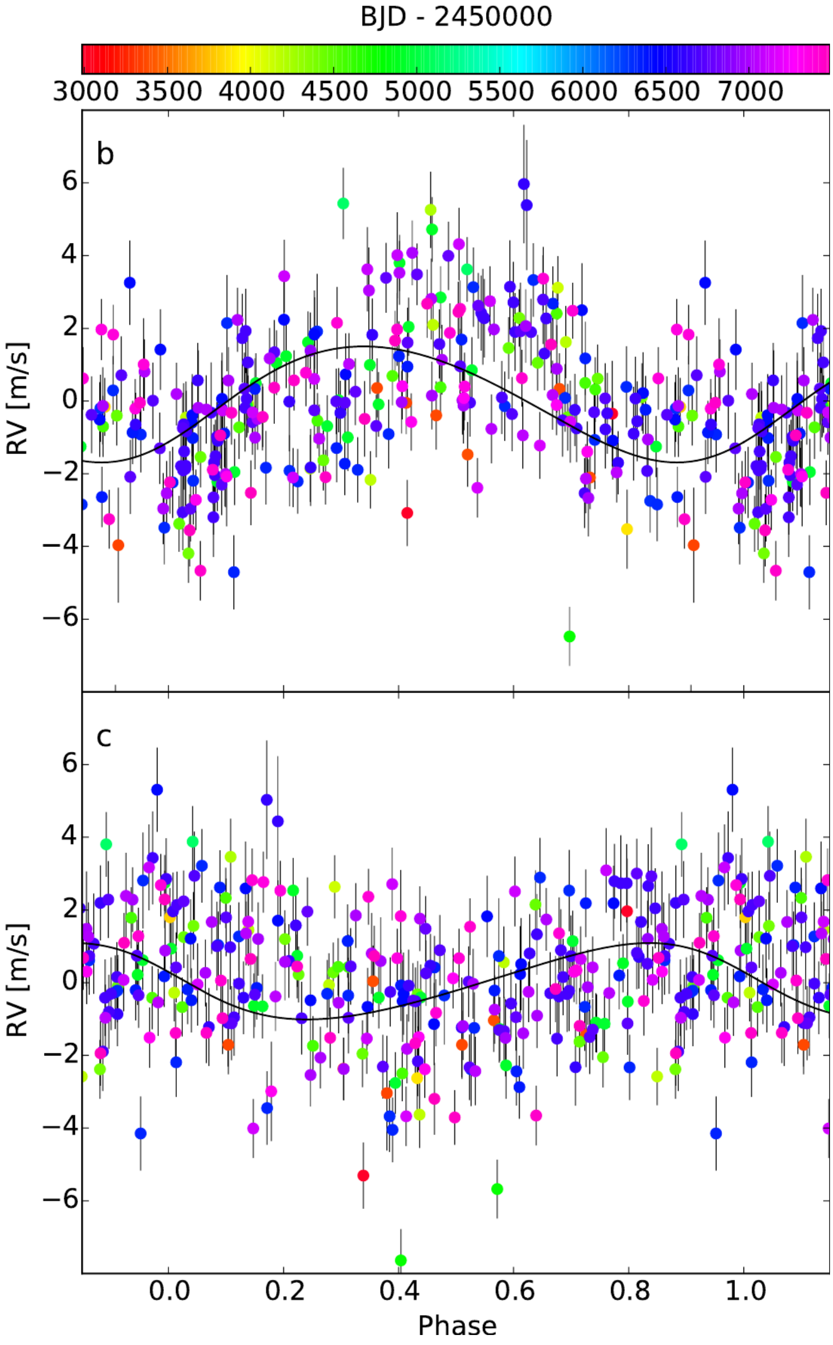

Figure 4.3: Phase folded RVs for the 18.7 d (top) and 4.7 d (bottom) periods, along with the best fit Keplerian solution (solid line). The colour scale represent the observing epochs. (from Astudillo-Defru et al., 2017)

Table 4.2: Published solution for the Keplerian model for the GJ273 system from Astudillo-Defru et al. (2017).

K_b [m s^{-1}]	$1.61^{+0.15}_{-0.15}$
P_b [d]	$18.6498^{+0.0059}_{-0.0052}$
$\lambda_{0,b}$ at BJD= 2456238.2124 d	$229.6^{+5.3}_{-5.5}$
$m_b \sin i_b$ [$\mathrm{M}_\oplus$]	$2.89^{+0.27}_{-0.26}$
K_c [m s^{-1}]	$1.06^{+0.15}_{-0.15}$
P_c [d]	$4.7234^{+0.0004}_{-0.0004}$
$\lambda_{0,c}$ at BJD= 2456238.2124 d	$75.6^{+8.1}_{-8.4}$
$m_c \sin i_c$ [$\mathrm{M}_\oplus$]	$1.18^{+0.16}_{-0.16}$

4.2.2 Candidate planet detection

Due to the fascinating super-Earth in the habitable zone, and being the two planetary signals quite small ($K_b \simeq 1.6$ m s^{-1}, $K_c \simeq 1.1$ m s^{-1}) we decided to re-analyse the public RV time series of the systems, applying our technique as described in Sec. 4.1.2. In particular we wanted to test how our GP modelling of the stellar activity, which proved to be very reliable throughout the RV challenge, would affect the two planets orbital parameters.

We followed the step-by-step approach described in Sec. 4.1.2, with the following modifications:

- on the contrary to the RV challenge, for this system the rotation period was known from the literature to be ∼ 99 d, thus during Step 2 we narrowed the uniform prior of the θ parameter in a small interval around 100 d;
- we omitted Step 3 and accepted the preliminary results of the GLS analysis by Astudillo-Defru et al. (2017);
- during Step 4, we tested only a two planet plus stellar noise model, and used the published orbital parameters as initial guess for the model in the MCMC analysis, but used non-informative priors to allow the random walkers to explore freely the parameter space;
- we omitted Step 5, since only one model was tested.

Due to the low significance of the eccentricities reported by Astudillo-Defru et al. (2017) we tested a model with both planets in circular orbits.

The results of the two planet and stellar noise model are listed in the central column of Table 4.3. As we can see the orbital parameters didn't change very much, remaining within 2-σ of the published solution. The GP model seems to correctly fit the stellar activity signal, and the best-fit value of the θ hyperparameter is very close to the published value of the rotation period of GJ273.

Even if no large variation of the two planets parameters was recorded, still an interesting feature emerged: in the analysis of the RV residuals, after subtracting the planetary and stellar signals, we found in the GLS periodogram a clear

Table 4.3: Planetary parameter best-fit values obtained through a joint modelling of Keplerian signals and correlated stellar noise, using Gaussian process regression.

Parameter	Two-planet model Best-fit value	Three-planet model Best-fit value
h [m s^{-1}]	$3.05^{+0.41}_{-0.34}$	$3.04^{+0.44}_{-0.35}$
λ [d]	96^{+22}_{-25}	97^{+21}_{-25}
w	$0.84^{+0.10}_{-0.13}$	$0.82^{+0.11}_{-0.13}$
θ [d]	$98.4^{+7.4}_{-9.5}$	$96.4^{+7.0}_{-10.0}$
K_b [m s^{-1}]	$1.495^{+0.100}_{-0.095}$	$1.533^{+0.101}_{-0.101}$
P_b [d]	$18.6395^{+0.0036}_{-0.0036}$	$18.6382^{+0.0036}_{-0.0037}$
$T_{0,b}$ [BJD$-$2450000]	$7517.70^{+0.31}_{-0.30}$	$7517.65^{+0.30}_{-0.30}$
$m_b \sin i_b$ [$\mathrm{M}_\oplus$]	$2.72^{+0.18}_{-0.17}$	$2.79^{+0.18}_{-0.18}$
K_c [m s^{-1}]	$0.908^{+0.080}_{-0.079}$	$0.933^{+0.080}_{-0.082}$
P_c [d]	$4.72280^{+0.00030}_{-0.00028}$	$4.72288^{+0.00028}_{-0.00028}$
$T_{0,c}$ [BJD$-$2450000]	$7504.10^{+0.11}_{-0.11}$	$7504.19^{+0.11}_{-0.10}$
$m_c \sin i_c$ [$\mathrm{M}_\oplus$]	$1.045^{+0.092}_{-0.091}$	$1.074^{+0.092}_{-0.094}$
K_d [m s^{-1}]	-	$0.443^{+0.089}_{-0.086}$
P_d [d]	-	$8.6412^{+0.0021}_{-0.0021}$
$T_{0,d}$ [BJD$-$2450000]	-	$7504.73^{+0.40}_{-0.40}$
$m_d \sin i_d$ [$\mathrm{M}_\oplus$]	-	$0.62^{+0.12}_{-0.12}$

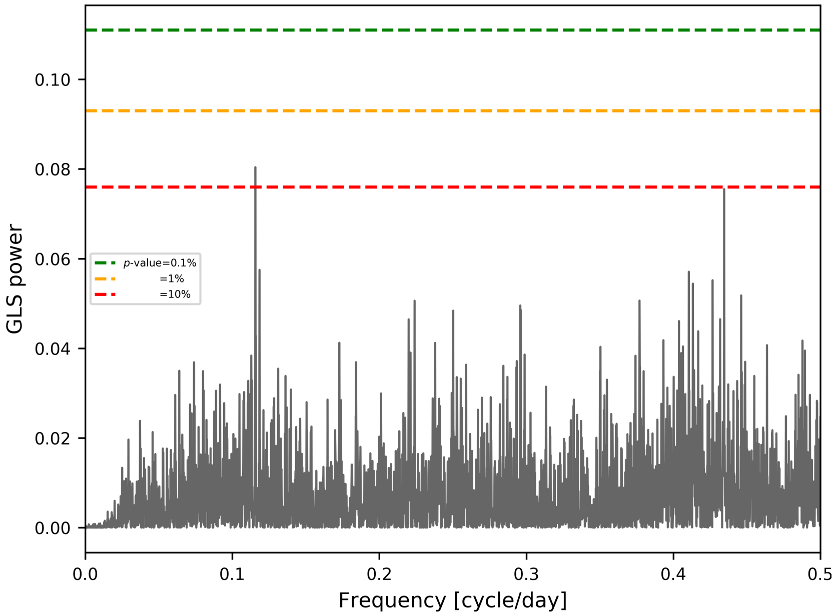

Figure 4.4: GLS of the residuals of the two planet plus stellar noise model, with reference levels of FAP (dashed lines).

though small signal at $P = 8.64$ d. From a bootstrap analysis we derived a FAP of $\sim 6\%$. The GLS periodogram of the residuals and the 10%, 1%, and 0.1% FAP levels are shown in Fig. 4.4. It's worth noticing that Astudillo-Defru et al. (2017) never report a similar signal in their GLS analysis.

We then tested a three-planet plus stellar noise model, adopting normal distributions as priors for the two known planets parameters, centred on the best-fit values and using twice the mean uncertainty as standard deviation. For the additional planet, hereafter planet d, we adopted a non-informative prior, with the period in a $[5, 15]$ d interval. The results of the analysis are listed in the right column of Tab. 4.3. We can see that there is no significant shift in planet b and c parameters, while a small but significant signal ($K > 5\sigma_K$) is recovered for planet d. The Bayesian comparison between the two models, calculated with the estimator by Chib and Jeliazkov (2001), resulted in a strong statistical evidence in favour of the three-planet model, with the Bayesian evidence $\mathcal{Z}$ rising from $\log \mathcal{Z} \simeq -522$ to $\log \mathcal{Z} \simeq -510$ from the two- to the three-planet model respectively.

The candidate planet GJ273 d is quite fascinating, with its amplitude $K_d = 0.443$ m s^{-1} it would be one of the smallest[3] RV signals ever detected.[4] On the other hand its presence is by no means clear: even if its amplitude is significantly different from zero, and the Bayesian evidence support its presence, the very low amplitude of the signal, especially if compared to the amplitude h of the stellar model, ~ 7 times large, and the uncomfortably large FAP of the signal as seen in the residuals are still enough reasons to be distrustful.

---

[3] Source: NASA Exoplanet Archive - 18 October 2017

[4] It was i fact the smallest, until the recent announcement in August 2017 of the four-planet system around τ Ceti (Feng et al., 2017).

Table 4.4: Numerical simulation of GJ273 d results.

	C	FP fraction	R
RV residuals			
GLS	18.9%	2.2%	89.6%
BGLS	24.2%	2.4%	90.9%
FREDEC	10.7%	20.0%	35.0%
Planet d injected			
GLS	20.2%	6.6%	75.3%
BGLS	17.9%	4.5%	79.9%
FREDEC	23.8%	14.4%	62.2%
Planet d absent			
GLS	0.3%	7.3%	4.0%
BGLS	0.3%	6.6%	4.1%
FREDEC	0.1%	7.6%	0.9%

Thus we decided to statistically investigate the presence of the candidate planet d in the RV time series.

4.2.3 Statistical validation

Such a small amplitude signal could be just an artifact due to the observational epochs or due to the treatment of the stellar activity.

To validate the presence, as a genuine planetary signal, of the $P_d = 8.64$ d signal first seen in the residuals of the two-planet plus stellar noise model, we decided to generate different realizations of the GJ273 RV time series, and study them with the three periodogram algorithms discussed in Chapter 3 (Pinamonti et al., 2017). The comparison of the results of the different algorithms, applied on a statistically large sample of data, could help clarify the effective presence of the planetary signal.

First we generated a catalog of 10000 time series, each obtained by subtracting from the HARPS time series a realization of the two-planet plus stellar noise model, with each parameter normally distributed around the best-fit value (from the middle column of Table 4.3 and standard deviation equal to the mean uncertainty. Then the datasets were analysed applying the three algorithms, GLS, BGLS, and FREDEC. The results were described by means of the two performance metrics C and R, and of the False Positives fraction, to compare the results to those of Sec. 3.3, with the difference that we defined as “input” signal the candidate signal $P_d = 8.64$ d. Thus the completeness C was calculated as the fraction of systems in which the 8.64 d signal was recovered with FAP lower than the threshold, and we considered as “false positive” any significant signal with a period $P \neq P_d$. Due to the expected low significance of the signal, we adopted a higher FAP threshold then in the previous Chapter: $FAP < 10\%$. The results of this first analysis are listed in the upper panel of Table 4.4.

We can see that the completeness C is low for all three algorithms, with BGLS showing the best performance. This is to be expected at such regimes of $K/\sigma \simeq 1/1$, which, even if not investigated in Chap. 3 can be extrapolated from Fig. 3.4: the FAP dependence on K/σ has a constant slope for GLS and FREDEC, while it tends to smooth at low K/σ for BGLS. Thus low amplitude signals have a higher significance for BGLS. The low R value for FREDEC is also expected, due to the presence of spurious multi-frequency solutions, which are recovered by FREDEC independently of the K/σ level (bottom left panel of Fig. 3.4).

Due to the overall low detection fraction of the candidate signal at $P = 8.64$ d for all the algorithms employed, the second step was to generate a comparison catalog, of synthetic time series with all the three planetary signals injected, along with the GP model for the stellar signal. The time series where generated from the three-planets plus stellar noise model, with each parameter normally distributed around the best-fit value (from the right column of Table 4.3 and standard deviation equal to the mean uncertainty. The epochs and measurements errors where those of the original HARPS time series. The single data points where then normally displaced within their error bars. From each time series the signals of the known planets and stellar activity were subtracted as in the previous case. The results are listed in the middle panel of Table 4.4.

The completeness C is again around $\sim 20\%$ for all three algorithms, roughly equal to the value for GLS and BGLS in the previous case. There is a reversal between GLS's and BGLS's C values, with GLS performing slightly better than the other one, while FREDEC performs $\sim 13\%$ better than in the previous case, even if still showing the lowest R value, which can be ascribed to the same reasons as before. Fluctuations as such are to be expected at such small amplitudes, and the different relative performances of the three algorithms can be associated to the different modelling of the errors in the simulations: we can see that the mean rms of the residuals of the two planets plus stellar models is somewhat higher ($1.10 > 0.99$ m s^{-1}) in the simulations than in the real data. This could be due to overestimate of the instrumental errors $\sigma_{\rm RV}$, which we used to displace the generated data points prior to the model subtraction.

The last experiment was to study a set of synthetic time series analogous to the previous case but with only the two known planetary signals injected. Again the residuals were generated subtracting the two planet plus stellar noise model as before. The results are listed in the lower panel of Table 4.4. We can see that the signal is almost never recovered ($C \sim 0\%$ for all the algorithms) and that is watered down by a much larger number of False Positives (i.e. spurious signals with $P \neq 8.64$ d).

The absence of similar $P = 8.64$ d signals in the third catalog suggests that the detected periodicity is not an alias of the observational sampling, nor a spurious signal caused by the GP treatment of the stellar activity. On the other hand the similar features observed in the real data residuals and synthetic three planet catalog suggest that the candidate planet d is in fact of planetary nature. Due to the uncertain nature of such small signal, however, we are still performing some additional test to ascertain the detection, as well as to study the nature of a $P \simeq 2.3$ d signal which could be present in the data (the peak just below the FAP= 10% line on the right of Fig. 4.4).

Chapter 5

Global Architecture of Planetary Systems

After several studies on synthetic and archival data sets, the final part of my PhD work was carried out as part of the GAPS consortium, to detect and characterize planetary systems around M dwarfs from observational data collected with the HARPS-N@TNG spectrograph as part of the HADES survey. Most of the techniques mastered during the studies described in the previous Chapters were applied in these analysis, the results of which are described in details in the following Chapters.

In this Chapter, I describe the main characteristics of the HARPS-N spectrograph, and then outline the structure and main results of the GAPS collaboration, and of the HADES RV programme.

5.1 HARPS-N@TNG

The HARPS-N (High Accuracy Radial velocity Planet Searcher for the Northern hemisphere, Cosentino et al., 2012) spectrograph, was installed at the Telescopio Nazionale Galileo (TNG), at the Observatory of the Roque de los Muchachos in La Palma Island, in April 2012. Its design was based on the HARPS spectrograph installed at the ESO 3.6m telescope in La Silla, and it is specifically planned to optimise the precision of the radial velocity measurements. Its main scientific goal is the detection and characterization of terrestrial mass planets, with a particular focus of the Guaranteed Time of Observation on the confirmation of transiting planets observed by the Kepler spacecraft.

It is an Echelle spectrograph, and several precaution have been taken into its construction to minimize the spectral drift and to maximize the radial velocity accuracy. A schematic view of the instrument setup and its coupling to the telescope are shown in Fig. 5.1.

To guarantee the highest possible stability the instrument is set under extreme precision temperature control, given by a liquid nitrogen CFC (continuous flow cryostat) supplied by ESO, inside a vacuum chamber to avoid pressure perturbation, on the ground floor of the observatory to avoid vibration due to the telescope motion, and it is fed with octagonal fibre to optimise the light scrambling in the detector feed. The octagonal fibres exemplify the improvement

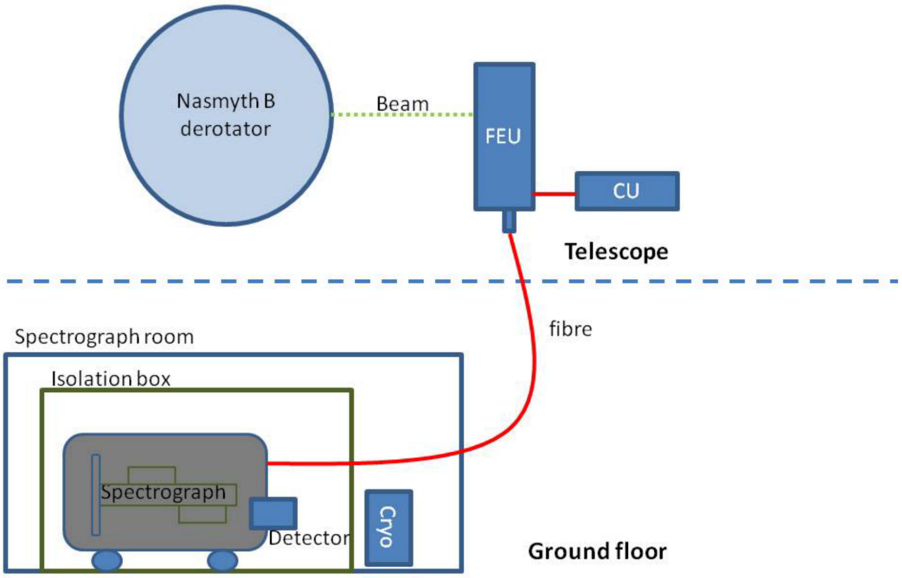

Figure 5.1: HARPS-N general schematic view. (from Cosentino et al., 2012)

made with respect to its predecessor HARPS south: the southern instrument was sensitive to the de-centring of the star with respect of the circular fibre, which caused a shift in the RV of the order f $3-4$ m s^{-1}, due to the non-optimal scrambling of the light; with the adoption of octagonal fibres, this effect has been reduced by about a factor of 10 (Chazelas et al., 2010).[1]

Two fibres are used for simultaneous reference of the spectra, and both of them are calibrated at the start of each observing night. As shown in Fig. 5.1 the Front End Unit (FEU) collimates the incoming light from the telescope and from the Calibration Unit (CU) into the fibres. The CU contains the Th-Ar lamp used for calibration (see Sec. 2.1.1 for the details of the simultaneous calibration technique).

In Table 5.1 is shown a summary of the main characteristics of the instrument.

The HARPS-N spectrograph is also supplied with a automatic Data Reduction System (DRS, Sosnowska et al., 2012), which carries out a complete reduction of the acquired data within just a few seconds after the end of the exposure. First the full spectra is reduced with dark and bias correction, flat-fielding, cosmic ray correction, and wavelength calibration, using the optimal extraction method by Horne (1986). The DRS then computes the RV of the target from the Cross-Correlation Function (CCF) of the spectra (e.g. Pepe et al., 2002), which is calculated by multiplying the observed spectra by a template mask (e.g. in the case of M dwarfs analysis an M2 binary mask composed of 9000 wavelength intervals) and then fitted with a Gaussian function whose peak corresponds to the RV. This procedure is implemented over each of the diffraction order of the Echelle spectra, and the final RV value is the flux-weighted

---

[1] In May 2015 the HARPS circular fibres were also replaced with octagonal fibres, to better stabilize the illumination of the detector (Lo Curto et al., 2015).

Table 5.1: HARPS-N main characteristics (from Cosentino et al., 2012)

Spectrograph type	Fibre fed, cross-dispersed Echelle spectrograph
Spectral resolution	R = 115000
Fibre field	FOV = 1”
Wavelength range	383 nm − 690 nm
Total efficiency	e = 8% @ 550 nm (incl. telescope and atmosphere @ 0.8” seeing)
Sampling	s = 3.3 px per FWHM
Calibration	ThAr + Simultaneous reference (fed by 2 fibres)
CCD	Back-illuminated 4k4 E2V CCd231 (graded coating)
Pixel size	15 μm
Environment	Vacuum operation - 0.001 K temperature stability
Global short-term precision	0.3 m s^{-1} (10E-9)
Global long-term precision	better than 0.6 m s^{-1} (2x10E-9)
Observational efficiency	SNR = 50 per extracted pixel on a Mv = 8, TExp = 60 s
Wavelength accuracy	60 m s^{-1} (2x10E-7) on a single line

mean of all the different values.

5.2 The GAPS project

The ”Global Architecture of Planetary Systems“ (GAPS) is an Italian Large Project, aimed to the search and characterization of exoplanetary systems around host stars of different characteristics: as discussed in Chapter 2, M dwarfs planetary systems show different properties with respect to Solar-like star systems, and similar differences may arise also from different stellar characteristics, as metallicity or environment.

The GAPS project started with an open call to Italian scientists involved in the field of exoplanetology in order to join their specific knowledge and expertise to optimize the science return of HARPS-N open time. The second objective was to create a coordinated community working together to reach a significant impact in the international context of exoplanetary science. The GAPS project was competitively selected by INAF’s TNG Time Allocation Committee as long-term program, starting its observations with HARPS-N in August 2012. The consortium currently includes 61 scientists from 14 INAF structures and Italian universities, plus 18 external collaborators working at research institutes and universities across Europe and the United States. Another key aspect of the project was the training of young researchers in the field of exoplanetology, with several fellowships and some PhD students, such as myself. Such young astronomers were deeply involved in the research projects, and wrote as first

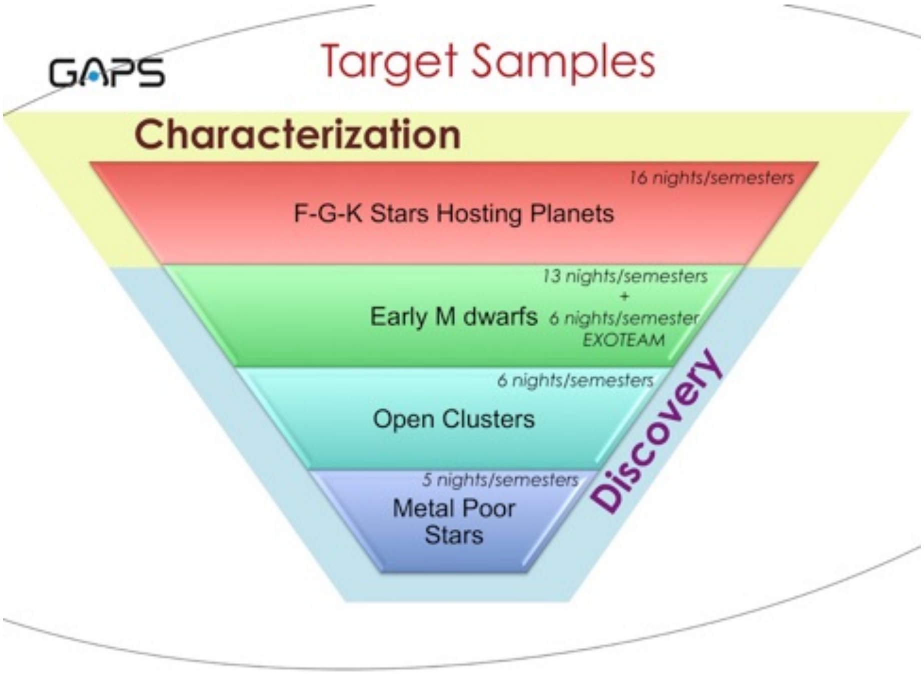

Figure 5.2: The structure of the GAPS sub-programs, with the average number of dedicated nights for each semester.

authors many of the GAPS papers.

The scientific goal of the project was to understand the architectures of planetary systems and their properties, as well as their dependence on the host star characteristics. For this reason the adopted strategy was to divide the observing time obtained with the HARPS-N spectrograph at the TNG (Telescopio Nazionale Galileo) in different sub-programs, each of them focused on the study of a well-defined class of stars. Along with this detection programs, part of the time was also invested in the study of known planetary systems, to better characterize their properties due to the outstanding capabilities of HARPS-N.

The 4 main subprograms were the following:

- F-G-K Stars Hosting Planets: this subprogram focused on the search for additional low-mass planets in known systems with giant planets, both long-period, aiming to determine the frequency of scaled versions of our own Solar System, and hot-Jupiters, to study their multiplicity properties;
- Early M Dwarfs: this subprogram targeted low-mass dM0-dM3 stars, and was carried out in concert with the Spanish EXOTEAM group (I will discuss it in more details in Sec. 5.3);
- Open Clusters: this subprogram consisted in the search for close-in planetary companions to stars belonging to nearby clusters, to verify the impact of a crowded environment on the planetary formation process;
- Metal Poor Stars: this subprogram studied a sample of low-metallicity

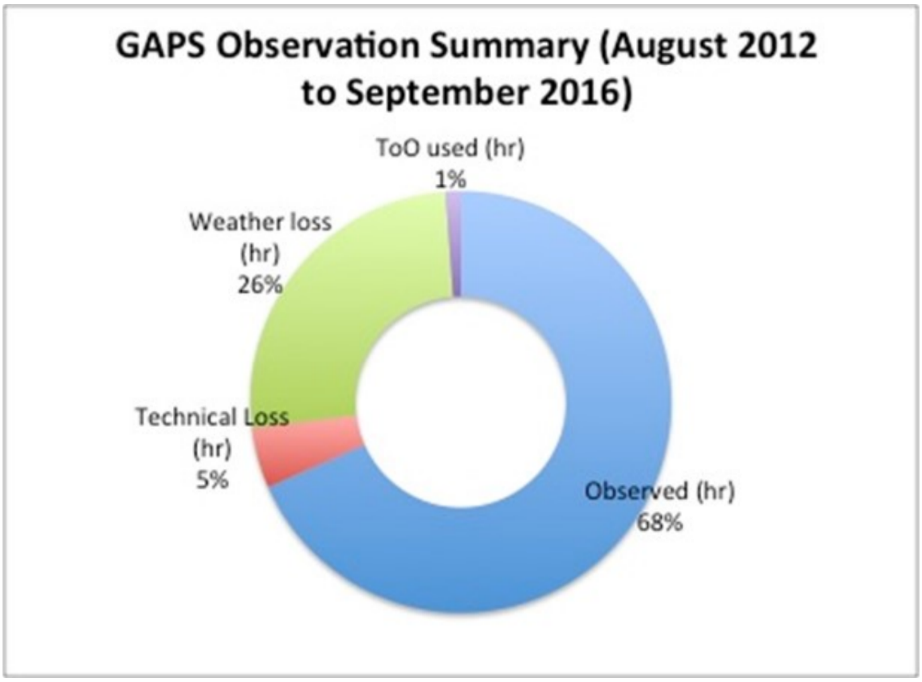

Figure 5.3: Schematics of the use of GAPS observing time from AOT26 to AOT33.

stars, to test the effect of metallicity variations on the formation of small mass planets;

The subprograms and the typical time allocation during the observing semester is shown in Figure 5.2. Also as part of the project were performed some characterization studies of Rossiter-McLaughlin effect, asteroseismology and star-planet interactions.

The GAPS observations at TNG started in August 2012 (AOT26), and since then ~ 2500 observing hours have been allocated, resulting in ~ 7000 collected spectra of a sample of ~ 300 stars. The first observing semester was affected by a failure of the HARPS-N detector, which caused a significant loss of observing time. After those first problems the losses due to technical reasons were extremely low ($\sim 2\%$). The statistics of the observing nights is shown in Figure 5.3. As part of the GAPS projects, also ancillary photometric observations were collected, mostly by means of the APACHE (Sozzetti et al., 2013) and EXORAP[2] surveys.

The GAPS programme has produced a large amount of scientific results, with 15 publications on refereed journals (without counting the results of the HADES survey, which I will discuss later) and a lot more still in preparation. Due to the several uncertainties in the detection of low amplitude planetary signals in the presence of significant stellar noise, even if most of the targets were selected for their low activity levels, it was decided for a cautious approach on new planets announcements. For this reason the promising systems were

---

[2] EXOplanetary systems Robotic APT2 Photometry

intensively monitored, in order to collect large amount of data and to constraint as tightly as possible the orbital parameters of the new-found planets.

I will now discuss a handful of the main results of the GAPS project. A more complete overview can be found in Poretti et al. (2016) and Benatti et al. (2017) and references therein.

5.2.1 Results overview

The first planetary system announced by the GAPS consortium was XO-2S (Desidera et al., 2014), for which two planets were discovered: XO-2S b with a period $P_b = 18.157 \pm 0.034$ d and minimum mass $m_b \sin i_b = 0.259 \pm 0.014$ $\mathrm{M_J}$, and XO-2S c with a period $P_c = 120.80 \pm 0.34$ d and minimum mass $m_c \sin i_b = 1.370 \pm 0.053$ $\mathrm{M_J}$. This system was of great interest because the binary companion, XO-2N, was already known to host a transiting hot-Jupiter with mass $m = 0.57 \pm 0.06$ $\mathrm{M_J}$ (Burke et al., 2007), which made it the first binary system with known planetary systems around each component. For this reason both stars were intensively monitored, and studied from different point of view to examine this unique architecture, because, as I will discuss in the next Chapter, binary stars are particularly informative laboratories to study planetary formation and dynamical evolution. Both stars were extensively analysed, and several differences were found in them which could be correlated with the different architectures of the two planetary systems, as for example the much higher metallicity of the hot-Jupiter hosting component XO-2N (Damasso et al., 2015; Biazzo et al., 2015).

Another interesting system was HIP11952, which was considered to be the most metal-poor planet-hosting star known, hosting two planets with masses $m_b = 0.78$ $\mathrm{M_J}$ and $m_c = 2.93$ $\mathrm{M_J}$ (Setiawan et al., 2012). This system posed a severe threat to the core-accretion model of giant planets formation, which predicts rareness of giant planets around metal-poor stars (e.g. Mordasini et al., 2012). As shown in Fig. 5.5, the combination of HARPS and HARPS-N measurements, presented in Desidera et al. (2013), clearly ruled out the presence of the claimed planets, supporting the current vision of planetary formation.

The study of Open Clusters produced the discovery of a long period eccentric ($e > 0.6$) planet in the Pr0211 system, announced by Malavolta et al. (2016). The system was known to already host an hot-Jupiter, with period $P_b = 2.14$ d and minimum mass $m_b \sin i_b = 1.88$ $\mathrm{M_J}$ (Quinn et al., 2012). This made Pr0211 the first multi-planet system in an open cluster ever discovered. This system, with both an hot-Jupiter and a distant eccentric giant planet, is an interesting laboratory to study the dynamical influence of crowded environment on the architecture of planetary systems.

One of the most important results of the last year of the GAPS project was the intensive study on giant planet migration history performed by Bonomo et al. (2017). Two are the main migration scenarios which can predict the formation of hot-Jupiters: the disc-driven migration, in which the giant planet loses angular momentum due to the friction of the protoplanetary disk itself, and the high-eccentricity migration, in which the planet is excited in a high-eccentricity orbit via various mechanism (e.g. the Lidov-Kozai oscillations, discussed in Sec. 6.5) and then has its orbit circularized by the tidal interaction with the host star. This two scenarios would produce slightly different distributions of eccentricities and semi-major axis for giant planets. For this reason Bonomo et al.

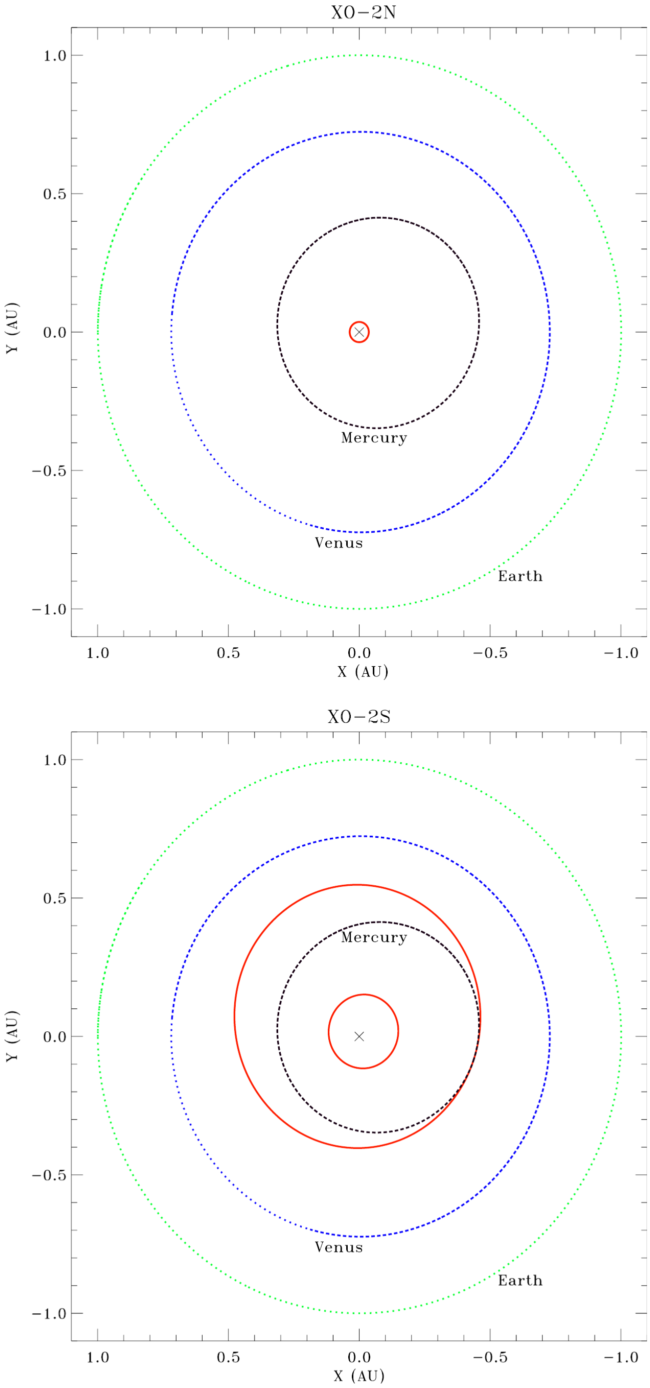

Figure 5.4: Comparison of the architectures of the XO-2 planetary systems, with the Solar System as reference: the red solid lines represent the planets of the XO-2N (upper panel) and X-2S (lower panel) systems, while the dotted lines represent the Solar System inner planets (Damasso et al., 2015).

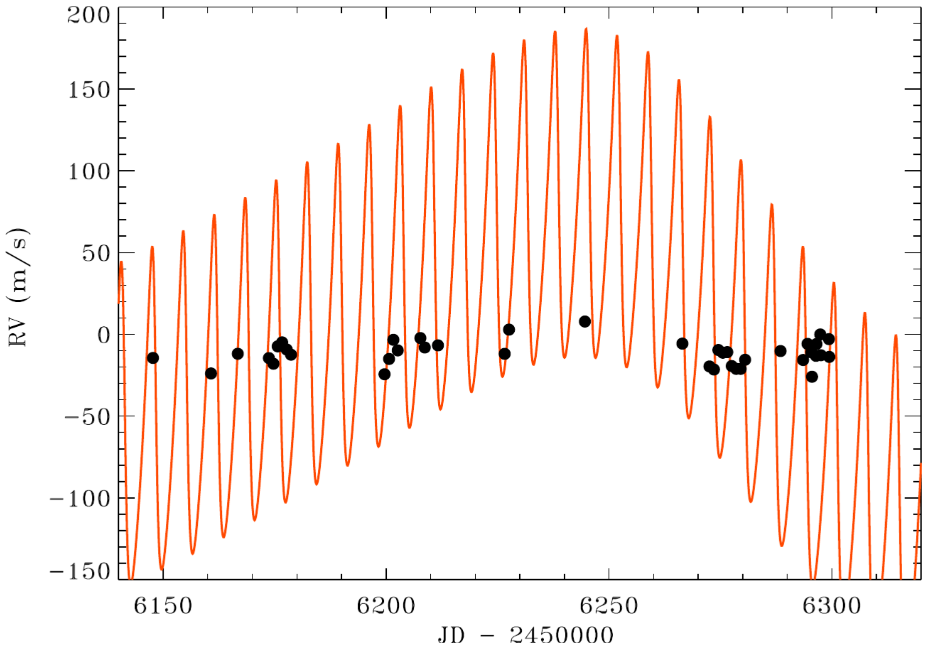

Figure 5.5: HARPS-N and HARPS measurements of HIP11952 compared with the predicted RV signal of the claimed planets (Desidera et al., 2013).

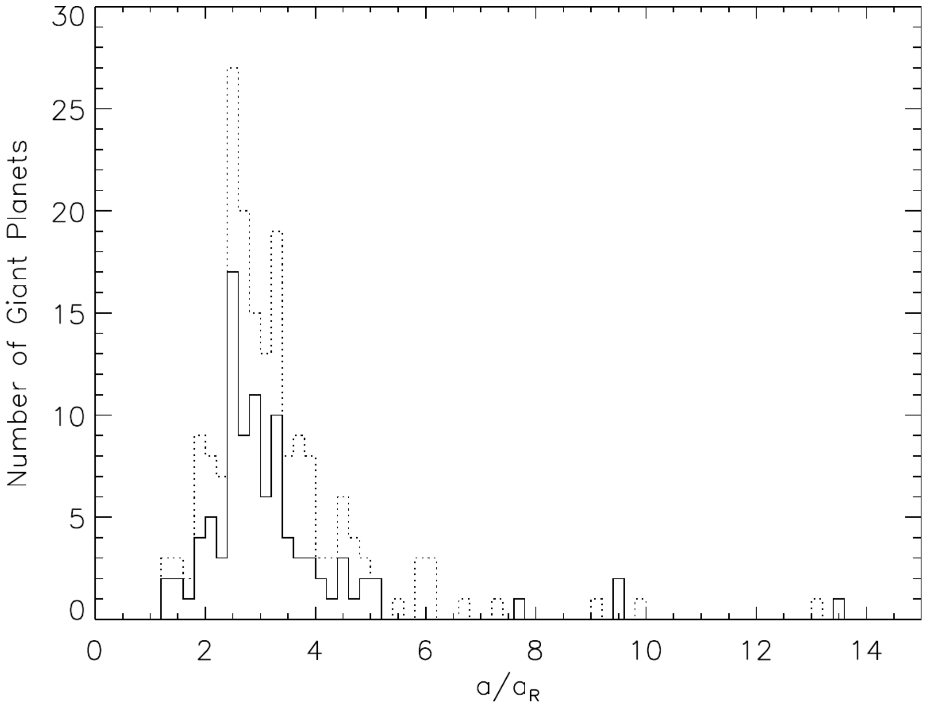

Figure 5.6: Distribution of semi-major axis in unit of the Roche limit a_R, for circular orbits (solid line) and both circular and undetermined orbits (dashed line) (Bonomo et al., 2017).

(2017) carried out a thorough Bayesian analysis of a sample of 231 transiting giant planets, using HARPS-N and archival RV data to better constraint their measured eccentricity, as well as homogeneously re-determining the stellar, orbital and planetary parameters. For example, the high-eccentricity migration predicts the final semi-major axis of the affected planet to be greater or equal to twice the Roche limit. Such feature was recovered in the semi-major axis distribution of the studied sample, shown in Figure 5.6, which peaks at $2.5\,a_{\mathrm{R}}$. Other observed features also pointed towards the high-eccentricity migration as the main architect of the observed hot- and warm-Jupiters, even if the disk driven migration could still produce some of the observed systems.

5.3 The HADES programme

The Spanish consortium EXOTEAM, is a collaboration between the Spanish Institut de Ciències de l'Espai (ICE/CSIC) in Barcelona and the Instituto de Astrofísica de Canarias (IAC) in Tenerife, and pursued similar goal to the GAPS-M subgroup in the study of exoplanetary systems around M-dwarfs hosts. For this reason in July 2014 a Memorandum of Understanding was signed between the two groups, starting the HADES (HArps-n red Dwarf Exoplanet Survey) programme.

This coordinated effort has the goal to create a strong synergy between the two groups expertise in data analysis and interpretation of detected signals, as well as to optimise the observing schedule by adding 105 observing nights from the Spanish TNG time to our observations, with a gain of 1525 additional spectra.

The complete sample was constructed by selecting 106 targets from the Lépine and Gaidos (2013) and PMSU (Palomar/michigan State University Reid et al., 1995) catalogs. As additional criteria the star were required to have spectral type between dM0 and dM3, a visual magnitude $V < 12$, and both to have a high number of Gaia mission visits and to be part of the APACHE catalog.

Several targets were successively discarded, as they were discovered to be ill-suited for planet search, due to close binary companions, fast rotation, high activity and/or incorrect spectral type.

As mentioned in Sec. 6.2, the simultaneous Th-Ar calibration was not used in the M dwarf observations of the survey, since it could contaminate the stellar spectra due to the faintness of the observed stars and the long integration times required to reach high SNR levels (900 s).

All the stellar properties of the targets were derived from the HADES HARPS-N measurements with the techniques from Maldonado et al. (2015), which allowed precise estimates of spectral types, metallicities and effective temperatures, and lead to the aforementioned rejection of part of the initial sample.

The first published result of the HADES project was the discovery of a two-planet system orbiting around the M1 star GJ3998, announced by Affer et al. (2016). The two planets have periods $P_b = 2.6498 \pm 0.0010$ d and $P_c = 12.741 \pm 0.020$ d, and minimum masses of $m_b \sin i_b = 2.46^{+0.34}_{-0.32}$ M$_\oplus$ and $m_c \sin i_c = 6.12^{+1.00}_{-0.95}$ M$_\oplus$, i.e. both of them are expected to be super-Earths. The analysis of the HARPS-N RV time series was performed with a procedure very similar to that described in Sec. 4.1.2, proving it to be effective in the discovery of small mass planets in real data, considering that the two planetary signals have low

K/N ratios, $K/N \lesssim 7.5$ (see Sec. 4.1.3 for the definition of the K/N ratio). Ancillary photometric observations were used to constrain the stellar activity signals of the star, which were correctly modelled from the GP analysis. The system time series showed periodic signals both at the stellar rotation period of 30 d and at 42.5 d, which is probably due to the differential rotation of the star. The latter signal was easily identified as non-planetary, due to its presence in both the RV and activity indicators time series. The system has also been recently target of Spitzer observations (Gillon et al., 2016), aimed to detect the inner planet transit, since its close orbit correspond to a high ($\sim 8\%$) transit probability (see Eq. 2.17). While the data acquired are still under analysis, preliminary results seem to exclude the transit of planet b.

The HADES programme recently led also to the discovery of small-mass planets in the GJ625 and GJ3942 systems, announced in Suárez Mascareño et al. (2017a) and Perger et al. (2017b). GJ625 b lies just inside the inner edge of the circumstellar habitable zone, thus could allow liquid water on its surface, even if at such close distance from the parent star the surface temperature is strongly dependent on the exact atmospheric structure and composition.

The last exoplanet detected by the HADES programme is a long-period companion around the nearby M dwarf GJ15A, but I will discuss in details this analysis, permormed by myself and several other members of the GAPS-M subgroup, in the next Chapter.

Apart from the several planets discovered, with some more yet to be announced, the HADES programme also focused on statistical studies of the sample stellar and magnetic properties. I already discussed in Sec. 2.2.4 the studies by Maldonado et al. (2017) and Scandariato et al. (2017) which analysed from a statistical point of view the activity indicators and stellar parameters of the whole sample, while Perger et al. (2017a) performed an initial study of the global exoplanet detectability and occurrence rate in the survey sample, but I will come back to this in Chapter 7.

The first studies on the HADES systems (Affer et al., 2016; Perger et al., 2017a), also analysed the performances of the DRS pipeline on the M dwarfs time series. The M2 binary mask used by the DRS could be not optimal for M dwarfs, which have heavily blended spectra, that could affect the RV precision. The studied alternative was to calculate the RV with the TERRA pipeline (Template-Enhanced Radial velocity Re-analysis Application, Anglada-Escudé and Butler, 2012). To compute the RV, TERRA generate a template by co-adding all the high S/N spectra, after a first RV correction based on a least-squares fit with the highest S/N spectra, ad uses this template for a second computation of precise RVs for each spectra. This procedure can moreover be customised by selecting which spectral orders to use in the computation.

Perger et al. (2017a) compared the two methods by studying the RV rms for each time series with the two methods: smaller rms should correspond to more reliable measurements, assuming the same underlying signals. In Fig. 5.7 we can see the distribution of the difference between the TERRA ($\mathrm{RV_T}$) and DRS ($\mathrm{RV_Y}$) rms, and it is clear how the TERRA RVs tend to show smaller dispersions, with an average difference of -0.63 m s^{-1}. For this reason the TERRA pipeline was chosen to derive all the survey RV for all the subsequent HADES studies, as it has previously been done by Affer et al. (2016).

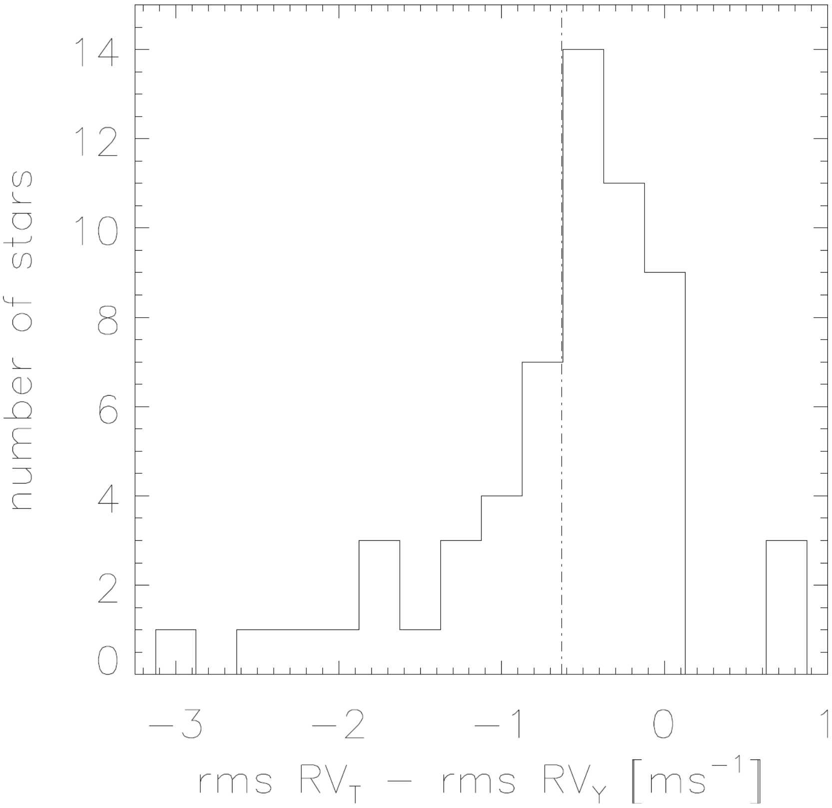

Figure 5.7: Distribution of deviation between TERRA and DRS rms for the HADES systems with more than one observation. The dash-dotted line indicate the mean value. (from Perger et al., 2017a)

Chapter 6

GJ15A: A multiple wide planetary system sculpted by binary interaction

As part of my work within the GAPS community I analysed the HADES target GJ15A, which proved to be the perfect playground to test and refine the knowledge acquired in my previous study of analysis tools for the study of RV time series. The presence of a stellar mass companion to GJ15A allowed me also to approach the complex topic of dynamical interaction and orbital sculpture of planetary systems by high-mass companions, which are widely thought to have a crucial influence in modelling the current observed population of exoplanets (e.g. Bonomo et al., 2017, and references therein).

In this chapter, I report in details my work of analysis of the GJ15A planetary and binary system. This work has recently been submitted to A&Aas Pinamonti et al.

6.1 Introduction

Extrasolar planetary systems always showed a huge variety of orbital architectures, ever since the very first exoplanet orbiting a main sequence star was discovered (Mayor and Queloz, 1995). In the following two decades the number of known exoplanets grew up to more than 3500[1], mainly discovered from transit (e.g., Kepler) and radial-velocity (e.g, HARPS, HARPS-N) observations, over a wide spread range of masses, radii and orbital separations, aiming down to the identification of small mass rocky Earth-twins (e.g. Pepe et al., 2011).

Low mass M dwarfs are the most common of main sequence stars, comprising $\sim 70\%$ of the stars in the Solar Neighbourhood (Henry et al., 2006). Furthermore, M dwarfs have become the most promising ground for the hunt for low-mass, rocky planets (e.g. Dressing and Charbonneau, 2013; Sozzetti et al., 2013; Astudillo-Defru et al., 2017), due to their more advantageous mass and radius ratios compared to solar-type stars.

---

[1] `https://exoplanetarchive.ipac.caltech.edu/` - 18/09/2017

There is a solid evidence, arising both from HARPS and Kepler observations, that Super Earths and Neptunes usually reside in multiple systems (e.g. Udry et al., 2017; Rowe et al., 2014, and references therein).

The nearby M1 dwarf GJ15A was studied by Howard et al. (2014), who found a short-period super-Earth orbiting the star: they measured a period of 11.44 d and an amplitude of 2.94 m s^{-1}. They also studied the activity signals of the host star, identifying the rotational period of the star to be 44 d, both from the $S_{\rm HK}$ index analysis and also from the precise photometric light-curve, collected with the automatic photometric telescope (APT) at Fairborn Observatory (Eaton et al., 2003). GJ15A has also a known M3.5 binary companion, GJ15B, identified astrometrically by Lippincott (1972) from a small fragment of its orbit, with a measured orbital separation of 146 AU, and an orbital period of 2600 yr.

In this framework we present the clear detection of a long-period eccentric super-Neptune planet around GJ15A, from 5 years of high-precision Doppler monitoring with the HARPS-N high-resolution (resolving power $R \sim 115000$) optical Echelle spectrograph (Cosentino et al., 2012) at the Telescopio Nazionale Galileo (TNG), combined with 15 years of archival RV data from the LCES HIRES/Keck Precision Radial Velocity survey (Butler et al., 2017). The HARPS-N data were collected as part of the HADES (Harps-n red Dwarf Exoplanet Survey) programme, a collaboration between the Italian GAPS (Global Architecture of Planetary Systems, Covino et al., 2013; Desidera et al., 2013; Poretti et al., 2016) Consortium[2], the Institut de Ciències de l'Espai de Catalunya (ICE) and the Instituto de Astrofísica de Canarias (IAC). We also confirm the presence and update the amplitude of the GJ15A b RV signal, significantly reducing its minimum mass, while confirming the orbital period measured by Howard et al. (2014). Our findings are also discussed in the light of the recent non-detection of GJ15A b in the CARMENES visual RV time series by Trifonov et al. (2017).

With tens of exoplanets orbiting binary stars observed to date (e.g. Eggenberger, 2010), including a confirmed wide binary system with planetary companions orbiting both components (Desidera et al., 2014), it is debated how the presence of stellar companions influenced the distribution of planetary orbital parameters. For this reason, we derived new orbital parameters for the stellar companion GJ15B, using HARPS-N RV measurements along with astrometric measurements from the WDS (Washington Double Star, Mason et al., 2001) catalogue, and performed several numerical simulations to test the dynamical influence of GJ15B on the planetary system.

We describe the Doppler and photometric measurements collected for the analysis in Sect. 6.2, and then, in Sect. 6.3, we describe the host star and binary companion updated properties. The complete analysis of the RVs and activity indices of the system is presented in Sect. 6.4. We then analyse the binary orbit and the perturbations produced on the two planets orbits in Sect. 6.5. We summarize and discuss our findings in Sect. 6.6.

6.2 Observations and catalog data

As part of the HADES RV programme, GJ15A has been observed from BJD = 2456166.7 (27th of August 2012) to BJD = 2457772.4 (18th of January 2017).

---

[2] `http://www.oact.inaf.it/exoit/EXO-IT/Projects/Entries/2011/12/27_GAPS.html`

The total number of data points acquired was 115, over a time span of 1605 days. The HARPS-N spectra were obtained using an exposure time of 15 minutes, and achieving an average signal-to-noise ratio (S/N) of 150 at 5500 Å. Of the 115 epochs, 49 were obtained within the GAPS time and 67 within the Spanish time. Since the simultaneous Th-Ar calibration could contaminate the Ca II H & K lines, which are crucial in the analysis of stellar activity of M dwarfs (Forveille et al., 2009; Lovis et al., 2011a), the observations were gathered without it. However, to correct for instrumental drift during the night, we used other GAPS targets spectra, gathered by the Italian team during the same nights as the GJ15A observations using the simultaneous Th-Ar calibration.

The data reduction and RV extraction were performed using the TERRA pipeline (Template-Enhanced Radial velocity Re-analysis Application, Anglada-Escudé and Butler, 2012), which is considered to be more accurate when applied to M-dwarfs, with respect to the HARPS-N Data Reduction Software (DRS, Lovis and Pepe, 2007). For a more thorough discussion of the DRS and TERRA performances on the HADES targets see Perger et al. (2017a). The rms of the TERRA RVs is 2.69 m s^{-1}, while the mean error is 0.62 m s $^{-1}$. The TERRA pipeline also corrected the RV data for the perspective acceleration of GJ15A, $dv_r/t = 0.69$ m s^{-1} yr^{-1}.

We also use in our analysis the HIRES-Keck binned data for GJ15A, downloaded from the LCES HIRES/Keck Precision Radial Velocity Exoplanet Survey. The HIRES time series spans 6541 days, from BJD = 2450461.8 (13th of January 1997) to BJD = 2457002.7 (11th of December 2014). These data were newly reduced with respect of the original RVs used by Howard et al. (2014), and also new data have been observed with the HIRES spectrograph since the paper came out. For a full description of the catalog and data reduction see Butler et al. (2017). We discard the last data point of the HIRES time series (BJD = 2457002.7, since it is almost ~ 10 m s^{-1} off with respect of the rest of the data. We thus use in our analysis 169 HIRES RVs, showing a variation of 3.26 m s^{-1} and an average error of 0.84 m s^{-1}. The RV dataset from the Keck archive was already corrected for the perspective acceleration of the host star.

We combine the HARPS-N and HIRES RV datasets, obtaining a 290 points time series, spanning 7310 days. The complete RV time series has rms = 3.08 m s^{-1}, mean error = 0.71 m s $^{-1}$. Figure 6.1 shows the combined RV time series, with the respective mean RV subtracted from each dataset to visually compensate for the offset expected between the measurements of the two instruments.

As a part of the analysis of the binary orbit performed in Section 6.5, we obtained with HARPS-N 5 RV data points of the companion star GJ15B, collected from BJD = 2457753.9 (31st of December 2016) to BJD = 2457771.9 (18th of January 2017). The rms of the time series is 1.26 m s^{-1}, while the mean error is 2.42 m s $^{-1}$.

As for every target in the HADES survey, GJ15A was also monitored photometrically by the EXORAP (EXOplanetary systems Robotic APT2 Photometry) program, to estimate the stellar rotation from the periodic modulation in the differential light curve.

The observations were performed by INAF-Catania Astrophysical Observatory at Serra la Nave on Mt. Etna (+14.973°E, +37.692°N, 1725m a.s.l.) with the APT2 telescope, which is an 80cm f/8 Ritchey-Chretien robotic telescope. The detector is a 2k×2k e2v CCD 230-42, operated with standard Johnson-Cousins $UBVRI$ filters. The IDL routine *aper.pro* was used to implement the

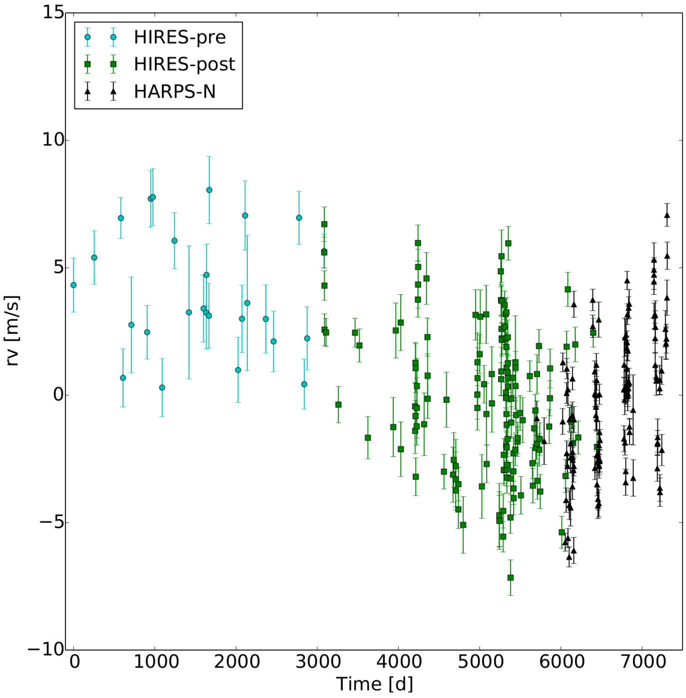

Figure 6.1: Combined HARPS-N HIRES RV time series. As described in Section 6.4.3, we considered the HIRES data as split in two separate datasets for the purpose of the RV analysis.

aperture photometry. The data were collected from the 13th of August 2013 to the 15th of June 2017, for a total 242 and 233 data points, for the B and V photometry respectively.

6.3 Stellar Properties of GJ15A and GJ15B

GJ15A is a high proper motion nearby ($\pi = 280.3 \pm 1.0$ mas) early-M dwarf, of type M1. We used the stellar parameters published by Maldonado et al. (2017), which were calculated applying the empirical relations by Maldonado et al. (2015) on the same HARPS-N spectra from which we derived the RV time series. This technique calculates stellar temperatures from ratios of pseudo-equivalent widths of spectral features, and calibrate the metallicity on combinations and ratios of different features. Although such techniques are mainly used for solar-type stars, Maldonado et al. (2015) proved them to be just as effective on low-mass stars.

Howard et al. (2014) derived a rotational period of 43.82 ± 0.56 d, both from their Keck-HIRES measurements of the S_{HK} index and their APT photometric observations at Fairborn Observatory. Recently Suárez Mascareño et al. (2017b) analysed the potential signatures of magnetic activity in the CaII H&K and Hα activity indicators of the HADES M-dwarfs sample: for GJ15A they computed a mean level of chromospheric emission $\log R'_{\mathrm{HK}} = -5.27 \pm 0.04$, and a rotation period $P_{\mathrm{rot}} = 45.0 \pm 4.4$ d, fully consistent with the value found by Howard et al. (2014).

All the stellar parameters for GJ15A used in this work are summarized in the left column of Table 6.1. We can see that most of them are fully consistent with the values used by Howard et al. (2014).

The stellar companion of GJ15A, GJ15B, is a type M3.5 dwarf whose orbit was measured astrometrically by Lippincott (1972). For the purpose of our orbital analysis in Sect. 6.5, we took 5 HARPS-N spectra of GJ15B during the last observing season at TNG (see next Section) and we applied on them the Maldonado et al. (2015)'s techniques to calculate updated stellar properties. The derived values are listed in the right column of Tab. 6.1.

6.3.1 Photometric analysis

In order to identify the potential modulation in the stellar photometry due to the presence of active regions, we analyse with the GLS periodogram (Zechmeister and Kürster, 2009) the B and V time series collected within the EXORAP survey, composed of 242 and 233 points respectively, taken over five seasons from the 13th of August 2013 to the 15th of June 2017. No evident periodicity is found in either time series, in contrast with the findings of Howard et al. (2014) who found a clear signal at 43.82 days (their Figure 4), identified as the rotation period of the star, with a corresponding signal seen in the CaII activity index. The discrepancy between the two analysis may be due to the different photometric precision of the observations: the amplitude of the signal found by Howard et al. (2014) was only of 6 mmag, which is below the sensitivity of the EXORAP survey for targets in the magnitude range of GJ15A.

Table 6.1: Stellar parameters for the two stars GJ15A and GJ15B

Parameter	GJ15A	GJ15B
Spectral Type	M1 [a]	M3.5 [g]
T_{eff} [K]	3607 ± 68 [a]	3304 ± 70 [g]
[Fe/H] [dex]	-0.34 ± 0.09 [a]	-0.37 ± 0.10 [g]
Mass [$M_\odot$]	0.38 ± 0.05 [a]	0.15 ± 0.02 [g]
Radius [$R_\odot$]	0.38 ± 0.05 [a]	0.18 ± 0.03 [g]
$\log g$ [cgs]	4.87 ± 0.04 [a]	5.08 ± 0.15 [g]
$\log L_*/L_\odot$	-1.655 ± 0.112 [a]	-3.070 ± 1.221 [g]
$v \sin i$ [km s^{-1}]	1.09 ± 0.79 [a]	
$\log R'_{\text{HK}}$	-5.27 ± 0.04 [b]	
α (J2000)	00^h:18^m:20.5^s [c]	
δ (J2000)	$+44°$:$01'$:$19''$ [c]	
$B - V$ [mag]	1.55 [d]	
V [mag]	8.13 [e]	
J [mag]	5.25 [f]	
H [mag]	4.48 [f]	
K [mag]	4.02 [f]	
π [arcsec]	0.2803 ± 0.0010 [c]	
μ_α [arcsec yr^{-1}]	2.888 [c]	
μ_δ [arcsec yr^{-1}]	0.409 [c]	

[a] Maldonado et al. (2017)
[b] Suárez Mascareño et al. (2017b)
[c] ESA (1997)
[d] Leggett (1992)
[e] Høg et al. (2000)
[f] Cutri et al. (2003)
[g] This work

6.4 Spectroscopic data analysis

In Figure 6.1 an evident long period signal can be seen. Howard et al. (2014) identified in their HIRES data a hint of a long period decreasing trend, which they included in their model as a constant negative acceleration of -0.26 ± 0.09 m s^{-1} yr^{-1}, and concluded it to be consistent with the orbit of the GJ15AB system as calculated by Lippincott (1972). But considering also the new HARPS-N data, it becomes clear how the long term RV variation cannot be modeled as a linear trend.

Even if it could no longer be treated as a constant acceleration, the long period signal could still be due to the binary reflex motion of GJ15A, so we investigate this possibility. To model the possible RV signal due to the stellar companion we follow the procedure used by Kipping et al. (2011) to study the presence of a long-period companion in the HAT-P-31 system: they modelled the long-period signal as a quadratic trend, and then derived a range of orbital parameters from the quadratic coefficients. The ratio between the semi-amplitude, K_B, and period, P_B, of the companion signal is given by the second-order term of the trend, $\ddot{\gamma}$, as (their Equation (4)):

$$\frac{K_B}{P_B^2} = \frac{\ddot{\gamma}}{4\pi^2}, \tag{6.1}$$

and, since K_B depends on the orbital period and on the mass of the two stars, the orbital period can be derived as a function of the second order term and the masses $P_B = P_B(\ddot{\gamma}, M_A, M_B)$.

From the fit of the complete RV time series we obtain: $\ddot{\gamma} = 3.95 \times 10^{-7}$ m s^{-1} day^{-2}. Using the stellar masses listed in Table 6.1, the resulting period is $P_B \simeq 680$ yr, which would correspond to a semi-major axis $a_B \simeq 63$ AU. This solution is clearly unphysical, since the presumed semi-major axis is less than half the observed orbital separation of the two objects.

Moreover, several high-contrast imaging surveys ruled out the presence of additional co-moving stellar objects close to GJ15A: van Buren et al. (1998) excluded the possibility of objects with $M_\star > 0.084$ M$_\odot$ at separations of $9-36$ AU, while Tanner et al. (2010) ruled out objects up to a magnitude contrast of $\Delta K_s \simeq 6.95$ mag within $1''$ (3.57 AU) and $\Delta K_s \simeq 10.24$ mag within $5''$ (17.8 AU).

The long-period signal observed in the RV time series is therefore very unlikely to be caused either by GJ15B or by additional stellar companions. Instead a long-period planetary-mass companion orbiting around GJ15A could be a possible explanation of the observed signal. We now investigate this hypothesis, by analysing both the potential presence of a Keplerian signal in the RVs and the stellar activity signals in the chromospheric indicators, which could also cause long-period variations due to the star magnetic cycle.

6.4.1 The MCMC model

Bearing in mind that a signal tightly linked to the stellar rotation period is clearly present in the RV data, as shown by Howard et al. (2014), we have selected the Gaussian process (GP) regression as a useful, and physically robust, tool both to investigate the presence of periodicities in the chromospheric activity indicators and to mitigate the stellar activity contribution to the RV variability. The GP regression is becoming a commonly used method to suppress the stellar activity correlated "noise" in RV time series (e.g. Dumusque et al., 2017, and references therein), especially when adopting a *quasi-periodic* covariance function. This function is described by four parameters, called *hyperparameters*, and it can model some of the physical phenomena underlying the stellar noise through a simple, but efficient, analytical representation. The quasi-periodic kernel is described by the covariance matrix

$$K(t,t') = h^2 \cdot \exp\left[-\frac{(t-t')^2}{2\lambda^2} - \frac{sin^2(\dfrac{\pi(t-t')}{\theta})}{2w^2}\right] + \\ + (\sigma^2_{\rm instr,data}(t) + \sigma^2_{\rm inst,jit}) \cdot \delta_{\rm t,t'}, \tag{6.2}$$

where t and t' indicate two different epochs.

This kernel is composed by a periodic and an exponential decay term, so that it can model a recurrent signal linked to stellar rotation, also taking into account the finite-lifetime of the active regions. Such approach is therefore particularly suitable when modelling signals of short-term timescales, as those modulated by the stellar rotation period.

About the covariance function hyperparameters, h is the amplitude of the correlations; θ represents the rotation period of the star; w is the length scale of the periodic component, linked to the size evolution of the active regions; and λ is the correlation decay timescale, that can be related to the active regions lifetime. In Eq. 6.2, $\sigma_{\rm instr,data}(t)$ is the data internal error at time t for each instrument; $\sigma_{\rm instr,jit}$ is the additional uncorrelated 'jitter' term, one for each instrument, that we add in quadrature to the internal errors in the analysis of the RV datasets to take into account additional instrumental effects and noise sources neither included in $\sigma_{\rm instr,data}(t)$ nor modelled by the quasi-periodic kernel; $\delta_{\rm t,t'}$ is the Kronecker delta function.

In the GP framework, the log-likelihood function to be maximized by the Markov chain Monte Carlo (MCMC) procedure is:

$$\ln \mathcal{L} = -\frac{n}{2}\ln(2\pi) - \frac{1}{2}\ln(det\,\mathbf{K}) - \frac{1}{2}\overline{r}^T \cdot \mathbf{K}^{-1} \cdot \overline{r}, \tag{6.3}$$

where n is the number of the data points, $\mathbf{K}$ is the covariance matrix built from the covariance function in Equation (6.2), and $\overline{r}$ is the data vector.

We use the publicly available `emcee` algorithm (Foreman-Mackey et al., 2013) to perform the MCMC analysis, and the publicly available `GEORGE` Python library to perform the GP fitting within the MCMC framework (Ambikasaran et al., 2014). We used 150 random walkers to sample the parameter space. The posterior distributions have been derived after applying a burn-in as explained in Eastman et al. (2013) (and references therein).

6.4.2 Analysis of the activity indexes

We first investigate both the HIRES and HARPS-N CaII H&K and Hα index time series, in order to test the potential stellar origin of the long period variation seen in the combined RV times series shown in Figure 6.1. No long period trend is found in either the HIRES or HARPS-N datasets. Suárez Mascareño et al.

(2017b) found a magnetic-cycle type periodicity at $P_{\rm cycle} = 2.8 \pm 0.5$ yr in the HARPS-N CaII H&K and Hα indexes, even if we don't find any similar signal in the respective HIRES time series. Nevertheless the period of this cycle is far from the time span of the long-period signal we care to investigate, so it could not be the origin of it. Another clue of the stellar origin of the long-period modulation of the RVs could be the correlation between the activity indexes and RV time series, which we computed via the Spearman's rank correlation coefficients. No significant correlation was identified ($|\rho| < 0.5$ for all the indexes).

These suggest that the long-period signal is not due to the star magnetic cycle or chromospheric activity, and reinforces the hypothesis of it be due to a wide-orbit planetary companion.

To further test the effect of the activity of GJ15A, we then investigate the stellar activity behaviour over the four seasons covered by HARPS-N observations by analysing chromospheric activity indicators based on the Ca II H and K, and Hα spectroscopic lines. They were extracted using the definition of the line cores and of the reference intervals given in Gomes da Silva et al. (2011). We analyse here only measurements obtained from HARPS-N spectra because they represent an homogeneous dataset. By spanning more than 1600 days, the HARPS-N data alone can provide robust insights into the long- and short-term stellar activity variability. The average S/N was 18 for the CaII H&K index and 213 for the Hα.

We performed an analysis of the activity indicators based on a Gaussian process (GP) regression, as detailed in the previous Section. By adopting the same covariance function (Eq. 6.2) we use to model the stellar contribution present in the RV variations in the following section, our primary goal is to investigate some properties of the stellar activity and use them to constrain some parameter priors in the analysis of the radial velocities. This represents a reasonable expectation, because neither the activity indicators nor the RVs have been pre-whitened, and the variability patterns in the former could be present with similar properties in the latter, as was noticed by Affer et al. (2016) during the analysis of another HADES target. In this sense, results from the analysis of the activity indicators can be used to train the GP regression of the RVs, by keeping unchanged the way the stellar activity contribution is modelled. Here we use Eq. 6.2 to describe the variability correlated with the stellar rotation period $P_{\rm rot}$, by adopting a uniform prior for the corresponding hyperparameter θ which is constrained between 40 and 60 days (the list of priors is shown in Table 6.2). The posterior distributions of the model parameters are shown in Fig. 6.2, and the best-fit estimates are listed in Table 6.2. We note that the estimates of the stellar rotation periods are well constrained but slightly different for the two activity indicators. The value found from the CaII H&K index is very similar to that found by Howard et al. (2014) for the CaII H&K S-index derived from HIRES spectra. The hyper-parameter θ found in the analyses of the two time series is in very good agreement with the rotation period found by Suárez Mascareño et al. (2017b) with a GLS analysis of the activity indexes time series of GJ15A.

6.4.3 Analysis of the combined RV time series

First we study the HARPS-N RV time series for confirmation of the presence of the GJ15A b signal found by Howard et al. (2014). We perform a GLS analysis

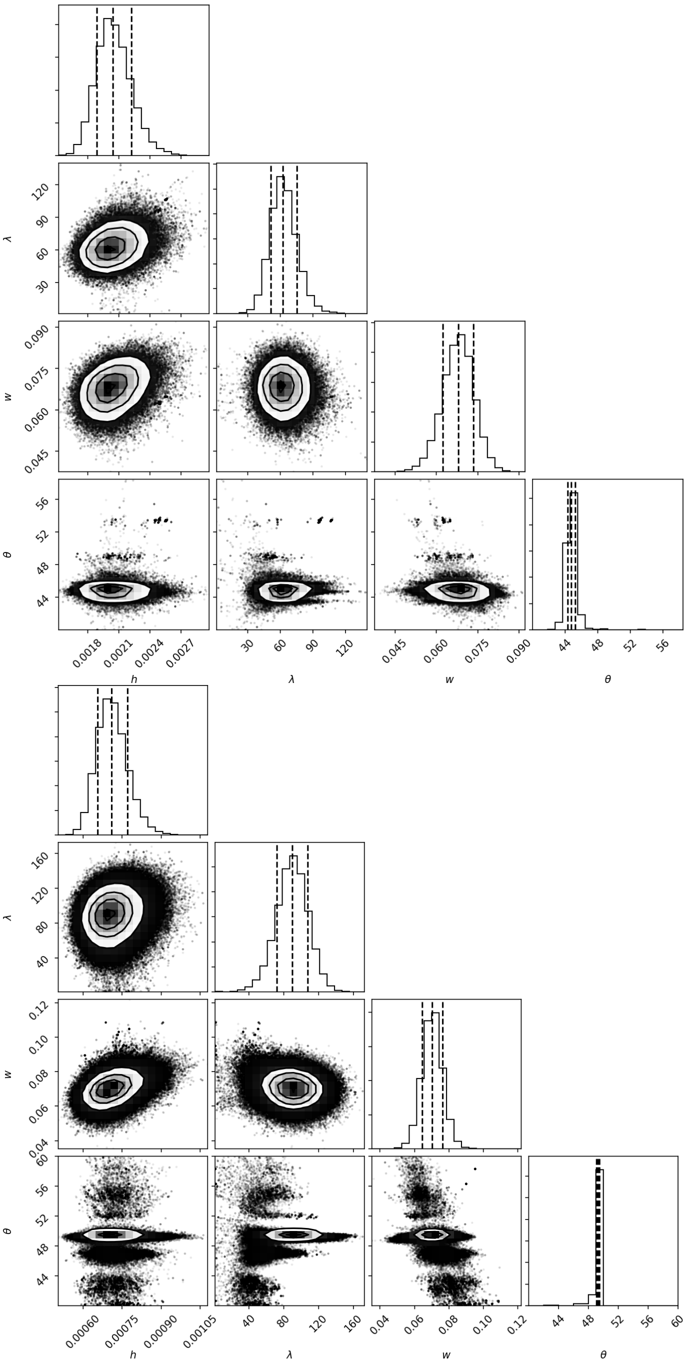

Figure 6.2: Posterior distributions of the fitted (hyper-)parameters of the GP quasi-periodic model applied to the time series of CaII H&K (upper panel) and Hα (lower panel) activity indexes. The vertical lines denote the median (solid) and the $16^{th} - 84^{th}$ percentiles (dashed).

Table 6.2: Priors and best-fit results for the Gaussian process regression analysis of the chromospheric activity indicators extracted from the HARPS-N spectra of GJ15A.

Jump parameter	prior	Best-fit value	
		CaII H&K	Hα
h	$\mathcal{U}(0,0.5)$	0.0020±0.0002	$(7.1 \pm 0.6) \times 10^{-4}$
λ [days]	$\mathcal{U}(0,10\,000)$	62^{+13}_{-11}	90±18
w	$\mathcal{U}(0,1)$	$0.068^{+0.005}_{-0.006}$	0.070±0.006
θ [days]	$\mathcal{U}(40,60)$	$44.7^{+0.5}_{-0.4}$	49.3±0.2

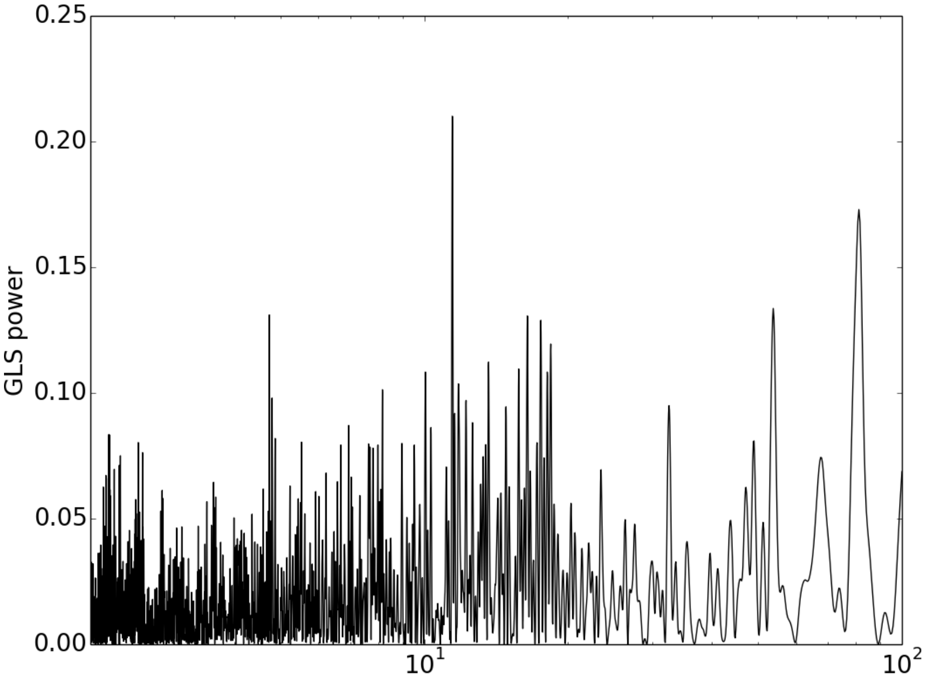

Figure 6.3: GLS periodogram of the complete HARPS-N RV dataset

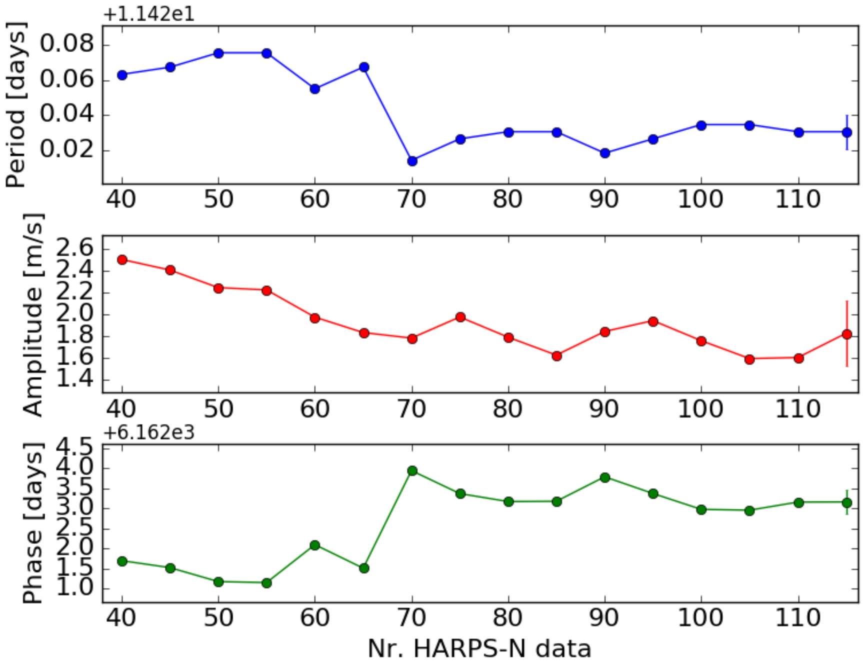

(a)

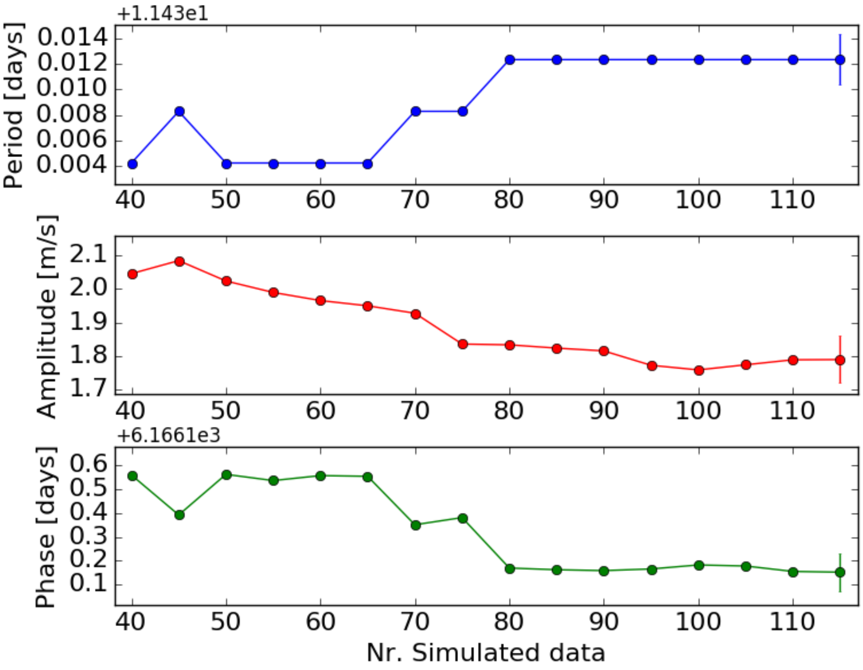

(b)

Figure 6.4: a) Evolution of the GLS orbital parameters as a function of the number of HARPS-N RV measurements; b) evolution of the GLS orbital parameters as a function of the number of simulated data. The error bars on the final points are shown as references.

to identify any periodicity in our data in $P \in [2, 100]$ d. In the periodogram, shown in Fig. 6.3, we can see that the $P = 11.44$ d period of planet GJ15A b is clearly recovered. As a confirmation of the coherence of the signal throughout the entire HARPS-N time series, Fig. 6.4a shows the evolution of the period, amplitude and phase recovered by the GLS periodogram as a function of the number of observations: we can clearly see how from ~ 70 forward the period and phase of the signal remain stable, with small oscillations of the order of the final error on the parameters, even if the remainder of the observations covers almost one and a half years. We also studied the periodogram of the CaII H&K and Hα HARPS-N time series, and found no significant signal at periods close to the inner planet period P_b, thus confirming its planetary nature as announced by Howard et al. (2014).

It's worth noticing that, as can be seen in Fig. 6.3, the final amplitude recovered by the GLS periodogram on the HARPS-N dataset, $K_{\rm b} = 1.82 \pm 0.31$ m s^{-1}, is smaller than the one published by Howard et al. (2014), $K_{\rm b,How} = 2.94 \pm 0.28$ m s^{-1}. The decreasing behaviour of the amplitude recovered by GLS with increasing number of observation is not unexpected, as the sampling of the signal strongly influence the periodogram structure and fit, and we tested that a similar behaviour can be observed also in simulated datasets with the same epochs as our HARPS-N time series but containing only the planetary signal and white noise, as shown in 6.4b. The lower amplitude value than that found by Howard et al. (2014) can also be explained similarly, since the HARPS-N time series is composed of five years of continuous high-cadence observations of the target, while the dataset used by Howard et al. (2014) consisted in mostly sparse measurements with an intensive high-cadence monitoring only in the last seasons, which could affect the signal recovery. Moreover it's worth noticing that the HIRES data from the now public LCES HIRES/Keck archive have been reduced with a different and more effective technique (Butler et al., 2017) than the data used by Howard et al. (2014), and performing a GLS analysis of the two time series we obtain the same peak periodicity but an amplitude K_b $\sim 23\%$ smaller in the new archive data.

Since no other short period signal emerges from the GLS analysis of the RVs, we focus our attention on the study of the long-period signal, which we assume to be due to a planetary-mass wide-orbit companion.

To estimate the orbital and physical parameters of the known planet GJ15A b and the candidate companion, hereafter GJ15A c, we have performed a Markov chain Monte Carlo analysis of the RVs.

Following the prescription of Howard et al. (2014), we model the RVs dividing the HIRES dataset in a pre-upgrade and a post-upgrade sublist, due to the HIRES CCD upgrade occurred on August 2004. Each subsample is then treated as an independent dataset, with its own zero-point offset and additional jitter term.

In this case, the $\overline{r}$ in Eq. 6.3 represents the RV residuals, obtained by subtracting the Keplerian signal(s) from the original RV dataset.

The general form for the models that we tested in this work is given by the equation

$$\begin{aligned}\Delta RV(t) = \gamma_{\mathrm{instr}} + \sum_{\mathrm{j=1}}^{n_{\mathrm{planet}}} \Delta RV_{\mathrm{Kep,j}}(t) + \Delta R\dot{V}(t) + \\ + \Delta RV(t)_{(\mathrm{activity,\,short-term})} = \\ = \gamma_{\mathrm{instr.}} + \sum_{\mathrm{j=1}}^{n_{\mathrm{planet}}} K_{\mathrm{j}}[\cos(\nu_j(t, e_{\mathrm{j}}, T_{0,\mathrm{j}}, P_{\mathrm{j}}) + \omega_{\mathrm{j}}) + e_{\mathrm{j}}\cos(\omega_{\mathrm{j}})] + \\ + \Delta R\dot{V}(t) + GP\end{aligned} \tag{6.4}$$

where $n_{\mathrm{planet}} = 1, 2$; ν is a function of time t, time of the inferior conjunction $T_{0,\mathrm{j}}$, orbital period P_{j}, eccentricity e and argument of periastron ω_{j}; γ_{instr} is the RV offset, one for each instrument; $\Delta R\dot{V}(t)$ is the residual acceleration; GP is the stellar noise modelled with the Gaussian Process. Instead of fitting separately e_{j} and ω_{j}, we use the auxiliary parameters $C_{\mathrm{j}} = \sqrt{e_{\mathrm{j}}} \cdot \cos\omega_{\mathrm{j}}$ and $S_{\mathrm{j}} = \sqrt{e_{\mathrm{j}}} \cdot \sin\omega_{\mathrm{j}}$ to reduce the covariance between e_{j} and ω_{j}. Our analysis assumes a circular orbit for the planet GJ15A b, relying on the result of Howard et al. (2014), who concluded the eccentricity e_b to be consistent with zero.

Except for very few parameters, for our analysis we assumed uniform priors. Our choice for the range of λ is justified by the results obtained from the GP analysis of the Ca II and Hα spectroscopic activity indexes (see Table 6.2), and from a preliminary, quick MCMC test on the data, which showed that the chains were converging towards values not far from the expected stellar rotation period. For the semi-amplitudes K of the Doppler signals we used the modified invariant scale prior:

$$f(K) = \frac{1}{K - K_0} \frac{1}{\ln(1 + K_{max}/K_0)}, \tag{6.5}$$

following the prescription in Gregory (2010). For the orbital period of GJ15A b we used a normal distribution centred on the best-fit value found by Howard et al. (2014) (circular case), adopting twice the uncertainty as the standard deviation. For the orbital period of the candidate planet GJ15A c we used a logarithmic prior to assume all the orders of magnitude equally likely.

Table 6.3 summarizes the best-fit values for each of the 19 free parameters of our model, together with the details of the prior distributions used to draw the samples. The posterior distributions of the model parameters are shown in Fig. 6.5.

About the best-fit values for the free parameters, we first note that the semi-amplitude of the Doppler signal induced by GJ15A b is even lower than the estimate obtained from the GLS periodogram, differing from the estimate of Howard et al. (2014) (2.94 ± 0.28 m s^{-1}) for more than 3.5-σ, resulting in a lower minimum mass. In addition to the previously discussed effect, this is a consequence of our global model, where planetary signals are fitted jointly with a term describing the stellar correlated noise, and also explains the lower values of $\sigma_{\mathrm{HIRES,jit}}$ required by our fit.

Our dataset does not cover a complete orbit of the outer planet GJ15A c, then we cannot reliably constrain the eccentricity, which appears to be significant within less than 1.5-σ ($e < 0.33$ at a 68% level of confidence). Our estimate for the minimum mass of GJ15A c places this companion in the group of the

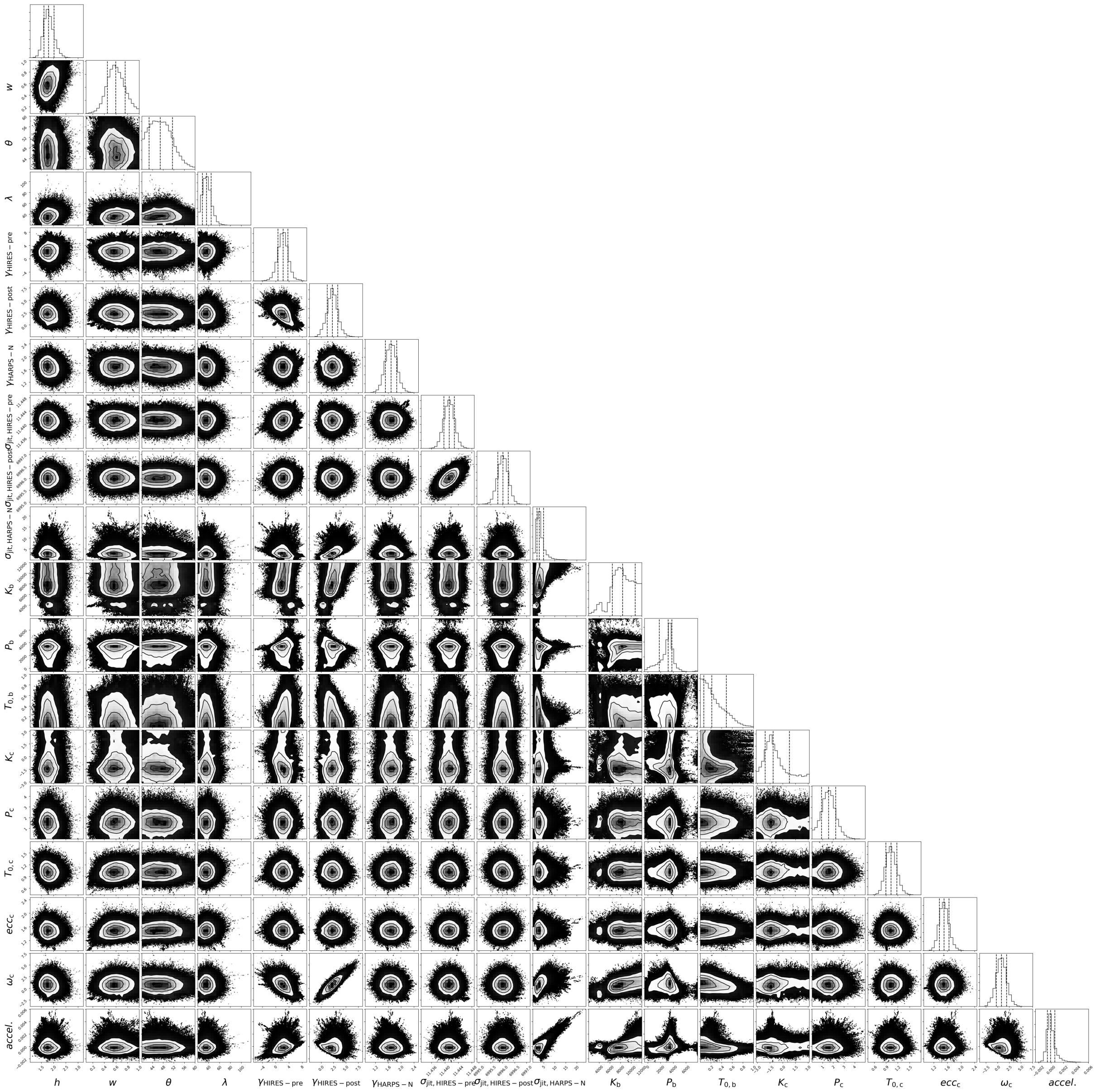

Figure 6.5: Posterior distributions of the fitted (hyper-)parameters of the two-planet model, where the stellar correlated noise has been modelled with a GP regression using a quasi-periodic kernel. On the y-axis is shown the logarithm of the product between the likelihood and the prior. The vertical red lines denote the median (solid) and the $16^{th} - 84^{th}$ percentiles (dashed).

so-called super-Neptunes, as are generally referred planets in the $[20, 80]$ $M_\oplus$ mass range.

Fig. 6.6 shows the RV curves folded at the best-fit orbital periods for the known planet GJ15A b and the detected outer companion GJ15A c. In Fig. 6.7 we show the RV residuals, after the two Keplerians have been removed, with superposed the best-fit stellar correlated, quasi-periodic signal.

It's worth noticing that Howard et al. (2014) also tested an eccentric single-planet model for the orbital solution of GJ15A b, which resulted in an eccentricity of $e_b = 0.12^{+0.08}_{-0.06}$, but was discarded for lack of statistical evidence to justify the additional parameters. For this reason, we test also a two-planet model with a prior for the eccentricity of the inner planet a normal distribution centred on the value found by Howard et al. (2014). No significant change is observed in the posterior distribution of GJ15A c's orbital parameters, nor of GJ15A b's period and semi-amplitude (not shown). We thus decide to maintain the hypothesis of circularity for the inner planet's orbit.

As for the GP hyperparameters, the stellar rotation period θ assumes a value which is in agreement with that expected, and the highest uncertainties than those for the activity indicators (Tab. 6.2) should be due to the longer timespan covered by the RVs, which include HIRES data. The longer timespan should also explain why the active-region evolutionary timescale λ sets on a value less than those found for the activity indicators. Without any ancillary data available as photometry, covering the same timespan of the RVs, we cannot conclude if the value for λ is actually physically robust, but a value not far from the rotation period seems not unreliable, as it was observed before in previous studies of different systems (e.g. Affer et al., 2016). Also, the h hyper-parameter, corresponding to the mean amplitude of the stellar signal, is fully compatible with the expected value derived by Suárez Mascareño et al. (2017b) from the mean activity level of the star, $\log R'_{\mathrm{HK}}$, that is $K_{\mathrm{exp}} = 1.9 \pm 0.4$ m s^{-1}.

6.5 Binary orbital interaction

The orbital eccentricity of the outer planet, GJ15A c, is quite uncertain: as shown in Fig. 6.5, the posterior distribution has no clear peak, only constraining the eccentricity towards small values, with a 68% probability to be < 0.33 and 99% probability to be < 0.66. This would normally point towards the adoption of a circular orbit as best fit solution for the system, lacking a significant evidence of eccentricity.

But this would be to reckon without the stellar companion.

The presence of GJ15B cannot be ignored, especially when studying a wide orbit such as that of GJ15A c.

We thus investigate how the dynamical interaction with the companion star could influence the GJ15A system. One of the main mechanisms to excite exoplanets eccentricities is the Lidov-Kozai effect, in which the presence of an external perturber causes oscillations of the eccentricity, e, and the inclination, i, with the same period but opposite phase. It was originally studied by Lidov (1962) and Kozai (1962) to compute the orbits of high inclination small Solar System bodies, like asteroids and artificial satellites, and it is strongly dependent on the eccentricities and mutual inclination of the involved objects.

Thus, in order to better estimate the strength of Lidov-Kozai oscillations in

Table 6.3: Planetary parameter best-fit values obtained through a joint modelling of Keplerian signals and correlated stellar noise, using Gaussian process regression.

Jump parameter	prior	Best-fit value
h [m s^{-1}]	$\mathcal{U}$(0,10)	$1.79^{+0.23}_{-0.18}$
λ [days]	$\mathcal{U}$(20,150)	$36.0^{+8.6}_{-7.5}$
w	$\mathcal{U}$(0,1)	$0.59^{+0.16}_{-0.14}$
θ [days]	$\mathcal{U}(40, 60)$	$46.9^{+4.6}_{-4.2}$
$\sigma_{\mathrm{jit,HIRES-pre}}$ [m s^{-1}]	$\mathcal{U}(0, 5)$	1.54±0.66
$\sigma_{\mathrm{jit,HIRES-post}}$ [m s^{-1}]	$\mathcal{U}(0, 5)$	$1.02^{+0.15}_{-0.13}$
$\sigma_{\mathrm{jit,HARPS-N}}$ [m s^{-1}]	$\mathcal{U}(0, 5)$	1.50±0.14
$\gamma_{\mathrm{HIRES-pre}}$ [m s^{-1}]	$\mathcal{U}$(-100,100)	2.16±1.49
$\gamma_{\mathrm{HIRES-post}}$ [m s^{-1}]	$\mathcal{U}$(-100,100)	2.24±1.06
$\gamma_{\mathrm{HARPS-N}}$ [m s^{-1}]	$\mathcal{U}$(-100,100)	0.78±1.11
K_{b} [m s^{-1}]	Modified scale invariant K_0=1; K_{max}=10	1.68±0.18
P_{b} [days]	$\mathcal{N}(11.4433, 0.0032^2)$	11.4412±0.0016
$T_{0,\mathrm{b}}$ [BJD-2 450 000]	$\mathcal{U}(6994, 7008)$	6996.01±0.22
e_{b}		0 (fixed)
K_{c} [m s^{-1}]	Modified scale invariant K_0=1; K_{max}=100	$2.88^{+1.93}_{-1.03}$
$\ln P_{\mathrm{c}}$ [ln days]	$\mathcal{U}(\ln 2000, \ln 12000)$	$9.03^{+0.25}_{-0.26}$
		8362^{+2371}_{-1934} [days]
$T_{0,\mathrm{c}}$ [BJD-2 450 000]	$\mathcal{U}(0, 12000)$	3185^{+579}_{-1420}
$\sqrt{e_{\mathrm{c}}} \cdot \cos \omega_{\mathrm{c}}$	$\mathcal{U}$(-1,1)	$0.05^{+0.30}_{-0.31}$
$\sqrt{e_{\mathrm{c}}} \cdot \sin \omega_{\mathrm{c}}$	$\mathcal{U}$(-1,1)	$-0.28^{+0.38}_{-0.31}$
dV_{r}/dt [m s^{-1} day^{-1}]	$\mathcal{U}$(-0.1,0.1)	$-0.00012^{+0.00069}_{-0.00050}$
Derived quantities[a]		
e_{c}		$0.21^{+0.27}_{-0.15}$
		¡0.33 (68.3th percentile)
ω_{c} [rad]		$-1.15^{+1.91}_{-0.95}$
$M_{\mathrm{p,b}} \sin i$ ($M_\oplus$)		$3.06^{+0.46}_{-0.44}$
$a_{\mathrm{p,b}}$ (AU)		$0.072^{+0.0034}_{-0.0038}$
$M_{\mathrm{p,c}} \sin i$ ($M_\oplus$)		$44.4^{+38.2}_{-19.9}$
$a_{\mathrm{p,c}}$ (AU)		$5.8^{+1.1}_{-1.0}$

[a] Derived quantities from the posterior distributions. We used the following equations (assuming $M_{\mathrm{s}} + m_{\mathrm{p}} \cong M_{\mathrm{s}}$): $M_{\mathrm{p}} \sin i \cong (K_{\mathrm{p}} \cdot M_{\mathrm{s}}^{\frac{2}{3}} \cdot \sqrt{1-e^2} \cdot P_{\mathrm{p}}^{\frac{1}{3}})/(2\pi G)^{\frac{1}{3}}$; $a \cong [(M_{\mathrm{s}} \cdot G)^{\frac{1}{3}} \cdot P_{\mathrm{p}}^{\frac{2}{3}}]/(2\pi)^{\frac{2}{3}}$, where G is the gravitational constant.

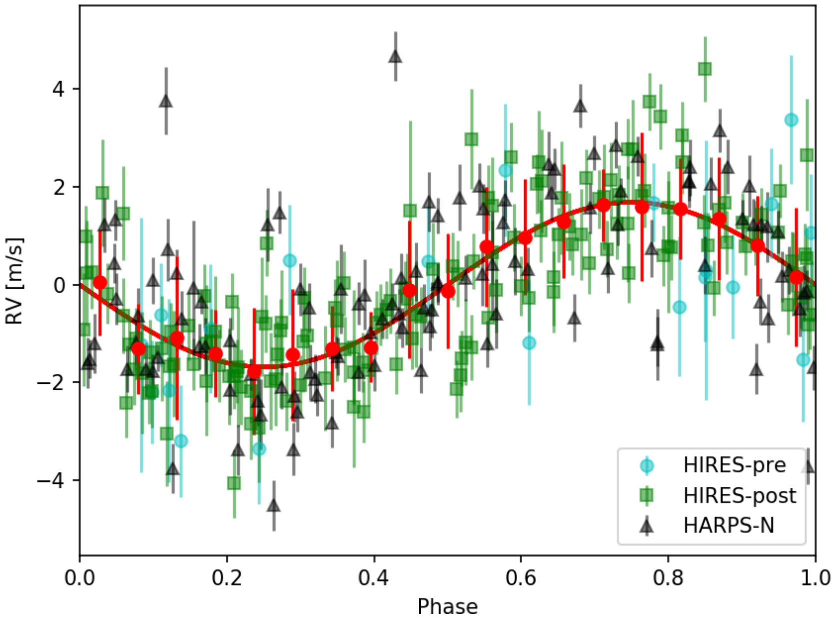

(a)

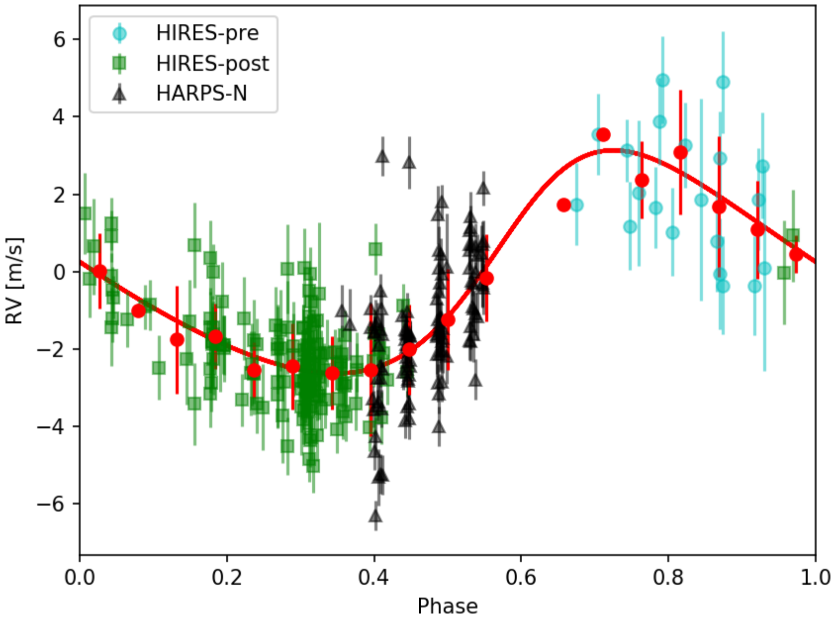

(b)

Figure 6.6: Phase folded RV curves for a) GJ15A b and b) GJ15A c. Each curve shows the residuals after the subtraction of the other planet and the stellar correlated signal. The red curve represents the best-fit Keplerian orbit, while the red dots and error bars represent the binned averages and standard deviations of the RVs.

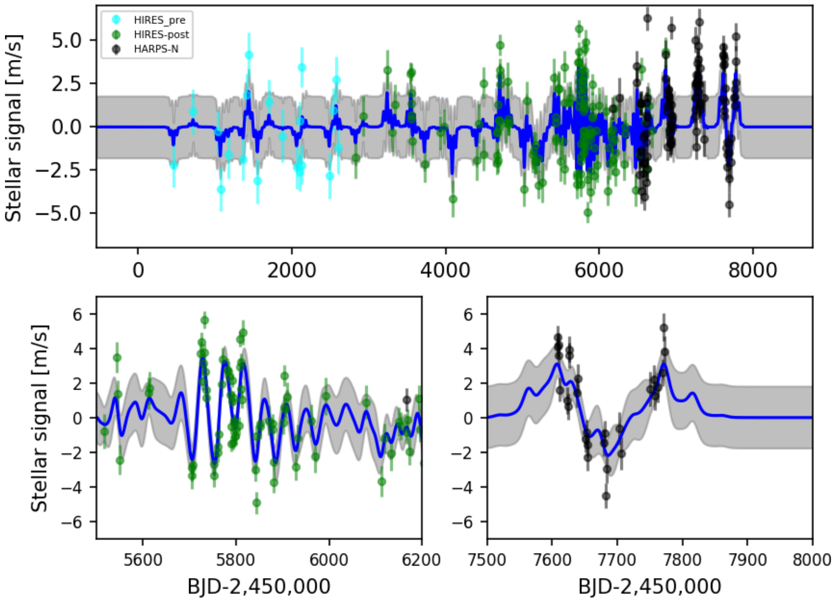

Figure 6.7: Upper panel: best fit stellar quasi-periodic signal (blue line) compared to the RV residuals. Lower panels: blow-up of the high-cadence HIRES/KECK observations (left) and of the last HARPS-N observing season (right).

the GJ15A planetary system, we need to understand as precisely as possible the orbit of the stellar companion GJ15B.

6.5.1 Orbital modeling from astrometry and RV data

The first obstacle in the dynamical analysis of the system was the poorly constrained orbital parameters of the companion. Lippincott (1972) estimated a period of 2600 yr from ∼ 100 yr of astrometric measurements, which cover less than 4% of the orbit.

Dealing with a similar case of an eccentric planet hosted by a wide binary system, Hauser and Marcy (1999) developed a technique for constraining long-period binary orbital parameters, combining astrometric and radial velocity measurements. The method is based on the fact that, being Newtonian mechanics deterministic, knowing the instantaneous full position and velocity vector, $[x, y, z, V_x, V_y, V_z]$, of one mass with respect to the other, you can compute the exact orbit of the system. Therefore, even by observing a small fragment of the orbit, we should be able to gather all the orbital parameters of the stellar companion. Of course astrometry, which is restrained in the plane of the sky, cannot provide the complete 3D information needed for this analysis, so additional data from radial velocity, to compute the third component of the velocity vector, and parallax distance, to convert astrometric positions in Cartesian coordinates, is necessary.

Following the procedure of Hauser and Marcy (1999), we downloaded 122 astrometric observations of the GJ15 system from the WDS catalogue, spanning from 1860 to 2015. The variations of the position angle θ of GJ15B relative to

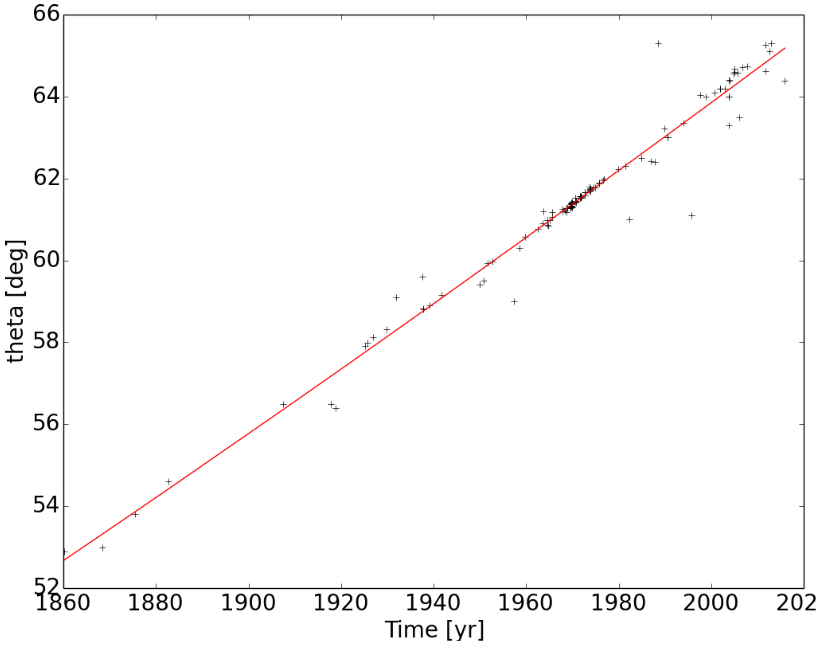

(a)

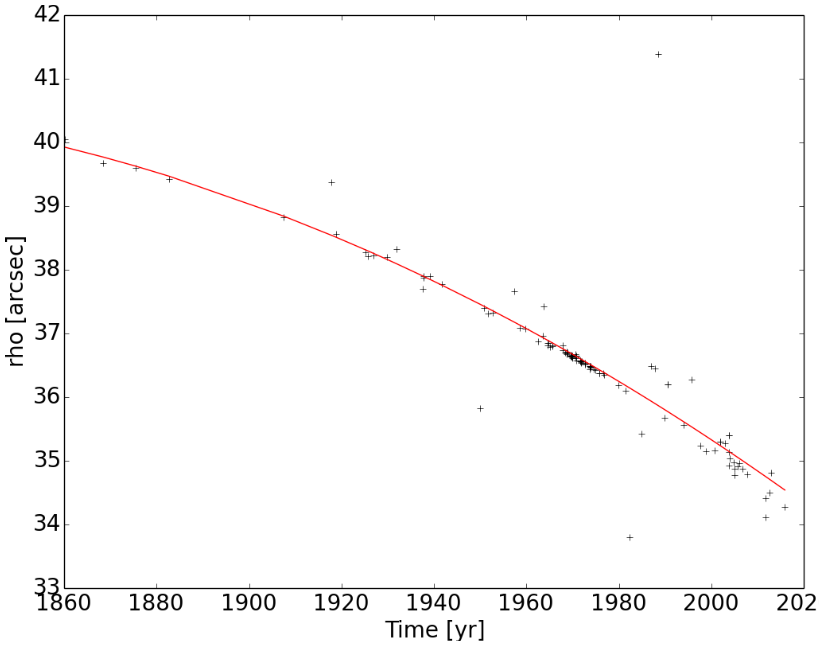

(b)

Figure 6.8: Position angle (a) and angular separation (b) of GJ15B with respect to GJ15A. Position angle is measured from north towards east. The red lines in both panels represent the second order polynomial fits.

GJ15A and the angular separation ρ are shown in Fig. 6.8. To derive θ and ρ at a specific time, along with their derivatives $d\theta/dt$ and $d\rho/dt$ which we need to calculate the velocity component in the plane of the sky, we fitted the data with a second order polynomial:

$$\theta_{\rm fit} = a_\theta + b_\theta t + c_\theta t^2, \tag{6.6}$$

$$\rho_{\rm fit} = a_\rho + b_\rho t + c_\rho t^2. \tag{6.7}$$

From these we can easily derive $d\theta_{\rm fit}/dt$ and $d\rho_{\rm fit}/dt$ as:

$$\frac{d\theta_{\rm fit}}{dt} = b_\theta + 2c_\theta t, \tag{6.8}$$

$$\frac{d\rho_{\rm fit}}{dt} = b_\rho + 2c_\rho t. \tag{6.9}$$

Adopting the parallax value from Table 6.1, $\pi_P = 280.3 \pm 1$ mas, we can derive the Cartesian position and velocity using their Equations (1)-(4):

$$x(\mathrm{AU}) = \frac{\rho_{\rm fit}}{\pi_P}\cos\theta_{\rm fit}, \tag{6.10}$$

$$y(\mathrm{AU}) = \frac{\rho_{\rm fit}}{\pi_P}\sin\theta_{\rm fit}, \tag{6.11}$$

$$V_x = \frac{1}{\pi_P}\frac{d\rho_{\rm fit}}{dt}\cos\theta_{\rm fit} - \frac{\rho_{\rm fit}}{\pi_P}\frac{d\theta_{\rm fit}}{dt}\sin\theta_{\rm fit}, \tag{6.12}$$

$$V_y = \frac{1}{\pi_P}\frac{d\rho_{\rm fit}}{dt}\sin\theta_{\rm fit} + \frac{\rho_{\rm fit}}{\pi_P}\frac{d\theta_{\rm fit}}{dt}\cos\theta_{\rm fit}, \tag{6.13}$$

thus we gained 4 of the desired physical components, $[x, y, V_x, V_y]$, as a function of time t, through $\theta_{\rm fit}$ and $\rho_{\rm fit}$ (Eq. 6.6, 6.7).

To obtain the third component of the velocity vector, V_z, we use the combined Doppler information of the two stars: from the same HARPS-N spectra we used to obtain the RV time series for the planet detection, collected as illustrated in Sect. 6.2, we extract the absolute radial velocities with the DRS pipeline. We use the DRS pipeline instead of TERRA since the latter only produce relative RV, which cannot be used in the comparison of two different objects. For GJ15A we take all the 115 HARPS-N epochs, and subtract from the absolute RV the planetary and stellar signals, as derived in Sect. 6.4.3. For GJ15B we use the 5 spectra we took on January 2017, as described in Section 6.2. The two datasets are illustrated in Fig. 6.9. To derive the binary orbit we need to know all the position and velocity components at the same instant. Therefore we fit the two RV time series with first-order polynomials. From the difference of the two linear fits we obtain the relative line-of-sight velocity V_z of GJ15B with respect to GJ15A. We can then select an epoch, and compute the values of $[x, y, V_x, V_y, V_z]$ for that time.

The selected epoch to derive the binary orbit is BJD = 2457754.5, that is January 1st 2017, which is well in between all the datasets, and close to the GJ15B RV time series, which is the shortest and most uncertain.

The last missing piece of the puzzle is, of course, the line-of-sight separation z, which cannot be measured, but can be constrained imposing the condition

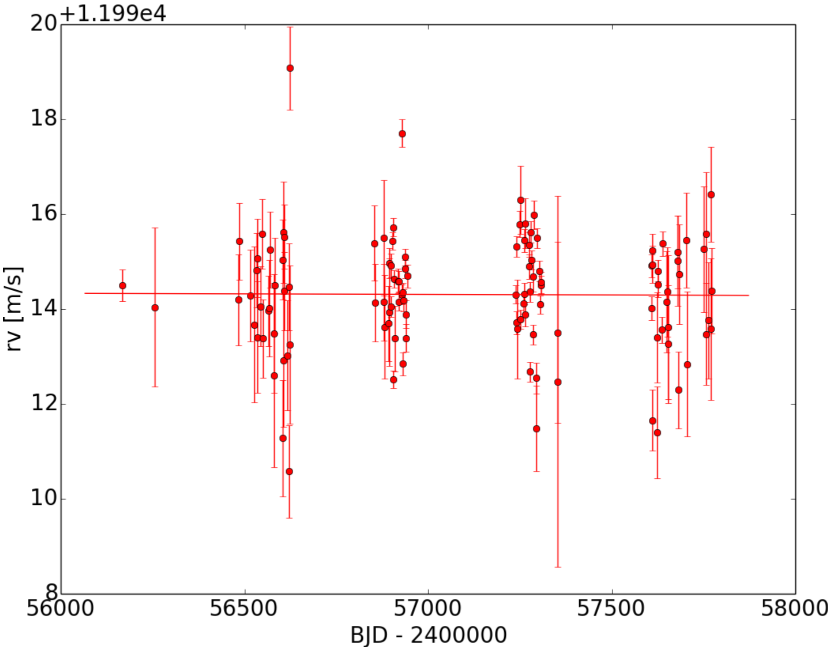

(a)

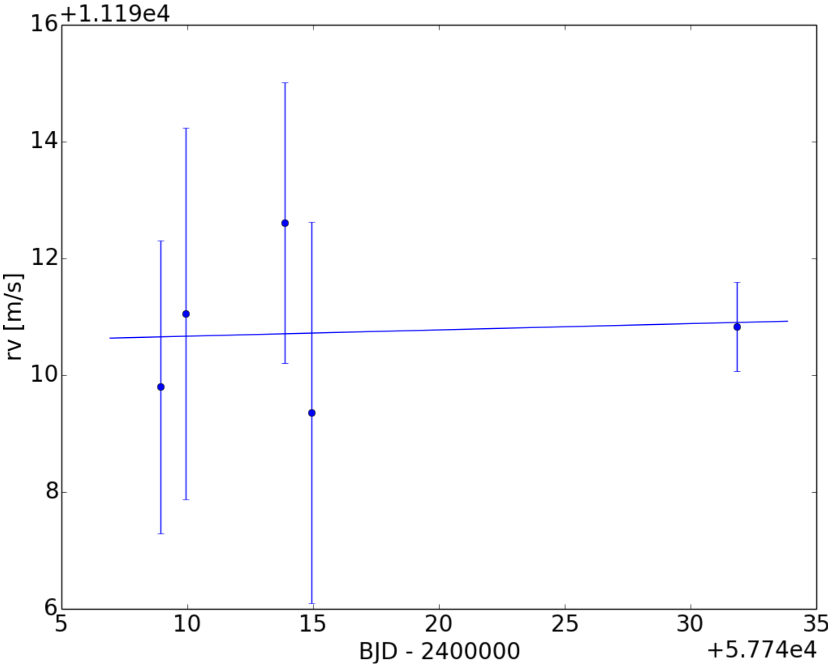

(b)

Figure 6.9: Radial velocities of (a) GJ15A (after subtracting the planetary and stellar signals) and (b) GJ15B. The solid lines show the respective first order polynomial fits.

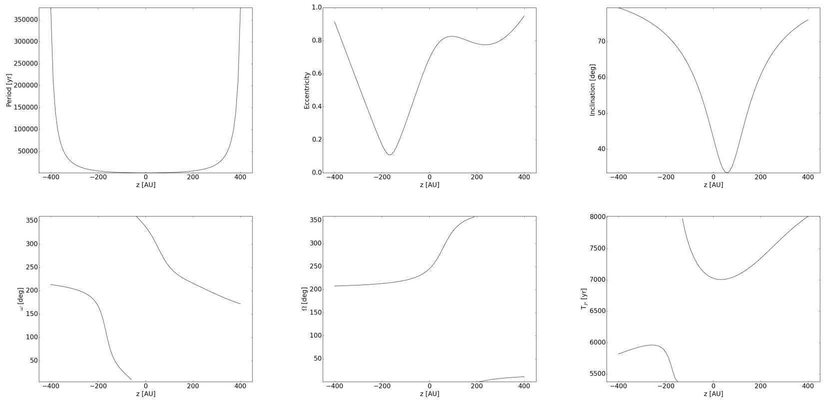

Figure 6.10: Orbital parameters of GJ15B as a function of the line-of-sight separation z with GJ15A.

of a bound orbit for the binary system, which is expected due to the similar spectral type and proximity of the two stars. The condition of bound orbit translate into a condition on the total energy of the system:

$$E = \frac{1}{2}\mu v^2 - \frac{GM_AM_B}{r} < 0, \tag{6.14}$$

where $\mu = G(M_A+M_B)$, $v = \sqrt{V_x^2 + V_y^2 + V_z^2}$ and, of course, $r = \sqrt{x^2 + y^2 + z^2}$. From this we get a range of acceptable z values $-400 \lesssim z \lesssim 400$ AU. From every value of z is possible to compute all the orbital parameters $[P, e, i, \omega, \Omega, T_P]$ for the binary system (see Hauser and Marcy, 1999, Eq. (7)-(15)). The results are shown in Fig. 6.10. As we can see, there is a wide variety of possible orbits, with completely different eccentricities and orientations, even with the bound orbit constrain, and this is still insufficient for any meaningful dynamical analysis.

The procedure by Hauser and Marcy (1999) provides the orbital solution for every single value of z, but does not in any way distinguish between the more probable configurations. But those orbital configurations are not all equally likely: from theory and observations of binary systems we know the expected distributions for different orbital parameters. From this information we can extract some priors to help us identify the most probable orbital configuration for the system, that is the best fit value of the line-of-sight separation z.

To do this we perform a Monte Carlo simulation in which the priors on the orbital parameters are injected via rejection sampling. Not all the a priori distributions of the orbital parameters are known, so we restricted the prior selection to the parameters that have a strong impact on the outcome and for which a good information is available. Due to the central role played by the eccentricity of the perturber in the Lidov-Kozai perturbation, we apply a prior on e, to have the best possible constraint on it. We select the eccentricity distribution from Tokovinin and Kiyaeva (2016), who studied a sample of 477 wide binaries within 67 pc from the Sun with median projected separation of

Table 6.4: Best orbital parameters for the GJ15 binary system from the MC simulation with priors on period and eccentricity.

P	[yr]	1230^{+930}_{-110}
a	[AU]	93^{+42}_{-6}
e		$0.53^{+0.23}_{-0.28}$
i	[deg]	54^{+11}_{-16}
ω	[deg]	2^{+35}_{-43}
Ω	[deg]	230^{+30}_{-10}
T_P	[yr]	7140^{+560}_{-140}

~ 120 AU, very close to that of the GJ15 system. The aforementioned prior is:

$$f(e) = 1.2e + 0.4. \tag{6.15}$$

The second choice is a prior on the orbital period, in order to penalize long period poorly bound orbits. The chosen prior is the one suggested by Duchêne and Kraus (2013) for low-mass binary stars, that is a log-normal distribution, with $\bar{a} \approx 5.2$ AU and $\sigma_{\log P} \approx 1.3$.

The results of the Monte Carlo simulation are illustrated in Fig. 6.11. As we can see there are three main peaks in the distribution. The third one, on the far right, represents orbits almost unbound, so it can be ignored, both because, as we said, the two stars are expected to be in a binary system, and because, even if bound, such wide orbits would have no influence whatsoever on the dynamics of the planetary system we intended to study. The latter can be said also on the peak on the left, which correspond to a period of $P = 22000^{+175000}_{-15000}$ yr, and a semi-major axis of $a = 640^{+2100}_{-350}$ AU, again too distant from the planetary system to have a significant influence.

We thus use the central peak of Fig. 6.11 to derive the orbital parameters best solutions and error bars. To do this we fit a truncated normal distribution in the range $z \in [-200, 200]$ AU, and use the mean value μ_z to calculate the corresponding best solution orbital parameters as described before. The upper and lower errors on the orbital parameters are calculated by taking $\mu_z + \sigma_z$ and $\mu_z - \sigma_z$ and deriving the corresponding values of $[P, e, i, \omega, \Omega, T_P]$. The orbital parameters solutions and errors are listed in Table 6.4.

6.5.2 Lidov-Kozai Interaction modeling

The results of the previous section show that the most likely orbit of the stellar companion GJ15B has a high eccentricity, $e = 0.53$. This is a further clue that strong orbital perturbation could affect the planetary system.

The interaction mechanism studied is the Eccentric Lidov-Kozai effect (commonly referred to with the literature-coined acronym EKL). This mechanism applies to hierarchical triple-body systems, and consists in eccentricity and inclination oscillations on timescales much larger than the orbital period of the influenced body. We can safely ignore the mutual interaction between the two planets of the GJ15A system, except in the event of close encounters, and thus

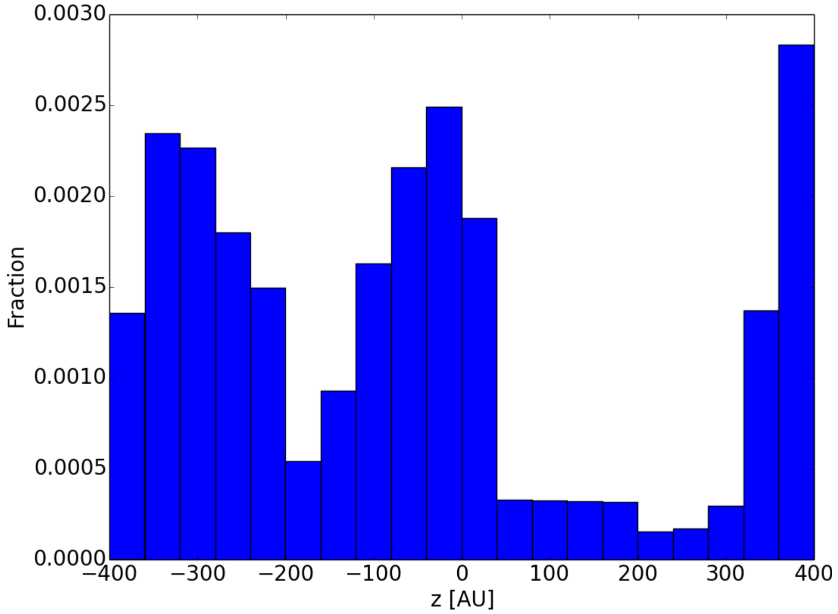

Figure 6.11: Distribution of z resulting from the Monte Carlo simulation with the e and P priors injected.

treat their interaction with the binary separately, as three body systems.

The EKL mechanism is very sensitive to the mutual orientations of the orbits of the perturber, i.e. the companion star, and of the influenced body, i.e. the planet. We have derived i, ω, Ω of GJ15B, but we do not know either i or Ω of the two planets GJ15A b and GJ15A c. Thus, some assumptions are to be made about their orbital orientation. To compare the results of the dynamical interaction model with the posterior distribution found by the MCMC analysis, we calculate the fraction of time spent by the system below $e = 0.33$ and $e = 0.66$ ($f(e < 0.33)$ e $f(e < 0.66)$), which can be considered a proxy of the probabilities to observe the system with eccentricities under those thresholds (e.g. Anderson and Lai, 2017).

We perform some preliminary tests to verify the various mechanisms which could be involved in the dynamical evolution of the system: we prove that the inner planet, GJ15A b, is too distant from GJ15B for any significant interaction, so we focus our efforts to study the orbit of the newly discovered GJ15A c; we also check for the influence of dissipative tides, which could lessen the orbital eccentricity, and find that they act on much longer timescales than the EKL mechanism, so we neglected them in our analysis.

We denote the orbital parameters of GJ15B with the subscript $_B$ and the ones of GJ15A c with $_c$. All the EKL integrations were performed with a timescale of ~ 10 Myr. Since we cannot rule out planet-planet scattering events to have occurred in the early phases of the system's evolution, we consider different values of the initial eccentricity $e_{c,0} = 0.0, 0.1, 0.2, 0.3, 0.4$. The other unknown is the longitude of the ascending node of the outer planet Ω_c. However, the longitude of the ascending node influences the EKL interaction mainly by changing the relative inclination the two orbits, θ, which derives from the parameters of the two orbits as:

$$\theta = \arccos(\sin i_c \cos \Omega_c \sin i_B \cos \Omega_B + \sin i_c \sin \Omega_c \sin i_B \sin \Omega_B + \cos i_c \cos i_B), \quad (6.16)$$

and thus can be ignored as long as θ is conveniently sampled, which can be obtained by changing i_c. For our analysis we fix $\Omega_c = 0°$ and vary the planet orbital inclination in the interval $i_c \in [-5°, 90°]$.

The results are shown in Figure 6.12. In some cases the EKL oscillations are so extreme that the numerical integration has to be stopped due to the planet passing too close to the host star; the corresponding systems are clearly unstable, and so we consider $f(e < 0.33) = f(e < 0.66) = 0$ to represent the incompatibility with the observed case. We also considered as unstable the cases in which the outer planet's orbit becomes too close to the inner planet's possibly producing planet-planet scattering events, that is when:

$$a_c(1 - e_{c,\max}) < a_b, \quad (6.17)$$

where $e_{c,\max}$ is the maximum eccentricity reached during the EKL oscillations. In these cases we also consider $f(e < 0.33) = f(e < 0.66) = 0$.

As we can see in both the panels of Fig. 6.12, there are regions in the i_c space that are unstable regardless of the initial eccentricity of the planet $e_{c,0}$: between 15° and 30° and around 0°. We can also see that the Lidov-Kozai interaction is weak for $i_c \sim 90°$ and strengthen as i_c decreases. The top panel of Fig. 6.12 shows that for $i_c \in [75°, 90°]$ the resulting eccentricity ranges are compatible with the observed values. The constraints for the $e < 0.66$ threshold are somewhat looser, but pointing in the same direction.

Since as previously said we do not know the initial eccentricity of the system, another way to consider the dynamical evolution is to consider the average of the results of the single integrations. This can be seen in Fig. 6.13, which confirms the trends just discussed.

6.6 Discussion and conclusions

We present in this paper the fifth planet detected by the HADES programme conducted with HARPS-N at TNG. This long period planet was found orbiting the planet-host M1 star GJ15A, from the analysis of high precision, high resolution RV measurements collected as part of the survey in conjunction with archive RV data from the HIRES/Keck spectrograph.

The different trends observed in the two datasets suggest the presence of a long-period companion, which is confirmed by the homogeneous Bayesian analysis of the combined RV time series. The known inner planet GJ15A b is also recovered. The minimum masses derived from our analysis are $M_{p,b} \sin i_b = 3.06^{+0.46}_{-0.44}$ $\mathrm{M}_\oplus$ and $M_{p,c} \sin i_b = 44.4^{+38.2}_{-19.9}$ $\mathrm{M}_\oplus$ for the inner and outer planet respectively. The mass we find for GJ15A b is much smaller than the value found by Howard et al. (2014), which was almost double due to the higher signals amplitude. The smaller value we find, can be easily explained by the additional information brought by the high-precision HARPS-N RVs, along with the new

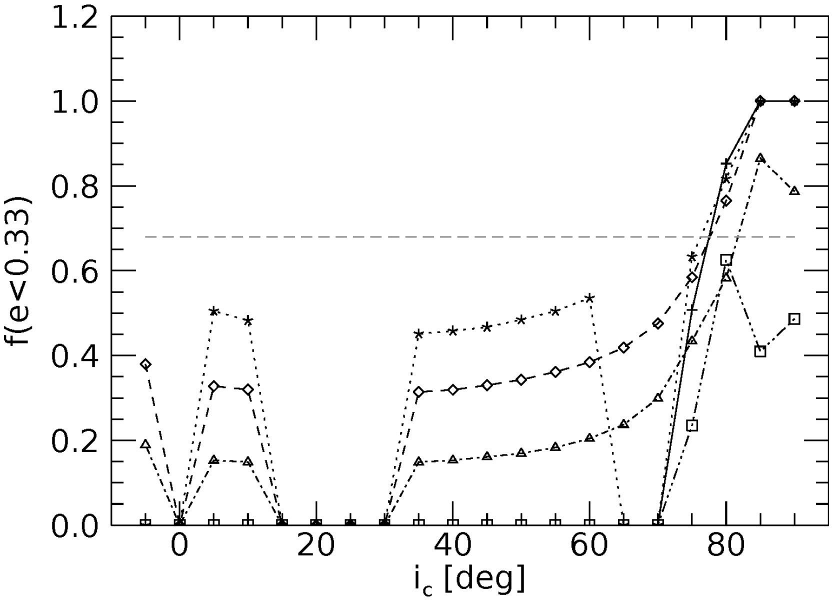

(a)

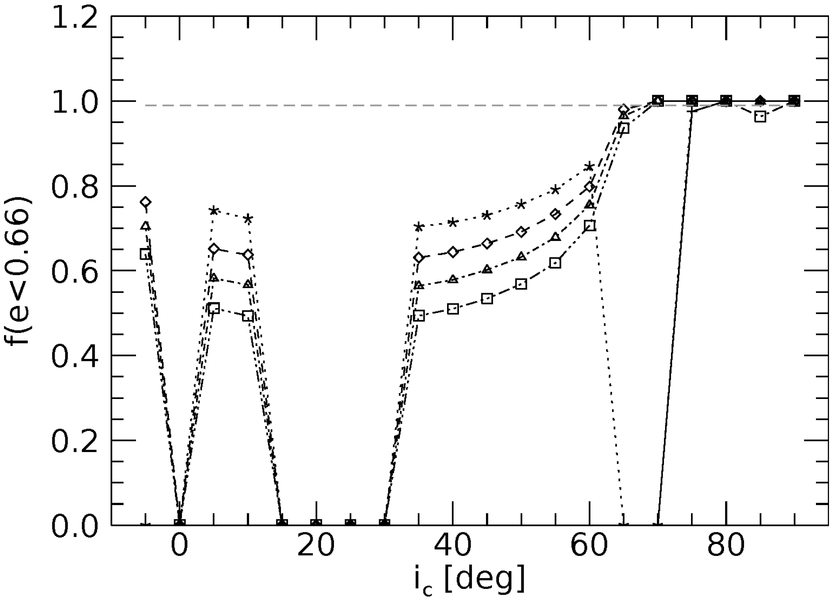

(b)

Figure 6.12: Fraction of time spent below the a) $e = 0.33$ and b) $e = 0.66$ thresholds. The different line styles and symbols correspond to different values of $e_{c,0}$: solid and plus signs - $e_{c,0} = 0$; dotted and asterisks - $e_{c,0} = 0.1$; dashed and diamonds - $e_{c,0} = 0.2$; dash dot and triangles - $e_{c,0} = 0.3$; dash dot dot and squares $e_{c,0} = 0.4$. The horizontal dashed grey lines indicate the corresponding probability from the MCMC (a) 68%, b) 99%).

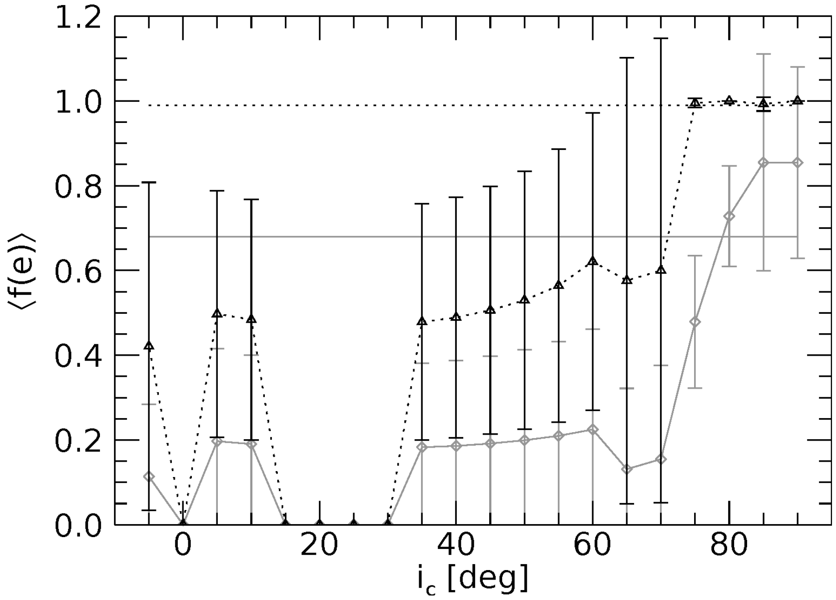

Figure 6.13: Fraction of time spent below the $e = 0.33$ (solid grey) and $e = 0.66$ (dotted black) thresholds, averaged on the initial eccentricity $e_{c,0}$. The errorbars show the standard deviation.

calibration of the archival HIRES data published by Butler et al. (2017). The combined dataset is almost twice as large that the one analysed by Howard et al. (2014), stretched on a significantly longer timespan, with better sampling and precision. This, together with the simultaneous modelling of the stellar activity signal, can explain the much smaller uncertainty on the minimum mass of GJ15A b. It also highlights the importance of taking into account the chromospheric stellar activity for the correct identification of planetary signals. It's worth noticing that instead the orbital period P_b is almost unchanged from the previous estimate.

With its period of $\simeq$ 23 yr, GJ15A c is the longest-period sub-Jovian planet detected up to date with the RV method[3], the second being HD 10180 h (Lovis et al., 2011b) with a period of $\simeq$ 6 yr and a minimum mass of 65.74 $M_\oplus$ (Kane and Gelino, 2014). With the confirmed presence of two widely spaced planetary mass companions, GJ15A is now the multi-planet system closest to our Sun, at a distance of only 3.57 pc.

In a very recent work, Trifonov et al. (2017) have published an RV analysis at optical wavelengths of the GJ15A system as part of the CARMENES survey. The RVs derived from the visible arm of CARMENES showed no evidence of the presence of GJ15A b, thus the authors concluded it to be an artifact due to the stellar noise. The authors also identified a long-term trend in the combined Keck+CARMENES dataset which they proposed as due to a distant low-mass companion. As discussed in Sec. 6.4.3, our HARPS-N data alone clearly confirm the presence of the 11.44 d period due to GJ15A b, albeit with a reduced amplitude and mass, and the analysis of the combined HARPS-N+Keck

---

[3] `https://exoplanetarchive.ipac.caltech.edu/` - 28/09/2017

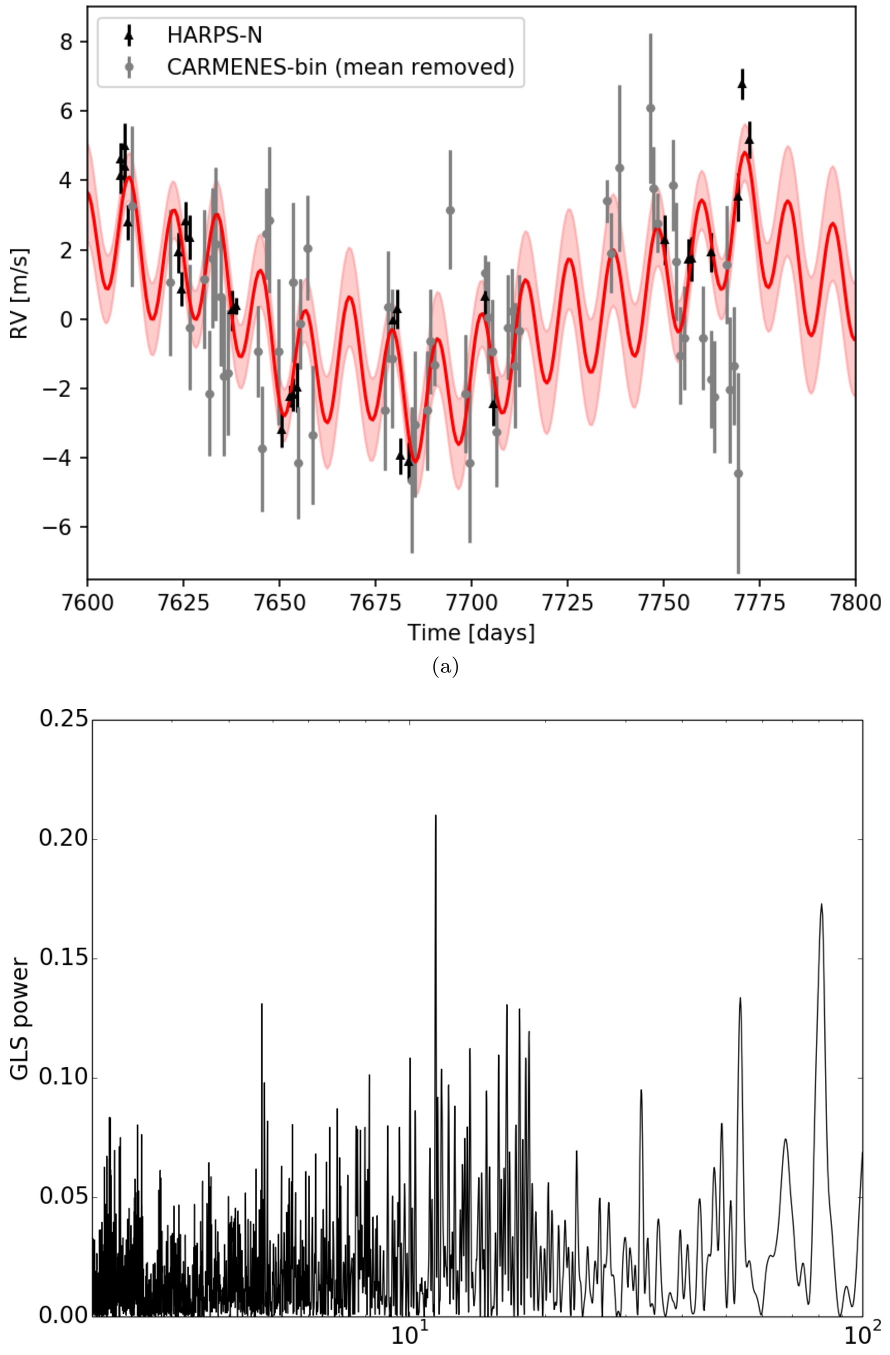

(a)

(b)

Figure 6.14: a) Comparison between the last season HARPS-N data (black triangles) and the overlapping CARMENES data (grey dots). The red solid line represents our two-planet plus stellar noise model, with the pink shaded area representing the 1-σ uncertainties on the GP hyper-parameters ; b) GLS periodogram of the combined HARPS-N and CARMENES RV datasets.

datasets makes a decisive case for the existence of the long-period low-mass giant GJ15A c based on a 5-yr time-span of HARPS-N observations, partly overlapping with the Keck time-series. The orbital elements for GJ15A c derived in this work have larger formal uncertainties than those reported in Trifonov et al. (2017) due to the likely much longer orbital period inferred for the planet, but the inferred companion mass is fully in agreement with the preliminary CARMENES estimate.

Things notwithstanding, however, the reason why CARMENES does not see the signal of GJ15A b is not fully clear, but the higher quality, and much longer timespan, of the HARPS-N data, combined with our modelling of the stellar activity quasi-periodic signal could be a possible explanations for the non-detection based on the CARMENES data alone: in Fig. 6.14a we can see the last season of HARPS-N observations, that overlaps with most of the CARMENES data, compared to our two-Keplerian plus correlated stellar noise model. This season is clearly dominated by activity-related variations in the optical HARPS-N spectra, while the internal errors for HARPS-N are typically 3 times smaller than those of CARMENES (0.6 m s^{-1} vs. 1.8 m s^{-1}). We nonetheless tested the effect of combining the HARPS-N and CARMENES datasets: the GLS periodogram, shown in Fig. 6.14b, clearly peaks on the 11.44 d period of GJ15A b, and remarkably resembles Fig. 6.3, recovering the same amplitude as that recovered on the HARPS-N dataset alone. We also tested our two planet + stellar noise model described in Sec. 6.4.3 on the complete dataset obtained combining the HIRES, HARPS-N and CARMENES time series, and we obtained values of the system parameters entirely in line with those presented in Table 6.3. Given the intrinsically higher quality of the HARPS-N data, that drive the GP regression modelling and in which the coherence of the signal from the inner planet GJ15A b is clearly present, we decide to stick to the results in Table 6.3 for the purpose of our analysis.

Trifonov et al. (2017) also stated, as an argument in favour of the non-Keplerian interpretation of GJ15A b, that the 11.44 d signal disappeared when analysing the last two years of HIRES observations, subsequent to the time series used by Howard et al. (2014). Studying the same time span of data, we observed that, when ignoring the outlier described in Sec. 6.2, the 11.44 days signal is still clearly visible in the GLS periodogram.

The CARMENES visual arm contains a spectral region extending all the way to 0.95 μm, i.e. a significantly redder spectral range than that covered by HIRES and HARPS-N. As the amplitude of activity induced RV variations is known to be chromatic (Reiners et al., 2010), the non-detection of the 11.44 d signal in the CARMENES time series could be an indication of a wavelength dependent-amplitude of the signal, that would clearly indicate its stellar origin. However, the CARMENES visual arm spectral range still importantly overlaps with that of HIRES and HARPS-N and thus it must be affected by stellar activity in a similar way. Based on the higher RV precision of HARPS-N, allowing a detailed modelling of quasi-periodic stellar signal (as shown in Fig. 6.7), and on the coherence of the period and phase of the signal over the 20 yr time span covered by the combined HIRES and HARPS-N time series, the Keplerian origin of the signal still seems the most straightforward explanation for the observed data. It would be however interesting to carry out a systematic study on both CARMENES and HARPS-N time series of this target, adopting the same strategy outlined by Feng et al. (2017) for Tau Ceti, that is to study separately the RVs derived from different regions of the spectra, for a systematic investigation of potential differences in the amplitude of the 11.44 d signal, as a function of the wavelength, but this lies well beyond the scope of this paper.

Dwarf stars are known to turn up much more frequently in multiple systems than they do in isolation, with a binary fraction as high as $\simeq 57\%$ for Sun-like stars (Duquennoy and Mayor, 1991) and somewhat lower for M dwarfs (Bergfors et al., 2012). Many young binaries possess either circumstellar or circumbinary disks (e.g. Monin et al., 2007), and the existence of stable planetary orbits in binary systems was postulated well in advance of the first exoplanets discoveries (Dvorak, 1982).

Early studies proposed different mass-period relations for planets around binaries and single stars (Zucker and Mazeh, 2002) but in the following years the evidence of such diversity decreased (e.g. Desidera and Barbieri, 2007; Eggenberger, 2010), until most recently Ngo et al. (2017) claimed not to be any difference of planetary properties between the two kind of systems. On the other hand, recent works like Moutou et al. (2017) find statistical evidence for a much higher binary fraction in extrasolar systems hosting eccentric exoplanets than in the ones hosting only circular planets: this points towards the confirmation of the role of stellar multiplicity in orbital excitation of planetary systems, as predicted by theoretical studies which suggested a strong orbital influence of stellar companions on planetary systems, via mechanisms such as the eccentric Lidov-Kozai (EKL) oscillations.

Our numerical analysis of the EKL effect proved the strong influence of the GJ15B on the planetary system. We show that for a narrow range of initial inclination, $75^\circ - 90^\circ$, the outer planet maintains a low eccentricity orbit, regardless of the initial status of the system was due to possible planet-planet-scattering events. We also pointed out the presence of a forbidden ranges of inclination, $15^\circ - 30^\circ$ and $\sim 0^\circ$, in which the Lidov-Kozai interaction become so strong that no stable orbit can be achieved, regardless of the initial eccentricity of GJ15A c.

The orbital parameters of GJ15A c have still large uncertainties due to the observation time-span shorter than the orbital periods, and the semi-amplitude K_c is significant only at a 3-σ level, although the strong combined observational evidence from RV and imaging leaves no doubt as to the presence of a long-period planetary-mass companion. Additional RV observations in the years to come will, however, be very helpful to better constrain the orbit, and thus the mass of GJ15A c.

Our knowledge of this system will be also greatly improved by the results published in future Gaia data releases. For a circular orbit and assuming the minimum mass value for GJ15A c, the expected astrometric signature on the primary is 570 μas. Gaia astrometry will only cover $\sim 20\% - 25\%$ of the full orbit. However, based on the Torres (1999) formalism curvature effects in the stellar motion should typically amount to $20 - 30$ μas yr^{-2}, thus they should be easily revealed by Gaia, that for such a bright star as GJ15A will be able to deliver end-of-mission proper motion accuracies $\lesssim 10$ μas yr^{-1} (e.g. Gaia Collaboration et al., 2016).

Yet even with the orbital solution now available, our analysis shows how interesting dynamical studies can be performed on the system, which, due to the presence of the eccentric binary companion, is an excellent playground to test orbital interaction mechanisms and their influence on the evolution of planetary systems.

Chapter 7

HADES statistical analysis - occurrence rate and global detectability

The statistical knowledge of vast samples of systems can shed light on the complexity of the formation processes and evolutionary histories of stars and planetary systems. As I discussed in Sec. 2.3.1, several studies were performed aiming to compute the occurrence rate of extrasolar planets of different kinds around low-mass stars, with the general results pointing towards a high number of low-mass planets orbiting at different distances from their hosts, and a scarcity of high-mass giant planets. The HADES programme M dwarfs catalog was selected aiming to fully characterize the population of exoplanetary systems on a consistent sample of stars with well known properties. In Sec. 5.3 I described the structure of the survey and outlined its first results.

In this Chapter, I illustrate the statistical properties of the studied M dwarf sample, as well as describe the preliminary statistical analysis performed to study the detection efficiency of the survey. I then outline the robust Bayesian approach which has been selected to thoroughly characterize the planetary population statistics and global detectability of the survey, and discuss the reference case of similar analysis to which our results will be compared to. The final results of this ongoing analysis will be the content of Pinamonti et al. (in prep.).

7.1 Stellar sample statistics

In Fig. 7.1 is shown the distribution of visual magnitudes V for the stars of the sample, in the range [8.1,12.0] mag, with a mean magnitude of $\langle V \rangle \sim 10.7$ mag.

From the start of the HADES programme in August 2012 to October 2017, 4214 spectra were collected, with an mean number of observations per star of 53.3 and a median of 35.0. The distribution of observation per target is shown in Figure 7.2. All spectra were taken with a minimum integration time of 900 s, which could be extended in case of bad seeing up to 1200 s for faint target. These resulted on SNR in the range $[23, 163]$ at spectral order 46, due to the magnitudes of the sample objects (Perger et al., 2017a).

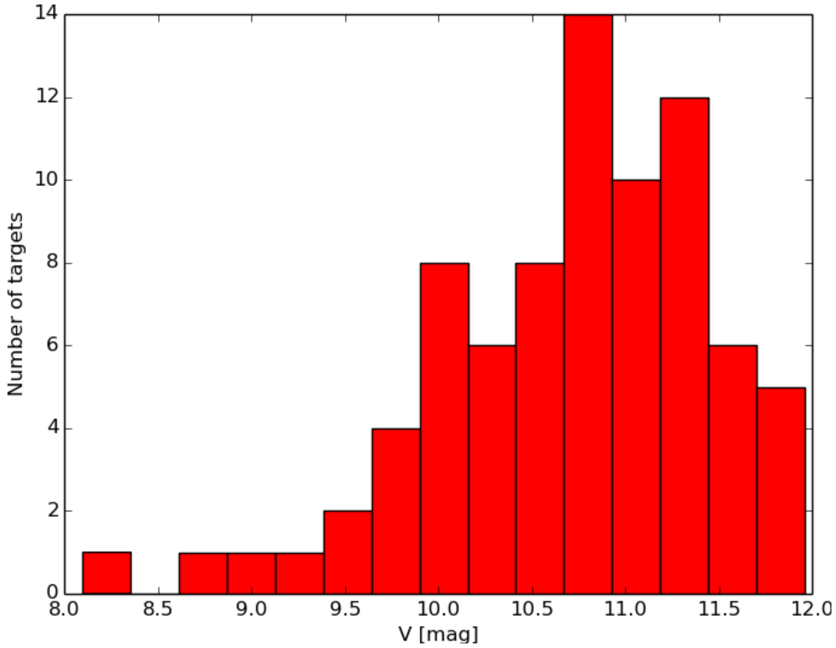

Figure 7.1: Distribution of visual magnitudes for HADES targets.

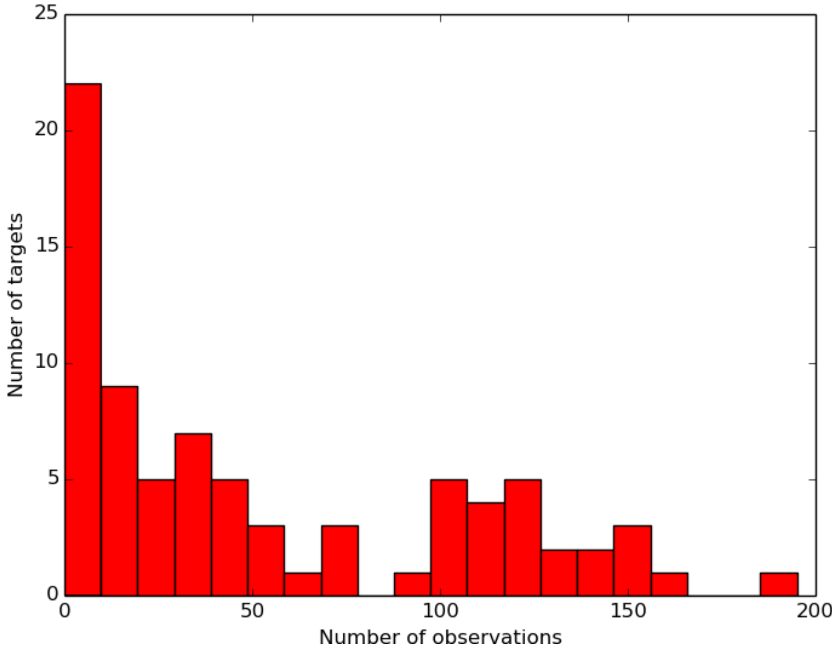

Figure 7.2: Distribution of number of observations for HADES targets as of October 2017.

Maldonado et al. (2017) computed the stellar parameters for the HADES targets, applying the spectral ratios method from Maldonado et al. (2015) to the stellar spectra. In the case in which more than one spectra of the same star was available (i.e. most of the targets), a single high-SNR spectra was obtained combining the single observations with the technique from Scandariato et al. (2017). The distributions of the masses and radii of the stars in the sample are shown in Fig. 7.3. The complete set of stellar parameters for the HADES targets is listed in Table 7.1.

The only previous RV survey aimed to exoplanet detection and characterization around low-mass stars, complete down to super-Earth and Neptunes, was the HARPS M dwarfs survey, which observed 102 targets over the course of 6 years (Bonfils et al., 2013a). In Sec. 2.3.1 I discussed the statistical results of that survey. Since 2013 many more observations of M dwarfs have been carried for the survey as part of a ESO Large Programme, also studying many transiting systems from the K2 survey (Howell et al., 2014). Even if many system have been studied and discovered as part of the survey (e.g. Astudillo-Defru et al., 2017), there has not been any updates on the statistical analysis, so the best reference for M dwarfs population properties from ground based RV surveys remains the work from Bonfils et al. (2013a), along with the analysis by Tuomi et al. (2014) which I will discuss in details in Sec. 7.3.1.

The average number of observations in the Bonfils et al. (2013a) study was 20, and it was considered as a lower limit for planetary detections in the HADES programme (Perger et al., 2017a). Up to October 2016, 48 stars were observed more than 20 times each.

On the contrary to the HADES programme, the HARPS M survey selected targets over a wide range of spectral types, increasing the number of parameters to be taken into account for a meaningful statistical analysis. In Figure 7.4 are shown the distributions of spectral types for the two surveys.

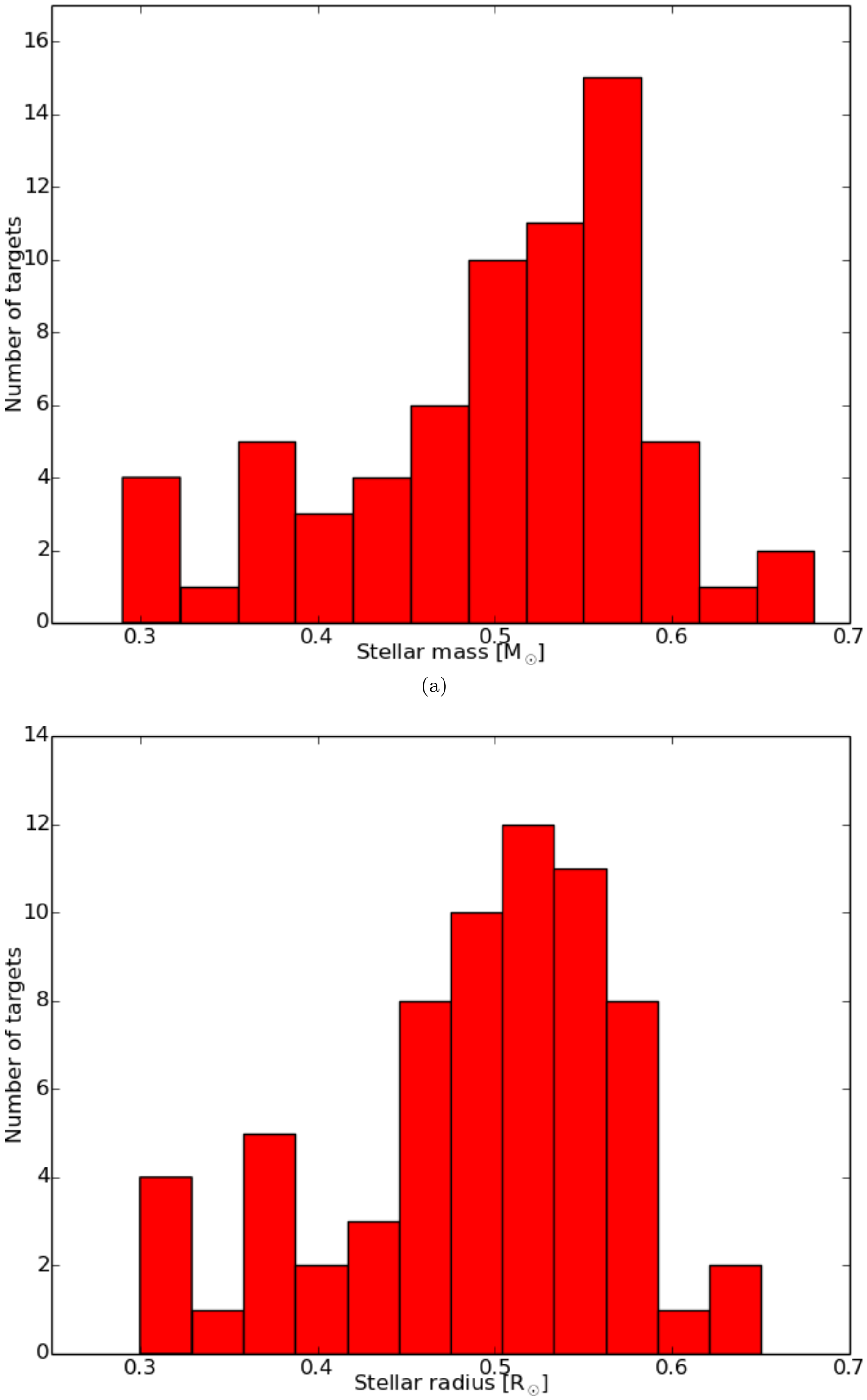

(a)

(b)

Figure 7.3: Distribution of masses (upper panel) and radii (lower panel) for HADES targets, as computed by Maldonado et al. (2017).

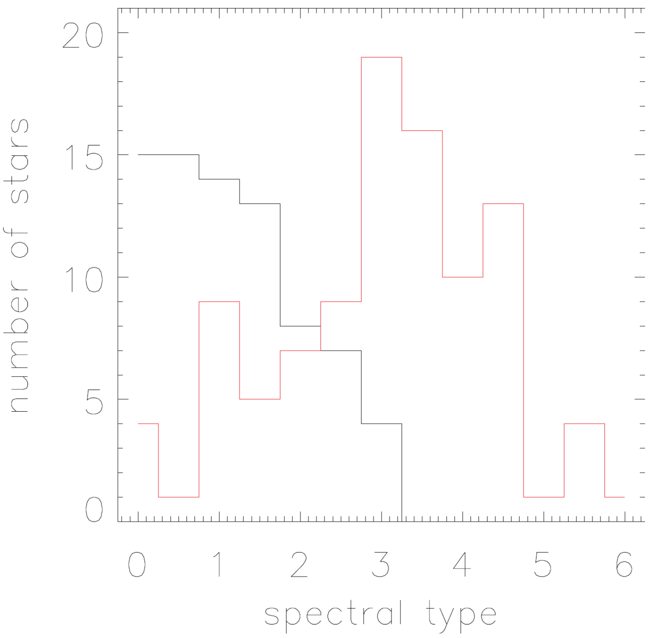

Figure 7.4: Distribution of spectral types for the HADES (black) and HARPS M (red) targets. (from Perger et al., 2017a)

Table 7.1: Basic stellar parameters of the stellar sample, from Maldonado et al. (2017). † 2MASS J22353504+3712131; ‡ The star falls out of the range of applicability of the metallicity calibrations given in Maldonado et al. (2015). Metallicities are computed using the photometric calibration by Neves et al. (2012), masses from Henry and McCarthy (1993), radius using the calibration by Maldonado et al. (2015, Eq. 4), surface gravities from masses and radius, and luminosities by applying the Stefan-Boltzmann law.

Star (1)	$T_{\rm eff}$ [K] (2)	Sp-Type (3)	[Fe/H] [dex] (4)	$M_\star$ [$M_\odot$] (5)	$R_\star$ [$R_\odot$] (6)	$\log g$ [cgs] (7)	$\log(L_\star/L_\odot)$ (8)	$v \sin i$ [km s^{-1}] (9)
GJ 2	3713 ± 68	M1	-0.14 ± 0.09	0.51 ± 0.05	0.49 ± 0.05	4.76 ± 0.04	-1.380 ± 0.087	0.98 ± 0.54
GJ 3014	3695 ± 69	M1.5	-0.19 ± 0.09	0.48 ± 0.05	0.47 ± 0.05	4.79 ± 0.04	-1.433 ± 0.090	< 1.08
GJ 16	3673 ± 68	M1.5	-0.16 ± 0.09	0.48 ± 0.05	0.47 ± 0.05	4.78 ± 0.04	-1.441 ± 0.090	< 1.02
GJ 15A	3607 ± 68	M1	-0.34 ± 0.09	0.38 ± 0.05	0.38 ± 0.05	4.87 ± 0.04	-1.655 ± 0.112	1.09 ± 0.79
GJ 21	3746 ± 68	M1	-0.12 ± 0.09	0.53 ± 0.05	0.52 ± 0.05	4.74 ± 0.04	-1.328 ± 0.086	1.46 ± 0.36
GJ 26	3484 ± 68	M2.5	-0.17 ± 0.09	0.37 ± 0.07	0.37 ± 0.06	4.88 ± 0.06	-1.741 ± 0.150	< 0.94
GJ 47	3525 ± 68	M2	-0.26 ± 0.09	0.36 ± 0.06	0.37 ± 0.06	4.88 ± 0.05	-1.730 ± 0.135	< 1.81
GJ 49	3712 ± 68	M1.5	-0.03 ± 0.09	0.55 ± 0.05	0.53 ± 0.05	4.73 ± 0.04	-1.317 ± 0.081	1.32 ± 0.37
GJ 1030	3658 ± 68	M2	-0.08 ± 0.09	0.50 ± 0.05	0.49 ± 0.05	4.76 ± 0.04	-1.409 ± 0.086	< 0.93
NLTT 4188	3810 ± 69	M0.5	-0.06 ± 0.09	0.59 ± 0.06	0.57 ± 0.05	4.70 ± 0.05	-1.213 ± 0.088	1.11 ± 0.45
GJ 70	3511 ± 68	M2.5	-0.21 ± 0.09	0.37 ± 0.06	0.38 ± 0.06	4.87 ± 0.06	-1.717 ± 0.137	< 1.02
GJ 3117A	3549 ± 68	M2.5	-0.13 ± 0.09	0.43 ± 0.06	0.43 ± 0.05	4.82 ± 0.05	-1.588 ± 0.111	< 0.91
GJ 3126	3505 ± 68	M3	0.01 ± 0.09	0.45 ± 0.07	0.45 ± 0.06	4.80 ± 0.06	-1.567 ± 0.118	< 0.83
GJ 3186	3768 ± 68	M1	-0.14 ± 0.09	0.53 ± 0.05	0.52 ± 0.05	4.74 ± 0.05	-1.313 ± 0.088	< 1.02
GJ 119A	3761 ± 69	M1	-0.08 ± 0.09	0.55 ± 0.05	0.54 ± 0.05	4.72 ± 0.04	-1.286 ± 0.085	< 0.98
GJ119B	3508 ± 69	M3	0.05 ± 0.09	0.47 ± 0.06	0.46 ± 0.06	4.79 ± 0.06	-1.535 ± 0.114	< 0.81
TYC 1795-941-1‡	3774 ± 67	M0	0.01 ± 0.23	0.66 ± 0.13	0.64 ± 0.14	4.65 ± 0.20	-1.128 ± 0.192	3.30 ± 0.16
NLTT 10614	3728 ± 69	M1.5	-0.06 ± 0.09	0.54 ± 0.05	0.53 ± 0.05	4.73 ± 0.04	-1.315 ± 0.083	< 2.07
TYC 3720-426-1‡	3822 ± 70	M0	0.12 ± 0.07	0.66 ± 0.1	0.64 ± 0.11	4.64 ± 0.16	-1.106 ± 0.153	4.13 ± 0.13
GJ 150.1B	3730 ± 68	M1	-0.16 ± 0.09	0.51 ± 0.05	0.49 ± 0.05	4.76 ± 0.04	-1.372 ± 0.088	0.87 ± 0.65
GJ 156.1A	3745 ± 69	M1.5	-0.05 ± 0.09	0.55 ± 0.05	0.54 ± 0.05	4.72 ± 0.04	-1.289 ± 0.083	< 2.85
GJ 162	3746 ± 68	M1	-0.19 ± 0.09	0.50 ± 0.05	0.49 ± 0.05	4.77 ± 0.04	-1.370 ± 0.090	0.93 ± 0.66
GJ 1074	3765 ± 69	M0.5	-0.16 ± 0.09	0.52 ± 0.05	0.51 ± 0.05	4.75 ± 0.05	-1.327 ± 0.089	1.13 ± 0.50
GJ 184	3752 ± 69	M0.5	-0.10 ± 0.09	0.54 ± 0.05	0.53 ± 0.05	4.73 ± 0.04	-1.310 ± 0.086	< 1.45
GJ 3352	3809 ± 69	M0.5	-0.13 ± 0.09	0.56 ± 0.06	0.54 ± 0.05	4.72 ± 0.05	-1.252 ± 0.091	< 1.47
TYC 3379-1077-1	3896 ± 71	M0	0.04 ± 0.09	0.69 ± 0.08	0.67 ± 0.07	4.61 ± 0.07	-1.038 ± 0.099	1.85 ± 0.26

Table 7.1: Continued (from Maldonado et al. (2017)).

Star (1)	$T_{\rm eff}$ [K] (2)	Sp-Type (3)	[Fe/H] [dex] (4)	$M_\star$ [$M_\odot$] (5)	$R_\star$ [$R_\odot$] (6)	$\log g$ [cgs] (7)	$\log(L_\star/L_\odot)$ (8)	$v \sin i$ [km s^{-1}] (9)
TYC7 43-1836-1	3846 ± 70	M0	-0.03 ± 0.09	0.62 ± 0.06	0.60 ± 0.06	4.67 ± 0.06	-1.148 ± 0.092	1.73 ± 0.30
GJ 272	3747 ± 68	M1	-0.19 ± 0.09	0.50 ± 0.05	0.49 ± 0.05	4.77 ± 0.04	-1.368 ± 0.090	< 1.09
StKM 1-650	3874 ± 69	M0.5	-0.11 ± 0.09	0.61 ± 0.07	0.60 ± 0.07	4.67 ± 0.06	-1.144 ± 0.101	1.12 ± 0.45
NLTT 21156	3616 ± 68	M2	-0.05 ± 0.09	0.50 ± 0.05	0.49 ± 0.05	4.77 ± 0.04	-1.442 ± 0.090	0.70 ± 0.61
GJ 399	3563 ± 68	M2.5	0.15 ± 0.10	0.55 ± 0.06	0.53 ± 0.05	4.72 ± 0.05	-1.391 ± 0.093	< 0.88
GJ 408	3472 ± 68	M2.5	-0.19 ± 0.09	0.35 ± 0.07	0.35 ± 0.06	4.89 ± 0.06	-1.787 ± 0.163	< 0.97
GJ 412A	3631 ± 68	M0.5	-0.38 ± 0.09	0.38 ± 0.05	0.38 ± 0.05	4.87 ± 0.04	-1.652 ± 0.111	1.20 ± 0.82
GJ 414B	3661 ± 68	M2	-0.09 ± 0.09	0.50 ± 0.05	0.49 ± 0.05	4.76 ± 0.04	-1.411 ± 0.087	< 0.94
GJ 3649	3691 ± 68	M1.5	-0.14 ± 0.09	0.50 ± 0.05	0.49 ± 0.05	4.77 ± 0.04	-1.406 ± 0.087	< 1.55
GJ 450	3649 ± 68	M1.5	-0.20 ± 0.09	0.45 ± 0.05	0.45 ± 0.05	4.80 ± 0.04	-1.497 ± 0.094	1.15 ± 0.51
GJ9404	3875 ± 70	M0.5	-0.10 ± 0.09	0.62 ± 0.07	0.60 ± 0.07	4.67 ± 0.06	-1.138 ± 0.101	1.25 ± 0.40
GJ 476	3498 ± 69	M3	-0.16 ± 0.09	0.38 ± 0.07	0.38 ± 0.06	4.86 ± 0.06	-1.703 ± 0.139	< 0.93
GJ 9440	3710 ± 68	M1.5	-0.13 ± 0.09	0.51 ± 0.05	0.50 ± 0.05	4.76 ± 0.04	-1.378 ± 0.086	< 0.99
GJ 521A	3601 ± 68	M1.5	-0.09 ± 0.09	0.47 ± 0.05	0.47 ± 0.05	4.79 ± 0.04	-1.486 ± 0.094	< 0.90
GJ 3822	3821 ± 70	M0.5	-0.13 ± 0.09	0.56 ± 0.06	0.55 ± 0.06	4.71 ± 0.05	-1.235 ± 0.094	0.98 ± 0.55
GJ 548A	3903 ± 70	M0	-0.13 ± 0.09	0.63 ± 0.08	0.61 ± 0.07	4.66 ± 0.07	-1.106 ± 0.108	1.11 ± 0.47
GJ 552	3589 ± 68	M2	-0.09 ± 0.09	0.47 ± 0.05	0.46 ± 0.05	4.79 ± 0.05	-1.503 ± 0.097	< 0.90
GJ 606	3665 ± 68	M1.5	-0.21 ± 0.09	0.46 ± 0.05	0.45 ± 0.05	4.80 ± 0.04	-1.484 ± 0.093	< 1.57
GJ 3942	3867 ± 69	M0	-0.04 ± 0.09	0.63 ± 0.07	0.61 ± 0.06	4.65 ± 0.06	-1.121 ± 0.096	1.67 ± 0.30
GJ 625	3499 ± 68	M2	-0.38 ± 0.09	0.30 ± 0.07	0.31 ± 0.06	4.94 ± 0.06	-1.894 ± 0.170	1.32 ± 0.67
GJ 3997	3754 ± 69	M0	-0.24 ± 0.09	0.49 ± 0.05	0.48 ± 0.05	4.78 ± 0.04	-1.391 ± 0.093	0.94 ± 0.76
GJ 3998	3722 ± 68	M1	-0.16 ± 0.09	0.50 ± 0.05	0.49 ± 0.05	4.77 ± 0.04	-1.382 ± 0.088	< 1.56
GJ 2128	3518 ± 68	M2.5	-0.30 ± 0.09	0.34 ± 0.06	0.35 ± 0.06	4.90 ± 0.05	-1.777 ± 0.144	< 1.19
GJ 671	3422 ± 68	M2.5	-0.17 ± 0.09	0.31 ± 0.09	0.32 ± 0.08	4.93 ± 0.08	-1.909 ± 0.216	< 0.91
GJ 685	3816 ± 69	M0.5	-0.15 ± 0.09	0.55 ± 0.06	0.54 ± 0.05	4.72 ± 0.05	-1.253 ± 0.094	1.33 ± 0.42
GJ 686	3663 ± 68	M1	-0.30 ± 0.09	0.42 ± 0.05	0.42 ± 0.05	4.83 ± 0.04	-1.548 ± 0.099	1.01 ± 0.80
GJ 694.2	3847 ± 69	M0.5	-0.21 ± 0.09	0.55 ± 0.06	0.54 ± 0.06	4.72 ± 0.06	-1.241 ± 0.102	< 1.13
GJ 4057	3873 ± 69	M0	-0.15 ± 0.09	0.59 ± 0.07	0.58 ± 0.07	4.69 ± 0.06	-1.167 ± 0.103	0.81 ± 0.69
GJ 720A	3837 ± 69	M0.5	-0.14 ± 0.09	0.57 ± 0.06	0.56 ± 0.06	4.71 ± 0.05	-1.217 ± 0.096	< 1.49
GJ 731	3844 ± 69	M0	-0.16 ± 0.09	0.57 ± 0.06	0.56 ± 0.06	4.71 ± 0.06	-1.217 ± 0.098	< 1.59
GJ 740	3845 ± 69	M0.5	-0.14 ± 0.09	0.58 ± 0.06	0.56 ± 0.06	4.70 ± 0.06	-1.206 ± 0.097	0.92 ± 0.59

Table 7.1: Continued (from Maldonado et al. (2017)).

Star (1)	$T_{\rm eff}$ [K] (2)	Sp-Type (3)	[Fe/H] [dex] (4)	$M_\star$ [$M_\odot$] (5)	$R_\star$ [$R_\odot$] (6)	$\log g$ [cgs] (7)	$\log(L_\star/L_\odot)$ (8)	$v \sin i$ [km s^{-1}] (9)
GJ 4092	3858 ± 69	M0.5	-0.06 ± 0.09	0.62 ± 0.07	0.60 ± 0.06	4.67 ± 0.06	-1.145 ± 0.095	1.20 ± 0.41
GJ 9689	3824 ± 69	M0.5	-0.13 ± 0.09	0.57 ± 0.06	0.55 ± 0.06	4.71 ± 0.05	-1.231 ± 0.093	< 1.47
GJ 793	3461 ± 68	M3	-0.21 ± 0.09	0.33 ± 0.08	0.34 ± 0.07	4.91 ± 0.07	-1.833 ± 0.176	< 1.00
BPM 96441	3896 ± 72	M0	-0.03 ± 0.09	0.66 ± 0.08	0.64 ± 0.07	4.63 ± 0.07	-1.071 ± 0.103	2.05 ± 0.24
TYC 2710-691-1	3867 ± 71	K7.5	0.02 ± 0.09	0.65 ± 0.07	0.64 ± 0.07	4.63 ± 0.06	-1.092 ± 0.094	2.41 ± 0.21
TYC 2703-706-1	3822 ± 70	M0.5	0.06 ± 0.09	0.64 ± 0.06	0.62 ± 0.06	4.65 ± 0.05	-1.136 ± 0.085	3.32 ± 0.16
GJ 4196	3666 ± 68	M1	0.07 ± 0.10	0.56 ± 0.05	0.55 ± 0.05	4.71 ± 0.04	-1.313 ± 0.082	2.40 ± 0.19
NLTT 52021	3687 ± 68	M2	-0.12 ± 0.09	0.50 ± 0.05	0.49 ± 0.05	4.77 ± 0.04	-1.400 ± 0.086	< 0.97
NLTT 53166	3832 ± 70	M0	-0.11 ± 0.09	0.58 ± 0.06	0.57 ± 0.06	4.70 ± 0.05	-1.209 ± 0.094	< 1.45
2MASS J2235†	3891 ± 70	K7.5	-0.13 ± 0.09	0.62 ± 0.07	0.60 ± 0.07	4.67 ± 0.07	-1.127 ± 0.106	1.92 ± 0.28
GJ 9793‡	3881 ± 70	M0	0.24 ± 0.05	0.75 ± 0.12	0.73 ± 0.12	4.58 ± 0.16	-0.965 ± 0.146	2.77 ± 0.22
GJ 4306	3763 ± 69	M1	-0.13 ± 0.09	0.53 ± 0.05	0.52 ± 0.05	4.74 ± 0.05	-1.313 ± 0.088	< 1.01
GJ 895	3748 ± 68	M1.5	-0.09 ± 0.09	0.54 ± 0.05	0.53 ± 0.05	4.73 ± 0.04	-1.308 ± 0.085	< 1.70
V* BRPsc	3553 ± 68	M1.5	-0.29 ± 0.09	0.37 ± 0.06	0.37 ± 0.05	4.88 ± 0.05	-1.704 ± 0.125	0.88 ± 0.82

7.2 Observation strategy statistical study

Perger et al. (2017a) studied the results of the HADES programme up to March 2016 and used the inferred planetary distribution from other studies to evaluate the expected number of detected planets. A planetary population was simulated, and synthetic RV time series were generated adopting the actual observation epochs from the survey and modelling the uncertainties to reproduce the observed errorbars and rms. The planetary characteristics distributions adopted were a combination of those derived in various studies of surveys both from transits and RVs.

In particular the distribution of the orbital periods, P_p is adapted from the statistics of Kepler planets by Fressin et al. (2013) and Dressing and Charbonneau (2015), for high and low mass planets respectively, resulting in the following distribution:

$$\mathcal{P}(P_p)dP_p = D \cdot 10^{a+b\cdot\log(P_p)+c\cdot\log^2(P_p)}dP_p, \tag{7.1}$$

with $a = -4$, $b = 2.205$, $c = -0.835$, and $D = 3.13$ for $M_p > 30$ M$_\oplus$ and $a = -2$, $b = 0.954$, $c = -0.637$, and $D = 1.04$ for $M_p < 30$ M$_\oplus$.

The mass distribution implemented was instead that derived by Mayor et al. (2011), who studied a sample of inactive late-F to late-K dwarfs observed with HARPS, which can be expressed as:

$$\mathcal{P}(M_p)dM_p = 1.40 \cdot M_p^{-2.40}dM_p. \tag{7.2}$$

Finally, Perger et al. (2017a) adopted as eccentricity distribution the one derived by Kipping (2013) (see Eq. 3.2), while the multiplicity distribution is again taken from Dressing and Charbonneau (2015), resulting in an average of 1.70 planets per star.

To average out numerical errors, 1000 realizations of the sample of 78 systems were generated. The RV time series were then analysed with the GLS periodogram, adopting a 0.1% FAP threshold. The found signal was successively subtracted, assuming circular orbits, and the residuals re-analysed until no significant signal was found.

The distribution of detected planets parameters is shown in Fig. 7.5, compared to the simulated distributions. As can be seen, the detection rates reaches its highest level for masses between $5 - 25$ M$_\oplus$ and periods between $10 - 25$ d. The histograms show also the number of false positives detected by the analysis, showing how the reliability of detections drops for masses $\lesssim 3$ M$_\oplus$ and periods $\lesssim 3$ d.

From these distributions Perger et al. (2017a) derived the global detection rate of the survey, and estimated it to be $\sim 1.9\%$, corresponding to a total number of detected planets equal to 2.4 ± 1.5. This was well in agreement with the total of three planets detected back then by the programme: GJ3998 a and b (Affer et al., 2016) and GJ3942 b (Perger et al., 2017b, which was in preparation at the time of the analysis). By now we are already stretching the limit of these estimate, with the additional detection of GJ625 b (Suárez Mascareño et al., 2017a) and GJ15A c (see Chap. 6), leading to a total of five planets detected, with some more on their way. Even if GJ15A c should not be accounted for while testing the accuracy of the detection rate estimate by Perger

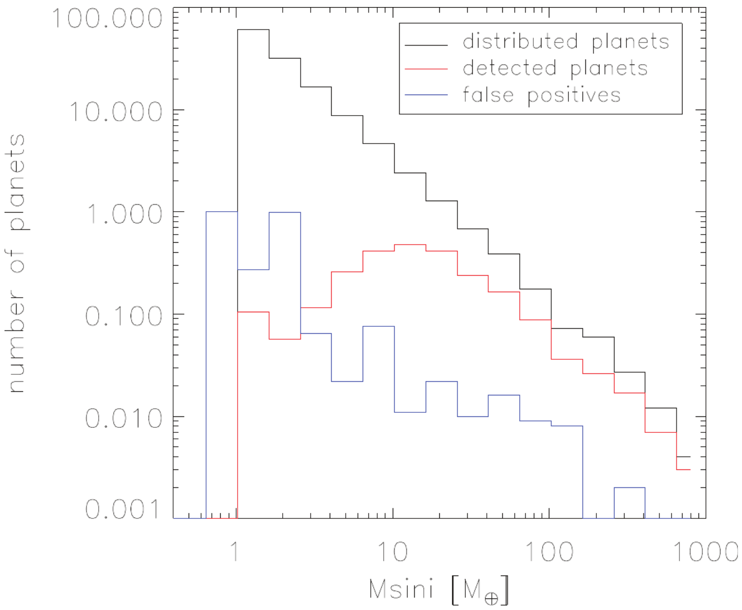

(a)

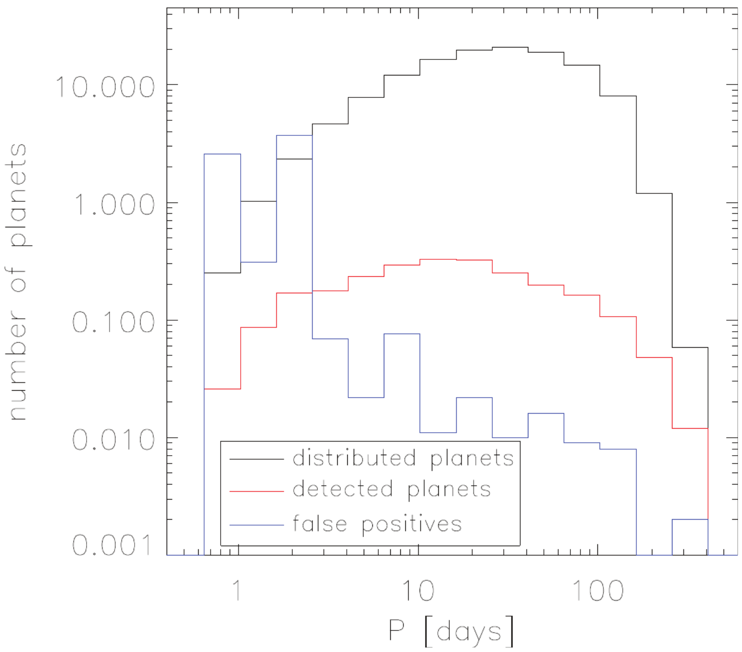

(b)

Figure 7.5: Distribution of minimum masses (upper panel) and periods (lower panel) for injected (black) and detected (red) planets in the HADES sample. The false positives (blu) are shown for reference. (from Perger et al., 2017a)

et al. (2017a), because lies outside of the simulated period range of $[0.5, 418]$ d, it is still clear how the final performances of the survey will depart from this first estimate of the detection rate, consequently changing the estimate of the planets occurrence rate.

7.3 Complete HADES statistical study

Now that the GAPS project and HADES programme are ending, one of the objectives of our M dwarfs exoplanet survey is to go beyond the preliminary statistical analysis of the sample (Perger et al., 2017a), and to perform a complete Bayesian analysis of the survey. The focus of Perger et al. (2017a) study was to gauge the efficiency of the survey and derive the best observing strategy for the HADES and similar programmes, while the aim of our analysis is to compute the effective planetary frequencies around the observed systems. The landmark for our statistical analysis is the work by Tuomi et al. (2014), who studied a sample of M dwarfs with UVES and HARPS radial velocities time series in order to calculate the occurrence rates of planets around small mass stars.

7.3.1 Landmark Bayesian analysis

Tuomi et al. (2014) used Bayesian statistics to estimate the occurrence rate and detectability function of extrasolar planets around M dwarfs. I will here briefly describe their analysis method, which will be the foundation of our study of the HADES statistics.

Tuomi et al. (2014) analysed the datasets in their sample with a Delayed Rejection and Adaptive Metropolis (DRAM) sampling algorithm (Haario et al., 2001) using a statistical benchmark model with a first order moving average term to account for stellar noise (Tuomi et al., 2013). This technique has proven to be most effective in the identification of planetary signals in RV time series, and was successfully applied in the RV fitting challenge (see Sec. 4.1) by Mikko Tuomi and Guillem Anglada-Escudé (Team 1). As detection criteria for a k Keplerian signals model Tuomi et al. (2014) required its posterior probability to be at least s times greater than that of the $k-1$ signals model. Two thresholds in s were selected, one for strong detections $s = 10^4$ and one for Signals Requiring Confirmation (SRC) $s = 150$.

For each time series of their sample, they assumed the observed number of planet in a given period-mass interval $\Delta_{P,M}$ can be expressed as:

$$f_{\mathrm{obs},i}(\Delta_{P,M}) = f_{\mathrm{occ},i}(\Delta_{P,M}) \cdot p_i(\Delta_{P,M}), \tag{7.3}$$

where the subscript i indicates the ith system, $f_{\mathrm{occ},i}$ is the occurrence rate of planets around the ith star, and p_i is the detectability function, i.e. the possibility of a planet in the parameter interval $\Delta_{P,M}$ to be detected in the ith time series. $f_{\mathrm{obs},i}$ is simply computed as the number of planet detected from each time series in each parameter interval. The tricky part is to correctly estimate p_i.

Assuming that k_i Keplerian signals were detected in the ith dataset, Tuomi et al. (2014) estimated the detectability function p_i by analysing with the DRAM algorithm the time series imposing a $k+1$ signals model. In this way following the regions of the (P, M) parameter space that the parameters of the hypothetical $k+1$th planet, which cannot be significantly detected in the data, it is possible to identify all the regions of the parameter space were the detection technique is not able to detect significant signals. The areas that were not explored by the Markov chains are in fact the areas where signals detection could have been possible, if significant signal were present in the data. The detectability function can therefore be approximated as:

$$p_i = 1 - \hat{p}_i, \tag{7.4}$$

where $\hat{p}_i$ is equal to one in the regions of parameters space explored by the $k+1$th Keplerian, and zero otherwise.

The observed frequency of planets in the whole sample of N datasets can be computed by the sum over i of Eq. 7.3:

$$\begin{aligned} f_{\mathrm{obs}}(\Delta_{P,M}) &= \sum_{i=1}^{N} f_{\mathrm{obs},i}(\Delta_{P,M}) \\ &= f_{\mathrm{occ}}(\Delta_{P,M}) \left[N - \sum_{i=1}^{N} \hat{p}_i(\Delta_{P,M}) \right], \end{aligned} \tag{7.5}$$

assuming the occurrence rate f_{occ} to be common for all stars in the sample, $f_{\mathrm{occ}} = f_{\mathrm{occ},i}$ for all i. This is expected to be the case for a well defined sample as the HADES sample (see Fig. 7.3).

Since $f_{\mathrm{obs}}(\Delta_{P,M})$ is known and the square brackets term can be easily calculated, Eq. 7.5 allows to calculate the occurrence rate of planets across the (P, M) parameter space. The global detection probability function of the sample can instead be computed simply dividing the square brackets term by N.

For these estimates to be accurate there needs to be at least one planetary signal in most (P, M) grid points, thus Tuomi et al. (2014) chose a 4×3 grid over the $[1, 10^4]$ d and $[3, 100]$ $\mathrm{M}_{\oplus}$ intervals.

Tuomi et al. (2014) applied this technique to the 41 systems of the VLT-UVES M dwarf ESO survey (Zechmeister et al., 2009), collecting also the public HARPS-TERRA spectra when available. They discarded any system with less than four measurements in the combined datasets, while the others, even if undersampled, were taken into account since due to the use of Bayesian statistical techniques they could still bring meaningful results. To compute the detection probability of the sample Tuomi et al. (2014) used both the detected signals ($s = 10^4$) and SRC ($s = 150$), while, to avoid bias due to the possible presence of the false positives, excluded the SRCs from the computation of the occurrence rates. As I mentioned in Sec. 2.3.1, even if analysing a smaller sample than Bonfils et al. (2013a) they achieved a better precision in their estimates due to the exploitation of Bayesian statistics.

7.3.2 HADES team approach

To apply the Bayesian analysis technique by Tuomi et al. (2014) to our HADES sample, a few steps and variations are required.

The first step is of course to re-analyse the full sample in a homogeneous way, in order to identify all the planetary signals present in the data, excluding stellar activity and aliases due to the observational windows. Of the full survey sample, we choose to ignore all the objects with less than 10 obs, which don't have enough data points for a meaningful analysis. This leaves a sample of 56 objects with > 10 obs, comparable to that of Tuomi et al. (2014). This analysis will be composed of the following steps, to be carried out by different members of the GAPS M-dwarf group:

- RV periodic signals and aliases identification, performed with the GLS periodogram, in order to identify all the periodic signals present in the data, below the two FAP thresholds (1%, 0.1%) in order to identify two subsamples of weak and strong identifications respectively, corresponding to Tuomi et al. (2014) detections and SRCs;
- Activity index analysis, to look for periodic signals studying the GLS periodogram on the $S_{\rm HK}$ index, FWHM, and other activity indicators described in Sec. 2.2.1;
- Periodic signals comparison: cross-match study between the periodicities identified in the previous, in order to discard signals due to stellar activity, and to produce the final lists of planetary candidates and SRCs.

As a support to the analysis of the activity indices, the full sample will be studied in order to identify the stellar rotation periods in the photometric data from the APACHE and EXORAP programs. This will be done in parallel by the two groups in order to achieve two analysis as homogeneous as possible. The complete set of rotation periods for the whole sample would help to confirm the evidence of stellar signals from the activity indices. In support to the photometric analysis, a complete analysis of the survey spectroscopy to compute the rotational periods of the stars has been led by the Spanish EXOTEAM group (Suárez Mascareño et al., 2017b). The comparison between the photometric and spectroscopic analysis will allow a fine knowledge of the sample rotation and thus a great awareness about the stellar activity signals hidden in the data.

The final step will be the estimate of the detection probability p_i and planet occurrence rate $f_{\rm occ}$, following the recipe by Tuomi et al. (2014) described in Sec. 7.3.1, which I will perform myself. Instead of the DRAM sampling algorithm used by Tuomi et al. (2014), I will apply in an analogous way our MCMC code described in Sec. 4.1.2. For the 27 targets with more than 70 observations, the GP will be used to model the stellar activity in the RV time series, using the rotation periods from the photometry and spectroscopy to guide the analysis. For the rest of the sample, since they have not enough data for a robust GP analysis, will be simply pre-treated subtracting the eventual linear correlation with the activity indices and by considering in the RV time series fit the presence of uncorrelated stellar jitter.

7.3.3 Preliminary results

Since both the complete homogeneous analysis of the HADES time series to detect all the planetary candidates and stellar signals and the implementation of the MCMC code for the computation of the Bayesian detection probability and occurrence rate are still in the making, I will here present some preliminary results, derived with a more standard if less comprehensive approach.

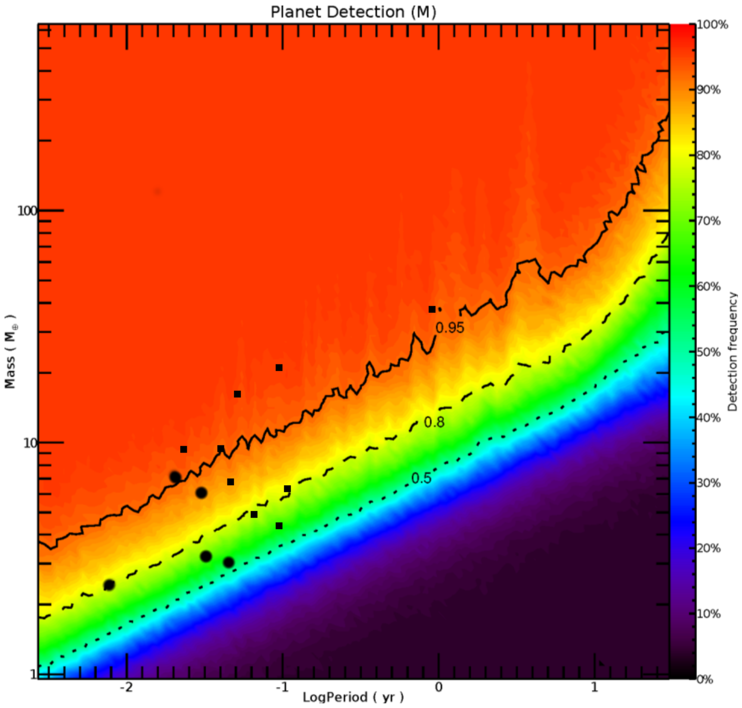

Figure 7.6: Detection probability in the HADES sample, as a function of mass and period. The black dots represent the confirmed planets (listed in Table 7.2), while the black squares represent the SRCs (listed in Table 7.3)

The detection probability is calculated following the standard recipe (e.g. Endl et al., 2001; Dumusque et al., 2011b; Mortier et al., 2012) of injecting trial circular orbits into the observed time series. Only the targets with more than 10 observations were taken into account for this analysis, resulting in a sample of 56 systems. Since the method assumes the datasets to contain only uncorrelated noise, first of all I subtracted from the respective time series the signals of the known planets GJ15A b (see Chap. 6), GJ3998 b and c, GJ625 b, and GJ3942 b (see Sect. 5.3). Also the time series were corrected for any long-period linear trend present in the data[1]. The time series could, of course, still contain stellar activity signals or eventual undetected planets, thus when generating the trial planetary orbits in the data, after the signal injection each datapoint was normally displaced with standard deviation equal to either the measurement error or the rms of the time series, whichever was larger.

The explored ranges were $[1.5, 365.25]$ d for the period and $[1, 636]$ $M_\oplus$ for the mass, covered by a 50×50 grid. For each mass-period couple 10 orbits uniformly distributed in phase were analysed with a GLS periodogram, and if all of them were recovered below a 0.1% FAP level the planet were considered to be detected.

The combined detection probability for the sample is shown in Fig. 7.6.

---

[1] Since the HARPS-N data only covers the ascending part of the orbit of GJ15A c, it was treated as a linear trend for the purposes of this analysis.

Table 7.2: Planet detected in the HADES datasets.

Planet	P_b [d]	$m_b \sin i_b$ [M$_\oplus$]
GJ3998 b	2.65	2.46
GJ3998 c	13.74	6.12
GJ625 b	14.63	2.82
GJ3942,b	6,91	7,1
GJ15A b	11,44	3.06

Table 7.3: SRC recovered from the preliminary GLS analysis of the HADES datasets.

Target ID	P_b [d]	$m_b \sin i_b$ [M$_\oplus$]
M17	31.8	5.85
M76	9.05	9.86
M80	19.5	13.11
M82	33.1	4.27
M91	13.4	9.06
M96	15.5	6.22
M101	472	34.3
M105	25.1	22.4
M106	25.1	5.26

A first estimate of the planet frequency, f_{occ}, can be assessed by means of a binomial distribution (Faria et al., 2016):

$$\mathcal{P}(d \mid N, f_{\text{occ}}) = \frac{N!}{k!(N-d)!} f_{\text{occ}}^{d} (1 - f_{\text{occ}})^{N-d}, \tag{7.6}$$

where N is the number of targets of the survey and d is the number of detected planets. The mode of the distribution can be used to express the expected value of planetary frequency, with the uncertainties corresponding to the 68% range in the distribution. The whole HADES sample is composed of $N = 56$ targets, around which have been confirmed so far a total of $d = 5$ planets, as discussed in Sec. 5.3, with the masses and periods listed in Table 7.2. We can use these confirmed planets for a preliminary estimate of the occurrence rate in our sample.

We see in Fig. 7.6 that all the five planets detected in the HADES sample lie within the $f_{\text{obs}} > 0.50$, that correspond to a occurrence rate of $f_{\text{occ}} = 0.18^{+0.09}_{-0.05}$, for periods $P < 0.1$ yr and masses $M > 2$ M$_\oplus$.

In addition to the confirmed planets, we ran a preliminary GLS analysis to identify other promising signals, with FAP $< 0.1\%$. The resulting signals' periods and masses, excluding those corresponding to the host star's rotation period, are listed in Table 7.3. Since these signals are yet to be thoroughly studied and tested for the possible influence of stellar activity as discussed in the previous Section, they should not be considered as solid detections. They can be instead classified as SRCs, as defined in Sec. 7.3.1. If we take into account also these SRCs, considering that all but one of them lie in the same period and mass interval defined before, in Eq. 7.6 the occurrence rate would rise to $f_{\rm occ} = 0.46^{+0.09}_{-0.09}$.

A qualitative comparison of these preliminary results with the findings of Bonfils et al. (2013a) and Tuomi et al. (2014), discussed in Sec. 2.3.1, seems to suggest that, if considering only the confirmed planets, the HADES sample shows a lower occurrence rate than estimated from the other two studies, which could be a hint of a lower occurrence of exoplanets around early-type M dwarfs with respect to later-types as those analysed by Bonfils et al. (2013a). On the other hand, if taking into account also the SRCs, which could be confirmed by the ongoing analysis, the occurrence rate become fully compatible with those presented in the literature.

Chapter 8

Summary and conclusions

The work I presented in this thesis was aimed to increase our knowledge of the formation and evolution of planetary systems, through an extended approach towards the detection and characterization of planetary systems around M dwarfs by means of high-precision Doppler monitoring. This has been carried out following two main paths of research: (i) the detailed study of the performances of low- and high-level tools for the analysis of RV time series, based on the analysis of synthetic datasets, focusing on the detectability of small-mass planets around small-mass stars, and on the effects of RV stellar signals due to chromospheric activity and the best methods to treat them; (ii) the analysis of real RV time series of cool stars, both from the literature and collected within the GAPS programme with HARPS-N at TNG, with the application of the mastered tools for the detection of multi-planet system in the presence of stellar noise and instrumental effects.

In this final Chapter, I summarise the main results of the studies I performed as part of my PhD thesis, and then discuss the potential future developments and prospects in the of exoplanetary systems around small mass stars, since many aspects are still to be investigated, and exciting new opportunities will soon be opened by incoming instruments and surveys.

8.1 Summary of results

8.1.1 Tools for data analysis

Several tools are currently used to analyse RV time series for exoplanets detection around M dwarfs. The basic techniques include different types of periodogram analysis to identify promising periodicities which could be due to planetary Keplerian signals. As discussed in Sec. 2.2, RV time series are also affected by stellar activity signals, which could easily mask or mimic planetary signals, leading to missed or false detections (Sec. 2.2.3). For this reason it is fundamental to develop robust tools for data analysis, in order to best distinguish between genuine planetary signals and aliases due to stellar activity or other observational effects. Since the true nature of real observational data is usually not completely understood, the best way to thoroughly test analysis algorithm is on simulated time series, which can be completely controlled, studying the effect of different combinations of input periodicities and noise structures on the recovered signals.

This perspective leads the studies described in Chapter 3 and the first part of Chapter 4 (Sec. 4.1), which approach the topic from two opposite and complementary directions.

In Chapter 3 I analysed in details the three main algorithms for periodogram analysis, GLS (Zechmeister and Kürster, 2009), BGLS (Mortier et al., 2015), and FREDEC (Baluev, 2013b), applying them on low-cadence RV observations of M dwarfs with characteristics similar to the typical survey datasets, e.g. similar to those of the HADES sample (Sec. 7.1). The performances of these tools were tested on several types and combinations of signals, with Keplerian signals from single- and multi-planet systems as well as some basic modelling of stellar activity. The complexity of the simulations was kept low on purpose, in order to better study the influence of a small number of parameters on the algorithms results. As detailed in Sec. 3.4, this extensive numerical analysis permitted to learn the precise performances of the three tested tools in different regimes of simulated signals, also comparing the results with several similar if less complete analysis from the literature (e.g. Cumming, 2004; Shen and Turner, 2008; Vanderburg et al., 2016). It is worth noticing that the detailed analysis of tools performances on multi-planet simulated time series was never performed before in the literature. The overall performances of GLS, BGLS, and FREDEC are quite similar, with all of them showing a completeness $C \simeq 100\%$ for $K/\sigma \gtrsim 2$ on signal-planet circular-orbit systems (Sec. 3.3.2), with losses of $\simeq 10\%$ in completeness for eccentric orbits (Sec. 3.3.3) and up to $\simeq 40\%$ in the presence of simple models of correlated stellar noise with $K_\star/K_P \gtrsim 1$ (Sec. 3.3.4). At the same time I pointed out the discrepancies due to the different frameworks adopted by the algorithms: the Bayesian framework of BGLS result in a slightly higher reliability than the other algorithms when dealing with single signals both from circular and eccentric orbits, but at the moment is still hindered by the presence of multiple overlapping signals, in which case loses $\sim 10\%$ in both C and R values with respect of GLS (Sec. 3.3.5 and 3.3.6). The multi-frequency approach of FREDEC, instead, results in a much smaller ($\sim 1/2$) fraction of false positive detections when studying multi-planet systems, even if similar completeness levels to those of GLS (Sec. 3.3.5 and 3.3.6). Given the different performances in different simulation regimes, none of the three algorithms seems to be always preferable over the others in the analysis of real complex datasets. Rather a combined application of several tools can give a more wide view of the underlying signals in the studied time series, even if none of them can produce robust results in the presence correlated and quasi-periodic noise.

An opposite approach was followed in the work described in Sec. 4.1, in which the research group I am part of, as part of a RV fitting challenge (Dumusque, 2016), blindly analysed a set of complex synthetic time series, simulating high-cadence observations of stars hosting multi-planet systems with up to seven planets each and different levels of stellar noise precisely reproduced from models and observations of different targets (Sec. 4.1.1). For this analysis we developed a suite of analysis techniques revolving around a MCMC fitting of the orbital data using Gaussian Process (GP) regression techniques to model the stellar activity quasi-periodic signals (Sec. 4.1.2). I took an active part in the analysis, mainly contributing to the identification of promising periodic signals and to the selection of the best-fit models for several of the analysed systems. As discussed in Sec. 4.1.3, our methodology was between the most successful in recovering the correct planetary signals present in the data. The results of the challenge outlined a threshold for clear detection of planetary signals in noisy time series, corresponding to $K/N \simeq 7.5$ (Eq. 4.6). This study also pointed out how model-selection methods based on Bayesian statistics seem to perform better when dealing with RV data affected by strong stellar noise (see Fig. 4.1). Another important lesson told by the challenge is the pivotal importance of a correct identification of the stellar rotation period, which correspond to the main periodicity of stellar activity signals: for some of the systems, the lack of ancillary observations to help constrain the rotation period led to uncorrected identification by our and other teams, which in turn resulted in false positives detections or rejection of genuine planetary signals.

8.1.2 Study of M dwarfs planetary systems

After the detailed studies of analysis tools performed on simulated datasets, I applied the gathered knowledge to the observational data of different M dwarfs systems, either collected as part of the GAPS and HADES programmes, or from publicly available RV archives. The two main stars I studied were GJ273 and GJ15A, both hosting known planetary systems (Astudillo-Defru et al., 2017; Howard et al., 2014). Due to the intrinsic peculiarity of each systems, the two analyses developed in very different direction, with the study of GJ273 focusing on the confirmation of a small mass planetary candidate, as discussed in Sec. 4.2, and the analysis of the GJ15A, reported in Chapter 6, encompassing a more wide study of different aspects of the system, including the dynamical interaction between the binary companion GJ15B and the detected outer planetary-mass companion GJ15A c.

The GJ273 system was fascinating due to the presence of an Earth-mass planet in the habitable zone ($P_b = 18.65$ d, $m_b \sin i_b = 2.89$ $\mathrm{M}_\oplus$), and we thus decided to apply on its public RV time series our analysis techniques, in order to see if the GP modelling of the stellar activity would produce changes in the orbital parameters of the planets. Some variations were, in fact, recovered, very small even if significant, but the main results was that we found in the GLS periodogram of the RV residuals of our model hints of the presence of an additional very low mass companion at $P = 8.64$ d (Sec. 4.2.2); this signal had however a high FAP $\sim 6\%$, which made us wary about its actual presence in the data. We tested an three-planet plus stellar noise model which resulted in the confirmation of the period $P_b = 8.64$ d and a semi-amplitude $k_b = 0.44$ m s^{-1}. Even if the Bayesian model comparison favoured the three-planet model over the previous one, we remain doubtful, also due to the very-low amplitude of the signal and the value of $K/N \simeq 7.5$ close to the detectability threshold. For these reasons I performed a series of numerical experiment, in which I applied the three algorithms discussed in Chapter 3 to both the residual time series of the systems and different synthetic datasets (Sec. 4.2.3). Generating different realisations of the the two-planet model residuals, the rate of recovery of the candidate third planet, expressed trough the C and R values defined in Sec. 3.3, was in line the results obtained analysing a set of simulated time series, generated from the three planet model recovered with the MCMC analysis, also containing the GP modelization of the stellar noise. On the contrary almost no signal at $P \simeq 8.64$ d was recovered when analysing similar time series but generated without the third planetary signal injected. This suggests that the identified signal is in fact of planetary nature, but we are still cautious on its nature, and more in depth analysis will follow in the future on this fascinating system.

The GJ15A system was known to host a short-period super-Earth ($P_b = 11.44$ d, $m_b \sin i_b = 5.35$ $M_\oplus$) identified from Doppler measurements from the HIRES spectrometer. The published data also presented a descending long-period trend which was imputed to the binary companion GJ15B (Howard et al., 2014). The HADES HARPS-N observations, however, showed an opposite ascending trend (Sec. 6.2). This convinced us to perform a thorough analysis to verify the nature of this long-period signal: after ruling out the effect due to GJ15B and possible undetected stellar companions (Sec. 6.4), we applied our MCMC+GP method on the activity indicators and RV time series, modelling the planetary and stellar signals in the data, resulting in the identification of the long-period signal as super-Neptune mass planet ($P_c \simeq 8400$ d, $m_c \sin i_c = 44.4$ $M_\oplus$). Even if the recovered orbit for planet GJ15A c shows a very small if any eccentricity, which is usually a clue of orbital perturbation, we decided to study the dynamical influence of GJ15B by means of the Eccentric Lidov-Kozai mechanism (Sec. 6.5). To better constrain the perturbing effect of the stellar companion, I derived a new orbital solution for the binary, combining the HARPS-N RV measurements of the two stars with astrometric data from the ADS archive (Sec. 6.5.1). A set of numerical simulation of the EKL oscillations were then performed taking advantage of the newly derived orbit for GJ15B (Sec. 6.5.2). This analysis shows how only a small range of initial inclinations for the planetary system ($i_0 = 75° - 90°$) produce the observed low-eccentricity orbit for GJ15A c, otherwise the EKL oscillations are likely to excite it in highly-eccentric states, or even make the system unstable ($i_0 = 0°, 15° - 30°$). This is in good agreement with recent estimates of the stellar inclination $i_\star \simeq 70° - 90°$ (Suárez Mascareño et al., 2017b), which can be used as a proxy of the inclination of the protoplanetary disk and thus of the initial state of the planetary system. It is important however to remind that these conditions do not result into constraint on the current inclination of the planetary orbits, since the EKL, even in its less effective regimes, produce oscillation in the orbital inclination of $\sim 20°$.

As I discussed in Sec. 2.3.1, the derivation of the underlying planetary frequency is one of the main goal of any exoplanetary detection survey, as well as constraining the detectability function of the survey itself. In order to produce similar and robust estimates for the HADES sample, I am leading the ongoing statistical analysis of the survey dataset, as described in Chapter 7. This analysis is modelled on the Bayesian technique developed by Tuomi et al. (2014), which allows to precise estimate of the detectability function (Sec. 7.3.1). I am currently adapting our MCMC+GP algorithm to their technique, in order to apply it on our M dwarfs sample, while all the GAPS-M subgroup is analysing the HADES RV time series in order to uncover any yet to be detected candidate planetary signal present in the data (Sec. 7.3.2). Some preliminary estimates of the detectability function and the planetary frequency can already be obtained from the sample, taking advantage of more standard if less effective techniques (Sec. 7.3.3).

8.2 Future prospects

In the ever-growing field of exoplanetology, the possibilities for future investigations in the study of cool planet-hosting stars are manifold. The different analysis techniques studied as part of my PhD work can be easily applied on different M dwarfs RV datasets, as well as on different types of host, which could benefit from the advanced techniques developed to try to solve the complex puzzle posed by small-mass stars. Also in the near future new instruments will become available for exoplanets observations, opening new exciting possibilities for studies such as those presented in this thesis.

I will here briefly overview some of the various possible future developments and applications suitable for my PhD work.

8.2.1 Further application of analysis techniques

After completing the Bayesian analysis of the HADES sample statistics, the most straightforward application of my work will of course be offered by set of potential additional planetary candidates detected during the analysis, such as those pointed out in Sec 7.3.3. These systems could be thoroughly studied by applying on them the complete algorithm described in Sec. 4.1.2, potentially leading to their confirmation or disproof, thus also refining the estimates of planetary frequency f_P derived from the survey.

Another direction could be to apply the developed Bayesian technique for survey analysis to the other samples collected as part of the GAPS programme, described in Sec. 5.2, such as the metal-poor sample, since the exoplanetary population orbiting metal-poor stars is still uncertain, due to the low detection rates in most of the dedicated surveys (e.g. Faria et al., 2016, and references therein).

Also, as proved by the analysis of GJ15A presented in Chapter 6, the analysis of archival RV time series (e.g. Butler et al., 2017) and their combination with recent Doppler observations can be of great impact in the detection of long-period planetary companions to known planet-hosting stars. These studies are crucial in understanding the global planetary population in multiple systems, since usually the long-period tail of the distribution is poorly sampled due to the difficulties in obtaining the long time spans required to properly sample such wide orbits. Even the orbit of GJ15A c, even if clearly detected in our data, is still poorly constrained and will greatly benefit from future additional observations. As mentioned in Sec. 6.6, the study of wide-orbit planetary companions will also greatly benefits from astrometric observations, in particular the orbital solutions in the future Gaia data releases, which should allow the identification of the orbital signatures of $\sim 1000 - 1500$ extrasolar planets orbiting M dwarfs within 100 pc from the Sun (Sozzetti et al., 2014).

8.2.2 Future opportunities

One of the greatest opportunities for M dwarfs planetary studies in the near future will be offered by the Transiting Exoplanet Survey Satellite mission (TESS, Ricker et al., 2014), which is scheduled to launch in early 2018. This mission will perform a two-year all-sky photometric survey, monitoring more than 200,000 bright nearby stars, most of which will of course be small mass M dwarfs. This mission is expected to find thousands of transiting planets smaller than Neptune ($R \lesssim 4$ R$_\oplus$), mostly with period $P \simeq 10$ d. These detections will open great possibilities for Doppler follow-up and RV confirmation of the candidate planets detected. The great advantage with respect to the Kepler mission will be that the TESS targets will be much closer and brighter than those observed by Kepler, fostering high-precision spectroscopic measurements. The RV monitoring will allow precise mass and density derivation for these planets, as well as potential detections of non-transiting or longer-period companions, greatly expanding our knowledge of the populations of planets orbiting nearby small-mass stars. Also, and maybe above all, TESS transiting planets will provide a great reservoir of candidates for atmospheric characterizations with JWST (Greene et al., 2016).

The other important progress in the study of M dwarfs planetary systems will be brought by the advent of high-resolution spectrographs allowing high-precision simultaneous RV measurements in the optical and infrared ranges, such as GIARPS (Claudi et al., 2017), the combination of the HARPS-N (Cosentino et al., 2012) and GIANO (Oliva et al., 2006) spectrographs. GIARPS will open a unique possibility for simultaneous high-precision RV monitoring in over the visual and near infrared wavelength range from 0.390 μm to 2.5 μm, due to the upgrade of the GIANO-B spectrograph with an absorption cell which will allow to reach internal errors as low as 3 m s^{-1} in the NIR wing of the spectra. This will produce two main improvement in the study of M dwarfs exoplanets: 1) cool stars are usually faint at optical wavelength, thus limiting the possibility to acquire high SNR spectra, while instead much brighter in the NIR; 2) the RV signals due to stellar activity are dependent on the wavelength of observation, being due to temperature contrast between active and inactive surface regions, thus NIR RVs will be less effected by stellar noise. The latter will also produce an efficient way to discern between planetary and stellar signal: RV modulations due to orbiting planets are of course wavelength independent, thus if the amplitude of an observed periodic signals lessen going from VIS to NIR RV it is probably caused by the star chromospheric activity. Other NIR and combined VIS-NIR spectrographs are on the way, such as SPIROU (Delfosse et al., 2013) and NIRPS (F. Wildi, 2017), or already operating, such as CARMENES (Quirrenbach et al., 2014). Examples of the effectiveness of infrared RV techniques have already been shown in the literature, using non-simultaneous VIS and NIR RV observations to confirm or retract previously detected planets (González-Álvarez et al., 2017; Huélamo et al., 2008).

Bibliography

L. Affer, G. Micela, M. Damasso, M. Perger, I. Ribas, A. Suárez Mascareño, J. I. González Hernández, R. Rebolo, E. Poretti, J. Maldonado, G. Leto, I. Pagano, G. Scandariato, R. Zanmar Sanchez, A. Sozzetti, A. S. Bonomo, L. Malavolta, J. C. Morales, A. Rosich, A. Bignamini, R. Gratton, S. Velasco, D. Cenadelli, R. Claudi, R. Cosentino, S. Desidera, P. Giacobbe, E. Herrero, M. Lafarga, A. F. Lanza, E. Molinari, and G. Piotto. HADES RV program with HARPS-N at the TNG GJ 3998: An early M-dwarf hosting a system of super-Earths. *A&A*, 593:A117, October 2016. doi: 10.1051/0004-6361/201628690.

S. Aigrain, F. Pont, and S. Zucker. A simple method to estimate radial velocity variations due to stellar activity using photometry. *MNRAS*, 419:3147–3158, February 2012. doi: 10.1111/j.1365-2966.2011.19960.x.

S. Ambikasaran, D. Foreman-Mackey, L. Greengard, D. W. Hogg, and M. O'Neil. Fast Direct Methods for Gaussian Processes. *ArXiv e-prints*, March 2014.

K. R. Anderson and D. Lai. Moderately Eccentric Warm Jupiters from Secular Interactions with Exterior Companions. *ArXiv e-prints*, May 2017.

G. Anglada-Escudé and R. P. Butler. The HARPS-TERRA Project. I. Description of the Algorithms, Performance, and New Measurements on a Few Remarkable Stars Observed by HARPS. *ApJS*, 200:15, June 2012. doi: 10.1088/0067-0049/200/2/15.

G. Anglada-Escudé and M. Tuomi. Comment on "Stellar activity masquerading as planets in the habitable zone of the M dwarf Gliese 581". *Science*, 347: 1080–1080, March 2015. doi: 10.1126/science.1260796.

G. Anglada-Escudé, P. Arriagada, M. Tuomi, M. Zechmeister, J. S. Jenkins, A. Ofir, S. Dreizler, E. Gerlach, C. J. Marvin, A. Reiners, S. V. Jeffers, R. P. Butler, S. S. Vogt, P. J. Amado, C. Rodríguez-López, Z. M. Berdiñas, J. Morin, J. D. Crane, S. A. Shectman, I. B. Thompson, M. Díaz, E. Rivera, L. F. Sarmiento, and H. R. A. Jones. Two planets around Kapteyn's star: a cold and a temperate super-Earth orbiting the nearest halo red dwarf. *MNRAS*, 443:L89–L93, September 2014. doi: 10.1093/mnrasl/slu076.

G. Anglada-Escudé, P. J. Amado, J. Barnes, Z. M. Berdiñas, R. P. Butler, G. A. L. Coleman, I. de La Cueva, S. Dreizler, M. Endl, B. Giesers, S. V. Jeffers, J. S. Jenkins, H. R. A. Jones, M. Kiraga, M. Kürster, M. J. López-González, C. J. Marvin, N. Morales, J. Morin, R. P. Nelson, J. L. Ortiz,

A. Ofir, S.-J. Paardekooper, A. Reiners, E. Rodríguez, C. Rodríguez-López, L. F. Sarmiento, J. P. Strachan, Y. Tsapras, M. Tuomi, and M. Zechmeister. A terrestrial planet candidate in a temperate orbit around Proxima Centauri. *Nature*, 536:437–440, August 2016a. doi: 10.1038/nature19106.

G. Anglada-Escudé, M. Tuomi, P. Arriagada, M. Zechmeister, J. S. Jenkins, A. Ofir, S. Dreizler, E. Gerlach, C. J. Marvin, A. Reiners, S. V. Jeffers, R. P. Butler, S. S. Vogt, P. J. Amado, C. Rodríguez-López, Z. M. Berdiñas, J. Morin, J. D. Crane, S. A. Shectman, M. R. Díaz, L. F. Sarmiento, and H. R. A. Jones. No Evidence for Activity Correlations in the Radial Velocities of Kapteyn's Star. *ApJ*, 830:74, October 2016b. doi: 10.3847/0004-637X/830/2/74.

N. Astudillo-Defru, X. Bonfils, X. Delfosse, D. Ségransan, T. Forveille, F. Bouchy, M. Gillon, C. Lovis, M. Mayor, V. Neves, F. Pepe, C. Perrier, D. Queloz, P. Rojo, N. C. Santos, and S. Udry. The HARPS search for southern extra-solar planets. XXXVI. Planetary systems and stellar activity of the M dwarfs GJ 3293, GJ 3341, and GJ 3543. *A&A*, 575:A119, March 2015. doi: 10.1051/0004-6361/201424253.

N. Astudillo-Defru, T. Forveille, X. Bonfils, D. Ségransan, F. Bouchy, X. Delfosse, C. Lovis, M. Mayor, F. Murgas, F. Pepe, N. C. Santos, S. Udry, and A. Wünsche. The HARPS search for southern extra-solar planets. XLI. A dozen planets around the M dwarfs GJ 3138, GJ 3323, GJ 273, GJ 628, and GJ 3293. *A&A*, 602:A88, June 2017. doi: 10.1051/0004-6361/201630153.

S. L. Baliunas, J. H. Horne, A. Porter, D. K. Duncan, J. Frazer, H. Lanning, A. Misch, J. Mueller, R. W. Noyes, D. Soyumer, A. H. Vaughan, and L. Woodard. Time-series measurements of chromospheric CA II H and K emission in cool stars and the search for differential rotation. *ApJ*, 294:310–325, July 1985. doi: 10.1086/163299.

R. V. Baluev. The impact of red noise in radial velocity planet searches: only three planets orbiting GJ 581? *MNRAS*, 429:2052–2068, March 2013a. doi: 10.1093/mnras/sts476.

R. V. Baluev. Detecting multiple periodicities in observational data with the multifrequency periodogram—II. Frequency Decomposer, a parallelized time-series analysis algorithm. *Astronomy and Computing*, 3:50–57, November 2013b. doi: 10.1016/j.ascom.2013.11.003.

J. R. Barnes, S. V. Jeffers, and H. R. A. Jones. The effect of M dwarf starspot activity on low-mass planet detection thresholds. *MNRAS*, 412:1599–1610, April 2011a. doi: 10.1111/j.1365-2966.2010.17979.x.

J. R. Barnes, S. V. Jeffers, and H. R. A. Jones. The effect of M dwarf starspot activity on low-mass planet detection thresholds. *MNRAS*, 412:1599–1610, April 2011b. doi: 10.1111/j.1365-2966.2010.17979.x.

N. M. Batalha, J. F. Rowe, S. T. Bryson, T. Barclay, C. J. Burke, D. A. Caldwell, J. L. Christiansen, F. Mullally, S. E. Thompson, T. M. Brown, A. K. Dupree, D. C. Fabrycky, E. B. Ford, J. J. Fortney, R. L. Gilliland, H. Isaacson, D. W. Latham, G. W. Marcy, S. N. Quinn, D. Ragozzine, A. Shporer,

W. J. Borucki, D. R. Ciardi, T. N. Gautier, III, M. R. Haas, J. M. Jenkins, D. G. Koch, J. J. Lissauer, W. Rapin, G. S. Basri, A. P. Boss, L. A. Buchhave, J. A. Carter, D. Charbonneau, J. Christensen-Dalsgaard, B. D. Clarke, W. D. Cochran, B.-O. Demory, J.-M. Desert, E. Devore, L. R. Doyle, G. A. Esquerdo, M. Everett, F. Fressin, J. C. Geary, F. R. Girouard, A. Gould, J. R. Hall, M. J. Holman, A. W. Howard, S. B. Howell, K. A. Ibrahim, K. Kinemuchi, H. Kjeldsen, T. C. Klaus, J. Li, P. W. Lucas, S. Meibom, R. L. Morris, A. Prša, E. Quintana, D. T. Sanderfer, D. Sasselov, S. E. Seader, J. C. Smith, J. H. Steffen, M. Still, M. C. Stumpe, J. C. Tarter, P. Tenenbaum, G. Torres, J. D. Twicken, K. Uddin, J. Van Cleve, L. Walkowicz, and W. F. Welsh. Planetary Candidates Observed by Kepler. III. Analysis of the First 16 Months of Data. *ApJS*, 204:24, February 2013. doi: 10.1088/0067-0049/204/2/24.

S. Benatti, R. Claudi, S. Desidera, R. Gratton, A. F. Lanza, G. Micela, I. Pagano, G. Piotto, A. Sozzetti, C. Boccato, R. Cosentino, E. Covino, A. Maggio, E. Molinari, E. Poretti, R. Smareglia, and the GAPS Team. The GAPS Project: First Results. *ArXiv e-prints*, August 2017.

C. Bergfors, W. Brandner, S. Hippler, T. Henning, M. Janson, and F. Hormuth. The AstraLux Binary M Dwarfs Survey. In M. T. Richards and I. Hubeny, editors, *From Interacting Binaries to Exoplanets: Essential Modeling Tools*, volume 282 of *IAU Symposium*, pages 460–461, April 2012. doi: 10.1017/S1743921311028080.

K. Biazzo, R. Gratton, S. Desidera, S. Lucatello, A. Sozzetti, A. S. Bonomo, M. Damasso, D. Gandolfi, L. Affer, C. Boccato, F. Borsa, R. Claudi, R. Cosentino, E. Covino, C. Knapic, A. F. Lanza, J. Maldonado, F. Marzari, G. Micela, P. Molaro, I. Pagano, M. Pedani, I. Pillitteri, G. Piotto, E. Poretti, M. Rainer, N. C. Santos, G. Scandariato, and R. Zanmar Sanchez. The GAPS programme with HARPS-N at TNG. X. Differential abundances in the XO-2 planet-hosting binary. *A&A*, 583:A135, November 2015. doi: 10.1051/0004-6361/201526375.

E. Bolmont, F. Selsis, J. E. Owen, I. Ribas, S. N. Raymond, J. Leconte, and M. Gillon. Water loss from terrestrial planets orbiting ultracool dwarfs: implications for the planets of TRAPPIST-1. *MNRAS*, 464:3728–3741, January 2017. doi: 10.1093/mnras/stw2578.

I. A. Bond, A. Udalski, M. Jaroszyński, N. J. Rattenbury, B. Paczyński, I. Soszyński, L. Wyrzykowski, M. K. Szymański, M. Kubiak, O. Szewczyk, K. Żebruń, G. Pietrzyński, F. Abe, D. P. Bennett, S. Eguchi, Y. Furuta, J. B. Hearnshaw, K. Kamiya, P. M. Kilmartin, Y. Kurata, K. Masuda, Y. Matsubara, Y. Muraki, S. Noda, K. Okajima, T. Sako, T. Sekiguchi, D. J. Sullivan, T. Sumi, P. J. Tristram, T. Yanagisawa, P. C. M. Yock, and OGLE Collaboration. OGLE 2003-BLG-235/MOA 2003-BLG-53: A Planetary Microlensing Event. *ApJ*, 606:L155–L158, May 2004. doi: 10.1086/420928.

X. Bonfils, T. Forveille, X. Delfosse, S. Udry, M. Mayor, C. Perrier, F. Bouchy, F. Pepe, D. Queloz, and J.-L. Bertaux. The HARPS search for southern extra-solar planets. VI. A Neptune-mass planet around the nearby M dwarf Gl 581. *A&A*, 443:L15–L18, December 2005. doi: 10.1051/0004-6361:200500193.

X. Bonfils, M. Mayor, X. Delfosse, T. Forveille, M. Gillon, C. Perrier, S. Udry, F. Bouchy, C. Lovis, F. Pepe, D. Queloz, N. C. Santos, and J.-L. Bertaux. The HARPS search for southern extra-solar planets. X. A m sin i = 11 $M_\oplus$ planet around the nearby spotted M dwarf GJ 674. *A&A*, 474:293–299, October 2007. doi: 10.1051/0004-6361:20077068.

X. Bonfils, X. Delfosse, S. Udry, T. Forveille, M. Mayor, C. Perrier, F. Bouchy, M. Gillon, C. Lovis, F. Pepe, D. Queloz, N. C. Santos, D. Ségransan, and J.-L. Bertaux. The HARPS search for southern extra-solar planets. XXXI. The M-dwarf sample. *A&A*, 549:A109, January 2013a. doi: 10.1051/0004-6361/201014704.

X. Bonfils, G. Lo Curto, A. C. M. Correia, J. Laskar, S. Udry, X. Delfosse, T. Forveille, N. Astudillo-Defru, W. Benz, F. Bouchy, M. Gillon, G. Hébrard, C. Lovis, M. Mayor, C. Moutou, D. Naef, V. Neves, F. Pepe, C. Perrier, D. Queloz, N. C. Santos, and D. Ségransan. The HARPS search for southern extra-solar planets. XXXIV. A planetary system around the nearby M dwarf GJ 163, with a super-Earth possibly in the habitable zone. *A&A*, 556:A110, August 2013b. doi: 10.1051/0004-6361/201220237.

A. S. Bonomo, S. Desidera, S. Benatti, F. Borsa, S. Crespi, M. Damasso, A. F. Lanza, A. Sozzetti, G. Lodato, F. Marzari, C. Boccato, R. U. Claudi, R. Cosentino, E. Covino, R. Gratton, A. Maggio, G. Micela, E. Molinari, I. Pagano, G. Piotto, E. Poretti, R. Smareglia, L. Affer, K. Biazzo, A. Bignamini, M. Esposito, P. Giacobbe, G. Hébrard, L. Malavolta, J. Maldonado, L. Mancini, A. Martinez Fiorenzano, S. Masiero, V. Nascimbeni, M. Pedani, M. Rainer, and G. Scandariato. The GAPS Programme with HARPS-N at TNG . XIV. Investigating giant planet migration history via improved eccentricity and mass determination for 231 transiting planets. *A&A*, 602:A107, June 2017. doi: 10.1051/0004-6361/201629882.

W. Borucki, D. Koch, N. Batalha, D. Caldwell, J. Christensen-Dalsgaard, W. D. Cochran, E. Dunham, T. N. Gautier, J. Geary, R. Gilliland, J. Jenkins, H. Kjeldsen, J. J. Lissauer, and J. Rowe. KEPLER: Search for Earth-Size Planets in the Habitable Zone. In F. Pont, D. Sasselov, and M. J. Holman, editors, *Transiting Planets*, volume 253 of *IAU Symposium*, pages 289–299, February 2009. doi: 10.1017/S1743921308026513.

V. Bozza, L. Mancini, and A. Sozzetti. Methods of Detecting Exoplanets. *Methods of Detecting Exoplanets: 1st Advanced School on Exoplanetary Science*, 428, 2016. doi: 10.1007/978-3-319-27458-4.

G. L. Bretthorst. Generalizing the Lomb-Scargle periodogram. In A. Mohammad-Djafari, editor, *Bayesian Inference and Maximum Entropy Methods in Science and Engineering*, volume 568 of *American Institute of Physics Conference Series*, pages 241–245, May 2001. doi: 10.1063/1.1381888.

M. Brogi, R. J. de Kok, J. L. Birkby, H. Schwarz, and I. A. G. Snellen. Carbon monoxide and water vapor in the atmosphere of the non-transiting exoplanet HD 179949 b. *A&A*, 565:A124, May 2014. doi: 10.1051/0004-6361/201423537.

L. A. Buchhave, M. Bizzarro, D. W. Latham, D. Sasselov, W. D. Cochran, M. Endl, H. Isaacson, D. Juncher, and G. W. Marcy. Three regimes of extrasolar planet radius inferred from host star metallicities. *Nature*, 509: 593–595, May 2014. doi: 10.1038/nature13254.

C. J. Burke, P. R. McCullough, J. A. Valenti, C. M. Johns-Krull, K. A. Janes, J. N. Heasley, F. J. Summers, J. E. Stys, R. Bissinger, M. L. Fleenor, C. N. Foote, E. García-Melendo, B. L. Gary, P. J. Howell, F. Mallia, G. Masi, B. Taylor, and T. Vanmunster. XO-2b: Transiting Hot Jupiter in a Metal-rich Common Proper Motion Binary. *ApJ*, 671:2115–2128, December 2007. doi: 10.1086/523087.

R. P. Butler, S. S. Vogt, G. W. Marcy, D. A. Fischer, J. T. Wright, G. W. Henry, G. Laughlin, and J. J. Lissauer. A Neptune-Mass Planet Orbiting the Nearby M Dwarf GJ 436. *ApJ*, 617:580–588, December 2004. doi: 10.1086/425173.

R. P. Butler, S. S. Vogt, G. Laughlin, J. A. Burt, E. J. Rivera, M. Tuomi, J. Teske, P. Arriagada, M. Diaz, B. Holden, and S. Keiser. The LCES HIRES/Keck Precision Radial Velocity Exoplanet Survey. *AJ*, 153:208, May 2017. doi: 10.3847/1538-3881/aa66ca.

B. Campbell and G. A. H. Walker. Precision radial velocities with an absorption cell. *PASP*, 91:540–545, August 1979. doi: 10.1086/130535.

D. Charbonneau, T. M. Brown, D. W. Latham, and M. Mayor. Detection of Planetary Transits Across a Sun-like Star. *ApJ*, 529:L45–L48, January 2000. doi: 10.1086/312457.

D. Charbonneau, Z. K. Berta, J. Irwin, C. J. Burke, P. Nutzman, L. A. Buchhave, C. Lovis, X. Bonfils, D. W. Latham, S. Udry, R. A. Murray-Clay, M. J. Holman, E. E. Falco, J. N. Winn, D. Queloz, F. Pepe, M. Mayor, X. Delfosse, and T. Forveille. A super-Earth transiting a nearby low-mass star. *Nature*, 462:891–894, December 2009. doi: 10.1038/nature08679.

B. Chazelas, F. Pepe, F. Wildi, F. Bouchy, S. Perruchot, and G. Avila. New scramblers for precision radial velocity: square and octagonal fibers. In *Modern Technologies in Space- and Ground-based Telescopes and Instrumentation*, volume 7739 of *Proc. SPIE*, page 773947, July 2010. doi: 10.1117/12.856874.

S. Chib and I. Jeliazkov. Marginal likelihood from the metropolis-hastings output. *Journal of the American Statistical Association*, 96:270–281, 2001. URL `https://EconPapers.repec.org/RePEc:bes:jnlasa:v:96:y:2001:m:march:p:270-281`.

J. Christensen-Dalsgaard. Physics of solar-like oscillations. *Sol. Phys.*, 220: 137–168, April 2004. doi: 10.1023/B:SOLA.0000031392.43227.7d.

C. Clanton and B. S. Gaudi. Synthesizing Exoplanet Demographics from Radial Velocity and Microlensing Surveys. II. The Frequency of Planets Orbiting M Dwarfs. *ApJ*, 791:91, August 2014. doi: 10.1088/0004-637X/791/2/91.

C. Clanton and B. S. Gaudi. Synthesizing Exoplanet Demographics: A Single Population of Long-period Planetary Companions to M Dwarfs Consistent with Microlensing, Radial Velocity, and Direct Imaging Surveys. *ApJ*, 819: 125, March 2016. doi: 10.3847/0004-637X/819/2/125.

R. Claudi, S. Benatti, I. Carleo, A. Ghedina, J. Guerra, G. Micela, E. Molinari, E. Oliva, M. Rainer, A. Tozzi, C. Baffa, A. Baruffolo, N. Buchschacher, M. Cecconi, R. Cosentino, D. Fantinel, L. Fini, F. Ghinassi, E. Giani, E. Gonzalez, M. Gonzalez, R. Gratton, A. Harutyunyan, N. Hernandez, M. Lodi, L. Malavolta, J. Maldonado, L. Origlia, N. Sanna, J. Sanjuan, S. Scuderi, U. Seemann, A. Sozzetti, H. Perez Ventura, M. Hernandez Diaz, A. Galli, C. Gonzalez, L. Riverol, and C. Riverol. GIARPS@TNG: GIANO-B and HARPS-N together for a wider wavelength range spectroscopy. *European Physical Journal Plus*, 132:364, August 2017. doi: 10.1140/epjp/i2017-11647-9.

R. Cosentino, C. Lovis, F. Pepe, A. Collier Cameron, D. W. Latham, E. Molinari, S. Udry, N. Bezawada, M. Black, A. Born, N. Buchschacher, D. Charbonneau, P. Figueira, M. Fleury, A. Galli, A. Gallie, X. Gao, A. Ghedina, C. Gonzalez, M. Gonzalez, J. Guerra, D. Henry, K. Horne, I. Hughes, D. Kelly, M. Lodi, D. Lunney, C. Maire, M. Mayor, G. Micela, M. P. Ordway, J. Peacock, D. Phillips, G. Piotto, D. Pollacco, D. Queloz, K. Rice, C. Riverol, L. Riverol, J. San Juan, D. Sasselov, D. Segransan, A. Sozzetti, D. Sosnowska, B. Stobie, A. Szentgyorgyi, A. Vick, and L. Weber. Harps-N: the new planet hunter at TNG. In *Ground-based and Airborne Instrumentation for Astronomy IV*, volume 8446 of *Proc. SPIE*, page 84461V, September 2012. doi: 10.1117/12.925738.

E. Covino, M. Esposito, M. Barbieri, L. Mancini, V. Nascimbeni, R. Claudi, S. Desidera, R. Gratton, A. F. Lanza, A. Sozzetti, K. Biazzo, L. Affer, D. Gandolfi, U. Munari, I. Pagano, A. S. Bonomo, A. Collier Cameron, G. Hébrard, A. Maggio, S. Messina, G. Micela, E. Molinari, F. Pepe, G. Piotto, I. Ribas, N. C. Santos, J. Southworth, E. Shkolnik, A. H. M. J. Triaud, L. Bedin, S. Benatti, C. Boccato, M. Bonavita, F. Borsa, L. Borsato, D. Brown, E. Carolo, S. Ciceri, R. Cosentino, M. Damasso, F. Faedi, A. F. Martínez Fiorenzano, D. W. Latham, C. Lovis, C. Mordasini, N. Nikolov, E. Poretti, M. Rainer, R. Rebolo López, G. Scandariato, R. Silvotti, R. Smareglia, J. M. Alcalá, A. Cunial, L. Di Fabrizio, M. P. Di Mauro, P. Giacobbe, V. Granata, A. Harutyunyan, C. Knapic, M. Lattanzi, G. Leto, G. Lodato, L. Malavolta, F. Marzari, M. Molinaro, D. Nardiello, M. Pedani, L. Prisinzano, and D. Turrini. The GAPS programme with HARPS-N at TNG. I. Observations of the Rossiter-McLaughlin effect and characterisation of the transiting system Qatar-1. *A&A*, 554:A28, June 2013. doi: 10.1051/0004-6361/201321298.

A. Cumming. Detectability of extrasolar planets in radial velocity surveys. *MNRAS*, 354:1165–1176, November 2004. doi: 10.1111/j.1365-2966.2004.08275.x.

A. Cumming, G. W. Marcy, and R. P. Butler. The Lick Planet Search: Detectability and Mass Thresholds. *ApJ*, 526:890–915, December 1999. doi: 10.1086/308020.

A. Cumming, R. P. Butler, G. W. Marcy, S. S. Vogt, J. T. Wright, and D. A. Fischer. The Keck Planet Search: Detectability and the Minimum Mass and Orbital Period Distribution of Extrasolar Planets. *PASP*, 120:531, May 2008. doi: 10.1086/588487.

R. M. Cutri, M. F. Skrutskie, S. van Dyk, C. A. Beichman, J. M. Carpenter, T. Chester, L. Cambresy, T. Evans, J. Fowler, J. Gizis, E. Howard, J. Huchra, T. Jarrett, E. L. Kopan, J. D. Kirkpatrick, R. M. Light, K. A. Marsh, H. McCallon, S. Schneider, R. Stiening, M. Sykes, M. Weinberg, W. A. Wheaton, S. Wheelock, and N. Zacarias. VizieR Online Data Catalog: 2MASS All-Sky Catalog of Point Sources (Cutri+ 2003). *VizieR Online Data Catalog*, 2246, June 2003.

T. H. Dall, N. C. Santos, T. Arentoft, T. R. Bedding, and H. Kjeldsen. Bisectors of the cross-correlation function applied to stellar spectra. Discriminating stellar activity, oscillations and planets. *A&A*, 454:341–348, July 2006. doi: 10.1051/0004-6361:20065021.

M. Damasso, K. Biazzo, A. S. Bonomo, S. Desidera, A. F. Lanza, V. Nascimbeni, M. Esposito, G. Scandariato, A. Sozzetti, R. Cosentino, R. Gratton, L. Malavolta, M. Rainer, D. Gandolfi, E. Poretti, R. Zanmar Sanchez, I. Ribas, N. Santos, L. Affer, G. Andreuzzi, M. Barbieri, L. R. Bedin, S. Benatti, A. Bernagozzi, E. Bertolini, M. Bonavita, F. Borsa, L. Borsato, W. Boschin, P. Calcidese, A. Carbognani, D. Cenadelli, J. M. Christille, R. U. Claudi, E. Covino, A. Cunial, P. Giacobbe, V. Granata, A. Harutyunyan, M. G. Lattanzi, G. Leto, M. Libralato, G. Lodato, V. Lorenzi, L. Mancini, A. F. Martinez Fiorenzano, F. Marzari, S. Masiero, G. Micela, E. Molinari, M. Molinaro, U. Munari, S. Murabito, I. Pagano, M. Pedani, G. Piotto, A. Rosenberg, R. Silvotti, and J. Southworth. The GAPS programme with HARPS-N at TNG. V. A comprehensive analysis of the XO-2 stellar and planetary systems. *A&A*, 575:A111, March 2015. doi: 10.1051/0004-6361/201425332.

H. Dekker, S. D'Odorico, A. Kaufer, B. Delabre, and H. Kotzlowski. Design, construction, and performance of UVES, the echelle spectrograph for the UT2 Kueyen Telescope at the ESO Paranal Observatory. In M. Iye and A. F. Moorwood, editors, *Optical and IR Telescope Instrumentation and Detectors*, volume 4008 of *Proc. SPIE*, pages 534–545, August 2000. doi: 10.1117/12.395512.

X. Delfosse, T. Forveille, M. Mayor, C. Perrier, D. Naef, and D. Queloz. The closest extrasolar planet. A giant planet around the M4 dwarf GL 876. *A&A*, 338:L67–L70, October 1998.

X. Delfosse, T. Forveille, J.-L. Beuzit, S. Udry, M. Mayor, and C. Perrier. New neighbours. I. 13 new companions to nearby M dwarfs. *A&A*, 344:897–910, April 1999.

X. Delfosse, J.-F. Donati, D. Kouach, G. Hébrard, R. Doyon, E. Artigau, F. Bouchy, I. Boisse, A. S. Brun, P. Hennebelle, T. Widemann, J. Bouvier, X. Bonfils, J. Morin, C. Moutou, F. Pepe, S. Udry, J.-D. do Nascimento, S. H. P. Alencar, B. V. Castilho, E. Martioli, S. Y. Wang, P. Figueira, and N. C. Santos. World-leading science with SPIRou - The nIR spectropolarimeter / high-precision velocimeter for CFHT. In L. Cambresy, F. Martins, E. Nuss, and A. Palacios, editors, *SF2A-2013: Proceedings of the Annual meeting of the French Society of Astronomy and Astrophysics*, pages 497–508, November 2013.

S. Desidera and M. Barbieri. Properties of planets in binary systems. The role of binary separation. *A&A*, 462:345–353, January 2007. doi: 10.1051/0004-6361:20066319.

S. Desidera, A. Sozzetti, A. S. Bonomo, R. Gratton, E. Poretti, R. Claudi, D. W. Latham, L. Affer, R. Cosentino, M. Damasso, M. Esposito, P. Giacobbe, L. Malavolta, V. Nascimbeni, G. Piotto, M. Rainer, M. Scardia, V. S. Schmid, A. F. Lanza, G. Micela, I. Pagano, L. R. Bedin, K. Biazzo, F. Borsa, E. Carolo, E. Covino, F. Faedi, G. Hébrard, C. Lovis, A. Maggio, L. Mancini, F. Marzari, S. Messina, E. Molinari, U. Munari, F. Pepe, N. Santos, G. Scandariato, E. Shkolnik, and J. Southworth. The GAPS programme with HARPS-N at TNG. II. No giant planets around the metal-poor star HIP 11952. *A&A*, 554:A29, June 2013. doi: 10.1051/0004-6361/201321155.

S. Desidera, A. S. Bonomo, R. U. Claudi, M. Damasso, K. Biazzo, A. Sozzetti, F. Marzari, S. Benatti, D. Gandolfi, R. Gratton, A. F. Lanza, V. Nascimbeni, G. Andreuzzi, L. Affer, M. Barbieri, L. R. Bedin, A. Bignamini, M. Bonavita, F. Borsa, P. Calcidese, J. M. Christille, R. Cosentino, E. Covino, M. Esposito, P. Giacobbe, A. Harutyunyan, D. Latham, M. Lattanzi, G. Leto, G. Lodato, C. Lovis, A. Maggio, L. Malavolta, L. Mancini, A. F. Martinez Fiorenzano, G. Micela, E. Molinari, C. Mordasini, U. Munari, I. Pagano, M. Pedani, F. Pepe, G. Piotto, E. Poretti, M. Rainer, I. Ribas, N. C. Santos, G. Scandariato, R. Silvotti, J. Southworth, and R. Zanmar Sanchez. The GAPS programme with HARPS-N at TNG. IV. A planetary system around XO-2S. *A&A*, 567:L6, July 2014. doi: 10.1051/0004-6361/201424339.

J. A. Dittmann, J. M. Irwin, D. Charbonneau, X. Bonfils, N. Astudillo-Defru, R. D. Haywood, Z. K. Berta-Thompson, E. R. Newton, J. E. Rodriguez, J. G. Winters, T.-G. Tan, J.-M. Almenara, F. Bouchy, X. Delfosse, T. Forveille, C. Lovis, F. Murgas, F. Pepe, N. C. Santos, S. Udry, A. Wünsche, G. A. Esquerdo, D. W. Latham, and C. D. Dressing. A temperate rocky super-Earth transiting a nearby cool star. *Nature*, 544:333–336, April 2017. doi: 10.1038/nature22055.

D. Dravins, L. Lindegren, and S. Madsen. Astrometric radial velocities. I. Non-spectroscopic methods for measuring stellar radial velocity. *A&A*, 348:1040–1051, August 1999.

C. D. Dressing and D. Charbonneau. The Occurrence Rate of Small Planets around Small Stars. *ApJ*, 767:95, April 2013. doi: 10.1088/0004-637X/767/1/95.

C. D. Dressing and D. Charbonneau. The Occurrence of Potentially Habitable Planets Orbiting M Dwarfs Estimated from the Full Kepler Dataset and an Empirical Measurement of the Detection Sensitivity. *ApJ*, 807:45, July 2015. doi: 10.1088/0004-637X/807/1/45.

G. Duchêne and A. Kraus. Stellar Multiplicity. *ARA&A*, 51:269–310, August 2013. doi: 10.1146/annurev-astro-081710-102602.

X. Dumusque. Radial velocity fitting challenge. I. Simulating the data set including realistic stellar radial-velocity signals. *A&A*, 593:A5, August 2016. doi: 10.1051/0004-6361/201628672.

X. Dumusque, C. Lovis, S. Udry, and N. C. Santos. Stellar noise and planet detection. II. Radial-velocity noise induced by magnetic cycles. In A. Sozzetti, M. G. Lattanzi, and A. P. Boss, editors, *The Astrophysics of Planetary Systems: Formation, Structure, and Dynamical Evolution*, volume 276 of *IAU Symposium*, pages 530–532, November 2011a. doi: 10.1017/S1743921311021090.

X. Dumusque, S. Udry, C. Lovis, N. C. Santos, and M. J. P. F. G. Monteiro. Planetary detection limits taking into account stellar noise. I. Observational strategies to reduce stellar oscillation and granulation effects. *A&A*, 525:A140, January 2011b. doi: 10.1051/0004-6361/201014097.

X. Dumusque, I. Boisse, and N. C. Santos. SOAP 2.0: A Tool to Estimate the Photometric and Radial Velocity Variations Induced by Stellar Spots and Plages. *ApJ*, 796:132, December 2014. doi: 10.1088/0004-637X/796/2/132.

X. Dumusque, F. Borsa, M. Damasso, R. F. Díaz, P. C. Gregory, N. C. Hara, A. Hatzes, V. Rajpaul, M. Tuomi, S. Aigrain, G. Anglada-Escudé, A. S. Bonomo, G. Boué, F. Dauvergne, G. Frustagli, P. Giacobbe, R. D. Haywood, H. R. A. Jones, J. Laskar, M. Pinamonti, E. Poretti, M. Rainer, D. Ségransan, A. Sozzetti, and S. Udry. Radial-velocity fitting challenge. II. First results of the analysis of the data set. *A&A*, 598:A133, February 2017. doi: 10.1051/0004-6361/201628671.

A. Duquennoy and M. Mayor. Multiplicity among solar-type stars in the solar neighbourhood. II - Distribution of the orbital elements in an unbiased sample. *A&A*, 248:485–524, August 1991.

R. Dvorak. Planetary orbits in double star systems. *Oesterreichische Akademie Wissenschaften Mathematisch naturwissenschaftliche Klasse Sitzungsberichte Abteilung*, 191:423–437, 1982.

F. W. Dyson, A. S. Eddington, and C. Davidson. A Determination of the Deflection of Light by the Sun's Gravitational Field, from Observations Made at the Total Eclipse of May 29, 1919. *Philosophical Transactions of the Royal Society of London Series A*, 220:291–333, 1920. doi: 10.1098/rsta.1920.0009.

J. Eastman, B. S. Gaudi, and E. Agol. EXOFAST: A Fast Exoplanetary Fitting Suite in IDL. *PASP*, 125:83, January 2013. doi: 10.1086/669497.

J. A. Eaton, G. W. Henry, and F. C. Fekel. Advantages of Automated Observing with Small Telescopes. In T. D. Oswalt, editor, *Astrophysics and Space Science Library*, volume 288 of *Astrophysics and Space Science Library*, page 189, June 2003. doi: 10.1007/978-94-010-0253-0_38.

A. Eggenberger. Detection and Characterization of Planets in Binary and Multiple Systems. In K. Goździewski, A. Niedzielski, and J. Schneider, editors, *EAS Publications Series*, volume 42 of *EAS Publications Series*, pages 19–37, April 2010. doi: 10.1051/eas/1042002.

J. A. Eisner and S. R. Kulkarni. Sensitivity of the Radial-Velocity Technique in Detecting Outer Planets. *ApJ*, 550:871–883, April 2001. doi: 10.1086/319801.

M. Endl, M. Kürster, S. Els, A. P. Hatzes, and W. D. Cochran. The planet search program at the ESO Coudé Echelle spectrometer. II. The alpha Centauri system: Limits for planetary companions. *A&A*, 374:675–681, August 2001. doi: 10.1051/0004-6361:20010723.

M. Endl, M. Kürster, S. Els, A. P. Hatzes, W. D. Cochran, K. Dennerl, and S. Döbereiner. The planet search program at the ESO Coudé Echelle spectrometer. III. The complete Long Camera survey results. *A&A*, 392:671–690, September 2002. doi: 10.1051/0004-6361:20020937.

M. Endl, W. D. Cochran, M. Kürster, D. B. Paulson, R. A. Wittenmyer, P. J. MacQueen, and R. G. Tull. Exploring the Frequency of Close-in Jovian Planets around M Dwarfs. *ApJ*, 649:436–443, September 2006. doi: 10.1086/506465.

ESA, editor. *The HIPPARCOS and TYCHO catalogues. Astrometric and photometric star catalogues derived from the ESA HIPPARCOS Space Astrometry Mission*, volume 1200 of *ESA Special Publication*, 1997.

V. Reshetov O. Hernandez L. Genolet U. Conod M. Sordet A. Segovilla J. L. Rasilla D. Brousseau S. Thibault B. Delabre T. Bandy M. Sarajlic A. Cabral S. Bovay Ph. Vallée F. Bouchy R. Doyon E. Artigau F. Pepe J. Hagelberg C. Melo X. Delfosse P. Figueira N. C. Santos J. I. González Hernández J. R. de Medeiros R. Rebolo Ch. Broeg W. Benz I. Boisse L. Malo U. Käufl L. Saddlemyer F. Wildi, N. Blind. Nirps: an adaptive-optics assisted radial velocity spectrograph to chase exoplanets around m-stars. volume 10400, pages 10400 – 10400 – 15, 2017. doi: 10.1117/12.2275660. URL `http://dx.doi.org/10.1117/12.2275660`.

D. C. Fabrycky, J. J. Lissauer, D. Ragozzine, J. F. Rowe, J. H. Steffen, E. Agol, T. Barclay, N. Batalha, W. Borucki, D. R. Ciardi, E. B. Ford, T. N. Gautier, J. C. Geary, M. J. Holman, J. M. Jenkins, J. Li, R. C. Morehead, R. L. Morris, A. Shporer, J. C. Smith, M. Still, and J. Van Cleve. Architecture of Kepler's Multi-transiting Systems. II. New Investigations with Twice as Many Candidates. *ApJ*, 790:146, August 2014. doi: 10.1088/0004-637X/790/2/146.

J. P. Faria, N. C. Santos, P. Figueira, A. Mortier, X. Dumusque, I. Boisse, G. Lo Curto, C. Lovis, M. Mayor, C. Melo, F. Pepe, D. Queloz, A. Santerne, D. Ségransan, S. G. Sousa, A. Sozzetti, and S. Udry. The HARPS search for southern extra-solar planets. XL. Searching for Neptunes around metal-poor stars. *A&A*, 589:A25, May 2016. doi: 10.1051/0004-6361/201527522.

F. Feng, M. Tuomi, H. R. A. Jones, J. Barnes, G. Anglada-Escudé, S. S. Vogt, and R. P. Butler. Color Difference Makes a Difference: Four Planet Candidates around τ Ceti. *AJ*, 154:135, October 2017. doi: 10.3847/1538-3881/aa83b4.

A. Fienga, J. Laskar, T. Morley, H. Manche, P. Kuchynka, C. Le Poncin-Lafitte, F. Budnik, M. Gastineau, and L. Somenzi. INPOP08, a 4-D planetary ephemeris: from asteroid and time-scale computations to ESA Mars Express and Venus Express contributions. *A&A*, 507:1675–1686, December 2009. doi: 10.1051/0004-6361/200911755.

E. B. Ford. Improving the Efficiency of Markov Chain Monte Carlo for Analyzing the Orbits of Extrasolar Planets. *ApJ*, 642:505–522, May 2006. doi: 10.1086/500802.

D. Foreman-Mackey, D. W. Hogg, D. Lang, and J. Goodman. emcee: The MCMC Hammer. *PASP*, 125:306–312, March 2013. doi: 10.1086/670067.

T. Forveille, X. Bonfils, X. Delfosse, M. Gillon, S. Udry, F. Bouchy, C. Lovis, M. Mayor, F. Pepe, C. Perrier, D. Queloz, N. Santos, and J.-L. Bertaux. The HARPS search for southern extra-solar planets. XIV. Gl 176b, a super-Earth rather than a Neptune, and at a different period. *A&A*, 493:645–650, January 2009. doi: 10.1051/0004-6361:200810557.

F. Fressin, G. Torres, D. Charbonneau, S. T. Bryson, J. Christiansen, C. D. Dressing, J. M. Jenkins, L. M. Walkowicz, and N. M. Batalha. The False Positive Rate of Kepler and the Occurrence of Planets. *ApJ*, 766:81, April 2013. doi: 10.1088/0004-637X/766/2/81.

Gaia Collaboration, T. Prusti, J. H. J. de Bruijne, A. G. A. Brown, A. Vallenari, C. Babusiaux, C. A. L. Bailer-Jones, U. Bastian, M. Biermann, D. W. Evans, and et al. The Gaia mission. *A&A*, 595:A1, November 2016. doi: 10.1051/0004-6361/201629272.

E. Gaidos and A. W. Mann. M Dwarf Metallicities and Giant Planet Occurrence: Ironing Out Uncertainties and Systematics. *ApJ*, 791:54, August 2014. doi: 10.1088/0004-637X/791/1/54.

E. Gaidos, A. W. Mann, A. L. Kraus, and M. Ireland. They are small worlds after all: revised properties of Kepler M dwarf stars and their planets. *MNRAS*, 457:2877–2899, April 2016. doi: 10.1093/mnras/stw097.

F. Galland, A.-M. Lagrange, S. Udry, A. Chelli, F. Pepe, D. Queloz, J.-L. Beuzit, and M. Mayor. Extrasolar planets and brown dwarfs around A-F type stars. I. Performances of radial velocity measurements, first analyses of variations. *A&A*, 443:337–345, November 2005. doi: 10.1051/0004-6361:20052938.

M. Gillon, L. Affer, A. Bonomo, M. Damasso, S. Desidera, G. Micela, R. Rebolo, I. Ribas, and A. Sozzetti. Search for the transit of a nearby 2 Earth-mass planet. Spitzer Proposal, August 2016.

M. Gillon, A. H. M. J. Triaud, B.-O. Demory, E. Jehin, E. Agol, K. M. Deck, S. M. Lederer, J. de Wit, A. Burdanov, J. G. Ingalls, E. Bolmont, J. Leconte, S. N. Raymond, F. Selsis, M. Turbet, K. Barkaoui, A. Burgasser, M. R. Burleigh, S. J. Carey, A. Chaushev, C. M. Copperwheat, L. Delrez, C. S. Fernandes, D. L. Holdsworth, E. J. Kotze, V. Van Grootel, Y. Almleaky, Z. Benkhaldoun, P. Magain, and D. Queloz. Seven temperate terrestrial planets around the nearby ultracool dwarf star TRAPPIST-1. *Nature*, 542:456–460, February 2017. doi: 10.1038/nature21360.

C. A. Giuppone, M. H. M. Morais, and A. C. M. Correia. A semi-empirical stability criterion for real planetary systems with eccentric orbits. *MNRAS*, 436:3547–3556, December 2013. doi: 10.1093/mnras/stt1831.

J. Gomes da Silva, N. C. Santos, X. Bonfils, X. Delfosse, T. Forveille, and S. Udry. Long-term magnetic activity of a sample of M-dwarf stars from the HARPS program. I. Comparison of activity indices. *A&A*, 534:A30, October 2011. doi: 10.1051/0004-6361/201116971.

E. González-Álvarez, L. Affer, G. Micela, J. Maldonado, I. Carleo, M. Damasso, V. D'Orazi, A. F. Lanza, K. Biazzo, E. Poretti, R. Gratton, A. Sozzetti, S. Desidera, N. Sanna, A. Harutyunyan, F. Massi, E. Oliva, R. Claudi, R. Cosentino, E. Covino, A. Maggio, S. Masiero, E. Molinari, I. Pagano, G. Piotto, R. Smareglia, S. Benatti, A. S. Bonomo, F. Borsa, M. Esposito, P. Giacobbe, L. Malavolta, A. Martinez-Fiorenzano, V. Nascimbeni, M. Pedani, M. Rainer, and G. Scandariato. The GAPS Programme with HARPS-N at TNG. XV. A substellar companion around a K giant star identified with quasi-simultaneous HARPS-N and GIANO measurements. *A&A*, 606:A51, October 2017. doi: 10.1051/0004-6361/201731124.

A. Gould, S. Dong, B. S. Gaudi, A. Udalski, I. A. Bond, J. Greenhill, R. A. Street, M. Dominik, T. Sumi, M. K. Szymański, C. Han, W. Allen, G. Bolt, M. Bos, G. W. Christie, D. L. DePoy, J. Drummond, J. D. Eastman, A. Gal-Yam, D. Higgins, J. Janczak, S. Kaspi, S. Kozłowski, C.-U. Lee, F. Mallia, A. Maury, D. Maoz, J. McCormick, L. A. G. Monard, D. Moorhouse, N. Morgan, T. Natusch, E. O. Ofek, B.-G. Park, R. W. Pogge, D. Polishook, R. Santallo, A. Shporer, O. Spector, G. Thornley, J. C. Yee, μFUN Collaboration, M. Kubiak, G. Pietrzyński, I. Soszyński, O. Szewczyk, Ł. Wyrzykowski, K. Ulaczyk, R. Poleski, OGLE Collaboration, F. Abe, D. P. Bennett, C. S. Botzler, D. Douchin, M. Freeman, A. Fukui, K. Furusawa, J. B. Hearnshaw, S. Hosaka, Y. Itow, K. Kamiya, P. M. Kilmartin, A. Korpela, W. Lin, C. H. Ling, S. Makita, K. Masuda, Y. Matsubara, N. Miyake, Y. Muraki, M. Nagaya, K. Nishimoto, K. Ohnishi, T. Okumura, Y. C. Perrott, L. Philpott, N. Rattenbury, T. Saito, T. Sako, D. J. Sullivan, W. L. Sweatman, P. J. Tristram, E. von Seggern, P. C. M. Yock, MOA Collaboration, M. Albrow, V. Batista, J. P. Beaulieu, S. Brillant, J. Caldwell, J. J. Calitz, A. Cassan, A. Cole, K. Cook, C. Coutures, S. Dieters, D. Dominis Prester, J. Donatowicz, P. Fouqué, K. Hill, M. Hoffman, F. Jablonski, S. R. Kane, N. Kains, D. Kubas, J.-B. Marquette, R. Martin, E. Martioli, P. Meintjes, J. Menzies, E. Pedretti, K. Pollard, K. C. Sahu, C. Vinter, J. Wambsganss, R. Watson, A. Williams, M. Zub, PLANET Collaboration, A. Allan, M. F. Bode, D. M. Bramich, M. J. Burgdorf, N. Clay, S. Fraser, E. Hawkins, K. Horne, E. Kerins, T. A. Lister, C. Mottram, E. S. Saunders, C. Snodgrass, I. A. Steele, Y. Tsapras, RoboNet Collaboration, U. G. Jørgensen, T. Anguita, V. Bozza, S. Calchi Novati, K. Harpsøe, T. C. Hinse, M. Hundertmark, P. Kjærgaard, C. Liebig, L. Mancini, G. Masi, M. Mathiasen, S. Rahvar, D. Ricci, G. Scarpetta, J. Southworth, J. Surdej, C. C. Thöne, and MiNDSTEp Consortium. Frequency of Solar-like Systems and of Ice and Gas Giants Beyond the Snow Line from High-magnification Microlensing Events in 2005-2008. *ApJ*, 720: 1073–1089, September 2010. doi: 10.1088/0004-637X/720/2/1073.

D. F. Gray and K. I. T. Brown. Precise Spectroscopic Radial Velocity Measurements Using Telluric Lines. *PASP*, 118:399–404, March 2006. doi: 10.1086/499928.

T. P. Greene, M. R. Line, C. Montero, J. J. Fortney, J. Lustig-Yaeger, and K. Luther. Characterizing Transiting Exoplanet Atmospheres with JWST. *ApJ*, 817:17, January 2016. doi: 10.3847/0004-637X/817/1/17.

P. Gregory. *Bayesian Logical Data Analysis for the Physical Sciences.* May 2010.

P. C. Gregory. Bayesian re-analysis of the Gliese 581 exoplanet system. *MNRAS*, 415:2523–2545, August 2011. doi: 10.1111/j.1365-2966.2011.18877.x.

J.-M. Grießmeier, A. Stadelmann, J. L. Grenfell, H. Lammer, and U. Motschmann. On the protection of extrasolar Earth-like planets around K/M stars against galactic cosmic rays. *Icarus*, 199:526–535, February 2009. doi: 10.1016/j.icarus.2008.09.015.

R. Griffin and R. Griffin. Accurate wavelengths of stellar and telluric absorption lines near lambda 7000 Angstroms. *MNRAS*, 162:255, 1973. doi: 10.1093/mnras/162.3.255.

Heikki Haario, Eero Saksman, and Johanna Tamminen. An adaptive metropolis algorithm. *Bernoulli*, 7(2):223–242, 04 2001. URL `https://projecteuclid.org:443/euclid.bj/1080222083`.

E. Han, S. X. Wang, J. T. Wright, Y. K. Feng, M. Zhao, O. Fakhouri, J. I. Brown, and C. Hancock. Exoplanet Orbit Database. II. Updates to Exoplanets.org. *PASP*, 126:827, September 2014. doi: 10.1086/678447.

N. C. Hara, G. Boué, J. Laskar, and A. C. M. Correia. Radial velocity data analysis with compressed sensing techniques. *MNRAS*, 464:1220–1246, January 2017. doi: 10.1093/mnras/stw2261.

J. D. Hartman, D. Bayliss, R. Brahm, G. Á. Bakos, L. Mancini, A. Jordán, K. Penev, M. Rabus, G. Zhou, R. P. Butler, N. Espinoza, M. de Val-Borro, W. Bhatti, Z. Csubry, S. Ciceri, T. Henning, B. Schmidt, P. Arriagada, S. Shectman, J. Crane, I. Thompson, V. Suc, B. Csák, T. G. Tan, R. W. Noyes, J. Lázár, I. Papp, and P. Sári. HATS-6b: A Warm Saturn Transiting an Early M Dwarf Star, and a Set of Empirical Relations for Characterizing K and M Dwarf Planet Hosts. *AJ*, 149:166, May 2015. doi: 10.1088/0004-6256/149/5/166.

A. P. Hatzes. Starspots and exoplanets. *Astronomische Nachrichten*, 323:392–394, July 2002. doi: 10.1002/1521-3994(200208)323:3/4⟨392::AID-ASNA392⟩3.0.CO;2-M.

A. P. Hatzes. An investigation into the radial velocity variability of GJ 581: On the significance of GJ 581g. *Astronomische Nachrichten*, 334:616, August 2013. doi: 10.1002/asna.201311913.

H. M. Hauser and G. W. Marcy. The Orbit of 16 Cygni AB. *PASP*, 111:321–334, March 1999. doi: 10.1086/316328.

T. J. Henry and D. W. McCarthy, Jr. The mass-luminosity relation for stars of mass 1.0 to 0.08 solar mass. *AJ*, 106:773–789, August 1993. doi: 10.1086/116685.

T. J. Henry, W.-C. Jao, J. P. Subasavage, T. D. Beaulieu, P. A. Ianna, E. Costa, and R. A. Méndez. The Solar Neighborhood. XVII. Parallax Results from the CTIOPI 0.9 m Program: 20 New Members of the RECONS 10 Parsec Sample. *AJ*, 132:2360–2371, December 2006. doi: 10.1086/508233.

E. Høg, C. Fabricius, V. V. Makarov, S. Urban, T. Corbin, G. Wycoff, U. Bastian, P. Schwekendiek, and A. Wicenec. The Tycho-2 catalogue of the 2.5 million brightest stars. *A&A*, 355:L27–L30, March 2000.

K. Horne. An optimal extraction algorithm for CCD spectroscopy. *PASP*, 98: 609–617, June 1986. doi: 10.1086/131801.

A. W. Howard. Observed Properties of Extrasolar Planets. *Science*, 340:572–576, May 2013. doi: 10.1126/science.1233545.

A. W. Howard, G. W. Marcy, S. T. Bryson, J. M. Jenkins, J. F. Rowe, N. M. Batalha, W. J. Borucki, D. G. Koch, E. W. Dunham, T. N. Gautier, III, J. Van Cleve, W. D. Cochran, D. W. Latham, J. J. Lissauer, G. Torres, T. M. Brown, R. L. Gilliland, L. A. Buchhave, D. A. Caldwell, J. Christensen-Dalsgaard, D. Ciardi, F. Fressin, M. R. Haas, S. B. Howell, H. Kjeldsen, S. Seager, L. Rogers, D. D. Sasselov, J. H. Steffen, G. S. Basri, D. Charbonneau, J. Christiansen, B. Clarke, A. Dupree, D. C. Fabrycky, D. A. Fischer, E. B. Ford, J. J. Fortney, J. Tarter, F. R. Girouard, M. J. Holman, J. A. Johnson, T. C. Klaus, P. Machalek, A. V. Moorhead, R. C. Morehead, D. Ragozzine, P. Tenenbaum, J. D. Twicken, S. N. Quinn, H. Isaacson, A. Shporer, P. W. Lucas, L. M. Walkowicz, W. F. Welsh, A. Boss, E. Devore, A. Gould, J. C. Smith, R. L. Morris, A. Prsa, T. D. Morton, M. Still, S. E. Thompson, F. Mullally, M. Endl, and P. J. MacQueen. Planet Occurrence within 0.25 AU of Solar-type Stars from Kepler. *ApJS*, 201:15, August 2012. doi: 10.1088/0067-0049/201/2/15.

A. W. Howard, G. W. Marcy, D. A. Fischer, H. Isaacson, P. S. Muirhead, G. W. Henry, T. S. Boyajian, K. von Braun, J. C. Becker, J. T. Wright, and J. A. Johnson. The NASA-UC-UH ETA-Earth Program. IV. A Low-mass Planet Orbiting an M Dwarf 3.6 PC from Earth. *ApJ*, 794:51, October 2014. doi: 10.1088/0004-637X/794/1/51.

S. B. Howell, C. Sobeck, M. Haas, M. Still, T. Barclay, F. Mullally, J. Troeltzsch, S. Aigrain, S. T. Bryson, D. Caldwell, W. J. Chaplin, W. D. Cochran, D. Huber, G. W. Marcy, A. Miglio, J. R. Najita, M. Smith, J. D. Twicken, and J. J. Fortney. The K2 Mission: Characterization and Early Results. *PASP*, 126:398, April 2014. doi: 10.1086/676406.

N. Huélamo, P. Figueira, X. Bonfils, N. C. Santos, F. Pepe, M. Gillon, R. Azevedo, T. Barman, M. Fernández, E. di Folco, E. W. Guenther, C. Lovis, C. H. F. Melo, D. Queloz, and S. Udry. TW Hydrae: evidence of stellar spots instead of a Hot Jupiter. *A&A*, 489:L9–L13, October 2008. doi: 10.1051/0004-6361:200810596.

J. M. Jenkins, J. D. Twicken, N. M. Batalha, D. A. Caldwell, W. D. Cochran, M. Endl, D. W. Latham, G. A. Esquerdo, S. Seader, A. Bieryla, E. Petigura, D. R. Ciardi, G. W. Marcy, H. Isaacson, D. Huber, J. F. Rowe, G. Torres, S. T. Bryson, L. Buchhave, I. Ramirez, A. Wolfgang, J. Li, J. R. Campbell,

P. Tenenbaum, D. Sanderfer, C. E. Henze, J. H. Catanzarite, R. L. Gilliland, and W. J. Borucki. Discovery and Validation of Kepler-452b: A 1.6 R $_\oplus$ Super Earth Exoplanet in the Habitable Zone of a G2 Star. *AJ*, 150:56, August 2015. doi: 10.1088/0004-6256/150/2/56.

J. S. Jenkins, L. W. Ramsey, H. R. A. Jones, Y. Pavlenko, J. Gallardo, J. R. Barnes, and D. J. Pinfield. Rotational Velocities for M Dwarfs. *ApJ*, 704: 975–988, October 2009. doi: 10.1088/0004-637X/704/2/975.

S. R. Kane and D. M. Gelino. On the Inclination and Habitability of the HD 10180 System. *ApJ*, 792:111, September 2014. doi: 10.1088/0004-637X/792/2/111.

J. F. Kasting, D. P. Whitmire, and R. T. Reynolds. Habitable Zones around Main Sequence Stars. *Icarus*, 101:108–128, January 1993. doi: 10.1006/icar.1993.1010.

D. M. Kipping. Parametrizing the exoplanet eccentricity distribution with the Beta distribution. *MNRAS*, 434:L51–L55, July 2013. doi: 10.1093/mnrasl/slt075.

D. M. Kipping, J. Hartman, G. Á. Bakos, G. Torres, D. W. Latham, D. Bayliss, L. L. Kiss, B. Sato, B. Béky, G. Kovács, S. N. Quinn, L. A. Buchhave, J. Andersen, G. W. Marcy, A. W. Howard, D. A. Fischer, J. A. Johnson, R. W. Noyes, D. D. Sasselov, R. P. Stefanik, J. Lázár, I. Papp, P. Sári, and G. Fűrész. HAT-P-31b,c: A Transiting, Eccentric, Hot Jupiter and a Long-period, Massive Third Body. *AJ*, 142:95, September 2011. doi: 10.1088/0004-6256/142/3/95.

M. Konacki, G. Torres, S. Jha, and D. D. Sasselov. An extrasolar planet that transits the disk of its parent star. *Nature*, 421:507–509, January 2003. doi: 10.1038/nature01379.

A. S. Konopliv, C. F. Yoder, E. M. Standish, D.-N. Yuan, and W. L. Sjogren. A global solution for the Mars static and seasonal gravity, Mars orientation, Phobos and Deimos masses, and Mars ephemeris. *Icarus*, 182:23–50, May 2006. doi: 10.1016/j.icarus.2005.12.025.

R. K. Kopparapu. A Revised Estimate of the Occurrence Rate of Terrestrial Planets in the Habitable Zones around Kepler M-dwarfs. *ApJ*, 767:L8, April 2013. doi: 10.1088/2041-8205/767/1/L8.

R. K. Kopparapu, R. Ramirez, J. F. Kasting, V. Eymet, T. D. Robinson, S. Mahadevan, R. C. Terrien, S. Domagal-Goldman, V. Meadows, and R. Deshpande. Habitable Zones around Main-sequence Stars: New Estimates. *ApJ*, 765:131, March 2013a. doi: 10.1088/0004-637X/765/2/131.

R. K. Kopparapu, R. Ramirez, J. F. Kasting, V. Eymet, T. D. Robinson, S. Mahadevan, R. C. Terrien, S. Domagal-Goldman, V. Meadows, and R. Deshpande. Erratum: "Habitable Zones around Main-sequence Stars: New Estimates" ¡A href="/abs/2013ApJ...765..131K"¿(2013, ApJ, 765, 131)¡/A¿. *ApJ*, 770:82, June 2013b. doi: 10.1088/0004-637X/770/1/82.

R. k. Kopparapu, E. T. Wolf, J. Haqq-Misra, J. Yang, J. F. Kasting, V. Meadows, R. Terrien, and S. Mahadevan. The Inner Edge of the Habitable Zone for Synchronously Rotating Planets around Low-mass Stars Using General Circulation Models. *ApJ*, 819:84, March 2016. doi: 10.3847/0004-637X/819/1/84.

R. k. Kopparapu, E. T. Wolf, G. Arney, N. E. Batalha, J. Haqq-Misra, S. L. Grimm, and K. Heng. Habitable Moist Atmospheres on Terrestrial Planets near the Inner Edge of the Habitable Zone around M Dwarfs. *ApJ*, 845:5, August 2017. doi: 10.3847/1538-4357/aa7cf9.

E. Kotoneva, K. Innanen, P. C. Dawson, P. R. Wood, and M. M. De Robertis. A study of Kapteyn's star. *A&A*, 438:957–962, August 2005. doi: 10.1051/0004-6361:20042287.

Y. Kozai. Secular perturbations of asteroids with high inclination and eccentricity. *AJ*, 67:591, November 1962. doi: 10.1086/108790.

M. Kürster, M. Endl, F. Rouesnel, S. Els, A. Kaufer, S. Brillant, A. P. Hatzes, S. H. Saar, and W. D. Cochran. The low-level radial velocity variability in Barnard's star (= GJ 699). Secular acceleration, indications for convective redshift, and planet mass limits. *A&A*, 403:1077–1087, June 2003. doi: 10.1051/0004-6361:20030396.

K. R. Lang. *Astrophysical Formulae. A Compendium for the Physicist and Astrophysicist.* 1980.

G. Laughlin, P. Bodenheimer, and F. C. Adams. The Core Accretion Model Predicts Few Jovian-Mass Planets Orbiting Red Dwarfs. *ApJ*, 612:L73–L76, September 2004. doi: 10.1086/424384.

S. K. Leggett. Infrared colors of low-mass stars. *ApJS*, 82:351–394, September 1992. doi: 10.1086/191720.

S. Lépine and E. Gaidos. The northern census of M dwarfs within 100 pc, and its potential for exoplanet surveys. *Astronomische Nachrichten*, 334:176, February 2013. doi: 10.1002/asna.201211769.

M. L. Lidov. The evolution of orbits of artificial satellites of planets under the action of gravitational perturbations of external bodies. *Planet. Space Sci.*, 9:719–759, October 1962. doi: 10.1016/0032-0633(62)90129-0.

L. Lindegren and D. Dravins. The fundamental definition of "radial velocity". *A&A*, 401:1185–1201, April 2003. doi: 10.1051/0004-6361:20030181.

S. L. Lippincott. Parallax and orbital motion of the two nearby long period visual binaries Groombridge 34 and ADS 9090. *AJ*, 77:165–168, March 1972. doi: 10.1086/111261.

J. J. Lissauer. Urey prize lecture: On the diversity of plausible planetary systems. *Icarus*, 114:217–236, April 1995. doi: 10.1006/icar.1995.1057.

G. Lo Curto, F. Pepe, G. Avila, H. Boffin, S. Bovay, B. Chazelas, A. Coffinet, M. Fleury, I. Hughes, C. Lovis, C. Maire, A. Manescau, L. Pasquini, S. Rihs, P. Sinclaire, and S. Udry. HARPS Gets New Fibres After 12 Years of Operations. *The Messenger*, 162:9–15, December 2015.

N. R. Lomb. Least-squares frequency analysis of unequally spaced data. *Ap&SS*, 39:447–462, February 1976. doi: 10.1007/BF00648343.

C. Lovis and F. Pepe. A new list of thorium and argon spectral lines in the visible. *A&A*, 468:1115–1121, June 2007. doi: 10.1051/0004-6361:20077249.

C. Lovis, X. Dumusque, N. C. Santos, F. Bouchy, M. Mayor, F. Pepe, D. Queloz, D. Ségransan, and S. Udry. The HARPS search for southern extra-solar planets. XXXI. Magnetic activity cycles in solar-type stars: statistics and impact on precise radial velocities. *ArXiv e-prints*, July 2011a.

C. Lovis, D. Ségransan, M. Mayor, S. Udry, W. Benz, J.-L. Bertaux, F. Bouchy, A. C. M. Correia, J. Laskar, G. Lo Curto, C. Mordasini, F. Pepe, D. Queloz, and N. C. Santos. The HARPS search for southern extra-solar planets. XXVIII. Up to seven planets orbiting HD 10180: probing the architecture of low-mass planetary systems. *A&A*, 528:A112, April 2011b. doi: 10.1051/0004-6361/201015577.

R. Luger, R. Barnes, E. Lopez, J. Fortney, B. Jackson, and V. Meadows. Habitable Evaporated Cores: Transforming Mini-Neptunes into Super-Earths in the Habitable Zones of M Dwarfs. *Astrobiology*, 15:57–88, January 2015. doi: 10.1089/ast.2014.1215.

L. Malavolta, V. Nascimbeni, G. Piotto, S. N. Quinn, L. Borsato, V. Granata, A. S. Bonomo, F. Marzari, L. R. Bedin, M. Rainer, S. Desidera, A. F. Lanza, E. Poretti, A. Sozzetti, R. J. White, D. W. Latham, A. Cunial, M. Libralato, D. Nardiello, C. Boccato, R. U. Claudi, R. Cosentino, E. Covino, R. Gratton, A. Maggio, G. Micela, E. Molinari, I. Pagano, R. Smareglia, L. Affer, G. Andreuzzi, A. Aparicio, S. Benatti, A. Bignamini, F. Borsa, M. Damasso, L. Di Fabrizio, A. Harutyunyan, M. Esposito, A. F. M. Fiorenzano, D. Gandolfi, P. Giacobbe, J. I. González Hernández, J. Maldonado, S. Masiero, M. Molinaro, M. Pedani, and G. Scandariato. The GAPS programme with HARPS-N at TNG. XI. Pr 0211 in M 44: the first multi-planet system in an open cluster. *A&A*, 588:A118, April 2016. doi: 10.1051/0004-6361/201527933.

J. Maldonado, L. Affer, G. Micela, G. Scandariato, M. Damasso, B. Stelzer, M. Barbieri, L. R. Bedin, K. Biazzo, A. Bignamini, F. Borsa, R. U. Claudi, E. Covino, S. Desidera, M. Esposito, R. Gratton, J. I. González Hernández, A. F. Lanza, A. Maggio, E. Molinari, I. Pagano, M. Perger, I. Pillitteri, G. Piotto, E. Poretti, L. Prisinzano, R. Rebolo, I. Ribas, E. Shkolnik, J. Southworth, A. Sozzetti, and A. Suárez Mascareño. Stellar parameters of early-M dwarfs from ratios of spectral features at optical wavelengths. *A&A*, 577: A132, May 2015. doi: 10.1051/0004-6361/201525797.

J. Maldonado, G. Scandariato, B. Stelzer, K. Biazzo, A. F. Lanza, A. Maggio, G. Micela, E. González-Álvarez, L. Affer, R. U. Claudi, R. Cosentino, M. Damasso, S. Desidera, J. I. González Hernández, R. Gratton, G. Leto, S. Messina, E. Molinari, I. Pagano, M. Perger, G. Piotto, R. Rebolo, I. Ribas, A. Sozzetti, A. Suárez Mascareño, and R. Zanmar Sanchez. HADES RV Programme with HARPS-N at TNG . III. Flux-flux and activity-rotation relationships of early-M dwarfs. *A&A*, 598:A27, January 2017. doi: 10.1051/0004-6361/201629223.

E. E. Mamajek and L. A. Hillenbrand. Improved Age Estimation for Solar-Type Dwarfs Using Activity-Rotation Diagnostics. *ApJ*, 687:1264-1293, November 2008. doi: 10.1086/591785.

A. W. Mann, E. Gaidos, A. Kraus, and E. J. Hilton. Testing the Metal of Late-type Kepler Planet Hosts with Iron-clad Methods. *ApJ*, 770:43, June 2013. doi: 10.1088/0004-637X/770/1/43.

G. Marcy. Extrasolar planets: Water world larger than Earth. *Nature*, 462: 853–854, December 2009. doi: 10.1038/462853a.

G. W. Marcy and R. P. Butler. Precision radial velocities with an iodine absorption cell. *PASP*, 104:270–277, April 1992. doi: 10.1086/132989.

G. W. Marcy, V. Lindsay, J. Bergengren, and D. Moore. A dynamical search for sub-stellar objects. In M. C. Kafatos, R. S. Harrington, and S. P. Maran, editors, *Astrophysics of Brown Dwarfs*, pages 50–56, 1986.

G. W. Marcy, R. P. Butler, S. S. Vogt, D. Fischer, and J. J. Lissauer. A Planetary Companion to a Nearby M4 Dwarf, Gliese 876. *ApJ*, 505:L147–L149, October 1998. doi: 10.1086/311623.

G. W. Marcy, R. P. Butler, D. Fischer, S. S. Vogt, J. J. Lissauer, and E. J. Rivera. A Pair of Resonant Planets Orbiting GJ 876. *ApJ*, 556:296–301, July 2001. doi: 10.1086/321552.

G. W. Marcy, R. P. Butler, S. S. Vogt, D. A. Fischer, J. T. Wright, J. A. Johnson, C. G. Tinney, H. R. A. Jones, B. D. Carter, J. Bailey, S. J. O'Toole, and S. Upadhyay. Exoplanet properties from Lick, Keck and AAT. *Physica Scripta Volume T*, 130(1):014001, August 2008. doi: 10.1088/0031-8949/2008/T130/014001.

B. D. Mason, G. L. Wycoff, W. I. Hartkopf, G. G. Douglass, and C. E. Worley. The 2001 US Naval Observatory Double Star CD-ROM. I. The Washington Double Star Catalog. *AJ*, 122:3466–3471, December 2001. doi: 10.1086/323920.

M. Mayor and D. Queloz. A Jupiter-mass companion to a solar-type star. *Nature*, 378:355–359, November 1995. doi: 10.1038/378355a0.

M. Mayor, F. Pepe, D. Queloz, F. Bouchy, G. Rupprecht, G. Lo Curto, G. Avila, W. Benz, J.-L. Bertaux, X. Bonfils, T. Dall, H. Dekker, B. Delabre, W. Eckert, M. Fleury, A. Gilliotte, D. Gojak, J. C. Guzman, D. Kohler, J.-L. Lizon, A. Longinotti, C. Lovis, D. Megevand, L. Pasquini, J. Reyes, J.-P. Sivan, D. Sosnowska, R. Soto, S. Udry, A. van Kesteren, L. Weber, and U. Weilenmann. Setting New Standards with HARPS. *The Messenger*, 114:20–24, December 2003.

M. Mayor, X. Bonfils, T. Forveille, X. Delfosse, S. Udry, J.-L. Bertaux, H. Beust, F. Bouchy, C. Lovis, F. Pepe, C. Perrier, D. Queloz, and N. C. Santos. The HARPS search for southern extra-solar planets. XVIII. An Earth-mass planet in the GJ 581 planetary system. *A&A*, 507:487–494, November 2009. doi: 10.1051/0004-6361/200912172.

M. Mayor, M. Marmier, C. Lovis, S. Udry, D. Ségransan, F. Pepe, W. Benz, J. . Bertaux, F. Bouchy, X. Dumusque, G. Lo Curto, C. Mordasini, D. Queloz, and N. C. Santos. The HARPS search for southern extra-solar planets XXXIV. Occurrence, mass distribution and orbital properties of super-Earths and Neptune-mass planets. *ArXiv e-prints*, September 2011.

S. Messina, B. Monard, K. Biazzo, C. H. F. Melo, and A. Frasca. Evidence from stellar rotation of enhanced disc dispersal. I. The case of the triple visual system BD-21 1074 in the β Pictoris association. *A&A*, 570:A19, October 2014. doi: 10.1051/0004-6361/201423832.

N. Meunier and A.-M. Lagrange. Using the Sun to estimate Earth-like planets detection capabilities. IV. Correcting for the convective component. *A&A*, 551:A101, March 2013. doi: 10.1051/0004-6361/201219917.

S. Millholland and G. Laughlin. Constraints on Planet Nine's Orbit and Sky Position within a Framework of Mean-motion Resonances. *AJ*, 153:91, March 2017. doi: 10.3847/1538-3881/153/3/91.

J.-L. Monin, C. J. Clarke, L. Prato, and C. McCabe. Disk Evolution in Young Binaries: From Observations to Theory. *Protostars and Planets V*, pages 395–409, 2007.

C. Mordasini, Y. Alibert, and W. Benz. Extrasolar planet population synthesis. I. Method, formation tracks, and mass-distance distribution. *A&A*, 501:1139–1160, July 2009. doi: 10.1051/0004-6361/200810301.

C. Mordasini, Y. Alibert, W. Benz, H. Klahr, and T. Henning. Extrasolar planet population synthesis . IV. Correlations with disk metallicity, mass, and lifetime. *A&A*, 541:A97, May 2012. doi: 10.1051/0004-6361/201117350.

A. Mortier, N. C. Santos, A. Sozzetti, M. Mayor, D. Latham, X. Bonfils, and S. Udry. The frequency of giant planets around metal-poor stars. *A&A*, 543: A45, July 2012. doi: 10.1051/0004-6361/201118651.

A. Mortier, J. P. Faria, C. M. Correia, A. Santerne, and N. C. Santos. BGLS: A Bayesian formalism for the generalised Lomb-Scargle periodogram. *A&A*, 573:A101, January 2015. doi: 10.1051/0004-6361/201424908.

C. Moutou, A. Vigan, D. Mesa, S. Desidera, P. Thébault, A. Zurlo, and G. Salter. Eccentricity in planetary systems and the role of binarity. Sample definition, initial results, and the system of HD 211847. *A&A*, 602:A87, June 2017. doi: 10.1051/0004-6361/201630173.

N. Murray, B. Hansen, M. Holman, and S. Tremaine. Migrating Planets. *Science*, 279:69, January 1998. doi: 10.1126/science.279.5347.69.

R. Narayan, A. Cumming, and D. N. C. Lin. Radial Velocity Detectability of Low-Mass Extrasolar Planets in Close Orbits. *ApJ*, 620:1002–1009, February 2005. doi: 10.1086/426380.

A. F. Nelson and J. R. P. Angel. The Range of Masses and Periods Explored by Radial Velocity Searches for Planetary Companions. *ApJ*, 500:940–957, June 1998. doi: 10.1086/305741.

V. Neves, X. Bonfils, N. C. Santos, X. Delfosse, T. Forveille, F. Allard, C. Natário, C. S. Fernandes, and S. Udry. Metallicity of M dwarfs. II. A comparative study of photometric metallicity scales. *A&A*, 538:A25, February 2012. doi: 10.1051/0004-6361/201118115.

E. R. Newton, J. Irwin, D. Charbonneau, Z. K. Berta-Thompson, and J. A. Dittmann. The Impact of Stellar Rotation on the Detectability of Habitable Planets around M Dwarfs. *ApJ*, 821:L19, April 2016. doi: 10.3847/2041-8205/821/1/L19.

H. Ngo, H. A. Knutson, M. L. Bryan, S. Blunt, E. L. Nielsen, K. Batygin, B. P. Bowler, J. R. Crepp, S. Hinkley, A. W. Howard, and D. Mawet. No Difference in Orbital Parameters of RV-detected Giant Planets between 0.1 and 5 au in Single versus Multi-stellar Systems. *AJ*, 153:242, June 2017. doi: 10.3847/1538-3881/aa6cac.

R. W. Noyes, L. W. Hartmann, S. L. Baliunas, D. K. Duncan, and A. H. Vaughan. Rotation, convection, and magnetic activity in lower main-sequence stars. *ApJ*, 279:763–777, April 1984. doi: 10.1086/161945.

E. Oliva, L. Origlia, C. Baffa, C. Biliotti, P. Bruno, F. D'Amato, C. Del Vecchio, G. Falcini, S. Gennari, F. Ghinassi, E. Giani, M. Gonzalez, F. Leone, M. Lolli, M. Lodi, R. Maiolino, F. Mannucci, G. Marcucci, I. Mochi, P. Montegriffo, E. Rossetti, S. Scuderi, and M. Sozzi. The GIANO-TNG spectrometer. In *Society of Photo-Optical Instrumentation Engineers (SPIE) Conference Series*, volume 6269 of *Proc. SPIE*, page 626919, June 2006. doi: 10.1117/12.670006.

J. T. O'Malley-James and L. Kaltenegger. UV surface habitability of the TRAPPIST-1 system. *MNRAS*, 469:L26–L30, July 2017. doi: 10.1093/mnrasl/slx047.

B. Paczynski. Gravitational microlensing at large optical depth. *ApJ*, 301:503–516, February 1986. doi: 10.1086/163919.

F. Pepe, M. Mayor, B. Delabre, D. Kohler, D. Lacroix, D. Queloz, S. Udry, W. Benz, J.-L. Bertaux, and J.-P. Sivan. HARPS: a new high-resolution spectrograph for the search of extrasolar planets. In M. Iye and A. F. Moorwood, editors, *Optical and IR Telescope Instrumentation and Detectors*, volume 4008 of *Proc. SPIE*, pages 582–592, August 2000. doi: 10.1117/12.395516.

F. Pepe, M. Mayor, F. Galland, D. Naef, D. Queloz, N. C. Santos, S. Udry, and M. Burnet. The CORALIE survey for southern extra-solar planets VII. Two short-period Saturnian companions to ¡ASTROBJ¿HD 108147¡/ASTROBJ¿ and ¡ASTROBJ¿HD 168746¡/ASTROBJ¿. *A&A*, 388:632–638, June 2002. doi: 10.1051/0004-6361:20020433.

F. Pepe, C. Lovis, D. Ségransan, W. Benz, F. Bouchy, X. Dumusque, M. Mayor, D. Queloz, N. C. Santos, and S. Udry. The HARPS search for Earth-like planets in the habitable zone. I. Very low-mass planets around ¡ASTROBJ¿HD 20794¡/ASTROBJ¿, ¡ASTROBJ¿HD 85512¡/ASTROBJ¿, and ¡ASTROBJ¿HD 192310¡/ASTROBJ¿. *A&A*, 534:A58, October 2011. doi: 10.1051/0004-6361/201117055.

F. Pepe, A. C. Cameron, D. W. Latham, E. Molinari, S. Udry, A. S. Bonomo, L. A. Buchhave, D. Charbonneau, R. Cosentino, C. D. Dressing, X. Dumusque, P. Figueira, A. F. M. Fiorenzano, S. Gettel, A. Harutyunyan, R. D. Haywood, K. Horne, M. Lopez-Morales, C. Lovis, L. Malavolta, M. Mayor, G. Micela, F. Motalebi, V. Nascimbeni, D. Phillips, G. Piotto, D. Pollacco, D. Queloz, K. Rice, D. Sasselov, D. Ségransan, A. Sozzetti, A. Szentgyorgyi, and C. A. Watson. An Earth-sized planet with an Earth-like density. *Nature*, 503:377–380, November 2013. doi: 10.1038/nature12768.

M. Perger, A. García-Piquer, I. Ribas, J. C. Morales, L. Affer, G. Micela, M. Damasso, A. Suárez-Mascareño, J. I. González-Hernández, R. Rebolo, E. Herrero, A. Rosich, M. Lafarga, A. Bignamini, A. Sozzetti, R. Claudi, R. Cosentino, E. Molinari, J. Maldonado, A. Maggio, A. F. Lanza, E. Poretti, I. Pagano, S. Desidera, R. Gratton, G. Piotto, A. S. Bonomo, A. F. Martinez Fiorenzano, P. Giacobbe, L. Malavolta, V. Nascimbeni, M. Rainer, and G. Scandariato. HADES RV Programme with HARPS-N at TNG. II. Data treatment and simulations. *A&A*, 598:A26, February 2017a. doi: 10.1051/0004-6361/201628985.

M. Perger, I. Ribas, M. Damasso, J. C. Morales, L. Affer, A. Suárez Mascareño, G. Micela, J. Maldonado, J. I. González Hernández, R. Rebolo, G. Scandariato, G. Leto, R. Zanmar Sanchez, S. Benatti, A. Bignamini, F. Borsa, A. Carbognani, R. Claudi, S. Desidera, M. Esposito, M. Lafarga, A. F. Martinez Fiorenzano, E. Herrero, E. Molinari, V. Nascimbeni, I. Pagano, M. Pedani, E. Poretti, M. Rainer, A. Rosich, A. Sozzetti, and B. Toledo-Padrón. HADES RV Programme with HARPS-N at TNG VI. GJ 3942 b behind dominant activity signals. *ArXiv e-prints*, September 2017b.

M. Perryman. *The Exoplanet Handbook*. May 2011.

M. Pinamonti, A. Sozzetti, A. S. Bonomo, and M. Damasso. Searching for planetary signals in Doppler time series: a performance evaluation of tools for periodogram analysis. *MNRAS*, 468:3775–3784, July 2017. doi: 10.1093/mnras/stx664.

F. Pont, D. K. Sing, N. P. Gibson, S. Aigrain, G. Henry, and N. Husnoo. The prevalence of dust on the exoplanet HD 189733b from Hubble and Spitzer observations. *MNRAS*, 432:2917–2944, July 2013. doi: 10.1093/mnras/stt651.

E. Poretti, C. Boccato, R. Claudi, R. Cosentino, E. Covino, S. Desidera, R. Gratton, A. F. Lanza, A. Maggio, G. Micela, E. Molinari, I. Pagano, G. Piotto, R. Smareglia, A. Sozzetti, and GAPS Collaboration. Global Architecture of Planetary Systems (GAPS), a project for the whole Italian Community. *Mem. Soc. Astron. Italiana*, 87:141, 2016.

D. Queloz, G. W. Henry, J. P. Sivan, S. L. Baliunas, J. L. Beuzit, R. A. Donahue, M. Mayor, D. Naef, C. Perrier, and S. Udry. No planet for HD 166435. *A&A*, 379:279–287, November 2001. doi: 10.1051/0004-6361:20011308.

S. N. Quinn, R. J. White, D. W. Latham, L. A. Buchhave, J. R. Cantrell, S. E. Dahm, G. Fűrész, A. H. Szentgyorgyi, J. C. Geary, G. Torres, A. Bieryla, P. Berlind, M. C. Calkins, G. A. Esquerdo, and R. P. Stefanik. Two "b"s in the Beehive: The Discovery of the First Hot Jupiters in an Open Cluster. *ApJ*, 756:L33, September 2012. doi: 10.1088/2041-8205/756/2/L33.

A. Quirrenbach, P. J. Amado, J. A. Caballero, R. Mundt, A. Reiners, I. Ribas, W. Seifert, M. Abril, J. Aceituno, F. J. Alonso-Floriano, M. Ammler-von Eiff, R. Antona Jiménez, H. Anwand-Heerwart, M. Azzaro, F. Bauer, D. Barrado, S. Becerril, V. J. S. Béjar, D. Benítez, Z. M. Berdiñas, M. C. Cárdenas, E. Casal, A. Claret, J. Colomé, M. Cortés-Contreras, S. Czesla, M. Doellinger, S. Dreizler, C. Feiz, M. Fernández, D. Galadí, M. C. Gálvez-Ortiz, A. García-Piquer, M. L. García-Vargas, R. Garrido, L. Gesa, V. Gómez Galera, E. González Álvarez, J. I. González Hernández, U. Grözinger, J. Guàrdia, E. W. Guenther, E. de Guindos, J. Gutiérrez-Soto, H.-J. Hagen, A. P. Hatzes, P. H. Hauschildt, J. Helmling, T. Henning, D. Hermann, L. Hernández Castaño, E. Herrero, D. Hidalgo, G. Holgado, A. Huber, K. F. Huber, S. Jeffers, V. Joergens, E. de Juan, M. Kehr, R. Klein, M. Kürster, A. Lamert, S. Lalitha, W. Laun, U. Lemke, R. Lenzen, M. López del Fresno, B. López Martí, J. López-Santiago, U. Mall, H. Mandel, E. L. Martín, S. Martín-Ruiz, H. Martínez-Rodríguez, C. J. Marvin, R. J. Mathar, E. Mirabet, D. Montes, R. Morales Muñoz, A. Moya, V. Naranjo, A. Ofir, R. Oreiro, E. Pallé, J. Panduro, V.-M. Passegger, A. Pérez-Calpena, D. Pérez Medialdea, M. Perger, M. Pluto, A. Ramón, R. Rebolo, P. Redondo, S. Reffert, S. Reinhardt, P. Rhode, H.-W. Rix, F. Rodler, E. Rodríguez, C. Rodríguez-López, E. Rodríguez-Pérez, R.-R. Rohloff, A. Rosich, E. Sánchez-Blanco, M. A. Sánchez Carrasco, J. Sanz-Forcada, L. F. Sarmiento, S. Schäfer, J. Schiller, C. Schmidt, J. H. M. M. Schmitt, E. Solano, O. Stahl, C. Storz, J. Stürmer, J. C. Suárez, R. G. Ulbrich, G. Veredas, K. Wagner, J. Winkler, M. R. Zapatero Osorio, M. Zechmeister, F. J. Abellán de Paco, G. Anglada-Escudé, C. del Burgo, A. Klutsch, J. L. Lizon, M. López-Morales, J. C. Morales, M. A. C. Perryman, S. M. Tulloch, and W. Xu. CARMENES instrument overview. In *Ground-based and Airborne Instrumentation for Astronomy V*, volume 9147 of *Proc. SPIE*, page 91471F, July 2014. doi: 10.1117/12.2056453.

V. Rajpaul, S. Aigrain, and S. Roberts. Ghost in the time series: no planet for Alpha Cen B. *MNRAS*, 456:L6–L10, February 2016. doi: 10.1093/mnrasl/slv164.

C. E. Rasmussen and C. K. I. Williams. *Gaussian Processes for Machine Learning.* 2006.

I. N. Reid, S. L. Hawley, and J. E. Gizis. The Palomar/MSU Nearby-Star Spectroscopic Survey. I. The Northern M Dwarfs -Bandstrengths and Kinematics. *AJ*, 110:1838, October 1995. doi: 10.1086/117655.

A. Reiners, J. L. Bean, K. F. Huber, S. Dreizler, A. Seifahrt, and S. Czesla. Detecting Planets Around Very Low Mass Stars with the Radial Velocity Method. *ApJ*, 710:432–443, February 2010. doi: 10.1088/0004-637X/710/1/432.

I. Ribas. Masses and Radii of Low-Mass Stars: Theory Versus Observations. *Ap&SS*, 304:89–92, August 2006. doi: 10.1007/s10509-006-9081-4.

G. R. Ricker, J. N. Winn, R. Vanderspek, D. W. Latham, G. Á. Bakos, J. L. Bean, Z. K. Berta-Thompson, T. M. Brown, L. Buchhave, N. R. Butler,

R. P. Butler, W. J. Chaplin, D. Charbonneau, J. Christensen-Dalsgaard, M. Clampin, D. Deming, J. Doty, N. De Lee, C. Dressing, E. W. Dunham, M. Endl, F. Fressin, J. Ge, T. Henning, M. J. Holman, A. W. Howard, S. Ida, J. Jenkins, G. Jernigan, J. A. Johnson, L. Kaltenegger, N. Kawai, H. Kjeldsen, G. Laughlin, A. M. Levine, D. Lin, J. J. Lissauer, P. MacQueen, G. Marcy, P. R. McCullough, T. D. Morton, N. Narita, M. Paegert, E. Palle, F. Pepe, J. Pepper, A. Quirrenbach, S. A. Rinehart, D. Sasselov, B. Sato, S. Seager, A. Sozzetti, K. G. Stassun, P. Sullivan, A. Szentgyorgyi, G. Torres, S. Udry, and J. Villasenor. Transiting Exoplanet Survey Satellite (TESS). In *Space Telescopes and Instrumentation 2014: Optical, Infrared, and Millimeter Wave*, volume 9143 of *Proc. SPIE*, page 914320, August 2014. doi: 10.1117/12.2063489.

E. J. Rivera, G. Laughlin, R. P. Butler, S. S. Vogt, N. Haghighipour, and S. Meschiari. The Lick-Carnegie Exoplanet Survey: a Uranus-Mass Fourth Planet for GJ 876 in an Extrasolar Laplace Configuration. *ApJ*, 719:890–899, August 2010. doi: 10.1088/0004-637X/719/1/890.

P. Robertson, M. Endl, W. D. Cochran, and S. E. Dodson-Robinson. Hα Activity of Old M Dwarfs: Stellar Cycles and Mean Activity Levels for 93 Low-mass Stars in the Solar Neighborhood. *ApJ*, 764:3, February 2013. doi: 10.1088/0004-637X/764/1/3.

P. Robertson, S. Mahadevan, M. Endl, and A. Roy. Stellar activity masquerading as planets in the habitable zone of the M dwarf Gliese 581. *Science*, 345: 440–444, July 2014. doi: 10.1126/science.1253253.

P. Robertson, S. Mahadevan, M. Endl, and A. Roy. Response to Comment on "Stellar activity masquerading as planets in the habitable zone of the M dwarf Gliese 581". *Science*, 347:1080–1080, March 2015a. doi: 10.1126/science.1260974.

P. Robertson, A. Roy, and S. Mahadevan. Stellar Activity Mimics a Habitable-zone Planet around Kapteyn's Star. *ApJ*, 805:L22, June 2015b. doi: 10.1088/2041-8205/805/2/L22.

B. Rojas-Ayala, K. R. Covey, P. S. Muirhead, and J. P. Lloyd. Metal-rich M-Dwarf Planet Hosts: Metallicities with K-band Spectra. *ApJ*, 720:L113–L118, September 2010. doi: 10.1088/2041-8205/720/1/L113.

J. F. Rowe, S. T. Bryson, G. W. Marcy, J. J. Lissauer, D. Jontof-Hutter, F. Mullally, R. L. Gilliland, H. Issacson, E. Ford, S. B. Howell, W. J. Borucki, M. Haas, D. Huber, J. H. Steffen, S. E. Thompson, E. Quintana, T. Barclay, M. Still, J. Fortney, T. N. Gautier, III, R. Hunter, D. A. Caldwell, D. R. Ciardi, E. Devore, W. Cochran, J. Jenkins, E. Agol, J. A. Carter, and J. Geary. Validation of Kepler's Multiple Planet Candidates. III. Light Curve Analysis and Announcement of Hundreds of New Multi-planet Systems. *ApJ*, 784:45, March 2014. doi: 10.1088/0004-637X/784/1/45.

S. P. Ruden. The Formation of Planets. In C. J. Lada and N. D. Kylafis, editors, *NATO Advanced Science Institutes (ASI) Series C*, volume 540 of *NATO Advanced Science Institutes (ASI) Series C*, page 643, 1999.

N. C. Santos, G. Israelian, M. Mayor, J. P. Bento, P. C. Almeida, S. G. Sousa, and A. Ecuvillon. Spectroscopic metallicities for planet-host stars: Extending the samples. *A&A*, 437:1127–1133, July 2005. doi: 10.1051/0004-6361:20052895.

G. Scandariato, J. Maldonado, L. Affer, K. Biazzo, G. Leto, B. Stelzer, R. Zanmar Sanchez, R. Claudi, R. Cosentino, M. Damasso, S. Desidera, E. González Álvarez, J. I. González Hernández, R. Gratton, A. F. Lanza, A. Maggio, S. Messina, G. Micela, I. Pagano, M. Perger, G. Piotto, R. Rebolo, I. Ribas, A. Rosich, A. Sozzetti, and A. Suárez Mascareño. HADES RV Programme with HARPS-N at TNG. IV. Time resolved analysis of the Ca ii H K and Hα chromospheric emission of low-activity early-type M dwarfs. *A&A*, 598:A28, February 2017. doi: 10.1051/0004-6361/201629382.

J. D. Scargle. Studies in astronomical time series analysis. II - Statistical aspects of spectral analysis of unevenly spaced data. *ApJ*, 263:835–853, December 1982. doi: 10.1086/160554.

S. Seager and D. Deming. Exoplanet Atmospheres. *ARA&A*, 48:631–672, September 2010. doi: 10.1146/annurev-astro-081309-130837.

S. Seager and G. Mallén-Ornelas. A Unique Solution of Planet and Star Parameters from an Extrasolar Planet Transit Light Curve. *ApJ*, 585:1038–1055, March 2003. doi: 10.1086/346105.

D. Ségransan, M. Mayor, S. Udry, C. Lovis, W. Benz, F. Bouchy, G. Lo Curto, C. Mordasini, C. Moutou, D. Naef, F. Pepe, D. Queloz, and N. Santos. The HARPS search for southern extra-solar planets. XXIX. Four new planets in orbit around the moderatly active dwarfs ¡ASTROBJ¿HD 63765¡/ASTROBJ¿, ¡ASTROBJ¿HD 104067¡/ASTROBJ¿, ¡ASTROBJ¿HD 125595¡/ASTROBJ¿, and ¡ASTROBJ¿HIP 70849¡/ASTROBJ¿. *A&A*, 535:A54, November 2011. doi: 10.1051/0004-6361/200913580.

F. Selsis, J. F. Kasting, B. Levrard, J. Paillet, I. Ribas, and X. Delfosse. Habitable planets around the star Gliese 581? *A&A*, 476:1373–1387, December 2007. doi: 10.1051/0004-6361:20078091.

J. Setiawan, V. Roccatagliata, D. Fedele, T. Henning, A. Pasquali, M. V. Rodríguez-Ledesma, E. Caffau, U. Seemann, and R. J. Klement. Planetary companions around the metal-poor star HIP 11952. *A&A*, 540:A141, April 2012. doi: 10.1051/0004-6361/201117826.

Y. Shen and E. L. Turner. On the Eccentricity Distribution of Exoplanets from Radial Velocity Surveys. *ApJ*, 685:553-559, September 2008. doi: 10.1086/590548.

D. Sosnowska, M. Lodi, X. Gao, N. Buchschacher, A. Vick, J. Guerra, M. Gonzalez, D. Kelly, C. Lovis, F. Pepe, E. Molinari, A. C. Cameron, D. Latham, and S. Udry. HARPS-N: software path from the observation block to the image. In *Software and Cyberinfrastructure for Astronomy II*, volume 8451 of *Proc. SPIE*, page 84511X, September 2012. doi: 10.1117/12.926208.

S. G. Sousa, N. C. Santos, M. Mayor, S. Udry, L. Casagrande, G. Israelian, F. Pepe, D. Queloz, and M. J. P. F. G. Monteiro. Spectroscopic parameters for 451 stars in the HARPS GTO planet search program. Stellar [Fe/H] and the frequency of exo-Neptunes. *A&A*, 487:373–381, August 2008. doi: 10.1051/0004-6361:200809698.

J. Southworth, P. J. Wheatley, and G. Sams. A method for the direct determination of the surface gravities of transiting extrasolar planets. *MNRAS*, 379: L11–L15, July 2007. doi: 10.1111/j.1745-3933.2007.00324.x.

A. Sozzetti, G. Torres, D. Charbonneau, D. W. Latham, M. J. Holman, J. N. Winn, J. B. Laird, and F. T. O'Donovan. Improving Stellar and Planetary Parameters of Transiting Planet Systems: The Case of TrES-2. *ApJ*, 664: 1190–1198, August 2007. doi: 10.1086/519214.

A. Sozzetti, A. Bernagozzi, E. Bertolini, P. Calcidese, A. Carbognani, D. Cenadelli, J.-M. Christille, M. Damasso, P. Giacobbe, L. Lanteri, M. G. Lattanzi, and R. Smart. The APACHE Project. In *European Physical Journal Web of Conferences*, volume 47 of *European Physical Journal Web of Conferences*, page 03006, April 2013. doi: 10.1051/epjconf/20134703006.

A. Sozzetti, P. Giacobbe, M. G. Lattanzi, G. Micela, R. Morbidelli, and G. Tinetti. Astrometric detection of giant planets around nearby M dwarfs: the Gaia potential. *MNRAS*, 437:497–509, January 2014. doi: 10.1093/mnras/stt1899.

J. H. Steffen and J. A. Hwang. The period ratio distribution of Kepler's candidate multiplanet systems. *MNRAS*, 448:1956–1972, April 2015. doi: 10.1093/mnras/stv104.

O. Struve. Proposal for a project of high-precision stellar radial velocity work. *The Observatory*, 72:199–200, October 1952.

A. Suárez Mascareño, J. I. González Hernández, R. Rebolo, S. Velasco, B. Toledo-Padrón, L. Affer, M. Perger, G. Micela, I. Ribas, J. Maldonado, G. Leto, R. Zanmar Sanchez, G. Scandariato, M. Damasso, A. Sozzetti, M. Esposito, E. Covino, A. Maggio, A. F. Lanza, S. Desidera, A. Rosich, A. Bignamini, R. Claudi, S. Benatti, F. Borsa, M. Pedani, E. Molinari, J. C. Morales, E. Herrero, and M. Lafarga. HADES RV Programme with HARPS-N at TNG. V. A super-Earth on the inner edge of the habitable zone of the nearby M dwarf GJ 625. *A&A*, 605:A92, September 2017a. doi: 10.1051/0004-6361/201730957.

A. Suárez Mascareño, R. Rebolo, J. I. González Hernández, B. Toledo-Padrón, M. Perger, I. Ribas, L. Affer, G. Micela, M. Damasso, J. Maldonado, E. González-Alvarez, G. Leto, I. Pagano, G. Scandariato, A. Sozzetti, A. F. Lanza, L. Malavolta, R. Claudi, R. Cosentino, S. Desidera, P. Giacobbe, A. Maggio, M. Rainer, M. Esposito, S. Benatti, M. Pedani, J. C. Morales, E. Herrero, M. Lafarga, A. Rosich, and M. Pinamonti. HADES RV Programme with HARPS-N at TNG. VII. Rotation and activity of M-Dwarfs from time-series high-resolution spectroscopy of chromospheric indicators. *ArXiv e-prints*, December 2017b.

T. Sumi, D. P. Bennett, I. A. Bond, A. Udalski, V. Batista, M. Dominik, P. Fouqué, D. Kubas, A. Gould, B. Macintosh, K. Cook, S. Dong, L. Skuljan, A. Cassan, F. Abe, C. S. Botzler, A. Fukui, K. Furusawa, J. B. Hearnshaw, Y. Itow, K. Kamiya, P. M. Kilmartin, A. Korpela, W. Lin, C. H. Ling, K. Masuda, Y. Matsubara, N. Miyake, Y. Muraki, M. Nagaya, T. Nagayama, K. Ohnishi, T. Okumura, Y. C. Perrott, N. Rattenbury, T. Saito, T. Sako, D. J. Sullivan, W. L. Sweatman, P. J. Tristram, P. C. M. Yock, MOA Collaboration, J. P. Beaulieu, A. Cole, C. Coutures, M. F. Duran, J. Greenhill, F. Jablonski, U. Marboeuf, E. Martioli, E. Pedretti, O. Pejcha, P. Rojo, M. D. Albrow, S. Brillant, M. Bode, D. M. Bramich, M. J. Burgdorf, J. A. R. Caldwell, H. Calitz, E. Corrales, S. Dieters, D. Dominis Prester, J. Donatowicz, K. Hill, M. Hoffman, K. Horne, U. G. Jørgensen, N. Kains, S. Kane, J. B. Marquette, R. Martin, P. Meintjes, J. Menzies, K. R. Pollard, K. C. Sahu, C. Snodgrass, I. Steele, R. Street, Y. Tsapras, J. Wambsganss, A. Williams, M. Zub, PLANET Collaboration, M. K. Szymański, M. Kubiak, G. Pietrzyński, I. Soszyński, O. Szewczyk, Ł. Wyrzykowski, K. Ulaczyk, OGLE Collaboration, W. Allen, G. W. Christie, D. L. DePoy, B. S. Gaudi, C. Han, J. Janczak, C.-U. Lee, J. McCormick, F. Mallia, B. Monard, T. Natusch, B.-G. Park, R. W. Pogge, R. Santallo, and μFUN Collaboration. A Cold Neptune-Mass Planet OGLE-2007-BLG-368Lb: Cold Neptunes Are Common. *ApJ*, 710: 1641–1653, February 2010. doi: 10.1088/0004-637X/710/2/1641.

O. Tamuz, D. Ségransan, S. Udry, M. Mayor, A. Eggenberger, D. Naef, F. Pepe, D. Queloz, N. C. Santos, B.-O. Demory, P. Figuera, M. Marmier, and G. Montagnier. The CORALIE survey for southern extra-solar planets. XV. Discovery of two eccentric planets orbiting ¡ASTROBJ¿HD 4113¡/ASTROBJ¿ and ¡ASTROBJ¿HD 156846¡/ASTROBJ¿. *A&A*, 480:L33–L36, March 2008. doi: 10.1051/0004-6361:20078737.

A. M. Tanner, C. R. Gelino, and N. M. Law. A High-Contrast Imaging Survey of SIM Lite Planet Search Targets. *PASP*, 122:1195, October 2010. doi: 10.1086/656481.

J. C. Tarter, P. R. Backus, R. L. Mancinelli, J. M. Aurnou, D. E. Backman, G. S. Basri, A. P. Boss, A. Clarke, D. Deming, L. R. Doyle, E. D. Feigelson, F. Freund, D. H. Grinspoon, R. M. Haberle, S. A. Hauck, II, M. J. Heath, T. J. Henry, J. L. Hollingsworth, M. M. Joshi, S. Kilston, M. C. Liu, E. Meikle, I. N. Reid, L. J. Rothschild, J. Scalo, A. Segura, C. M. Tang, J. M. Tiedje, M. C. Turnbull, L. M. Walkowicz, A. L. Weber, and R. E. Young. A Reappraisal of The Habitability of Planets around M Dwarf Stars. *Astrobiology*, 7:30–65, March 2007. doi: 10.1089/ast.2006.0124.

T. C. Teixeira, H. Kjeldsen, T. R. Bedding, F. Bouchy, J. Christensen-Dalsgaard, M. S. Cunha, T. Dall, S. Frandsen, C. Karoff, M. J. P. F. G. Monteiro, and F. P. Pijpers. Solar-like oscillations in the G8 V star τ Ceti. *A&A*, 494:237–242, January 2009. doi: 10.1051/0004-6361:200810746.

A. Tokovinin and O. Kiyaeva. Eccentricity distribution of wide binaries. *MNRAS*, 456:2070–2079, February 2016. doi: 10.1093/mnras/stv2825.

G. Torres. Substellar Companion Masses from Minimal Radial Velocity or Astrometric Information: a Monte Carlo Approach. *PASP*, 111:169–176, February 1999. doi: 10.1086/316313.

T. Trifonov, M. Kürster, M. Zechmeister, L. Tal-Or, J. A. Caballero, A. Quirrenbach, P. J. Amado, I. Ribas, A. Reiners, S. Reffert, S. Dreizler, A. P. Hatzes, A. Kaminski, R. Launhardt, T. Henning, D. Montes, V. J. S. Béjar, R. Mundt, A. Pavlov, J. H. M. M. Schmitt, W. Seifert, J. C. Morales, G. Nowak, S. V. Jeffers, C. Rodríguez-López, C. del Burgo, G. Anglada-Escudé, J. López-Santiago, R. J. Mathar, M. Ammler-von Eiff, E. W. Guenther, D. Barrado, J. I. González Hernández, L. Mancini, J. Stürmer, M. Abril, J. Aceituno, F. J. Alonso-Floriano, R. Antona, H. Anwand-Heerwart, B. Arroyo-Torres, M. Azzaro, D. Baroch, F. F. Bauer, S. Becerril, D. Benítez, Z. M. Berdiñas, G. Bergond, M. Blümcke, M. Brinkmöller, J. Cano, M. C. Cárdenas Vázquez, E. Casal, C. Cifuentes, A. Claret, J. Colomé, M. Cortés-Contreras, S. Czesla, E. Díez-Alonso, C. Feiz, M. Fernández, I. M. Ferro, B. Fuhrmeister, D. Galadí-Enríquez, A. Garcia-Piquer, M. L. García Vargas, L. Gesa, V. Gómez Galera, R. González-Peinado, U. Grözinger, S. Grohnert, J. Guàrdia, A. Guijarro, E. de Guindos, J. Gutiérrez-Soto, H.-J. Hagen, P. H. Hauschildt, R. P. Hedrosa, J. Helmling, I. Hermelo, R. Hernández Arabí, L. Hernández Castaño, F. Hernández Hernando, E. Herrero, A. Huber, P. Huke, E. Johnson, E. de Juan, M. Kim, R. Klein, J. Klüter, A. Klutsch, M. Lafarga, M. Lampón, L. M. Lara, W. Laun, U. Lemke, R. Lenzen, M. López del Fresno, J. López-González, M. López-Puertas, J. F. López Salas, R. Luque, H. Magán Madinabeitia, U. Mall, H. Mandel, E. Marfil, J. A. Marín Molina, D. Maroto Fernández, E. L. Martín, S. Martín-Ruiz, C. J. Marvin, E. Mirabet, A. Moya, M. E. Moreno-Raya, E. Nagel, V. Naranjo, L. Nortmann, A. Ofir, R. Oreiro, E. Pallé, J. Panduro, J. Pascual, V. M. Passegger, S. Pedraz, A. Pérez-Calpena, D. Pérez Medialdea, M. Perger, M. A. C. Perryman, M. Pluto, O. Rabaza, A. Ramón, R. Rebolo, P. Redondo, S. Reinhardt, P. Rhode, H.-W. Rix, F. Rodler, E. Rodríguez, A. Rodríguez Trinidad, R.-R. Rohloff, A. Rosich, S. Sadegi, E. Sánchez-Blanco, M. A. Sánchez Carrasco, A. Sánchez-López, J. Sanz-Forcada, P. Sarkis, L. F. Sarmiento, S. Schäfer, J. Schiller, P. Schöfer, A. Schweitzer, E. Solano, O. Stahl, J. B. P. Strachan, J. C. Suárez, H. M. Tabernero, M. Tala, S. M. Tulloch, G. Veredas, J. I. Vico Linares, F. Vilardell, K. Wagner, J. Winkler, V. Wolthoff, W. Xu, F. Yan, and M. R. Zapatero Osorio. The CARMENES search for exoplanets around M dwarfs. First visual-channel radial-velocity measurements and orbital parameter updates of seven M-dwarf planetary systems. *ArXiv e-prints*, October 2017.

M. Tuomi and H. R. A. Jones. Probabilities of exoplanet signals from posterior samplings. *A&A*, 544:A116, August 2012. doi: 10.1051/0004-6361/201118114.

M. Tuomi, H. R. A. Jones, J. S. Jenkins, C. G. Tinney, R. P. Butler, S. S. Vogt, J. R. Barnes, R. A. Wittenmyer, S. O'Toole, J. Horner, J. Bailey, B. D. Carter, D. J. Wright, G. S. Salter, and D. Pinfield. Signals embedded in the radial velocity noise. Periodic variations in the τ Ceti velocities. *A&A*, 551: A79, March 2013. doi: 10.1051/0004-6361/201220509.

M. Tuomi, H. R. A. Jones, J. R. Barnes, G. Anglada-Escudé, and J. S. Jenkins. Bayesian search for low-mass planets around nearby M dwarfs - estimates for occurrence rate based on global detectability statistics. *MNRAS*, 441: 1545–1569, June 2014. doi: 10.1093/mnras/stu358.

S. Udry and M. Mayor. Exoplanets: The Golden Age of Radial Velocities. In D. Fischer, F. A. Rasio, S. E. Thorsett, and A. Wolszczan, editors, *Extreme*

Solar Systems, volume 398 of *Astronomical Society of the Pacific Conference Series*, page 13, 2008.

S. Udry, X. Dumusque, C. Lovis, D. Segransan, R. F. Diaz, W. Benz, F. Bouchy, A. Coffinet, G. Lo Curto, M. Mayor, C. Mordasini, F. Motalebi, F. Pepe, D. Queloz, N. C. Santos, A. Wyttenbach, R. Alonso, A. Collier Cameron, M. Deleuil, P. Figueira, M. Gillon, C. Moutou, D. Pollacco, and E. Pompei. The HARPS search for southern extra-solar planets. XXXVI. Eight HARPS multi-planet systems hosting 20 super-Earth and Neptune-mass companions. *ArXiv e-prints*, May 2017.

J. A. Valenti and D. A. Fischer. VizieR Online Data Catalog: Spectroscopic properties of cool stars. I. (Valenti+, 2005). *VizieR Online Data Catalog*, 215, November 2005.

D. van Buren, M. Brundage, M. Ressler, and S. Terebey. 10 Micron Search for Cool Companions of Nearby Stars. *AJ*, 116:1992–1997, October 1998. doi: 10.1086/300530.

A. Vanderburg, P. Plavchan, J. A. Johnson, D. R. Ciardi, J. Swift, and S. R. Kane. Radial velocity planet detection biases at the stellar rotational period. *MNRAS*, 459:3565–3573, July 2016. doi: 10.1093/mnras/stw863.

G. Vladilo, L. Silva, G. Murante, L. Filippi, and A. Provenzale. Modeling the Surface Temperature of Earth-like Planets. *ApJ*, 804:50, May 2015. doi: 10.1088/0004-637X/804/1/50.

S. S. Vogt, R. P. Butler, E. J. Rivera, N. Haghighipour, G. W. Henry, and M. H. Williamson. The Lick-Carnegie Exoplanet Survey: A 3.1 $M_\oplus$ Planet in the Habitable Zone of the Nearby M3V Star Gliese 581. *ApJ*, 723:954–965, November 2010. doi: 10.1088/0004-637X/723/1/954.

H.-H. Voigt. "Drei-Strom-Modell" der Sonnenphotosphäre und Asymmetrie der Linien des infraroten Sauerstoff-Tripletts. Mit 12 Textabbildungen. *Z. Astrophys.*, 40:157, 1956.

G. A. H. Walker, A. R. Walker, A. W. Irwin, A. M. Larson, S. L. S. Yang, and D. C. Richardson. A search for Jupiter-mass companions to nearby stars. *Icarus*, 116:359–375, August 1995. doi: 10.1006/icar.1995.1130.

J. Wang and D. A. Fischer. Revealing a Universal Planet-Metallicity Correlation for Planets of Different Sizes Around Solar-type Stars. *AJ*, 149:14, January 2015. doi: 10.1088/0004-6256/149/1/14.

A. A. West, K. L. Weisenburger, J. Irwin, Z. K. Berta-Thompson, D. Charbonneau, J. Dittmann, and J. S. Pineda. An Activity-Rotation Relationship and Kinematic Analysis of Nearby Mid-to-Late-Type M Dwarfs. *ApJ*, 812:3, October 2015. doi: 10.1088/0004-637X/812/1/3.

J. N. Winn and D. C. Fabrycky. The Occurrence and Architecture of Exoplanetary Systems. *ARA&A*, 53:409–447, August 2015. doi: 10.1146/annurev-astro-082214-122246.

J. G. Winters, T. J. Henry, J. C. Lurie, N. C. Hambly, W.-C. Jao, J. L. Bartlett, M. R. Boyd, S. B. Dieterich, C. T. Finch, A. D. Hosey, P. A. Ianna, A. R. Riedel, K. J. Slatten, and J. P. Subasavage. The Solar Neighborhood. XXXV. Distances to 1404 m Dwarf Systems Within 25 pc in the Southern Sky. *AJ*, 149:5, January 2015. doi: 10.1088/0004-6256/149/1/5.

M. Zechmeister and M. Kürster. The generalised Lomb-Scargle periodogram. A new formalism for the floating-mean and Keplerian periodograms. *A&A*, 496:577–584, March 2009. doi: 10.1051/0004-6361:200811296.

M. Zechmeister, M. Kürster, and M. Endl. The M dwarf planet search programme at the ESO VLT + UVES. A search for terrestrial planets in the habitable zone of M dwarfs. *A&A*, 505:859–871, October 2009. doi: 10.1051/0004-6361/200912479.

S. Zucker and T. Mazeh. On the Mass-Period Correlation of the Extrasolar Planets. *ApJ*, 568:L113–L116, April 2002. doi: 10.1086/340373.